ADVACING ORGANELLE ANALYSIS: DEVELOPMENT OF TECHNIQUES FOR THE ENRICHMENT OF ENDOCYTIC ORGANELLES AND TO DETERMINE AUTOPHAGOSOME PROPERTIES

A DISSERTATION

SUBMITTED TO THE FACULTY OF THE GRADUATE SCHOOL

OF THE UNIVERSITY OF MINNESOTA

BY

CHAD PATRICK SATORI

IN PARTIAL FULFILLMENT OF THE REQUIREMENTS

FOR THE DEGREE OF

DOCTOR OF PHILOSOPHY

EDGAR A. ARRIAGA, ADVISER

JULY, 2013

Acknowledgements

I would like to thank my advisor, Dr. Edgar Arriaga. His leadership and confidence in my abilities allowed me to be successful in my dissertation research at a level that I previously did not believe possible. From him, I have learned a great deal. This is a debt I will not be able to repay.

I would like to thank the numerous graduate students and post-docs whom I have interacted with during my years at the University of Minnesota. This includes the Arriaga lab members, past and present, who were willing to provide me feedback and advice. I would like to specifically note Vratislav Kostal and Yaohua Wang. I learned a great deal from both Vrata and Yaohua about making yourself a better scientist each day. I would also like to thank Deirdre Manion-Fischer for proof-reading this thesis.

I would like to thank the LaDora Thompson, Christy Haynes, Anna Maria Cuervo, and Do-Hyung Kim laboratories as well as Joe Dalluge, Joe Koopmeiners, Pete Carr, and Fang Zhou for their feedback and guidance given to me for the thesis work presented here.

I would like to thank the numerous funding agencies for financial support and Baxter Healthcare for awarding me with a Young Investigator Award in 2011.

Finally and most importantly, I would like to thank my family. I would like to thank my parents, Larry and Sharon Satori, who are my role models for work ethic and dedication. I would also like to thank my wife, Anne Satori, who is my daily motivation to succeed and grow.

Dedication

This thesis is dedicated to my father, whose battle inspired me to research.

Abstract

Lysosomes and endocytic organelles are intracellular bodies present in eukaryotic cells responsible for the degradation of endocytosed extracellular targets. Autophagosomes traffic proteins, organelles, and other intracellular components to lysosomes to facilitate degradation during the degradative process of autophagy. Multiple disorders have been connected to malfunctions in lysosomes (Nieman pick, galactosialidosis, Danon disease) and autophagosomes (Alzheimers, Parkinson's, Huntington's).

Methods are needed to enrich organelles in order to study their properties without contamination from unwanted organelles. Current methods to enrich endocytic organelles do not result in highly enriched organelles (differential centrifugation), are time consuming and tedious (density gradient centrifugation), and can damage membranes. Methods are also needed to determine endocytic and autophagy organelle properties such as organelle molecular composition, organelle-specific biotransformation of anti-cancer drugs, individual organelle surface properties and marker protein levels, and pH. The work described in this thesis develops new techniques to improve our ability to enrich endocytic organelles and determine their properties. This work includes: (1) the magnetic enrichment of endocytic organelles and determination of pH by capillary cytometry, (2) the determination of the biotransformation of N-L-leucyldoxorubicin to doxorubicin, (3) the development of a workflow to determine preliminary identifications of enriched autophagosome samples and (4) determine temporal changes in individual autophagy organelle numbers, surface charge, and LC3-II levels from basal and rapamycin enhanced autophagy levels. These methods will improve our understanding of how lysosomes and autophagosomes contribute to disease, leading to better therapeutic strategies that may improve and lengthen people's lives.

Endocytic organelle enrichment was done by trafficking dextran coated magnetic iron oxide nanoparticles to lysosomes and endocytic organelles prior to magnetic separation. No detectable enzymatic activity from mitochondria and peroxisomes were observed in the enriched endocytic organelle fractions suggesting that the enriched

lysosomes were in high enrichment. A majority of enriched, individual endocytic organelles had an acidic pH as determined by capillary cytometry suggesting the enriched endocytic organelle fraction had intact membranes. Enriched endocytic organelle fractions were then used to determine the biotransformation of N-*L*-leucyldoxorubicin to doxorubicin. Previous reports had suggested endocytic organelles may be important for intracellular biotransformation. About 45% of the biotransformation from uterine sarcoma cell post nuclear fraction occurred in the enriched endocytic organelle fraction suggesting intracellular biotransformation may be more critical to prodrug activation than previously believed.

Ultra high performance liquid chromatography coupled to near-simultaneous low- and high-collision energy mass spectrometry was used to determine preliminary identifications of compounds enriched or unique to enriched autophagosome fractions. A workflow was developed to detect and confirm features (unidentified compounds with a characteristic chromatographic t_R and *m/z* value) in the enriched sample as well as making and confirming identifications from online databases. Multiple high-relevancy preliminary identifications were made that are relevant to autophagy as supported by literature searches. Following validation, these preliminary identifications could prove to be important to maintain autophagosome function and autophagy.

Capillary electrophoresis coupled to laser induced fluorescence detection (CE-LIF) was used to determine temporal changes in the detected number of individual autophagy organelle events (phagophores, autophagosomes, amphisomes, and autolysosomes), of GFP-LC3-II levels, and of surface charge by CE-LIF. Pharmacological treatment with vinblastine was used to accumulate autophagosomes and phagophores from basal and rapamycin enhanced autophagy do detect temporal changes in autophagy organelles characteristic of the autophagy level and its autophagy flux. The dramatic contrast between time dependent changes in individual organelle properties between basal and rapamycin enhanced autophagy conditions demonstrates an anticipated complexity of autophagy flux which likely plays critical role in response to drug treatments, aging, and disease.

Table of Contents

List of Tables

List of Figures

List of Abbreviations

Atg: autophagy-related proteins

BCA: bicinchoninic acid protein assay

Boc-Leu-OSu: *tert*-butoxycarbonyl-L-leucine succinimide ester

BSA: bovine serum albumin

CE: Chemical Entities of biological interest

CE-LIF: Capillary electrophoresis coupled to laser induced fluorescence detection

CS: ChemSpider

CTAB: cetyltrimethylammonium bromide

DCIP: dichloroindophenol

DI: Deionized water

DMEM: Dulbecco's Modified Eagle Medium

DMSO: dimethyl sulfoxide

Dox: doxorubicin

EDTA: Ethylenediaminetetraacetic acid
EOF: electroosmotic flow

FeDex: dextran-coated superparamagnetic iron oxide nanoparticles

FTD: fluorescein/TMRM-conjugated dextran

GFP-LC3: green fluorescent protein conjugated to light chain 3 protein

HEPES: 4-(2-hydroxyethyl)-1-piperazineethanesulfonic acid

HM: Human Metabolome Database

hr: hour

I.D.: inner diameter

LAMP1: lysosome associated membrane protein

LC-MS: Liquid chromatography coupled to mass spectrometry

LeuDox: N-*L*-leucyldoxorubicin

LM: LipidMaps

LMM: linear mixed model

LOD: limit of detection

MEKC-LIF: Micellar electrokinetic chromatography with laser induced fluorescence detection

min: minute

MPMC: Murine peritoneal mast cells

O.D. outer diameter

OPLS-DA: Orthogonal partial least squares with discriminate analysis

PBS: phosphate buffered saline

PEA: phosphatidylethanolamine

pI: isoelectric point

PMT: photomultiplier tube

PNF: post nuclear fraction

pNPP: *para*-nitrophenylphosphatase

PVA: poly-vinyl alcohol

QQ plot: quantile-quantile plot

R123: Rhodamine 123 standard

RA: relative activity

R_s: resolution

RSD: relative standard deviation

SA: the total specific activity

sec: seconds

SD: succinate dehydrogenase

SOT: Statistical overlap theory

TEM: transmission electron microscopy

TMRM: tetramethylrhodamine

TMSI: Trimethylsilyl iodide

UPLC-MS^{e}: ultra high performance liquid chromatography coupled to simultaneous low- and high-collision energy mass spectrometry

WCH: whole cell homogenate

XIC: extracted ion chromatograms

Chapter 1

Thesis Overview

Lysosomes and endocytic organelles are responsible for degradation of cellular components. Lysosomes degrade components by endocytosis, a process which internalizes extracellular components. Similarly, autophagy degrades intracellular components. Deficiencies in both endocytosis and autophagy have been associated with aging, lysosomal storage diseases, neurodegenerative diseases, and cancer.[1-10] To determine how loss of proper autophagy and endocytic organelle function contributes to these different biological states, new methods are needed to enrich lysosome and fractions devoid of contaminations from unwanted organelles and to determine endocytic and autophagy organelle properties. Currently, the field is limited by methods that cannot produce enriched organelle fractions from various biological systems and without damaging endocytic organelle membranes. In addition, properties of individual endocytic and autophagy organelles such as electrophoretic mobility, fluorescent protein intensity, numbers of organelle detected events, pH of enriched organelles, and molecular composition have not yet been determined. These studies would provide the scientific community with new insights regarding the effects of modified autophagy flux on biological systems and the function of endocytosis and autophagy

There are limitations with the current techniques used to enrich endocytic organelles and determine autophagy organelle properties. Current techniques used to enrich endocytic organelles can require large amounts of starting material, result in fractions with contamination from unwanted organelles, or result in fractions with disrupted organelle membranes. The lack of enrichment techniques that overcome these limitations prevents studies of endocytic organelle properties such as the capability of an organelle to biotransform drugs and prodrugs.

The dynamic nature of autophagy and the multiple autophagy organelles involved make bulk measurements, such as those done by Western blotting, inadequate to understand autophagy and its roles in aging and disease. Analytical techniques that monitor time-dependent changes in the properties and numbers of individual autophagy organelles are highly needed. Temporal measurements are needed to determine the properties of autophagy organelles from different autophagy conditions by accumulating au

tophagosomes and phagophores from basal and rapamycin enhanced autophagy conditions.

Untargeted analysis of autophagosome composition also has not been performed. Improved understanding of autophagosome composition could expand the number of identified molecules that affect autophagosome function and autophagy levels. The analysis of subcellular composition provides insight regarding biological pathways occurring in organelles and how these pathways can affect proper organelle function. Most studies of organelle composition have been targeted analyses that limit the detection of molecular classes such as proteins.

The goal of this thesis was to develop new techniques to enrich endocytic organelles with no detectable organelle contamination and intact endocytic organelle membranes and to develop new techniques to determine autophagosome properties. Biotransformation of N-L-leucyldoxorubicin to doxorubicin, an anti-cancer prodrug, specific to enriched endocytic organelles was determined. A new method was developed to monitor temporal changes of individual autophagy organelle numbers and properties. Furthermore, a new methodology was developed to gain insights of the small molecule composition of enriched autophagosomes by a non-targeted liquid chromatography-coupled to mass spectrometry method and development of a workflow to make preliminary identifications of autophagosome-enriched fractions.

Chapter 2 begins with an introduction of endocytic organelle and autophagy-related organelles (organelle with LC3-II). The discussion includes an introduction to endocytosis and autophagy, the pathways responsible for degradation of extra- and intra-cellular components. Techniques and methodologies used to enrich and determine the properties of isolated endocytic organelles and autophagosomes are also discussed including why techniques were chosen for determination of organelle properties.

Prior techniques used to enrich endocytic organelles were not capable of producing fractions without unwanted organelles, maintain intact endocytic organelle membranes, and reduce the experimental time needed to enrich endocytic organelles to minimize the loss of enzymatic activity.[11-15] The work described in Chapter 3 describes a

method for enriching magnetically-labeled endocytic organelles. Collected endocytic organelle fractions did not have detectable enzymatic activity of both mitochondria and peroxisomes. Enriched organelles fractions also had intact membranes as indicated by their acidic pH, determined by capillary cytometry. This provides enriched endocytic organelle fractions that in future studies can be used for determination of endocytic organelle dynamics, metabolomics of endocytic organelles, and endocytic-organelle specific anti-cancer prodrug biotransformation as done in the work described in Chapter 4.

Previous studies have suggested the anti-cancer prodrug N-*L*-leucyldoxorubicin (LeuDox) is biotransformed to doxorubicin (Dox) outside whole cells[16-18] until recently when LeuDox was discovered to be biotransformed in a fraction containing endocytic organelles.[19] This fraction, however, also likely contained unwanted organelles such as mitochondria and peroxisomes because differential centrifugation was used to enrich the endocytic organelle fraction. This makes it difficult to determine to what extend the endocytic organelles were responsible for the biotransformation. The work described in Chapter 4 discusses the biotransformation of the LeuDox to Dox in highly enriched endocytic organelle fractions. Enriched endocytic organelle fractions were treated with LeuDox. Micellar electrokinetic chromatography with laser induced fluorescence detection (MEKC-LIF) was used to determine concentrations remaining of LeuDox and accumulated Dox. Biotransformation of LeuDox to Dox was confirmed to occur in the enriched endocytic organelle fraction. The combination of highly enriched organelle fractions and excellent limits of detection of MEKC-LIF allowed for the determination of LeuDox to Dox biotransformation in the endocytic organelle fraction. This suggests endocytic organelles are responsible for intracellular LeuDox biotransformation to Dox and suggests the intracellular biotransformation of endocytic organelles needs to be accounted for in prodrug and drug design.

The work described in Chapters 5 and 6 discuss the development of two methodologies to determine autophagosome properties. Proteins[6] and lipids[20] such as LC3,[21] the Atg proteins,[22-26] phosphatidylethanolamine,[27] and ceramide[28] have been previously identified in autophagosomes with targeted approaches. However, the

composition of autophagosomes has not been investigated by untargeted techniques which can detect additional molecules enriched and provide insight into autophagosome composition and autophagy function. The work described in Chapter 5 discusses the preliminary identifications of compounds enriched or unique to enriched autophagosome fractions by ultra high performance liquid chromatography coupled to simultaneous low- and high-collision energy mass spectrometry (UPLC-MS^e). A data analysis approach was developed to ensure that preliminary detected features had extracted ion chromatograms (XIC) with chromatographic peak profiles, detect daughter ions supporting database identifications, and confirm daughter ions have matching XICs with their parent ions. Overall, 187 features (unidentified compounds) and 34 preliminary identifications were detected in the enriched autophagosome fractions. These detected molecules will be validated and analyzed further in the future to determine their role in autophagosome function, their role in autophagy flux, and their role in autophagosome-related diseases.

Current techniques to monitor autophagy detect LC3-II levels in bulk or whole cells.[29-33] These techniques do not assess temporal changes in individual autophagy organelles following pharmacological treatment to accumulate autophagosomes and phagophores. The work described in Chapter 6 determines temporal changes in autophagy organelle properties from basal and rapamycin enhanced autophagy by CE-LIF. Vinblastine was used to accumulate autophagosomes and phagophores. Under basal autophagy conditions, there was a net accumulation of organelles, which mostly represent autophagosomes; because autolysosomes also degrade, the higher GFP-LC3 fluorescence and more positive electrophoretic mobility of individual organelles likely represent differences between these two organelle types. When autophagy was enhanced by rapamycin treatment, disappearance of autophagy organelles (autolysosomes) prevailed over formation of other autophagy organelles, the GFP-LC3 fluorescence of individual organelles decreased suggesting accumulation of organelles with lower levels of this marker, and the individual electrophoretic mobilities were more negative suggesting that organelles formed have a different surface composition. The dramatic contrast between time dependent changes in individual organelle properties between basal and rapamycin-

driven conditions demonstrates an anticipated complexity of autophagy flux which likely plays critical role in response to drug treatments, aging, and disease.

In conclusion, the developments in this thesis add significantly to the field of organelle analysis and may result in new studies to determine the role endocytic and autophagy organelles in aging and disease. Endocytic organelle enrichments can be used to determine the composition, organelle surface properties, and biotransformation of anti-cancer drugs specific to endocytic organelles. The determination of intracellular biotransformation of drugs and prodrugs and can be applied to other prodrugs that may not only be activated both extracellularly and intracellularly. Furthermore, this technique may be useful to determine other biotransformations that are attributed to lysosomes and other endocytic organelles. The composition of autophagosomes, autophagy organelle numbers, and autophagy organelle properties can give new insights of autophagosome function and autophagy levels.

Chapter 2

Introduction

This chapter describes endocytic and autophagy-related organelles including their relevant biological properties. Current techniques are described that enrich endocytic and autophagy-related organelles as well as techniques that monitor autophagy and detect unwanted organelles in enriched organelle samples. Finally, this chapter describes ultra high performance liquid chromatography coupled to mass spectrometry (UPLC-MS) and capillary electrophoresis coupled to laser induced fluorescence detection (CE-LIF). These two techniques were used to preliminarily identify molecules enriched in autophagosome fractions (described in Chapter 5) and to determine the characteristics of autophagy flux by accumulating autophagosomes and phagosomes from basal and rapamycin enhanced autophagy (described in Chapter 6), respectively.

2.1. Lysosomes and acidic organelles

Lysosomes are endocytic organelles that degrade extracellular and intracellular cargo accumulated by either endocytosis or autophagy, respectively. Lysosomes have an acidic pH (~5.0) caused by an accumulation of protons in their lumen. Numerous hydrolases, oxidases, and transferases are enzymes localized in the lysosomes responsible for lysosome's degradative properties. These enzymes are responsible for the degradation of proteins, polysaccharides, nucleic acids, lipids, and organelles.[2, 34, 35] Nonfunctioning or missing lysosomal enzyme activity or enzymes are responsible for many lysosome-associated diseases such as Tay-Sachs (missing β-hexosaminidase α-chain), Schindler disease type 1 (missing α-N-acetylgalactosaminidase), mannosidosis (missing lysosomal α-mannosidase), and Niemann-Pick types a and b (missing sphingomyelin phosphodiesterase).[36-39]

Endocytosis is responsible for degradation of extracellular components. Endocytosis, including phagocytosis, pinocytosis, and macropinocytosis, is categorized based on the size (> 1 μm for phagocytosis) and entry method of the endocytosed cargo (binding to specific surface receptors such as clathrin and caveolin or non-selective internalization; Figure 2.1).[40, 41] After internalization, components are trafficked to different intracellular routes. Some cargo is trafficked to both sorting and early endosomes for cargo marked for recycling while cargo marked for degradation, such as

carbohydrates like dextran, traffics to the early endosome, then to the late endosome, and finally to the lysosomes. Dextran coated nanoparticles are endocytosed by macropinocytosis due to the dextran coating of the particle[42] and trafficked to late endosomes and lysosomes.[43, 44] These nanoparticles were used in the experiments described in Chapter 3 to traffic magnetic dextran coated iron oxide nanoparticles to late endosomes and lysosomes to facilitate their magnetic enrichment. The iron oxide nanoparticle is magnetic and is attracted to an external magnetic field. This allows for organelles sequestered to magnetic nanoparticles to be enriched. Once localized in the lysosomes, lysosomal enzymes degrade the dextran coating and iron oxide nanoparticles after 6 hours, allowing for enrichment during that time.[45, 46]

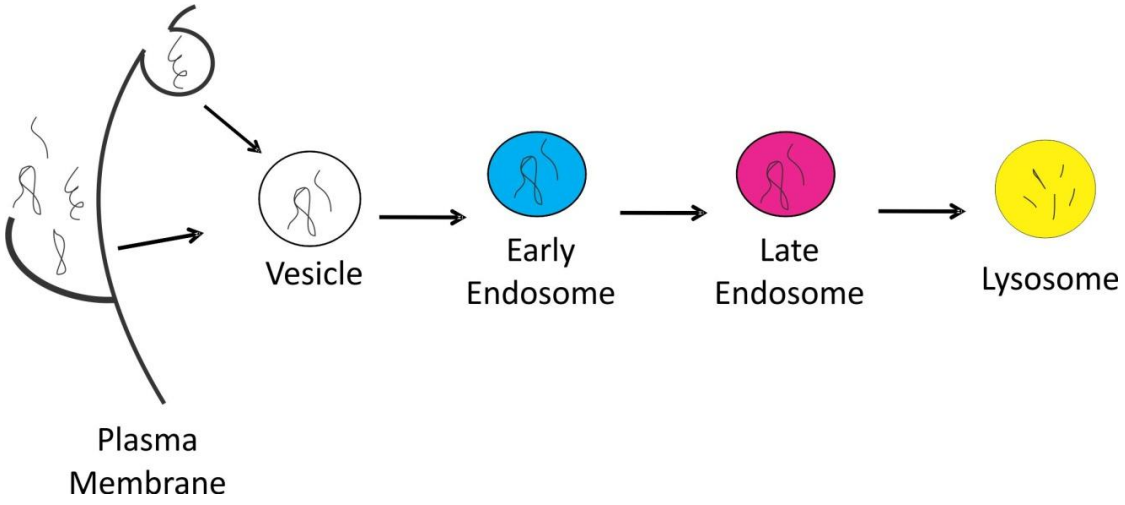

Figure 2.1. Relationship between endocytic organelles. Extracellular contents are endocytosed in a vesicle. The vesicle then matures to form, in sequential order, early endosomes, late endosomes, and lysosomes. Lysosomes are responsible for the degradation of both endocytosed and autophagocytosed contents.

Assessment of individual organelle pH following enrichment of endocytic organelles can indicate the lysosome lipid bilayer is intact because organelles with intact membranes may retain their acidic pH. The lysosome membrane is composed of a single lipid bilayer that contains v-type ATPases.[47] These ATPases cause accumulation of protons in the lysosome that decreases pH. If lysosome membranes are disrupted during enrichment, the proton gradient between the cytosol and lysosome lumen is lost and the

lysosome pH is increased. Following enrichment with dextran coated magnetic nanoparticles, the pH of enriched acidic organelles was determined using the ratio of a pH-dependent (fluorescein) and pH-independent (tetramethylrhodamine) fluorophores by capillary cytometry (described in Chapter 3).[48]

Weak bases are able to diffuse through lysosomal membranes into lysosomes and become positively charged which prevent their diffusion back to the cytosol.[49] Sequestration is due to the pK_a of weak bases being increased when compared to the pH of acidic organelles, as indicated by the Henderson-Hasselbalch equation (Equation 2.1) where [HB] and [B^-] are the protonated and de-protonated weak base, respectively.

$$pH = pK_a + \log\frac{[B]}{[HB^+]} \qquad \textbf{Equation 2.1.}$$

Considering the pH of lysosomes is generally 4-5, a majority of intracellular weak bases can be protonated and sequestered in the lysosome. These weak bases are defined as lysosomotropic agents,[49] an example of which is the fluorescent dyes Lysotracker Red (pK_a = 7.5) which is fluorescent upon protonation and drugs such as chloroquine (pK_a = 8.5).

Biotransformation of anti-cancer drugs in endocytic organelles is decreased for many drugs and cancer cell lines due to the increased pH of endocytic organelles. In some cancerous cell lines, the endocytic organelle pH is increased when compared to the endocytic organelle pH of non-cancerous cells.[49] This causes decreased trafficking of anti-cancer drugs into endocytic organelles of some cancerous cell lines.[49-52] Conversely, some anti-cancer drugs, such as N-*L*-leucyldoxorubicin (LeuDox, pK_a = 9.6) was believed to be biotransformed exclusively in the extracellular space.[16-18, 53] Recent evidence by the Arriaga lab has disputed this by suggesting intracellular LeuDox biotransformation occurs; increased biotransformation occurs in endocytic organelles.[19] Chapter 4 describes the determination of biotransformation of LeuDox to Dox specific to enriched endocytic organelle fractions.

2.2. Autophagosomes and autophagy-related organelles

Autophagosomes are involved in autophagy that, like endocytosis, is responsible for the degradation of intracellular cargo.[6, 54] During autophagy, autophagosomes accumulate functional and dysfunctional proteins, nucleic acids, lipids, and organelles. Perhaps the most distinct feature of autophagosomes is their double-membrane, lipid-bilayer.[55, 56] LC3-II is a protein localized on both sides of the membrane of autophagy-related organelles and is often used for monitoring either autophagy levels and/or autophagy flux in bulk samples.[57, 58] Lipidation of the isoform LC3-I with phosphatidylethanolamine produces the isoform LC3-II causing sequestration to the autophagy-related organelles (phagophores, autophagosomes, amphisomes, and autolysosomes, Figure 2.2). The work described in Chapter 5 uses LC3-II to monitor autophagosome organelle enrichment and the work described in Chapter 6 uses fluorescently labeled LC3-II to detect autophagy-related organelle events.

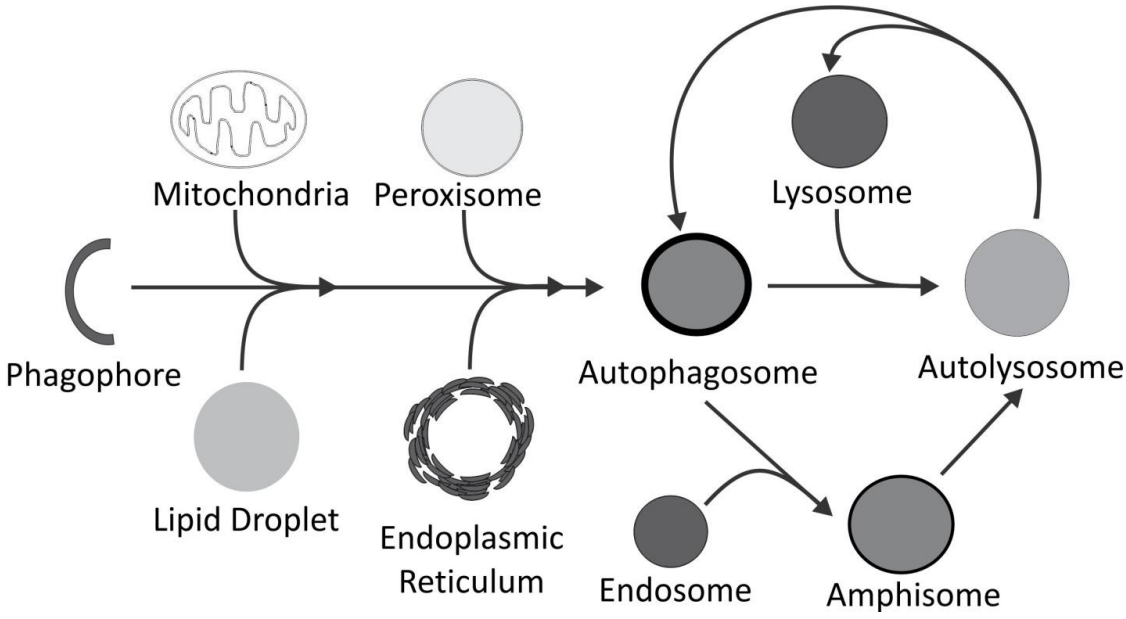

Figure 2.2. Relationship between autophagy organelles. Intracellular contents can be engulfed by a phagophore forming an autophagosome. The autophagosome then delivers its contents to autolysosomes by either fusion with lysosomes or fusion with endosomes to form amphisomes followed by maturation to autolysosomes. Following degradation, autolysosomes are recycled to form autophagosomes and lysosomes.

Autophagy can be divided into macroautophagy, microautophagy, and chaperone-mediated autophagy. During macroautophagy, phagophores form around cytosolic targets such as proteins and organelles (Figure 6.1). The phagophore membrane can originate from different subcellular locations such as the omegasome, which is a portion of the ER, mitochondria, Golgi, and plasma membrane. Therefore, autophagy organelles may have many different surface compositions.[59-62] Phagophores then form autophagosomes, membrane-bound organelles with internalized intracellular components. Autophagosomes then fuse with lysosomes to form autolysosomes where the sequestered components are degraded.[63, 64] This occurs through either (1) direct interaction with lysosomes to form autolysosomes where the hydrolases of the lysosome degrade the targets or (2) interaction with endosomes to form amphisomes followed by lysosome interaction.[65, 66] Following degradation, lysosomes are recycled form the autolysosome in a process defined as autophagic lysosome reformation[67] In microautophagy, intracellular components are delivered to pre-formed autophagosomes.[6, 8] In chaperone-mediated autophagy, intracellular components are delivered directly to lysosomes for degradation.[6, 68] Microautophagy and chaperone-mediated autophagy are not investigated in the work described in this thesis.

The Atg proteins are perhaps the best characterized components of autophagy organelles. These proteins were discovered in yeast using genetic screens by creating mutant cells with genetic knockdowns of Atg genes.[69] These cell lines had decreased protein degradation and electron microscopy was used to observe modified autophagosome morphology. Atg (autophagy-related) proteins were later discovered in mammalian cells[70] and led to the identification of protein complexes responsible for autophagosome formation.[71, 72] Lipids conjugated to proteins, such as LC3-II and phosphatidylethanolamine,[73] SNARE proteins, such as Sec9 and Tlg2,[74] and signaling proteins to mark degradation of other organelles,[75] such as Parkin,[76] were also discovered. These studies used Western blotting, fluorescence confocal microscopy, and thin layer chromatography to detect targeted molecules based on prior knowledge of the autophagosome composition in yeast and mammalian cells.

2.3. Techniques used to monitor autophagy flux

Autophagy flux is defined as the rate of sequestration of intracellular components and the rate of degradation of autophagocytosed cargo. Autophagocytosed cargo is degraded and trafficked to lysosomes in organelles possessing LC3-II. The disruption of basal autophagy flux (autophagy flux occurring in healthy cells) has been associated with Huntington's disease, Parkinson's disease, Alzheimer's disease, increased cancer rates, and aging.[6, 8, 9, 77, 78]

LC3-II has been used to monitor changes in autophagy. Because autophagy degradation requires autophagy-related organelles, LC3-II is formed and LC3-I levels decrease. Therefore, increased levels of LC3-II is indicative of increased numbers of autophagy organelles and increased autophagy levels.[57] Western blotting,[79] fluorescence confocal microscopy, and flow cytometry have all been used to assess autophagy levels. Western blotting qualitatively determines the levels of LC3-I and LC3-II in a biological system, however, the technique has limited sensitivity.[29] Issues also arise due to anti-LC3 antibodies with varying specificity for LC3-I and LC3-II detection.[29] Fluorescent-labeled LC3-II levels can be monitored by detecting punctates by fluorescence confocal microscopy.[31, 32, 65] Limitations of fluorescence confocal microscopy include discerning individual organelle punctates in images (from other organelles and diffuse, fluorescently labeled LC3-I) and LC3-I protein complexes which can be misidentified as autophagy-related organelles.[29, 80] Finally, flow cytometry has been used to monitor fluorescently labeled LC3-II levels in cells. Whole cells are treated with saponin to extract fluorescently-labeled LC3-I.[33] The GFP-LC3 fluorescence remaining following extraction is representative of GFP-LC3-II fluorescence and autophagy-related organelle levels. Similar limitations exist for flow cytometry as for fluorescence confocal microscopy and Western blotting.

Temporal measurements are used to determine the properties of autophagy organelles from different autophagy conditions. Pharmacological treatment with vinblastine halts autophagy just before the formation of autolysosomes.[81] For example, vinblastine treatment prevents autophagosomes and amphisomes from fusing with lysosomes due to microtubule degradation (Figure 2.2.).[81] This leads to accumulation of autophagosomes, phagophores, and a small number of amphisomes and the

disappearance of autolysosomes which are still recycled to lysosomes and LC3-I.[81, 82] The rates of accumulation and disappearance of numbers and properties of accumulated autophagy organelles can then be determined for different autophagy conditions.[83] Immunoblotting results in an increase in LC3-II signal when autophagosomes were accumulated for basal flux.[84] Enhancement of autophagy results in decreased GFP-LC3-II levels when compared to basal autophagy determined by immunoblotting.[83] Accumulation of autophagosomes by chloroquine treatment caused an accumulation of GFP-LC3-II levels as determined by flow cytometry.[33] The dynamic nature of autophagy and the multiple autophagy organelles involved make bulk measurements, such as those described above, inadequate to understand autophagy and its roles in aging and disease. The work described in Chapter 6 reports the first analysis of autophagy flux by CE-LIF and determining the properties of autophagosomes such as LC3-II levels and organelle surface charge under basal autophagy and rapamycin enhanced autophagy conditions.

2.4. Organelle enrichment

Organelle enrichment is done to eliminate unwanted, contaminating organelles and increase the level of desired organelles in collected fractions. In the absence of high organelle enrichments, organelle-specific properties cannot be determined. Organelle enrichment techniques used in this thesis are centrifugation, immunoenrichment, and magnetic-based techniques. Other techniques for organelle enrichment include free flow-based techniques, fluorescence activated organelle sorting, optical tweezers, and dielectrophoresis.[85] These techniques were not used in this thesis but are reviewed for the interested reader in our recent review.[85]

Differential centrifugation enriches organelles based on organelle sedimentation rate and density gradient centrifugation is based on isopycnic sedimentation rate (Equation 2.2) where d is the diameter of the organelle, ρ is the density of the organelle (ρ_o) and of the medium (ρ_m), g is the gravitational force, and μ is the medium viscosity. This is a common technique for enrichment of lysosomes and autophagosomes from tissue.[13, 14] From examining Equation 2.2, centrifugation-based enrichments are dependent on the size and density of the organelles being enriched.

$$sedimentation\ rate = \frac{d^2(\rho_o - \rho_m)}{18\mu} g$$ **Equation 2.2.**

Differential centrifugation typically produces three organelle fractions containing (1) nuclei and unbroken cells, (2) organelles, and (3) cytosol and cytosolic proteins (Figure 2.3). The technique is performed with a buffer that has similar osmolarity to isolated organelles and results in enriched organelles with intact membranes. The technique is also rapid compared to other enrichment techniques making it a desirable technique when high purity is not needed in the enriched fraction. This is often the case when specific organelles are labeled such as GFP-LC3 for autophagosomes. This technique was used to enrich organelles in the work described in Chapters 3, 5, and 6.

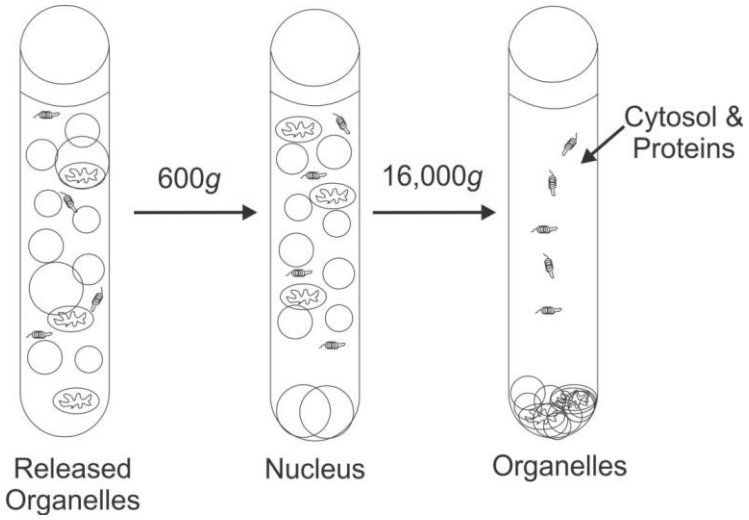

Figure 2.3. Differential centrifugation enrichment of organelles. The method results in three enriched organelle fractions: nuclei and unbroken cells, organelles, and cytosol.

Density gradient centrifugation is another common technique for organelle preparation and is similar to differential centrifugation but is done in a density gradient medium such as percoll or sucrose.[13] The gradient medium provides an isopycnic enrichment allowing organelles with different sedimentation rates to equilibrate in a portion of the density medium. As indicated by Equation 2.2, when the density of a medium approaches the organelle density, organelles can equilibrate in a specific portion, or band, of a medium. Density gradient centrifugation is capable of high enrichment of organelle types due to the gradient medium.

Large starting amounts of biological samples are needed for density gradient centrifugation due to the loss of material during each sample transfer and wash steps needed to remove the gradient medium, which makes the technique difficult to use for some cell culture preparations.[29] Enriched autophagosome and endocytic organelles may lose enzymatic activity, membrane integrity, and other functions due to the density media used or due to the time needed to perform the technique (density gradient centrifugation may exceed 4 hours).

Density gradient centrifugation with percoll medium was used in the work described in Chapter 3 and compared to the magnetic enrichment technique and density gradient centrifugation with Nycodenz medium was used to enrich autophagosomes in the work described in Chapter 5. Differential centrifugation was used in the work described in both Chapters 3 and 5 to remove nuclei and cytosol from un-enriched organelle fractions. Differential centrifugation was used in the work described in Chapter 6 to prepare an enriched autophagy-related organelle fraction and remove cytosol which contains GFP-LC3-I protein.

In the past decade, an influx of literature has been published discussing affinity-based enrichment techniques (Figure 2.4).[85] A majority of these techniques are immuno-based techniques with magnetic separations. Antibodies are raised against an organelle-specific protein and are conjugated to a molecule that facilitates its removal from the organelle suspension such as magnetic particles. After binding of the antibody to its organelle-specific protein, an external magnetic field can be applied causing separation of the magnetic fraction containing the targeted organelle. Immuno-enrichment provides excellent specificity for targeting organelles due to the antibody-protein interaction but is dependent on availability of antibodies for organelle-specific proteins. In addition to using the technique to enrich an organelle, it can also be used to remove an organelle from an enriched fraction. Determination of organelle electrophoretic mobility (the migration time of an organelle in an applied electric field during capillary electrophoresis) or organelle p*I* (isoelectric point of an organelle based on the many compounds localized on an organelle surface) are not ideal for immuno-based enrichment because antibodies can change these characteristics. Removal of antibodies while

maintaining the membranes of organelles is difficult. This technique was used in the work described in Chapter 5 to remove mitochondria from an autophagosome-enriched fraction.

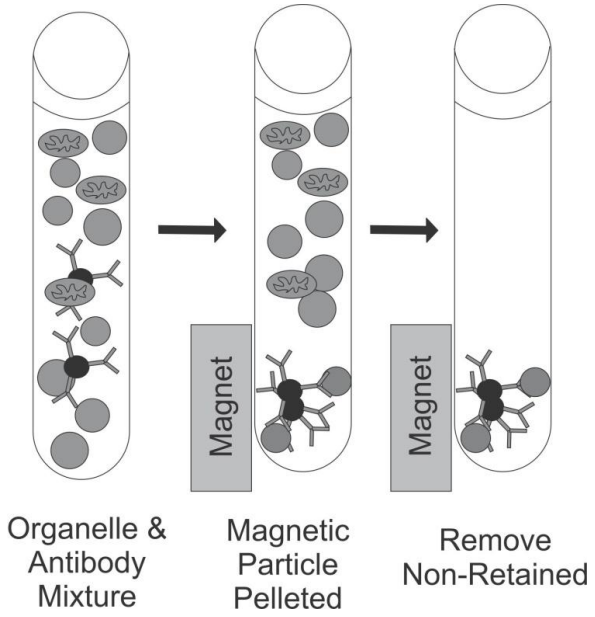

Figure 2.4. Immuno-enrichment of organelles with magnetic separation. Organelles (large gray spheres) are enriched by antibody-coated particles. Antibodies (Y-shaped molecules) are bound to magnetic particles (black spheres).

Various enrichment techniques have been developed for endocytic organelles and autophagosomes. Because endocytosis is able to internalize extracellular cargo and traffic the cargo to lysosomes, magnetic nanoparticles are capable of being trafficked directly to endocytic organelles. The use of magnetic nanoparticles to enrich acidic organelles on magnetic columns has excellent specificity, however, this technique has either caused damage to the endocytic organelle membrane due to the electromagnetic column[15] or endocytic organelle pH was not determined after enrichment.[11] This limits the endocytic organelle properties that can be investigated including prodrug biotransformation and examination of individual organelle pH. The work described in Chapter 3 utilizes dextran-coated iron oxide nanoparticles that are endocytosed to produce highly enriched endocytic organelle fractions. To ensure enriched organelles had intact membranes, organelle pH was determined by capillary cytometry.

Recent developments have also been made in autophagosome enrichment.[81] Enrichment was optimized by vinblastine treatment which prevents autophagosome fusion with autolysosomes and increased autophagosome yield. Glycyl-L-phenylnapthylamide, a substrate for a lysosome-specific enzyme, was used to cause osmotic rupture of lysosomes. A significant decrease in lysosome level was detected by Western blotting and accumulation of autophagosomes and amphisomes was attributed to vinblastine treatment. Vinblastine and glycyl-L-phenylnapthylamide were both used in the work described in Chapter 5 to increase autophagosome yield and remove unwanted lysosomes in enriched autophagosome fractions. Magnetic immunoaffinity-based selection of mitochondria was also used to remove unwanted mitochondria in enriched autophagosome fractions.

2.5. Organelle analysis

Methods are needed to determine organelle enrichment and to determine organelle properties such as pH, molecular composition, and surface charge, amongst others. In this thesis work, enzymatic assays, Western blotting, fluorescence confocal microscopy, and capillary cytometry with laser induced fluorescence detection were used to assess organelle enrichment. Two new methods were also developed using ultra high performance liquid chromatography coupled to low- and high-collision energy mass spectrometry (UPLC-MS^e) and CE-LIF to determine molecules enriched in autophagosomes (work described in Chapter 5) and autophagy flux (work described in Chapter 6), respectively. This section discusses techniques used for assessing organelle purity and instrumentation used to develop new methods for determining autophagosome composition and autophagy flux.

2.5.1. Examination of organelle enrichment

Enzymatic assays were used to quantify organelle enrichment and were used in the work described in Chapter 3 to determine that endocytic organelles were enriched in endocytic organelle fractions while mitochondria and peroxisome activity were not detectable. Substrates are modified by organelle-specific enzymatic reactions that indicate the presence of the organelle. The *para*-nitrophenylphosphatase (pNPP) assay

was used to determine the presence of lysosomes by the degradation of *para*-nitrophenol phosphate. The succinate dehydrogenase (SD) assay was used to determine the presence of mitochondria by the reduction of blue-colored dichloroindophenol. The catalase assay was used to determine the presence of peroxisomes by the degradation of hydrogen peroxide.

Western blotting is a technique used to detect organelle specific proteins in organelle enriched samples to confirm enrichment of the desired organelle and detect contamination from unwanted organelles. Western blotting was used in the work described in Chapter 5 to confirm organelle enrichment and detect contaminating organelles. Western blots have improved sensitivity for detecting very low levels of organelle contaminations compared to enzymatic assays but give limited quantitation due to their limited dynamic range (Section 2.3.).

2.5.2. Fluorescence confocal microscopy

Fluorescence confocal microscopy was used in this thesis as a benchmark technique for detecting organelles in intact cells (work described in Chapters 3 and 6), confirming that transfected proteins expressed fluorescence with the desired organelle-specific protein (work described in Chapter 6), and evaluating colocalization of endocytosed particles in organelles (work described in Chapter 3). Organelles were fluorescently labeled by transfection with plasmids containing genes for organelle-specific proteins conjugated to fluorescent fusion proteins such as green fluorescent protein (GFP), by fluorescent dyes that are sequestered into specific organelles such as LysoTracker in endocytic organelles, and by immuno-labeling with primary and fluorescently labeled secondary antibodies. Various fluorophores were used in this thesis work (Table 2.1). In the work described in Chapter 3, fluorescently labeled dextran coated iron oxide nanoparticles were confirmed to traffic to endocytic organelles by monitoring fluorescent overlap with LysoTracker Red fluorescence.[46] Statistical parameters such as the Manders, Pearson's Correlation, M2 coefficient, and ICQ correlation were used to determine overlap of LysoTracker Red fluorescence and

AlexaFluor 568 dextran-coated iron oxide nanoparticles to confirm the nanoparticles had localized in the endocytic organelles.[86]

Fluorescence confocal microscopy was used as previously discussed to examine autophagy levels[30-32] and to determine endocytic organelle pH.[48, 87] Fluorescence confocal microscopy has disadvantages including limited throughput to detect multiple organelles, limited organelle resolution preventing individual organelle detection after cell lysis, and the need for z-scans to confirm observation of single organelles.[29, 88] These disadvantages make fluorescence confocal microscopy difficult to determine individual organelle properties and make other techniques, such as CE-LIF, more advantageous

Fluorophore	Organelles	Conjugation	Excitation (nm) /Emission (nm)
AlexaFluor488	Endocytic	Dextran coated iron oxide nanoparticles	495 /519
Lysotracker Red	Endocytic	None	577 /590
Tetramethylrhodamine	Endocytic	Dextran	550 /580
Fluorescein	Endocytic	Dextran	480 /520
Green Fluorescent Protein (GFP)	Autophagosomes	GFP-LC3 fusion protein	395 and 470 /510
AlexaFluor568	Autophagosomes	Anti-LC3 secondary antibody	578 /603
4’6-diamidino-2-phenylindole (DAPI)	Nucleus	None	358 /461

Table 2.1. Fluorophores used in thesis.

2.5.3. Capillary electrophoresis with laser induced fluorescence detection

CE-LIF is used in this thesis for determination of LeuDox biotransformation (work described in Chapter 4) and individual autophagy-related organelle analysis (work described in Chapter 5). For organelle analysis, isolated organelles are injected into a

coated fused-silica capillary and separated in an electric field. The separation of organelles by CE-LIF is dependent on the surface charge of the organelle while other forces such as deformation of the ionic cloud surrounding the organelle have a limited effect as shown by the Arriaga lab.[89] Following separation, organelles exit the capillary and are detected with laser induced fluorescence detection.

CE-LIF injections (either electrokinetic or pressure-driven) can be as low as nanoliters, requiring small amounts of sample.[90] CE-LIF also has excellent limits of detection which approach sub-zeptomolar levels for fluorescent particles and organelles.[90] The combination of low injection volume, excellent limits of detection, and high throughput allows for individual organelle detection, which, in turn, allows for the diversity of organelles to be determined.[90]

The fused silica surface of capillaries is capable of adsorbing organelles due to the negative charge of the capillary and hydrophobic interactions with the basic proteins located on organelle surfaces.[91] To prevent this unwanted interaction, both permanent and transient coatings of poly(vinyl alcohol) have been used.[91] Both types of coatings reduce organelle-capillary interactions, however, transient coatings require reapplication in-between separations.[91] Poly(vinyl alcohol) was used as a permanent coating in the work described in Chapter 6 and a temporary coating was used in the work described in Chapter 3. The sheath flow-LIF detector provides excellent limits of detection (Figure 2.5).[92-94] Following separation, organelles enter a sheath-flow cuvette which focuses organelles into a narrow fluid stream. Excitation of fluorescently-labeled organelles occurs in the sheath flow cuvette. Two-channel fluorescence detection is possible by use of a dichroic mirror that splits different fluorescent wavelengths into perpendicular paths. Notch filters are used to reject a portion of the light spectrum removing interference from specific wavelengths of light, such as the wavelength of light of the laser. In the work described in this thesis, the notch filter rejected light from the 488-nm excitation laser. Band pass filters are used to filter and remove wavelengths of light not specific to the fluorophore being detected ensuring that only the desired wavelength is detected. This also removes light scattering from both Raleigh and Raman sources, which are also removed by notch filters. Light scattering is also removed spatially by pinhole filters, and

LIF detection at a 90° angle to excitation. Photomultiplier tubes are used to detect the emitted fluorescence. Data is digitized by a data board that allows for data points to be collected at 200 Hz. This data acquisition rate allows for multiple data points to be acquired for a single organelle peak and allowing organelle peak profiles to be well characterized. Overall, the combination of the sheath flow cuvette, notch and band pass filters, and data acquisition capabilities allows for fluorescence detection of single organelles.

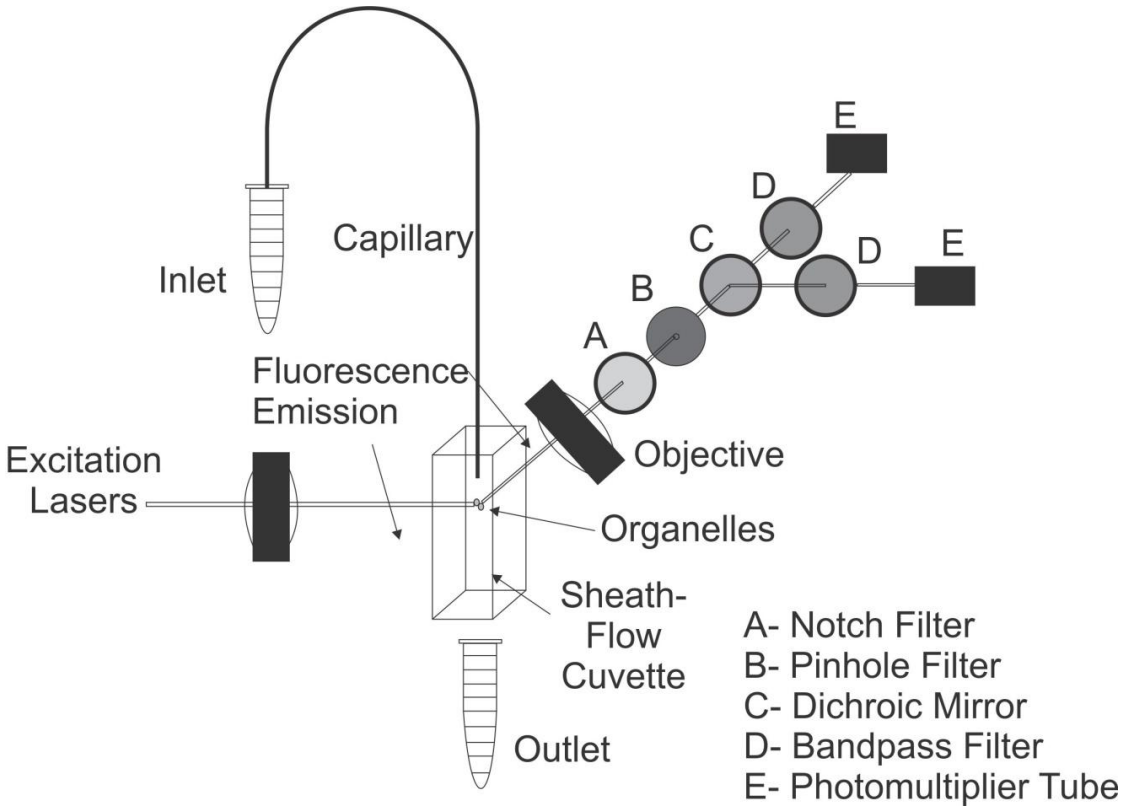

Figure 2.5. CE-LIF instrument design.

A similar instrument setup was used to examine the pH of enriched endocytic organelle fractions in the work described in Chapter 3 defined here as capillary cytometry. Isolated organelles are flowed through the capillary so determination of individual organelle fluorescence intensity can be determined. In the work described in Chapter 3, only the ratio of pH-dependent and pH-independent fluorescence emission is needed to determine individual endocytic organelle pH values.

2.5.4. Micellar electrokinetic chromatography

Micellar electrokinetic chromatography (MEKC) was used in the work described in Chapter 4 to separate N-L-leucyldoxorubicin and doxorubicin. CE buffers include charged species that create a diffuse layer on the capillary surface which is partially responsible for electroosmotic flow. In MEKC, the buffer also contains detergents that form micelles. The concentration of detergents exceeds the critical micelle concentration ensuring micelles are formed. The micelles allow for analytes with similar mass/size ratios, such as N-L-leucyldoxorubicin and doxorubicin, to be separated based upon their hydrophobicity. Different analytes may have different hydrophobicity and therefore partition into micelles with different rate constants. Since micelles have an electrophoretic mobility, an analyte that is partitioned into a micelle at a higher rate can be separated from an analyte that is either not partitioned or partitions at a lower rate into a micelle.

2.5.5. Organelle heterogeneity analysis

Organelle heterogeneity can be assessed with CE-LIF due to the capability of detecting individual organelles. Organelle heterogeneity is described as the range of values detected for individual organelle property measurements. Previously, heterogeneity was determined using other techniques such as transmission electron microscopy[95] and fluorescence confocal microscopy.[48] These techniques are not high throughput, however, and are limited in the properties of organelles that can be determined. CE-LIF instrumentation can determine the properties (fluorescent-protein level, electrophoretic mobility, pH) of individual organelles. Furthermore, thousands of organelles can be detected by CE-LIF. The Arriaga lab has examined the heterogeneity of mitochondria,[93, 96-103] nuclei,[104] and endocytic organelles.[48, 87, 105-107] Heterogeneity of mitochondria electrophoretic mobility,[93, 96] DNA copy numbers,[101] p*I*,[103] levels of reactive oxygen species,[106] cytoskeleton binding,[99] and nuclei electrophoretic mobility[104] have all been determined. The heterogeneity of endocytic organelles' fluorescent intensity and electrophoretic mobility was determined following labeling by endocytosed fluorescent microspheres.[107] Individual pH measurements of acidic organelles were

performed by CE-LIF from multiple cells[48] and from single cells using AlexaFluor488-bound dextran.[48, 87] The heterogeneity of doxorubicin levels in endocytic organelles, mitochondria, and nuclei was also determined.[106] To date, no studies have examined individual autophagy-related organelles properties by CE-LIF. The work described in Chapter 6 discusses the first determination of individual autophagosome properties (GFP-LC3-II levels and electrophoretic mobility). Thousands of organelles were detected.

2.5.6. Liquid chromatography coupled to mass spectrometry

Liquid chromatography coupled to mass spectrometry (LC-MS) is an attractive technique for studying the biological composition of samples. LC-MS provides excellent coverage of features (unidentified compounds with a characteristic chromatographic t_R and *m/z* value) enriched in a biological system. UPLC has increased pressure (flow rates exceeding 7 mm/sec) and decreased particle size (1.7 μm) packed in the column to improve resolution of adjacent chromatographic peaks allowing improved detection of features compared to high performance liquid chromatography (5-6 mm/sec flow rates; 3.5-10 μm particle size).[108] Following chromatographic separation, features are detected by mass spectrometry. Electrospray ionization (ESI) is used to ionize analytes producing multiply-charged ions. ESI is well suited for studying the biological composition of samples as minimal daughter ions are produced which allows compounds to be intact and studied in the mass spectrometer.[109] Quadrupole mass spectrometers with time of flight mass analyzers are commonly used for proteomic and metabolomic experiments due to their combination of mass accuracy and ability to fragment parent ions into daughter ions.[110]

MS^e acquires both low- and high-collision energy mass spectra.[111] Parent ions are continuously emitted from the quadrupole and enter the helium collision-induced dissociation cell. This cell alternates between low collision energy and high collision energy resulting in low- and high-collision energy mass spectra for all parent ions eluting from the UPLC column and entering the quadrupole at a given time. High collision energy results in fragmented parent ions and produces daughter ions specific to their parent ion. MS^e does not produce daughter ions for a specific parent ion but rather

produces numerous daughter ions for any parent ions eluted from the quadrupole at a given time. The advantages of this method include reduced experiment time compared to MS^2 and production of daughter ions that provide evidence for preliminary identifications. One drawback is that daughter fragments can be produced from multiple parent ions. Extracted ion chromatograms of parent and daughter ions can be compared. If the profiles of extracted ion chromatograms are identical, the daughter can be assigned to a parent ion. The instrument used in the work described in Chapter 5 is shown in Figure 2.6. UPLC-MS^e was used in the work described in Chapter 5 to preliminarily identify features from enriched autophagosome samples.

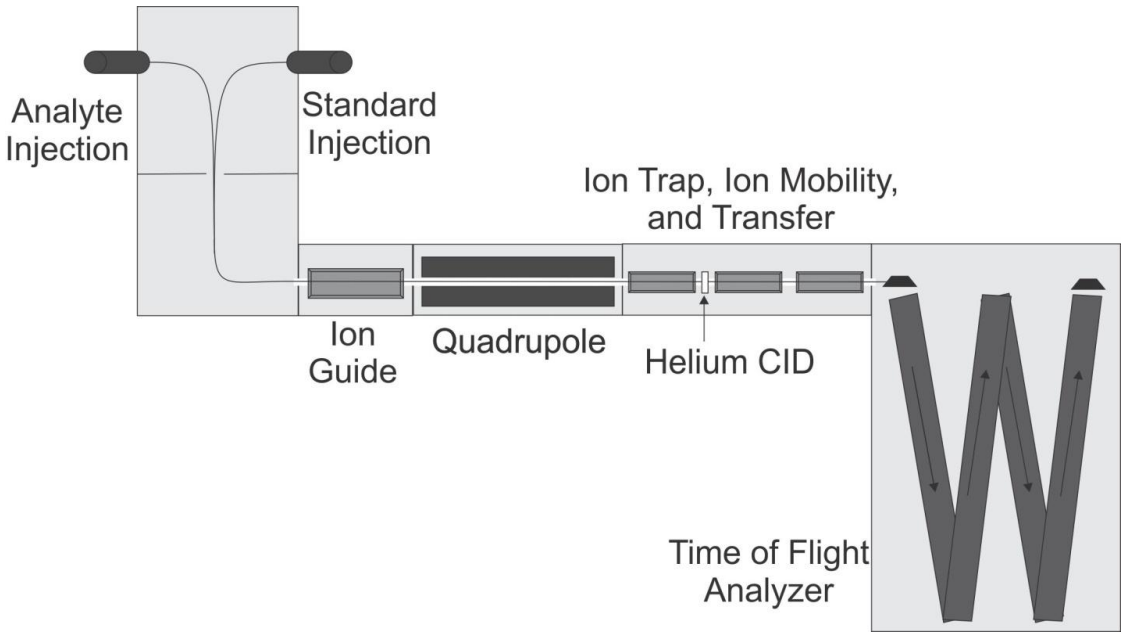

Figure 2.6. Block diagram of quadrupole-time of flight mass spectrometer used in the work described in Chapter 5.

2.5.7. Biological composition of autophagosomes

Most studies investigating the composition of autophagosomes have focused on targeted proteins as described in 2.3.[69-76] Non-targeted techniques have been used to determine the molecular composition of other enriched organelle fractions such as both chloroplasts and mitochondria,[112] vacuoles,[113] both mitochondria and vacuoles,[114] mitochondria,[115-118] and lipid droplets by liquid chromatography coupled to mass

spectrometry.[119, 120] Despite the study of other enriched organelle fractions, non-targeted techniques have not been applied to enriched autophagosome fractions. The work described in Chapter 5 describes the first study of autophagosome composition with an untargeted approach by UPLC-MS^e.

2.6. Summary

The work described in Chapter 3 discusses the development of a technique using dextran coated magnetic nanoparticles to enrich endocytic organelles with no detectable peroxisomes or mitochondria and with a majority of enriched endocytic organelles with acidic pH indicating endocytic organelle membranes are intact. The work described in Chapter 4 uses the technique described in Chapter 3 to determine endocytic organelle-specific biotransformations of N-*L*-leucyldoxorubicin to doxorubicin to by MEKC-LIF. The work described in Chapter 5 uses UPLC-MS^e to determine the composition of enriched autophagosome fractions. The work described in Chapter 6 uses CE-LIF to determine the number of detected autophagy-related organelle events and their properties from basal autophagy and rapamycin-enhanced autophagy.

Chapter 3

Individual organelle pH determinations of magnetically-enriched endocytic organelles via laser-induced fluorescence detection

Vratislav Kostal assisted in alignment of the capillary cytometry instrument. This work was supported by NIH grant RO1 AG020866 and NIH grant T32 GM8347. T.E.M. was carried out at the Institute of Technology Characterization Facility, University of Minnesota, member of the NSF-funded Materials Research Facilities Network. Hysteresis loop experiments were performed at the University of Minnesota Institute of Rock Magnetism. The authors would like to thank the Lee Penn laboratory for access to their x-ray diffraction equipment and the Christy Haynes laboratory for access to light scattering equipment.

The analysis of biotransformations that occur in lysosomes and other endocytic organelles is critical to studies on intracellular degradation, nutrient recycling and lysosomal storage disorders. Such analyses require bioactive organelle preparations that are devoid of other contaminating organelles. Commonly used differential centrifugation techniques produce impure fractions and may not compatible with micro-scale separation platforms. Density gradient centrifugation procedures reduce the level of impurities but may compromise bioactivity. Here we report on simple magnetic setup and a procedure that produce highly enriched bioactive organelles based on their magnetic capture as they traveled through open tubes. Following capture, in-line laser-induced fluorescence detection (LIF) determined for the first time that each magnetically retained individual endocytic organelles have an acidic pH. Unlike bulk measurements, this method was suitable to describe the distributions of pH values in endocytic organelles from L6 rat myoblasts treated with dextran-coated iron oxide nanoparticles (for magnetic retention) and fluorescein/TMRM-conjugated dextran (for pH measurements by LIF). Their individual pH values ranged from 4 to 6, which is typical of bioactive endocytic organelles. These analytical procedures are of high relevance to evaluate lysosomal-related degradation pathways in aging, storage disorders and drug development.

3.1. Introduction

Lysosomes are organelles that degrade endocytosed material[121] such as proteins,[3, 122] lipids,[123] fatty acids,[124] and carbohydrates.[122] These organelles play important roles in drug metabolism, biotransformation, reactive oxygen species production, autophagy, and lysosomal storage disorders.[125-128] Lack of lysosomal function can lead to many diseases (e.g. Fabry's,[129] Gaucher's,[130] and Niemann-Pick disease).[127] Lysosomes are also important in Alzheimer's disease,[131] because it has been shown that degradation of β-amyloid inside lysosomes may lead to novel disease treatments.

Investigating such roles and biological function of lysosomes usually involves studies done on enriched isolated lysosomes, devoid of other contaminating organelle types. For instance, proteomic studies aiming at identifying lysosomal proteomes usually require extensive lysosomal isolation procedures prior to proteomic analysis.[132-134]

Another example is the detection of reactive oxygen species in lysosomes that requires these organelles to be functional and free of contaminating mitochondria.[106, 125, 135] Lastly, many xenobiotics, such as penicillin G, tilmicosin, and vitamin E may be accumulated and biotransformed in the lysosomes, but confirmation that these processes occur in the lysosomes requires enriched functional lysosomes, devoid of contaminants in which similar processes may occur.[136-138] In the absence of high enrichment of a specific organelle, direct links cannot be made.

The most common methods to isolate and enrich lysosomes are differential centrifugation and density-gradient centrifugation. Differential centrifugation separates organelles based upon their sedimentation rate.[139] It is relatively quick (~ 2 hours), but peroxisomes and mitochondria are present as contaminants. Density-gradient centrifugation in self forming gradients of colloidal particles separates organelles directly[13, 14] or after loading of the lysosomes with compounds such as dextran,[140] iron,[141] and gold[142] to change their sedimentation rate. These methods often require multiple centrifugation and sample cleanup steps that can lead to a lengthy experimental time (~6 hours) and the potential dissipation of the acidic pH within lysosomes and other endocytic organelles. [143] Free flow electrophoresis has been shown to separate lysosomes based on their electrophoretic mobility, however it requires specialized instrumentation.[144]

Magnetic isolation based on antibody-coated paramagnetic beads, which is commonly used to isolate proteins and cells,[145-148] is another approach to isolate organelles such mitochondria, peroxisomes, and autophagosomes.[149-151] Magnetic isolation of lysosomes after endocytosis of dextran-coated superparamagnetic iron oxide nanoparticles (FeDex) has also been reported[11, 15, 151] and used to investigate pharmacological properties in bulk.[15, 152] These studies did not evaluate directly whether such organelles retained an acidic pH during the isolation procedure. Magnetic isolation of particles in microfluidic channels[153] and capillary[154] have been used to isolate and concentrate particles used in protein digestions[153], triglyceride analysis[155] and immunoassays,[156] but have not been applied to organelle studies.

Here, we report on the analysis of the pH of individual magnetically-enriched endocytic organelles after their release from a magnetic retention in an open tube. The post-nuclear fraction of L6 cells that had endocytosed both FeDex and fluorescein/TMRM-conjugated dextran was delivered through a fused silica capillary. This capillary passed through a custom-built on-line magnetic isolation device and ended at a post-column dual-channel laser induced fluorescence detector (LIF). For each individual organelle detected, the ratio of its fluorescence signals at each channel was used to determine its pH. Acidic pH values of the magnetically retained individual organelles suggested that magnetic isolation in an open tube is suitable to prepare functional endocytic organelles. Future magnetic purification of acidic organelles in open tubes would be highly beneficial to investigate the role of lysosomal activity in aging, storage disorders and metabolism.

3.2. Experimental

3.2.1. Reagents

Dulbecco's Modified Eagle Medium (DMEM) high glucose cell medium was obtained from Gibco. Bovine calf serum was obtained from Omega Scientific (Tarsana, CA). Gentamycin, iron (III) chloride hexahydrate, dextran from Leuconostoc mesenteroides, 1,10-phenanthroline, hydroxylamine hydrochloride, poly-L-lysine, magnesium chloride hexahydrate, protease inhibitor, dimethyl sulfoxide, 2,6-dicholoroindophenol, sodium azide, succinic acid disodium salt, Triton X-100, titanium oxysulfate sulfuric acid complex hydrate, cacodylate, glutaraldehyde, osmium tetroxide, polyvinyl alcohol, propylene oxide, 3-sn-phosphatidyl-L-serine, L-α-phosphatidylcholine, L-α-phosphatidylethanolamine, iron (II) chloride tetrahydrate, imidazole, and dichloroindophenol (DCIP) were obtained from Sigma-Aldrich (St. Louis, MO). Ammonium hydroxide, hydrochloric acid, potassium hydroxide, and hydrogen peroxide were obtained from Mallinckrodt (Phillipsburgh, NJ). Fluorescein, tetramethylrhodamine (TMRM), para-nitrophenylphosphate (pNPP), fluorescein/TMRM-conjugated dextran (70,000 MW) (FTD), LysoTracker Red, and AlexaFluor488-conjugated dextran (10,000 MW, referred thereafter as AlexaFluor488-dextran) were

obtained from Invitrogen (Carlsbad, CA). Sodium acetate trihydrate, 4,6-diamidino-2-phenylindole, and sulfuric acid were obtained from Fisher Scientific (Pittsburgh, PA). Bovine serum albumin was obtained from Roche (Basel, Switzerland). Ethanol was obtained from Pharmco-AAPER (Brookfield, CT). Phosphate buffered saline (10× PBS) is obtained from BioRad (Hercules, CA). UltraPure brand sucrose (99.9%) was obtained from MP Biomedicals, Inc. (Illkirch, France). Iron (96.0% pure) was obtained from VWR (Radnor, PA). Water was purified with a Millipore Synergy UV System (18.2 mΩ/cm, Bedford, MA).

A nigericin stock solution (1 mM) was made by mixing 5 mg nigericin with 6.89 mL water. Potassium phosphate solution (used with nigericin; 900 mM) was made by adding 3.92 g of the reagent to 20 mL of water. The pH was then adjusted to 6.1 with concentrated NaOH and brought to 25 mL. Buffer N, used for cell handling for enzyme assay procedures, was made by adding 27.01 g mannose (300 mM) and 240 mg MgCl2 (5.0 mM) to 50.0 mL of 10× PBS. The solution was then diluted to 450 mL with water. The pH was adjusted to 7.4 with concentrated NaOH and brought to 500 mL. Buffer M, used for cell handling for magnetic isolation procedures for determination of the pH of the retained organelles, was made by adding 19.12 g mannitol (210 mM), 11.98 g sucrose (70 mM), 596 mg 4-(2-hydroxyetheyl)-1-piperazineethanesulfonic acid (5 mM), and 731 mg ethylenediaminetetraacetic acid (5 mM) to 450 mL water. The pH was adjusted to 7.4 with concentrated NaOH and brought to 500 mL. The catalase assay solution was made the day of the experiment by adding 50 mg bovine serum albumin, 5 mL 0.2 M imidizole (pH 7.6), 1 mL 10 % w/v Triton X-100, 100 µL of 37 % H2O2, and was brought to 50 mL. The catalase stop buffer was made in a fume hood by adding 2.25 g TiOSO4 to 300 mL 2 N H2SO4. Once dissolved, the solution was brought to room temperature. A 200mL aliquot of the solution was added to 200 mL of 2N H2SO4. This solution was then diluted to 1 L. Unless noted otherwise, solutions were diluted with deionized water.

The synthesis of FeDex was prepared as described previously,[11] except for preparation of AlexaFluor 488-FeDex, that used a mixture of 5 mg of AlexaFluor488 dextran and 2 g of dextran. After synthesis, the particles were dialyzed against water in a

Fisher 4.8 nm seamless cellulose membrane for 48 hours at 4 °C. The dialysis water was exchanged after 24 hours. FeDex was filtered with a 0.22-μM filter under vacuum to remove large aggregates and impurities. FeDex (~ 4 mg/mL) was stored at 4 °C in water and used within 2 months.

FeDex particles were characterized by transmission electron microscopy (TEM), x-ray diffraction, light scattering and hysteresis loop measurements. For TEM characterization, FeDex particles were imaged on lacey carbon/formvar copper 200 mesh grids (Ted Pella Inc, Redding CA) on a JEOL 1200 transmission electron microscope. TEM does not display the dextran coating and revealed iron cores with irregular morphology with long-axis length of 7.4 ± 2.2 nm (average ± standard deviation, n=30; range: 4.3 - 14.4 nm), which are similar to those previously observed (8.7 ± 2.1 nm).[11] For x-ray diffraction, 80 mg FeDex were analyzed in a Pananalytical X'Pert PRO MRD x-ray diffraction instrument. Using the Scherrer equation the calculated crystalline volume was 16.5 ± 8 (average ± standard deviation, n=7), which is consistent with the dimensions observed by TEM. For light scattering, 4.0 mg/mL FeDex in water were analyzed in a Brookhaven Instruments 90Plus/BI-MAS particle sizing instrument. The average particle size was 61.2 ± 0.7 (average ± standard deviation, n = 3 trials). This is a hydrodynamic determination that includes the total particle dimensions, including the thickness of the dextran coating. Hysteresis loop measurements were done in a Princeton Measurements Alternating Gradient Magnetometer (23° C, 0T - 2.2T, 1 × 10-11 Am2, Princeton, NJ). The FeDex particles were superparamagnetic and were at 97% of their maximum magnetic moment (160.7 μAm2) when exposed to the maximum magnetic field obtained with the magnets used here.

3.2.2. Cell culture and homogenate preparation with differential centrifugation

The rat myoblast L6 cells (ATCC, Manassas, VA) were maintained in DMEM supplemented with 10% bovine serum and 0.01% gentamycin at 37 °C and 5% CO2. Cells were subcultured upon reaching 95% confluence in a 1:40 ratio. L6 cells were treated with nanoparticles FeDex (2.0 mg/mL) for 30 minutes in DMEM. Trypsin in PBS (0.5%) was used to release cells from T-flasks for subculture or collection of cells. Cells

used for determination of individual organelle pH values were treated with fluorescein/TMRM-conjugated dextran (2 mg/mL) for 18 hours before cell homogenization.

In most of the studies described here, after their release by trypsinization cells were harvested by centrifugation at 1,000g for 10 minutes and washed twice with 3 mL of buffer N. This was repeated a second time. Cells were then treated with 1% (v/v in DMSO) protease inhibitor cocktail and homogenized in a Dounce homogenizer (0.0025" clearance, Kontes Glass, Vineland, NJ) with 100 strokes. About 10% of the whole cell homogenate volume was retained for enzyme assays. The remaining 90% of homogenate was centrifuged at 600g for 10 minutes to remove the nuclear fraction and unlysed whole cells. The resulting supernatant was the post nuclear fraction (PNF) and contained lysosomes, mitochondria, peroxisomes, endosomes, and cytosol. For differential centrifugation studies, the PNF was centrifuged at 13,000g for 10 minutes to form a pellet that contained lysosomes among other organelles. The supernatant containing mainly cytosol and cytosolic proteins was removed with a pipette. The pellet was diluted with 1.1 mL of buffer N and then used in enzyme assays. In addition the whole cell homogenate fraction was diluted and characterized in a similar fashion.

3.2.3. Fluorescent microscopy of L6 cells

Cells seeded in a LabTek 4 chambered coverslip were labeled with Lysotracker Red (50 μM) for 45 minutes at 37 °C. After 15 minutes, cells were labeled with AlexaFluor488-FeDex (3 mg iron/mL) for the remaining 30 minutes at 37 °C. After labeling, the tray was washed twice by removing media, adding PBS with a pipette, removing the first wash solution, and replacing with 300 μL of PBS.

All images were taken with an Olympus IX81 inverted microscope (Melville, NY) equipped with an Olympus IX2-DSU disk scanning unit and a 60× (NA 1.45) oil immersion objective. A mercury lamp (Addison, TX) was used as the excitation source. AlexaFluor488 and Lysotracker Red fluorescence were detected respectively with filter sets GFP (excitation 460-500 nm; dichroic 505 nm; emission 510-560 nm) and RFP

(excitation 510-560 nm; dichroic 565 nm; emission 572-649 nm) (Chroma (Rockingham, VT). Imaging was done with a C9100-01 CCD camera (Hamamatsu, Bridgewater, NJ). CImaging Simple PCI 5.3 (Compix Inc., Cranberry Township, PA) software was used to control the microscope, image acquisition and processing. The levels of background fluorescence, AlexaFluor 488 cross talk, and Lysotracker Red cross talk were determined by observing unlabeled controls and samples labeled with only AlexaFluor488-FeDex or Lysotracker Red, respectively. The values of the crosstalk were undetectable and 3.6 ± 1.1 % (average ± standard deviation), respectively.

Image J-W Version 1.43s (National Institutes of Health) was used to calculate the Manders colocalization coefficients (M1 and M2) and the ICQ correlation coefficient (Section A-1). M1 and M2 range from zero to one representing total to total lack of colocalization of fluorophores.[86] ICQ values range from 0.5 to -0.5 representing same to opposite correlation, respectively, of the fluorescence intensities of the two fluorophores.

3.2.4. Enzyme assays

Enzyme assays specific to lysosomes, mitochondria, and peroxisomes were used to determine the abundance of these organelle types. The initial change of absorbance versus time was the enzymatic activity. After correcting for dilutions, the total specific activity (S.A.) was calculated as the ratio of enzymatic activity to protein concentration in the original sample. The relative activity (R.A.) of a sample was calculated as the ratio of its S.A. relative to the S.A. of the whole cell homogenate. The yield of a method was calculated as ratio of the total enzymatic activity in a recovered fraction over the total enzymatic activity of the PNF used in the fraction isolation procedure (i.e., differential centrifugation or magnetic isolation). Lysosomal abundance was determined with the pNPP assay.[157] First 150 µL of 25 mM pNPP and then 150 µL of the sample were added to a well of a 96-well plate (F96, Nunc, Rochester, NY). Absorbance readings at 405 nm ($\varepsilon = 1.80 \times 104$ cm-1 M-1)[158] were taken every 8 seconds for 15 minutes. Measurements were done in triplicate. LOD's for enzymatic assays were determined by calculating the enzymatic activity and protein concentration equivalent to three standard deviations above baseline. The LOD of the pNPP assay was 700 pmol pNPP/min/mg protein.

Mitochondrial abundance was determined with the succinate dehydrogenase assay.[159] The following reagents were added sequentially to a well of a 96-well plate: 130 µL of buffer N, 25 µL of 40 mM sodium azide, 25 µL of 200 mM succinate, and 25 µL aliquot of 0.050 mM DCIP. Then, 80 µL of the sample were added and thoroughly mixed. Absorbance readings at 600 nm ($\varepsilon = 1.88 \times 104$ cm-1 M-1)[160] were taken every 8 seconds for 15 minutes. The LOD of the succinate dehydrogenase assay was 1.0 nmol succinate/min/mg protein. Peroxisomal abundance was determined with the catalase assay.[161] A 50 µL aliquot of organelle sample was mixed with a 12 µL aliquot of the catalase assay solution. Samples were incubated for 8 minutes and then treated with a 205 µL aliquot catalase stop solution to quench the reaction and allows for remaining hydrogen peroxide to react with titanium (IV) oxysulfate. A 250 µL aliquot of the total solution was added to a well in a 96-well plate and read at 405 nm ($\varepsilon = 3.97 \times 105$ cm-1 M-1).[162] The LOD of the catalase assay was 7.6 nmol/min/mg protein. Protein concentrations were determined using the bicinchoninic acid protein assay (BCA kit, ThermoScientific, Wilmington, MA) according to the manufacturer's instructions.

3.2.5. On-line magnetic isolation device

Neodymium borate magnets (2.0 × 2.0 sq. in.; magnetized through their 0.5-inch thickness; K&J Magnetics, Inc., Jamison, PA) were modeled with Vizimag 3.18 software (Figure 3.1). The relative permeability of each magnet was set to 1.10 and the magnetic strength was set to 1.32 Tesla to match the manufacturer's values. The best configuration found had four magnets per pole (Figure 3.1A). For 1-cm gap, the predicted field was 817 mT. We adopted such configuration and positioned each set of magnets on an aluminum mount equipped with a high-precision micrometer to adjust the gap between zero and ten centimeters (Figure 3.1B). The magnetic field was measured with a hand held Gaussmeter (GM08, Hirst, Cornwell, United Kingdom) that fitted when the gap between the magnets was 1 cm or larger (Figure 3.1C). For 1-cm gap the measured magnetic field was 758 mT.

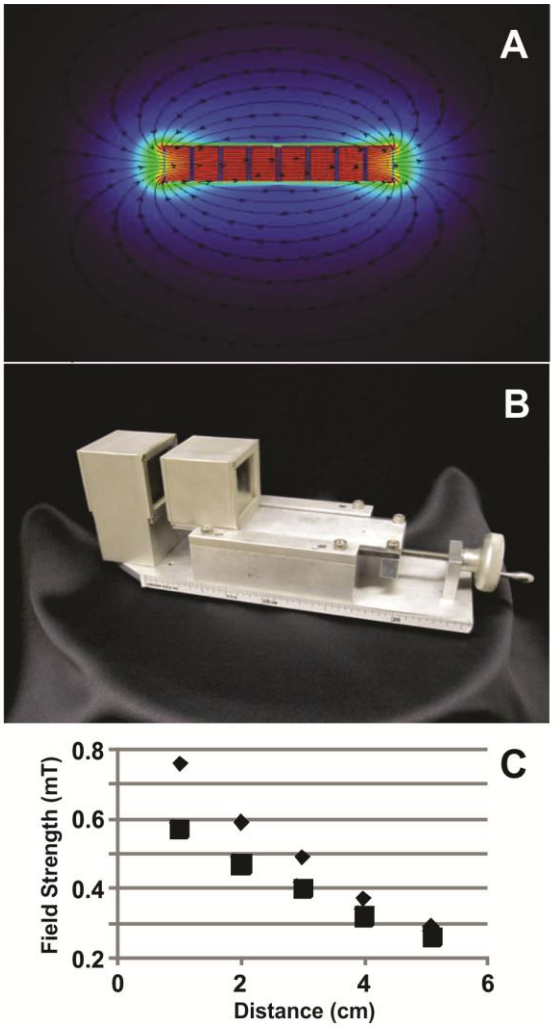

Figure 3.1. Characterization of magnet configuration. (A) Magnetic simulations of a cavity defined by two sets of four magnets each. This configuration shows a field strength of 817 mT when the gap is 1 cm. The simulation was done with Vizimag software. (B) On-line magnetic isolation device. (C) Field strength measurements at the center of the magnet cavity. Triangles and squares represent the experimental and the simulation data, respectively. Simulation data fitted the equation y = 0.0058x2 – 0.11x + 0.67 and predicted magnetic field strengths of 650 and 670 mT for gaps equivalent to those used for PEEK tubing and fused-silica capillary, respectively. Experimental data fitted the equation y = 0.012x2 – 0.19x + 0.93 and predicted magnetic field strengths of 900 and 930 mT for gaps equivalent to those used for PEEK tubing and fused-silica capillary, respectively.

3.2.6. Magnetic isolation procedures for enzymatic assays

A syringe pump (Model number 210, KDS Scientific, Holliston, MA) delivered ~ 100 µL of PNF from a 1-mL Hamilton RN syringe to PEEK tubing (#1531, IDEX Health and Science, Oak Harbor, WA) passing through the on-line magnetic isolation device. The syringe needle (22 g) was connected to the tubing with an adapter (VISF-2 and U-411, Chrom Tech, Inc, Apple Valley, MN). The PEEK tubing was positioned between the two magnet poles and held in place by reducing the gap until to the magnets slightly squeezed the tubing. The length of the tubing in the magnetic zone was 5.1 centimeters, which represents a volume of 2.6 µL within the tubing.

Following delivery of 15 µL of PNF through the tubing for loading of magnetic material into the magnetic zone, 25 µL of buffer N were delivered to wash off unretained material. The eluted volumes from the loading and wash steps contained unretained material. Upon completion of the wash step at 1.3 cm/min linear flow rate, the PEEK tubing was removed from the magnet gap. Then the previously retained magnetic material was eluted with at least 125 µL of buffer N. This elution step took under 9.5 minutes. The collected material was analyzed with the enzymatic assays described above. The linear velocity for the loading and elution steps was 21.9 cm/min. The linear velocities used for the wash step were 0, 0.6, and 1.32 cm/min, but only 1.32 cm/min was adequate to remove mitochondria and peroxisomes (Figure A.2).

3.2.7. Magnetic isolation procedures for determination of the pH of the retained organelles

To detect the pH of organelles, we used the setup shown in Figure 3.2. Fused-silica capillary replaced the PEEK tubing described above. A fused silica capillary (49-µm I.D., 150-µm O.D., 80-cm long, coated with 2% polyvinyl alcohol[91]) was immersed in a vial containing either the PNF or buffer N and pressurized at 4 psi with an argon tank. The linear flow velocity in the capillary was 7.7 cm/min. The magnetic separator was placed 40 cm from the injection end. The capillary position was fixed within the magnet gap because two pieces of tape at each side of the magnet cavity prevented it from moving (Figure 3.2A), wooden dowels confined it to the middle of magnet gap

(Figure 3.2B), and the gap was adjusted to match the capillary O.D. A capillary length of 5 cm was within the magnet gap and define an internal capillary volume of ~ 100 nL where magnetic capture occurred. When loading the capillary with PNF the plug length was ~ 5 cm long, matching the length of the capillary within the magnet gap. After loading the PNF, one capillary volume (1.6 µL) of buffer M was used to displace the PNF to the magnet gap and to wash off unretained material at a linear flow rate of 7.7 cm/min. Then, the capillary was removed from the magnet gap and retained organelles were mobilized by the pressure driven-flow. Upon completion of this step the capillary was flushed with methanol to reduce carry over into the next experimental run.

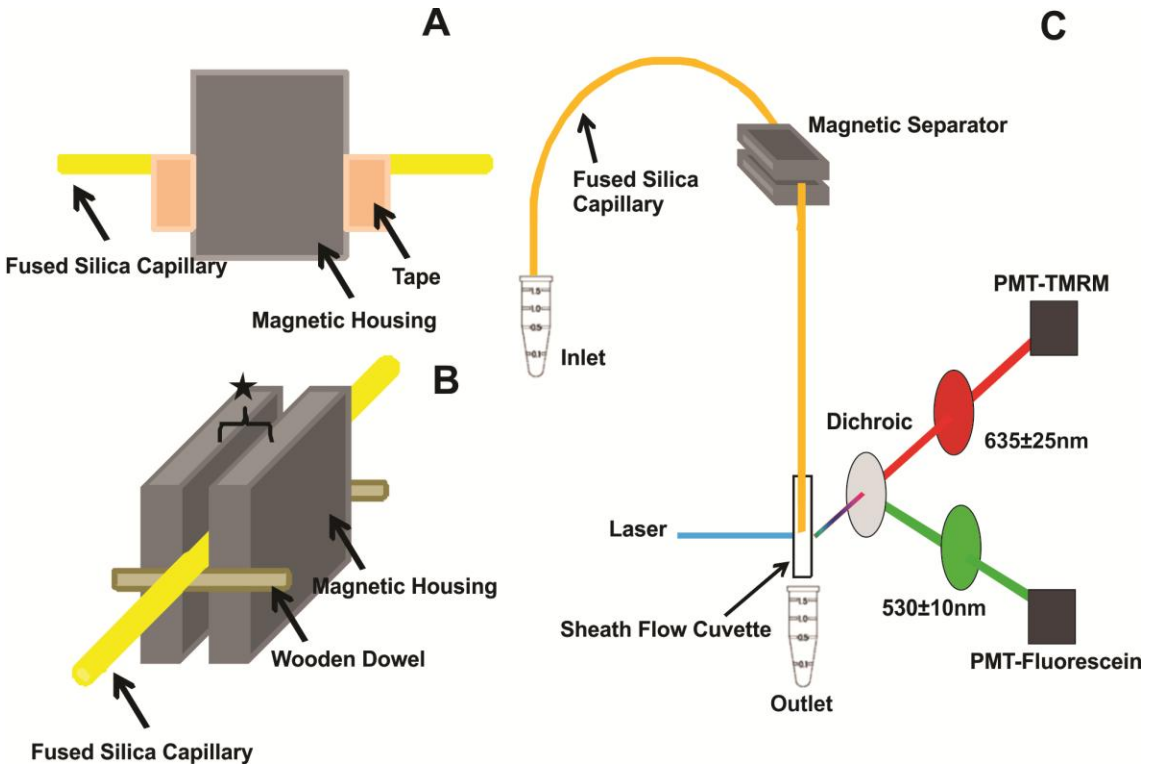

Figure 3.2. Detail of the on-line magnetic isolation device. (A) Tape ensured that the capillary did not shift along the capillary's length in the magnetic separator. (B) Wooden dowels attached to the magnetic housing kept the capillary in the middle of the magnetic housing. The star represents the gap adjusted to hold snug the PEEK tubing (gap ~ 1.59 mm) or the fused-silica capillary (gap ~ 0.150 mm). (C) An LIF detector placed ~ 40 cm after the device. Detection and excitation conditions are described in the Experimental section.

The detection end of the capillary was connected to a post-column LIF detector that has been previously described (Figure 3.2C.).[89] Briefly, the 488-nm argon-ion laser line was used for excitation. A 560 nm dichroic mirror (XF2016, Omega Optical, Brattleboro, VT) was used to reflect green fluorescence. A 635 ± 25 nm filter (XF3015, Omega Optical,) was used to select tetramethylrhodamine (TMRM) fluorescence and a 530 ± 10 nm filter (XF3017, Omega Optical) was used to select fluorescein and AlexaFluor488 fluorescence, respectively. Photomultiplier tubes were biased at 1,000V. The LOD of fluorescein was ~ 9 zmol. Fluorescently labeled organelles were detected as individual events as they eluted out during washing of the non-retained material and elution of the magnetically retained material. Events also occurred during the washing with buffer M and before elution of the fluorescently labeled organelles. These random false positives occurred at a low rate (0.049 ± 0.004 events/s). The non-retained fluorescent organelles (e.g. endocytic organelles with low FeDex contents but detectable levels of fluorescein/TMRM-conjugated dextran) appeared first at a rate of 0.17 ± 0.14 events/s. The retained fluorescent organelles (e.g. endocytic organelles with both FeDex and fluorescein/TMRM-conjugated dextran) appeared after ~100 s delay after removal of the capillary from the magnet. The yield of retained organelles was calculated as the ratio of the number of events in the retained zone to the number of events in both the unretained and retained zone.

Fluorescent data was analyzed using Igor Pro (WaveMetrics, Inc. Lake Oswego, OR). Broad bands corresponding to freely diffusing species were eliminated with a median filter. Individual organelle peak analysis was done with the custom-written program "coincidence analysis".[163] The average peak base width for peaks used in coincidence analysis was 24 ± 3 ms (n = 10,374) for TMRM peaks and 32 ± 3 ms (n = 10959) for fluorescein peaks. Peak intensities were corrected for spectral crosstalking (i.e, red-to-green ~ 16% and green-to-red ~ 6%). Peaks detected at the same time (± 20 msec) by the two PMTs of the LIF detector were used to calculate pH as previously reported[48] using a pH calibration curve of FTD-loaded liposomes with different internal pH's (Section A-3). Peak overlap between individual events defined by statistical overlap theory[164] was not significant for all the magnetically retained organelles and for most of

the non-retained organelles. For histogram distributions of individual pH values the bin width (2.0 pH units) was determined as the cubic root of total number of retained organelles, plus one.[165] This value is larger than the error of individual pH values calculated by error propagation (Section A-3). Because pH distributions are non-parametric, previously described Q-Q plots[166] were used for comparison of distributions.

3.2.8. Safety considerations

Biosafety level 1 was observed in all procedures involving L6 cells. Biological waste was treated with bleach prior to disposal. Used cell culture supplies were autoclaved prior to disposal.

3.3. Results & Discussion

Fluorescence confocal microscopy measurements confirmed endocytosis of FeDex by L6 cells and was used to assess localization of FeDex in endocytic organelles based on the colocalization of LysoTracker Red and AlexaFluor488-bound FeDex (Figure 3.3. and Figure A.1.). LysoTracker Red accumulates in acidic organelles because the dye's amine functional groups become protonated in acidic environments, which causes retention within the lumen of acidic organelles.[107, 167] Based on the M2 Manders coefficient, 93% AlexaFluor488 fluorescence was colocalized with Lysotraker Red fluorescence. The remaining 7% may correspond to AlexaFluor 488 found in the cytosol (i.e., released from the lysosomes upon dextran degradation) or organelles with undetectable levels of LysoTracker Red (e.g., early endosomes). Based on the M1 Manders coefficient, 74% of the LysoTracker Red fluorescence was colocalized with AlexaFluor488 fluorescence. This is not surprising because endocytosis of AlexaFluor488-bound FeDex is expected to distribute to endocytic organelles (late endosomes, lysosomes)[46, 168] excluding other non-endocytic acidic organelles (e.g. Golgi). ICQ suggested a positive correlation in the abundances of AlexaFluor488-bound FeDex and LysoTracker Red (ICQ = 0.34). Based on the fluorescence microscopy results and considering dextran's role as a lysosomal and endocytic organelle marker,[168, 169] we concluded that FeDex particles were mainly localized in late endocytic organelles, including lysosomes.

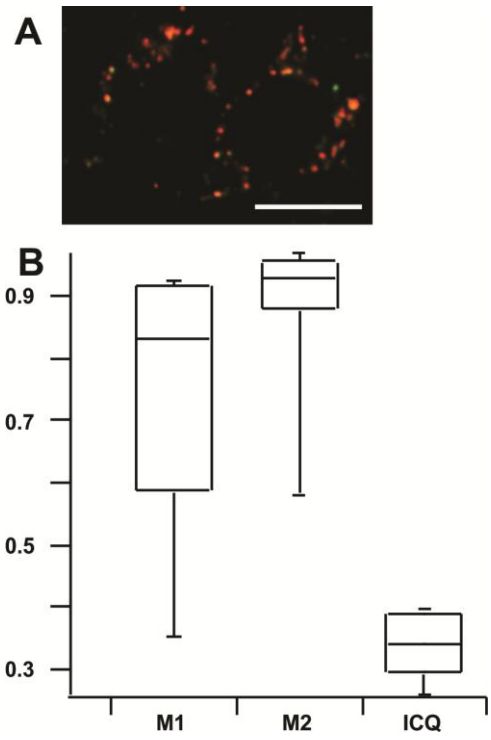

Figure 3.3. Intracellular colocalization of FeDex with acidic organelles. (A) Overlay of confocal fluorescent images of L6 myocytes after endocytosis of AlexaFluor488-FeDex (Green) and treatment with LysoTracker Red (Red). Scale bar = 10 μm. (B) Boxplots of colocalization statistics of 45 cells. The M1 statistic represents the fraction of red fluorescence pixels with green colocalization. The M2 statistic represents the fraction of green fluorescence pixels with red colocalization. The ICQ statistic is > 0 indicating that intensities of both fluorophores are correlated. The ICQ statistic ranges from -0.5 to 0.5.

3.3.1.Subcellular composition of magnetically isolated material

Organelle specific enzyme assays are commonly used to determine composition, enrichment (i.e. R.A), and yields of subcellular fractions.[136] We utilized the pNPP, succinate dehydrogenase, and catalase assays to compare the subcellular fractions prepared by (i) magnetically retaining organelles from PNF flowing through PEEK tubing or (ii) differential centrifugation. While the subcellular fraction prepared by differential centrifugation was positive for all the enzymatic markers tested here (i.e., lysosomes, mitochondria, peroxisomes), the fraction that was magnetically isolated had only lysosomal markers present (R.A. = 1.7 ± 0.5, average ± Std. Dev., n=3 independent

tests); other markers were below their limits of detection (Table 3.1). The R.A. for differential centrifugation for lysosomes was 1.2 ± 0.6 (average ± Std. Dev., n=3 independent tests). While the magnetic isolation procedure appears to have a higher yield than differential centrifugation, these values are not statistically different (p=0.05). Density gradient centrifugation has also been used for purification of lysosomal fractions.[13, 14] Unfortunately, this procedure did not provide sufficient material to perform the organelle marker assays used here (data not shown).

Organelle	Differential Centrifugation (R.A.)	Magnetic Isolation (R.A.)
Lysosome	1.2 ± 0.6	1.7 ± 0.5
Mitochondria	1.4 ± 0.5	<0.2
Peroxisome	1.7 ± 0.4	<0.1

Table 3.1. Enrichment and composition of organelle fractions. The abundance of each organelle type was determined using organelle-specific enzymatic markers. The relative abundance (R.A.) for each fraction was calculated a described in the Experimental. The para-nitrophenylphosphatase assay was used to determine lysosomal abundance (LOD = 700 pmol p-nitrophenol/min/mg protein). The succinate dehydrogenase assay was used to determine mitochondrial abundance (LOD = 1.0 nmol DCIP/min/mg protein) as used for mitochondria. The catalase assay was used to determine peroxisomal abundance (LOD = 7.6 nmol Ti(IV)peroxysulfate/min/mg protein).

The lysosomal yield of the magnetic isolation procedure was 18 ± 6% (average ± Std. Dev., n = 3 independent tests). The yield for differential centrifugation was 42 ± 10 (average ± Std. Dev., n = 3 independent tests). While the magnetic isolation procedure appears to have a lower yield than differential centrifugation, these values are not statistically different (p=0.05). When the goal is to isolate large amounts of material, the yield could be further improved by coiling the tubing within the magnet gap,[170] design of

other magnet geometries,[153] and further optimization isolation procedure. On the other hand, the current design is highly suitable when working with limited amounts of material (e.g., 5 µL of PNF).

3.3.2. Determination of the individual pH of magnetically isolated organelles

Lysosomes and other late endocytic organelles require an acidic pH to maintain biological activity.[121] For lysosomes to be enriched and to be of possible use for metabolic and biotransformation in vitro studies, their functionality must be retained. The first step to assess their biofunctionality is the determination of their pH. Determining the pH value of isolated organelles in bulk does not describe the ranges in pH values found in isolated endocytic organelles at the different stages of their maturation. Knowing the distribution of pH values is critical to associate pH with the overall bioactivity of the isolated organelles. Detection of the pH of individual organelles addresses this issue. We previously reported an LIF detection scheme to measure the pH of individual organelles.[48] In order to use this detection scheme, here we combine magnetic purification with the analysis of pH of individual organelles based on LIF detection. Organelles that were magnetically isolated and then detected had both FeDex nanoparticles and FTD. Since FTD has two fluorophores (Alexa 488 and TMRM) each with distinct pH dependence, While FeDex allows for magnetic retention, the ratio of fluorescence signals of FTD (Alexa 488 and TMR) are used calculate the pH of individual organelles (Section A.3).

The instrumental setup used for pH determinations consisted a fused silica capillary (50 µm. I.D.), which replaced the PEEK tubing, connected to a post-column LIF detector (Figure 3.2C). The LIF detection of individual organelles produced narrow events (i.e., 24 and 32 ms wide at their base for fluorescein and TMRM detection, respectively), with a separate fluorescence signal detected at each PMT for each fluorophore (Figure 3.4B). While the PNF was being loaded and before loaded sample reached the detector, only a small number of random events were detected (regions (i) and (ii) in Figure 3.4A). When the PNF material began reaching the LIF detector, organelles began to appear (region (iii) in Figure 3.4A). These events are the non-retained

organelles and decreased in frequency as washing with Buffer M proceeded. Once the frequency of appearance of events decreased to 0-5% of that of the most crowded region, the capillary was removed from the magnet gap. As expected, the frequency of events increased, indicating that the magnetically retained events were reaching the LIF detector (region (iv) in Figure 3.4A). This region lasted only 50-60 seconds and had a low number of events (~ 20), consistent with the small volume of capillary exposed to the magnetic field (Figure 3.2A). The combined results of three runs had 83 events (yield ~ 2.6% of the total number of events) detected after removal of the capillary from the magnetic field. The yield was lower than that calculated based on organelle markers because here we used a higher linear flow rate than that used for the PEEK tubing-based experiments (7.7 cm/min for fused silica capillary; 1.3 cm/min for PEEK tubing). As indicated in Figure A.2, the recovery decreased as the flow rate increases. The numbers of non-specific absorption and random events (12% and 4% of the detected events in region (iv), respectively) were not a problem because the non-specific absorption events are also endocytic organelles with pH values indicative of their bioactivity; the random events were rare and did not affect the interpretation of the pH results. Thus, we used the detected events in region (iv) to assess the pH of the magnetically isolated organelles.

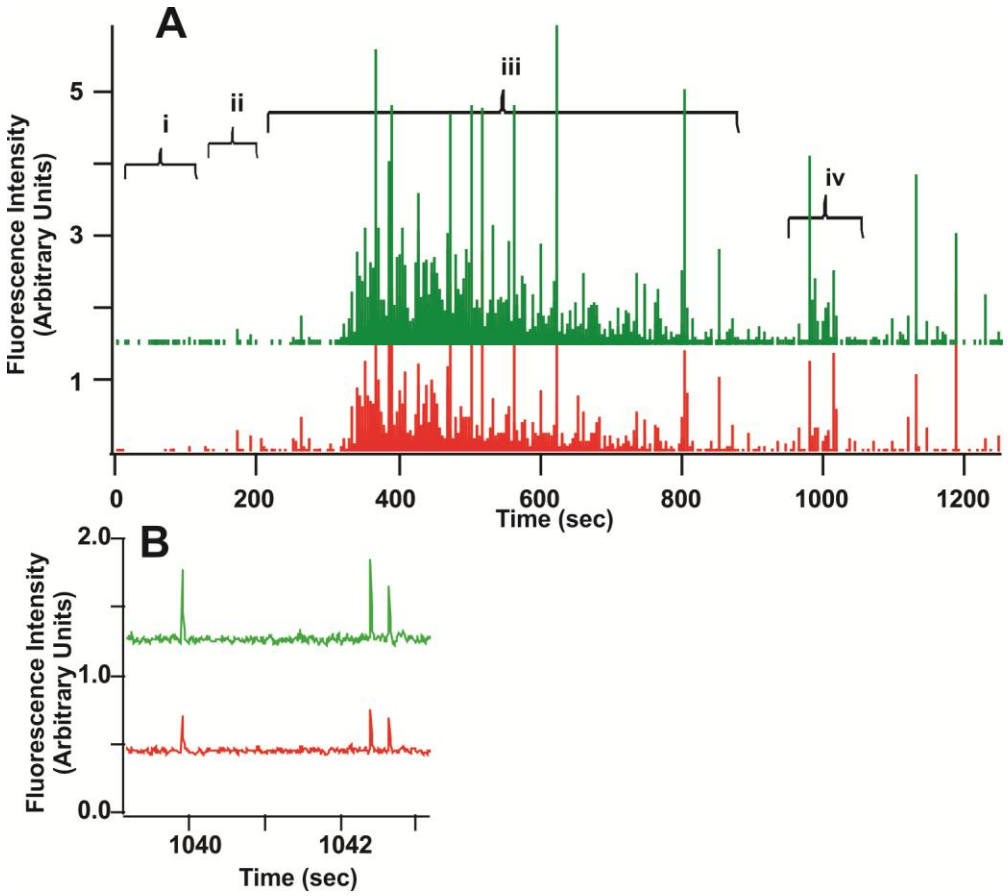

Figure 3.4. LIF detection of individual organelles loaded with FTD. (A) Detection of fluorescein (upper trace) and TMRM (lower trace). Both traces were modified with a median filter to remove broad bands corresponding to free fluorophores (Figure A.4).[107] The four regions shown in this plot include: (i) Detection while PNF was loaded and before organelles reached the LIF detection; (ii) dead time during the exchange of PNF for buffer M; (iii) detection of events from organelles that were not magnetically retained; (iv) detection of events that were magnetically retained. Before detection of events in region (iv) the frequency of events had been decreased to 0 – 2.3% of the event density observed at the beginning of region (iii). (B) Expanded view from 3.4A indicates that events are narrow as expected from the rapid passage of organelles through the LIF laser and they contain FTD because they are detected simultaneously in both channels.

As a reference, we determined the distribution of the pH of individual endocytic organelles in the PNF of L6 cells, treated only with FTD and prepared by differential

centrifugation (Figure 3.5A). The observed range of individual pH was 4-6, which is consistent with the expected pH of lysosomes and late endocytic organelles.[171] We also determined a distribution of pH of individual endocytic organelles in the PNF prepared from L6 cells treated with nigericin and FTD (Figure 3.5B). Nigericin dissipates the luminal pH in acidic organelles that acquire the pH of their surroundings.[172] The Q-Q plot of the distributions shown in Figure 3.5B confirmed that nigericin-treated organelles had an overall increase in pH (Figure A.5A).

We also investigated the effect of FeDex on the LIF determination of pHs of individual organelles. The presence of FeDex caused a systematic increase in pH (1.7 ± 0.1 pH units) relative those organelles from cells treated only with FTD (Table A.1, Figure A.5B). This may be the result from scattering or fluorescent quenching by the iron oxide nanoparticle.[173] This shift was used as a correction factor for pH values of individual organelles obtained from FeDex-treated L6 cells. After correction, both the pH of the retained (Figure 3.5C) and the eluted organelles (Figure A.5C) were consistent with previous literature reports.[171] Most importantly, the determination of the individual pH of magnetically retained organelles revealed how pH distributions shifted relative to the distribution of the organelles in the PNF (Figures 3.5C and 3.5A, respectively). This slight shift may indeed correspond to uncorrected biases caused by the FeDex particles or the additional time needed to carry out the magnetic isolation (~30 min) during which the pH gradient may begin to dissipate. On the other hand, a Q-Q plot comparing the individual pH values of magnetically retained and non-retained organelles in the same PNF revealed that their pH distributions are practically unbiased by the magnetic isolation procedure (Figure 3.5D).

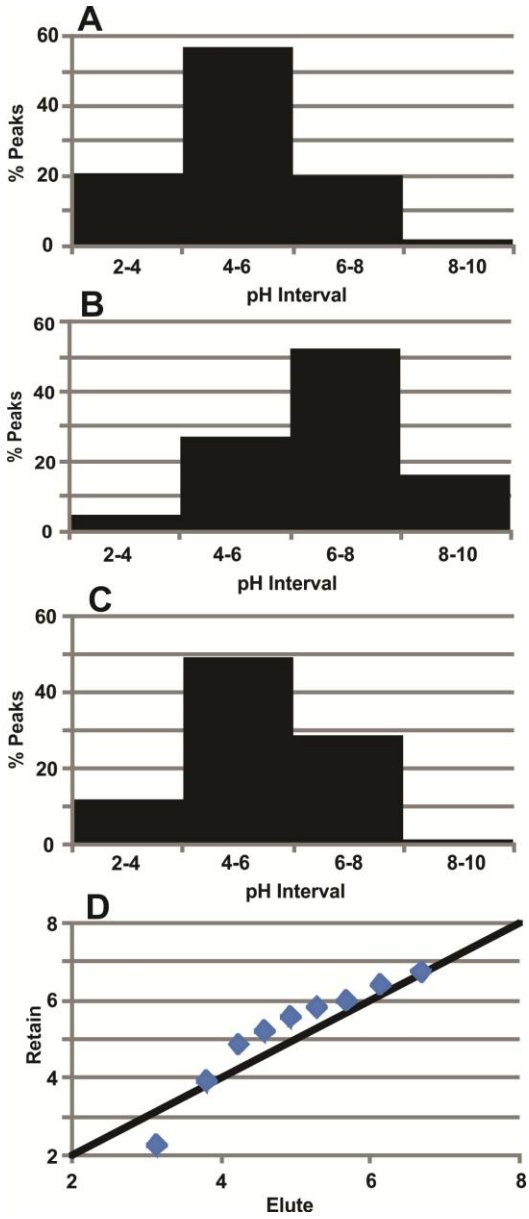

Figure 3.5. Individual organelle pH distributions. (A) The pH of organelles in a PNF from L6 cells not treated with FeDex (B) Same as in A, except for treatment with nigericin prior to cell homogenization. (C) The pH of magnetically retained organelles. (D) Q-Q plot of pH distributions of magnetically retained versus unretained organelles in the same run.

3.4. Conclusions

The magnetic isolation system described here was effective at isolating enriched lysosomes and endocytic organelles containing FeDex particles. Based on organelle enzyme markers, common contaminants in differential centrifugation preparations such as mitochondria and peroxisomes were not observed. Laser-induced fluorescence detection of the individual pH of magnetically retained organelles demonstrated that magnetic isolation does not influence the distribution of pH values relative to non-retained organelles. We found a pH for isolated organelles of 4 – 6, which is characteristic of lysosomes and endocytic organelles retaining acidic pH.

Future applications of the work described here include evaluation of different subpopulations of magnetically enriched organelles. This could be achieved with on-line magnetic capture of organelles followed by capillary electrophoresis coupled to LIF detection[48] or isolectric focusing of the organelles based upon either free flow electrophoresis[174] or within a capillary with LIF detection[103]. Future improvements also includes designing alternate open tube configurations (e.g. coiled[170] or parallel lines[15]) or microfabricating magnetic geometries that are more conducive to attaining higher organelle yields.[175] The advantages of newly proposed configurations could be easily explored using physical modeling using software packages such as ANSYS (fluid dynamics) and Maxwell (magnetism).[176] The device could also be used to magnetically isolate other subcellular compartments using magnetic beads coated with organelle-specific antibodies.[145-151] The bioactivity of such organelles could be evaluated using previously reported[177] or novel individual organelle assays. Lastly, the work described here has a great potential to become the basis for future magnetic purifications of endocytic organelles that are highly needed to investigate the role of lysosomal function in aging, storage disorders and metabolism.

Chapter 4

Magnetically Enriched Endocytic Organelles from Uterine Sarcoma Cells Biotransform the Prodrug *N*-L-Leucyldoxorubicin into Doxorubicin

Brandon Meyer synthesized N-L-leucyldoxorubicin, performed separations of drug and prodrug standards, and assisted in biotransformation experiments. Joseph J. Dalluge assisted with mass spectrometry. This work was supported by NIH grant T32 GM8347 and by the University of Minnesota's Undergraduate Research Opportunities Program (B.M.).

The biotransformation of *N*-L-leucyldoxorubicin (LeuDox) to the anti-cancer drug doxorubicin (Dox) occurs in the extracellular space, however, biotransformation may also occur intracellularly in endocytic organelles. In this study, magnetically enriched endocytic organelle fractions from human uterine sarcoma cells were treated with LeuDox, of which 10 % was biotransformed to Dox. This percentage accounts for 45% of the total LeuDox biotransformation observed in the post-nuclear fraction. This suggests endocytic organelles play a key role in the intracellular biotransformation of LeuDox to Dox. This technique allows for the determination of intracellular biotransformation of drugs and prodrugs. This process can be applied to other prodrugs that may not only be activated by metalloproteases and other extracellular enzymes, but also intracellularly. Furthermore, this technique may be useful to determine other biotransformations that are attributed to lysosomes and other endocytic organelles.

4.1. Introduction

Doxorubicin (Dox) is an anthracycline used to treat multiple hematological and solid tumors for decades.[178-180] Dox enters the nucleus of mammalian cells and inhibits cell replication by binding to both DNA and topoisomerase 2α and 2β forming the topoisomerase 2-doxorubicin-DNA cleavage complex, triggering cell death.[181, 182] Despite its high anti-cancer activity, severe cardiac and liver toxicity are examples of its severe side effects.[183-189] Cytotoxicity is both dose- and time-dependent[190] and is caused in healthy cardiocyte cells by binding between Dox and topoisomerase 2β. Binding leads to both DNA double-strand breaks and increased apoptosis which causes modification to the cellular transcriptome which in turn causes critical errors in both mitochondriogenesis and in mitochondrial metabolic function.[182]

Prodrugs increase drug efficacy and can target cancerous cells by adding a molecular signature to the active drug.[191] Prodrugs are practically inactive and are expected to release the drug once it reaches its targeted tissue or subcellular area. The prodrug is then cleaved forming the active drug. N-L-leucyldoxorubicin (LeuDox) is a Dox prodrug synthesized by conjugating L-leucine to the primary amine of Dox.[138]

Relative to Dox, reports have reported LeuDox is less cytotoxic and has higher tolerated dose than Dox.[16, 192-195]

It is accepted that the biotransformation of LeuDox to Dox occurs in the extracellular space. This was attributed to both the high rate of biotransformation of LeuDox[16] and the low cellular update of LeuDox.[16, 18, 196] In support of these studies, aminopeptidases, cathepsins, and metalloproteinases that are capable of LeuDox biotransformation into Dox have been identified in the extracellular space.[197, 198] It has also been hypothesized that LeuDox can be biotransformed to Dox intracellularly making intracellular activation of LeuDox a potentially important therapeutic route. Lysosomotropic amines, such as Dox and LeuDox, are weak bases which can diffuse into lysosomes and become protonated when their pKa is higher than the acidic pH of lysosomes, sequestering the amine in the lysosome.[172] The presence of enzymes, such as cathepsins, in the lysosome has the potential of activating LeuDox to Dox.[2, 199] One major caveat though is that some cancer cells have lysosomes with abnormally high pH, which would decrease sequestration of lysosomotropic amines into lysosomes such as LeuDox.[49]

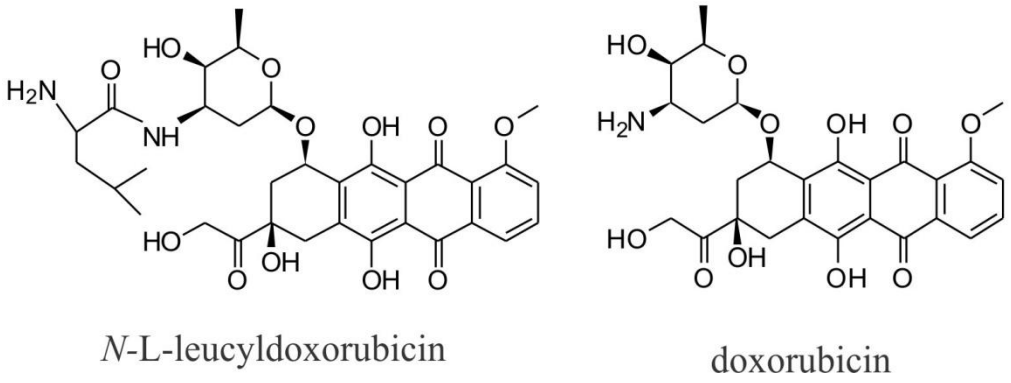

Figure 4.1. Structures of LeuDox and Dox.

Investigating the role of lysosomes and endocytic organelles in intracellular LeuDox biotransformation requires highly enriched fractions devoid of other contaminating organelle types. Previous studies used enriched, lysosomal enzymes from rat liver to show lysosome enzymes are capable of this biotransformation,[197, 200, 201] however, these studies could not evaluate if LeuDox enters intact lysosomes. To address

this issue, we previously investigated LeuDox biotransformation occurring in whole MES-SA human uterine sarcoma cells. Following LeuDox treatment and cell homogenization, we determined the Dox and LeuDox contents in the enriched organelle fractions.[138] The biotransformation of LeuDox into Dox in the enriched endocytic organelle fraction suggested that some of these organelle types, likely lysosomes, may be capable of the biotransformation of LeuDox into LeuDox. This study did not rule out the possibilities that LeuDox biotransformation into Dox may occur extracellularly or in other subcellular compartments, from which Dox traffics to organelles found in the enriched organelle fractions. In addition, the presence of other organelle types in the enriched endocytic organelle fraction prevented us from ruling out the participation of these other organelles in the LeuDox biotransformations.

Here we confirm that the biotransformation of LeuDox to Dox occurs in endocytic organelle fractions containing intact lysosomes and late endosomes. We magnetically enriched endocytic organelles from MES-SA cells using an approach in which the isolated endocytic organelles retain its acidic pH and in which other contaminating organelle types (i.e., mitochondria and peroxisomes) are absent (work described in Chapter 3).[88] Following treatment with LeuDox, the enriched fraction was analyzed by micellar electrokinetic chromatography coupled to laser induced fluorescence detection (MEKC-LIF), a technique previously used to monitor the biotransformation of LeuDox to Dox.[138] LeuDox to Dox biotransformations took place in the magnetically enriched endocytic organelle fractions containing intact lysosomes and late endosomes. This technique allows for the determination of intracellular biotransformation of drugs and prodrugs and can be applied to other prodrugs that may not only be activated both extracellularly and intracellularly. Furthermore, this technique may be useful to determine other biotransformations that are attributed to lysosomes and other endocytic organelles.

4.2. Material and Methods

4.2.1. Reagents

McCoy's 5A with L-glutamine was obtained from Fisher Scientific (Pittsburgh, PA). Bovine calf serum was obtained from Omega Scientific (Tarsana, CA). Gentamycin, protease inhibitor, iron(III) chloride hexahydrate, iron(II) chloride tetrahydrate, dextran from *Leuconostoc mesenteroides*, 1,10-phenanthroline, imidazole, cetyltrimethylammonium bromide (CTAB), tert-butoxycarbonyl-L-leucine succinimide ester (Boc-Leu-OSu), methanol, triflouroacetic acid, sodium hydroxide, sucrose, tris(hydroxymethyl)aminomethane hydrochloride (Tris-HCl), and tricine were obtained from Sigma-Aldrich (St. Louis, MO). Ethylenediaminetetraacetic acid (EDTA), hydrochloric acid, and potassium hydroxide were obtained from Mallinckrodt (Phillipsburgh, NJ). Fluorescein was obtained from Invitrogen (Carlsbad, CA). Bovine serum albumin was obtained from Roche (Basel, Switzerland). Ethanol was obtained from Pharmco-AAPER (Brookfield, CT). Phosphate buffered saline (10× PBS, 13.7 M NaCl, 270 mM KCl, 800 mM Na_2HPO_4, and 200 mM KH_2PO_4, pH 7.4) was obtained from BioRad (Hercules, CA). Iron (96.0% pure) was obtained from VWR (Radnor, PA). Pyridine, Silica Gel 150, acetonitrile and chloroform were obtained from Mallinckrodt (Phillipsburg, NJ, USA). Trimethylsilyl iodide (TMSI) was obtained from TCI America (Portland, OR, USA). Doxorubicin HCl (Dox) was obtained from Meiji Seika Kaisha (Tokyo, Japan). Deionized water was purified with a Millipore Synergy UV System (18.2 mΩ/cm, Bedford, MA).

Buffer A, used for cell handling, was made by adding sucrose (34.23 g; 200 mM), Tris-HCl (790 mg; 10 mM), and EDTA (20 mg; 0.1 mM) to 450.0 mL of deionized water. The pH was adjusted to 7.4 with NaOH and HCl and diluted to 500 mL with deionized water. CTAB buffer, used for MEKC-LIF, was made by adding CTAB (730 mg; 4 mM) and tricine (4.5 g; 40 mM) to 450 mL DI. The pH was adjusted to pH 8.5 with NaOH and HCl and diluted to 500 mL with DI.

Dextran coated iron oxide nanoparticles were prepared as described previously.[11] Following synthesis, coated nanoparticles were dialyzed against water in a Fisher 4.8 nm seamless cellulose membrane for 48 h at 4 °C. The dialysis water was exchanged after 24 hour. Coated nanoparticles were filtered with a 0.22-µM filter under vacuum to remove

large aggregates and impurities. Coated nanoparticles (4 mg/mL) were stored at 4 °C in water and used within 2 months of synthesis. Nanoparticles were characterized by transmission electron microscopy (TEM), x-ray diffraction, light scattering and hysteresis loop measurements as described previously.[88]

For the synthesis of LeuDox, Dox (5.0 mg, 9.2 μmole) and Boc-Leu-OSu (4.0 mg, 12 μmole) in pyridine (1.0 mL) was first stirred at 25 °C for 24 hour. Solvent was then removed at 60 °C on a rotating evaporator. The residue was dissolved in chloroform:methanol (10:1) and purified by silica gel chromatography with chloroform:methanol (10:1) as the eluent. Boc-Leu-Dox (3.0 mg, 46% yield) was obtained as a red-colored product. Boc-Leu-Dox (1.5 mg, 2.0 μmole) and TMS-I (800 μg, 4.0 μmole) in chloroform (200 μL) were reacted under nitrogen at 25 °C for 6 min. Next, deionized water (3 μL, 1.7×10^{-4} mole) was added to quench the excess TMS-I in the reaction mixture. Semi-preparatory HPLC with a gradient elution in a C18 column (10-μm particle size, 250 × 10.00 mm, Phenomenex, Torrance, CA) was used for purification. The mobile phase composition changed linearly from 100% water (0.1% trifluoroacetic acid) to 100% acetonitrile (0.1% trifluoroacetic acid) over 35 min and was maintained for another 35 min. Solvent was then removed at 60° C on a rotating evaporator. Leu-Dox (908 μg, 59% yield) was obtained as a red-colored powder product.

4.2.2. Cell culture

The human uterine sarcoma MES-SA cells (ATCC, Manassas, VA) were maintained in McCoy's 5A media with L-glutamine supplemented with 10% bovine serum and 0.01% gentamycin at 37 °C and 5% CO_2. Cells were subcultured to maintain upon reaching 95% confluence. Trypsin in PBS (0.5%) was used to release cells from T-flasks. MES-SA cells were treated with nanoparticles (2.0 mg/mL) for 30 min in McCoy's 5A media with L-glutamine supplemented with 10% bovine serum and 0.01% gentamycin at 37 °C and 5% CO_2.

4.2.3. Differential centrifugation

Cells were harvested by centrifugation at 1,000*g* for 10 min and washed twice with 3 mL of 137 mM NaCl, 2.70 mM KCl, 8.00 mM Na_2HPO_4, and 2.00 mM KH_2PO_4, pH 7.4 (1x PBS). This was repeated a second time. Cells were then treated with 1% (v/v in DMSO) protease inhibitor cocktail and homogenized in a Dounce homogenizer (0.0025" clearance, Kontes Glass, Vineland, NJ) with 100-150 strokes. The resulting solution was the whole cell homogenate (WCH) and 10% was kept for protein assays. The remaining 90% of WCH was centrifuged at 600*g* for 10 min to remove nuclei and unlysed whole cells. The resulting supernatant was the post nuclear fraction (PNF) and contained lysosomes, mitochondria, peroxisomes, endosomes, and cytosol. For biotransformation experiments, 6 µL of the PNF was aliquoted into 1.5 mL Eppendorf microcentrifuge tubes.

4.2.4. Biotransformations of LeuDox in MES-SA cells

MES-SA cells were treated with LeuDox to determine the amount of LeuDox biotransformed in living cells. MES-SA cells (1.2×10^6; 25 mL) were treated with LeuDox (889 µg; 47 µM) for 1 h at 37 °C. Cells were harvested and lysed. The PNF fraction was collected and treated with MEKC buffer (20 µL).

4.2.5. Biotransformation of LeuDox in MES-SA post-nuclear fractions

A post-nuclear fraction (PNF) of MES-SA cells was treated with LeuDox to determine the amount of LeuDox biotransformed in MES-SA PNF. MES-SA cells (1.2×10^6) were harvested and lysed. The PNF fraction (200 µL) was collected and treated with LeuDox (7.12 µg; 47 µM) at 37° C for 1 hour at 200 rpm with the Eppendorf AG thermomixer (Eppendorf, Hamberg, Germany). The sample was then quenched by adding an equal volume of MEKC buffer (200 µL).

4.2.6. Enrichment of lysosomes and endocytic organelle fractions

The enrichment of lysosome and endocytic organelle fractions was done as previously described.[88] In brief, neodymium borate magnets (2.0 × 2.0 sq. in., magnetized through their 0.5-inch thickness, K&J Magnetics, Inc., Jamison, PA) were arranged in 2 sets of 4 magnets on an aluminum mount equipped with a high-precision micrometer to

adjust the gap between the two magnet sets from zero to ten centimeters. A syringe pump (Model number 210, KDS Scientific, Holliston, MA) delivered ~ 100 µL of PNF at 21.9 cm/min to PEEK tubing (#1531, IDEX Health and Science, Oak Harbor, WA) positioned between the middle of two sets of magnets and held in place by a tight gap. The length of the tubing in the magnetic zone was 5.1 centimeters, which represents a volume of 2.6 µL.

To trap magnetic material, 12 µL of PNF was flowed through PEEK tubing held within the gap of the magnetic device. After trapping of the magnetic material, buffer A (20 µL; 1.3 cm/min) was then flowed through to remove unretained material. The PEEK tubing was removed from the magnet zone and the retained magnetic material was eluted with buffer A (20 µL; 212 cm/min). The non-retained fraction had a final volume of 32 µL and the retained magnetic fraction had a final volume of 20 µL.

The PNF, non-retained, and magnetic retained organelle fractions were treated with LeuDox (1.51-7.57 ng; 10-50 µM) immediately after collection. Samples were mixed by repeated aspiration and of the mixture with a pipette. Samples were incubated in a thermomixer (37° C, 1 hour, 200 rpm). Samples were then removed and treated with equal volume MEKC buffer (32 µL or 20 µL), vortexed for 30 s, and either frozen at -20°C for next day analysis or immediately characterized by MEKC-LIF.

4.2.7. Controls for LeuDox biotransformations

A control experiment was done to ensure that the magnetic nanoparticles used here were not catalyzing the biotransformation of LeuDox to Dox. An excess of FeDex (20 mg/mL; 20 µL) relative to that used for magnetic enrichment was treated with LeuDox (1.51 ng; 10 µM) and incubated in a thermomixer (37° C, 1 h, 200 rpm). Thereafter, the control mixture was treated with an equal volume of MEKC buffer, vortexed for 30 s, and either frozen for future analysis or immediately characterized by MEKC-LIF.

Buffers may cause hydrolysis of LeuDox to Dox. Buffer A and PBS were treated with LeuDox (1.51-7.57 ng; 10-50 µM). Buffer A or PBS treatments were then incubated

in a thermomixer (37° C, 1 h, 200 rpm) and quenched with equal volume of MEKC buffer, vortexed for 30 s, and either frozen for future analysis or immediately characterized by MEKC-LIF.

PNF fractions were treated with Dox to ensure Dox was not biotransformed into an additional product with a similar migration time to LeuDox. Dox may biotransform to Doxorubicinol.[138, 202] Overlap would cause an increased fluorescence signal for LeuDox resulting in incorrect determination of the moles of LeuDox. PNF (2.5×10^7 cells; 200 μL) was treated with Dox (5.11 μg; 47 μM). The sample was then incubated in a thermomixer (37° C, 1 h, 200 rpm) and quenched with equal volume of MEKC buffer, vortexed for 30 s, and either frozen for future analysis or immediately characterized by MEKC-LIF.

4.2.8. MEKC-LIF analysis of LeuDox biotransformations

The custom-built instrument used for this work has been previously described.[89] Dox standard (1.0×10^{-7} M) was prepared by serial diluting of Dox stock solution (1.0×10^{-3} M in methanol) in MEKC buffer. Leu-Dox standard (1.0×10^{-6} M) was prepared by dissolving Leu-Dox (760 μg) in 400 μL of methanol then diluting 100-fold in MEKC buffer. Rhodamine 123 standard (R123; 1×10^{-9} M) was prepared by serial diluting a R123 stock solution in methanol (1.0×10^{-3} M) in MEKC buffer. Uncoated, 50-μm i.d., 42-cm long fused-silica capillary (Polymicro; Phoenix, AZ) was conditioned with 100 mM NaOH, deionized water, and MEKC buffer under external pressure (20-25 kPa) for 30 min each prior to the first sample injection. Separations were performed at -400 V/cm because this MEKC buffer reverses electroosmotic flow.[138] Fluorescence excitation was done with a 488-nm line argon-ion laser powered at 12 mW (Milles Griot; Irvine, CA). Fluorescence emission was selected with a 635 ± 27.5 nm filter (Omega Optical; Brattlesboro, VT) and detected with an R1477 photomultiplier tube (R1477 Hamamatsu Photonics, Hamamatsu, Japan) biased at 1,000V. Data was digitized by a NiDaq I/O data board (PCI-MIO-16XE-50, National Instruments, Austin, TX), and operated by Labview 5.1 software (National Instruments).

Data was analyzed using Igor Pro (WaveMetrics, Inc. Lake Oswego, OR). The limit of detection (LOD) for R123, Dox, and LeuDox was calculated as described below:

$$LOD = 3\left(\frac{\sigma}{I}\right) \times [C] \times V_i \qquad \textbf{Equation 4.1.}$$

where σ was the standard deviation of the baseline, I was the intensity of the standard, [C] was the injected standard's concentration, and V_i was the volume injected. The LODs of R123, Dox, and LeuDox were 2×10^{-19}, 2×10^{-18}, and 1×10^{-17} moles, respectively. While the optical components and filters were not optimized as well as previous reports leading to increased LODs (e.g. 61 zmol Dox[203]), the sensitivity achieved for Dox and LeuDox was still improved compared to high performance liquid chromatography methods previously used to determine levels of Dox and LeuDox.[16]

The resolution (R_s) between Dox and LeuDox was calculated as

$$R_S = (2 \times \Delta t_m) / (w_1 + w_2) \qquad \textbf{Equation 4.2.}$$

where t_m is the migration time and w is the peak width at half the maximum intensity. R_s between Dox and LeuDox peaks were 2.4.

The migration time (t_m) of analytes in MEKC varies from run-to-run and calls for methods to correct for such variations.[204] The migration time of Dox was corrected using the retention time of one standard (R123) and LeuDox itself because it was present in all the samples. The corrected migration time of Dox (t_x) was calculated as:

$$t_x = \frac{1}{\frac{1}{t_{m,1}} - \frac{1}{r}\left(\frac{1}{\hat{t}_{m,1}} - \frac{1}{\hat{t}_x}\right)} \qquad \textbf{Equation 4.3.}$$

$$r = \frac{\frac{1}{\hat{t}_{m,1}} - \frac{1}{\hat{t}_{m,2}}}{\frac{1}{t_{m,1}} - \frac{1}{t_{m,2}}} \qquad \textbf{Equation 4.4.}$$

where $\hat{t}_x$ is the observed t_m of Dox, $\hat{t}_{m,1}$ is observed t_m of R123, $t_{m,1}$ is the average t_m of R123, $\hat{t}_{m,2}$ is observed t_m of LeuDox, and $t_{m,2}$ is the average t_m of LeuDox.

The mole percent of LeuDox biotransformed into Dox in either the retained (R) or unretained (U) fraction was calculated as shown below:

$$\% = 100 \times \left\{ \left(\frac{A_{Dox} \times \frac{m_{Dox,S}}{A_{Dox,s}}}{\left[A_{Dox} \times \frac{m_{Dox,S}}{A_{Dox,S}}\right] + \left[A_{LeuDox} \times \frac{m_{LeuDox,S}}{A_{LeuDox,S}}\right]} \right)_{R,U} - \left(\frac{A_{Dox} \times \frac{m_{Dox,S}}{A_{Dox,s}}}{\left[A_{Dox} \times \frac{m_{Dox,S}}{A_{Dox,S}}\right] + \left[A_{LeuDox} \times \frac{m_{LeuDox,S}}{A_{LeuDox,S}}\right]} \right)_{Ctl} \right\}$$

Equation 4.5.

where A_{Dox} and A_{LeuDox} are the respective areas of peaks for Dox and LeuDox observed for a given sample; while $A_{Dox,S}$ and $A_{LeuDox,S}$ are the respective areas of peaks for Dox and LeuDox standards when $m_{Dox,S}$ and $m_{LeuDox,S}$ moles of Dox and LeuDox, standards, respectively, were injected and analyzed in a separate run. 'Ctl' is the biotransformation in a control fraction which only contains buffer and LeuDox to account for non-specific biotransformation.

4.2.9. Safety considerations

Biosafety level 2 was observed in all procedures involving MES-SA cells. Biological waste was treated with bleach prior to disposal. Used cell culture supplies were autoclaved prior to disposal.

4.3. Results

4.3.1. MEKC-LIF analysis of LeuDox to Dox biotransformations

Previous studies have suggested LeuDox is biotransformed into Dox in endocytic organelles including lysosomes and acidic organelles.[138, 197, 200] To investigate whether this is indeed the case, we treated magnetically enriched endocytic organelles with LeuDox and monitored the reaction products by MEKC-LIF. Prior work demonstrated that such magnetic enrichment procedure was adequate to prepare endocytic organelles with an expected acidic pH, which suggests that they are functional and that the preparation was devoid of other unwanted organelles.[88]

The basic test for biotransformation of LeuDox to LeuDox was separation of these two species by MEKC-LIF. Analysis of standards showed two peaks in the

electropherograms (Figure 4.2). The difference in their electrophoretic mobility was 4.6 × 10^{-5} $cm^2 \times s^{-1} \times V^{-1}$, which is similar to a previously reported value (5.2× 10^{-5} $cm^2 \times s^{-1} \times V^{-1}$).[138] LeuDox appeared either as a single peak or as major peak with an unresolved, minor peak, which is consistent with a previous report previously (Figure 4.2).[138] The sporadic appearance of the minor peak may be explained by the stereoisomeric nature of LeuDox (Figure 4.1).[204] Stereoisomers may have small differences in electrophoretic mobility, which are barely resolved only on some days; day-to-day variation in MEKC-LIF is commonplace. Further evidence supporting that both peaks are LeuDox are a clean mass spectrum (Figure B.1.) and the major and minor peak decrease in magnitude during formation of Dox. Therefore, for quantification purposes, both areas of these two peaks were included when calculating the moles of LeuDox (Equation 4.5.). Most importantly, all major species R123 (standard), Dox, and LeuDox were fully resolved thereby enabling a quantification of the transformation of LeuDox into Dox.

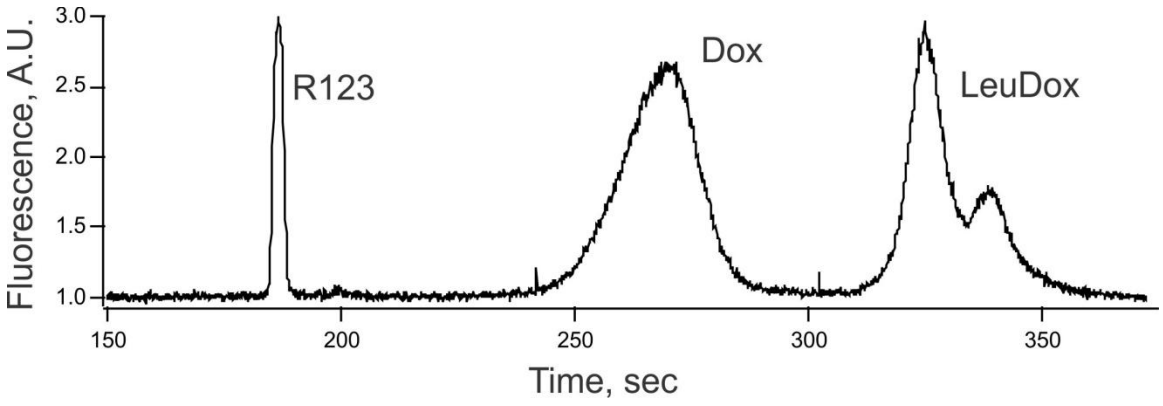

Figure 4.2. MEKC-LIF separation of LeuDox and Dox standards. Separation conditions: uncoated, 50-μm i.d., 42-cm long fused-silica capillary, -400 V/cm, MEKC buffer consisted of 4 mM CTAB, 40 mM tricine in deionized water, pH 8.5. Detection conditions: excitation with a 488-nm line argon-ion laser powered at 12 mW; emission was detected at 635 ± 27 nm. LeuDox (1.0 × 10^{-6} M concentration, t_m = ~430 s), Dox (1.0 × 10^{-7} M concentration, t_m = ~360 s), Rhodamine 123 (1 × 10^{-9} M, t_m = ~225 s).

Buffers or magnetic particles used for endocytic organelle enrichment may cause biotransformation of LeuDox into Dox.[191] We confirmed that Dox formation is due only to biotransformation of LeuDox in endocytic organelles and not to other hydrolysis

caused by material that could become in contact with LeuDox during the procedure. Dox formation was not detected when LeuDox was mixed with the homogenization buffer or PBS prior to MEKC-LIF analysis (Figure 4.3). Furthermore, Dox formation was not observed when magnetic nanoparticles in homogenization buffer were treated with LeuDox prior to MEKC-LIF analysis. These controls demonstrate that the biotransformation of LeuDox to Dox was likely caused by the endocytic organelles.

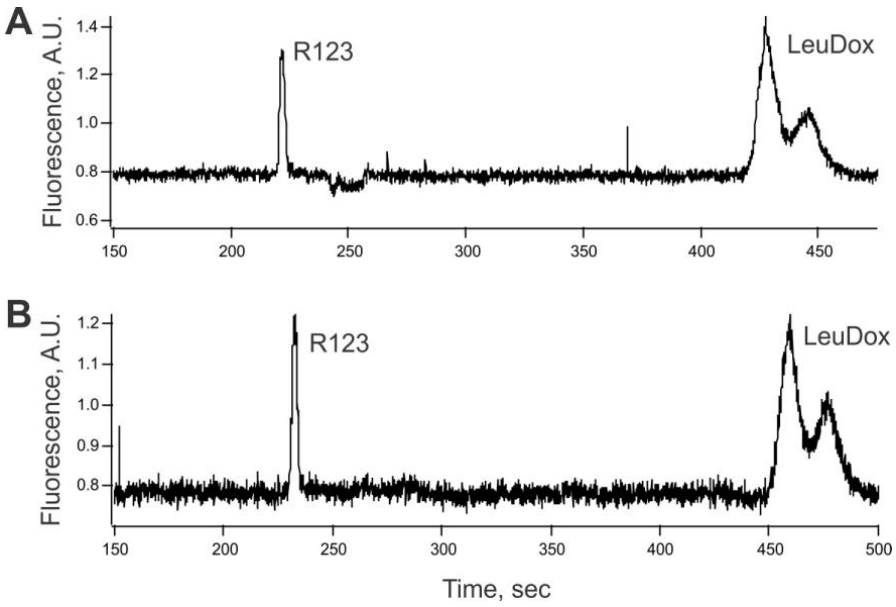

Figure 4.3. Controls for LeuDox to Dox biotransformations. (A) LeuDox in homogenization buffer (5×10^{-4} M LeuDox, t_m = ~430 s). (B) LeuDox in the presence of magnetic nanoparticles (20 mg/mL) suspended in homogenization buffer. Treatment time was 1 h. See Figure 4.2. for additional information.

One of the Dox metabolites in MES-SA cell lines is Doxorubicinol.[138, 202] If Doxorubicinol was formed, it may be detected and overlap with LeuDox peaks. Therefore, we performed a control experiment to determine whether Dox is metabolized to other products such as Doxorubicinol that have overlapping migration times with LeuDox. Overlapping products would bias the quantitation of LeuDox in a sample. To investigate this possibility, we treated the post-nuclear fraction with Dox. No biotransformation products with similar migration times to those of LeuDox were observed. The only indication of biotransformation of Dox was a broad band with peak

maximum at t_m = ~340 s. The difference in observed mobilities between Dox and the unidentified peak was the same as reported by Wang et al. for the differences between Dox and Doxorubicinol mobilities (6.2×10^{-5} $cm^2 \times s^{-1} \times V^{-1}$).[138] Thus, it is unlikely that Dox metabolism is forming compounds that bias the analysis of LeuDox is suggests the fluorescence levels detected for LeuDox in MES-SA cells and in enriched subcellular fractions prepared from this cell line (Figure 4.4).

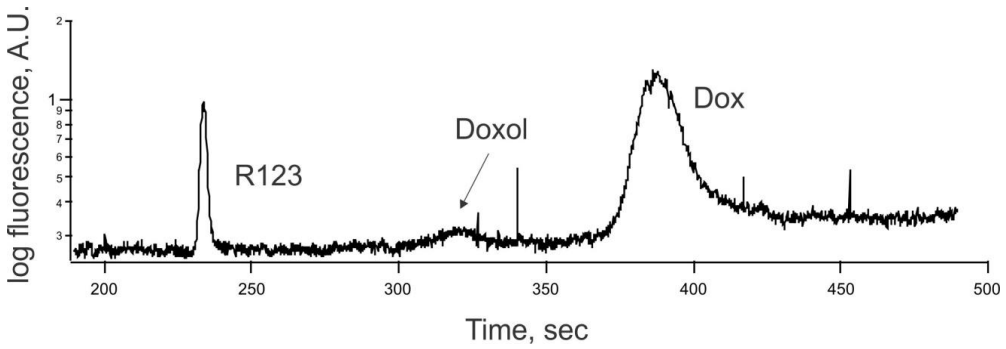

Figure 4.4. Biotransformation of Dox in PNF. The PDF was treated with Dox (4.7×10^{-6} M for 1 h, t_m = 400 s) and the only peak observed at t_m = ~335 s did not overlap with the LeuDox peak (t_m = ~450-500 s). See Figure 4.2. for additional information.

4.3.2. Biotransformations of LeuDox in MES-SA cells and MES-SA PNF

The biotransformation of LeuDox into Dox was 9.5% in living MES-SA cells. A parallel analysis using PNF instead of living MES-SA cells showed 23% of LeuDox is biotransformed into Dox in the PNF of these cells; a previous study reported that ~ 26% LeuDox biotransforms into Dox in the PNF of MES-SA cells.[138] The higher biotransformation of LeuDox in the PNF was anticipated because LeuDox can more readily access endocytic organelles when these have been released from whole cells. One caveat in these studies is that other organelles present in the PNF may be contributing to the biotransformation of LeuDox.

4.3.3. Biotransformation of LeuDox in magnetically enriched and non-enriched endocytic organelle fractions

The biotransformation of LeuDox into Dox in magnetically enriched and non-enriched endocytic organelle fractions was determined by MEKC-LIF (Figure 4.5.). Because the biotransformation did not occur in the presence of only buffers or magnetic particles, LeuDox biotransformation was attributed to endocytic organelles. Dox was successfully identified as a peak with migration time of 326 ± 30 s, (average ± st.dev, n = 2 independently prepared endocytic organelle fractions). The mole percent of LeuDox biotransformed to Dox was 10% (n=2) and 13% (n=2) in this magnetic enriched and non-retained fractions, respectively. This suggests 45% of the biotransformation occurred in the enriched organelle fraction.

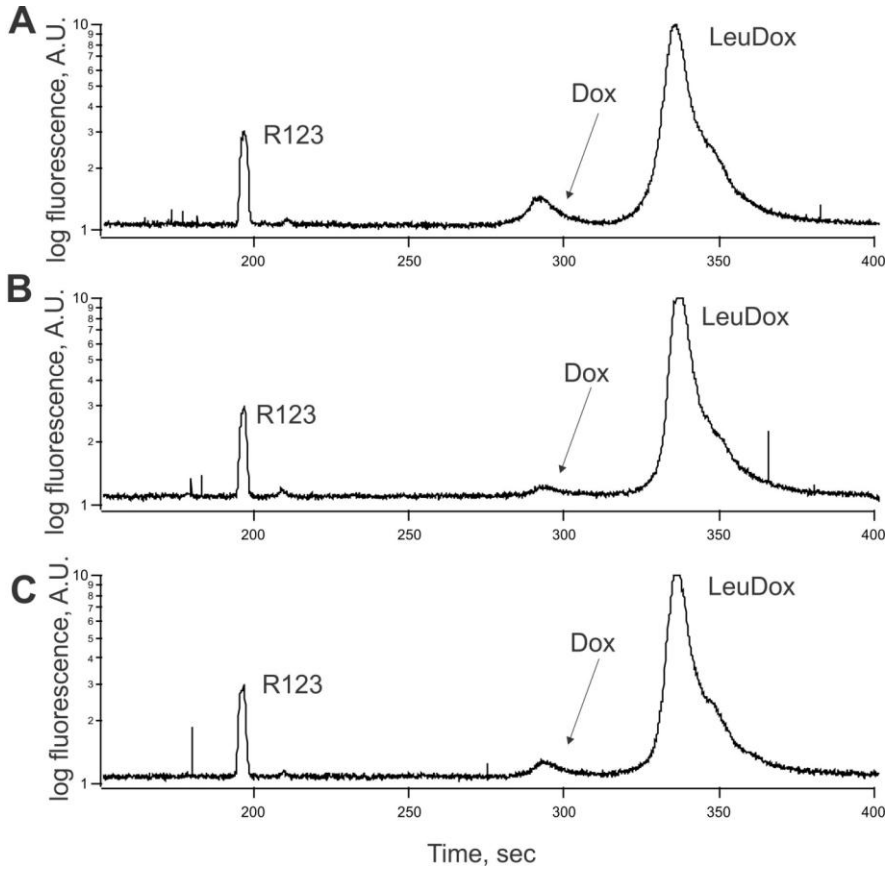

Figure 4.5. Biotransformations of LeuDox in the PNF of magnetically enriched endocytic organelle fraction. Fractions were treated with 5×10^{-4} M LeuDox for 1 hr, (A) Post-nuclear fraction (B). Non-enriched fraction. (C) Enriched fraction. See Figure 4.2. for additional information.

4.4. Discussion

In this study, we determined that 45% of the intracellular biotransformation of LeuDox into Dox occurs in a magnetically enriched fraction which contains endocytic organelles including lysosomes. We previously reported that the organelles in this fraction maintain an acidic pH (~ 4-6) and do not have detectable levels of mitochondria or peroxisomes.[88] Because the hydrolytic properties of endocytic organelles are unique to late endosomes and lysosomes and the enzymes involved require an acidic pH, we concluded that the LeuDox biotransformation into Dox occurs intracellularly in lysosomes and possibly in late endosomes.

The magnetic enrichment method did not capture all the endocytic organelles, which explains why LeuDox biotransformation was also observed in the non-retained fraction. Although we cannot rule out biotransformations caused by other organelle types (e.g. mitochondria) in the non-retained fraction, prior work indirectly suggested it is indeed endocytic organelles in the non-retained fraction that cause LeuDox biotransformation. In this prior work, the magnetically enriched and non-retained fractions had 18% and 82% of the endocytic organelles in the post-nuclear fraction, respectively.[88] Using this proportion of endocytic organelles in the two fractions, we anticipated that biotransformation of LeuDox in the magnetically retained and non-retained fractions would occur in similar proportions. Surprisingly, 45% of LeuDox transformation occurred in the magnetically retained fraction; this percentage increases to 95% when accounting for the endocytic organelle yield. This suggests that the retained organelles maintain higher specific biotransformation activity than those that were not retained.

A previous study treated living MES-SA cells with LeuDox for 12 hours and then determined that the fraction containing acidic organelles, prepared by differential centrifugation, biotransformed ~63% LeuDox into Dox.[138] This ratio is larger than the percentage determined in the magnetically retained fraction reported here (45%), which is not surprising because the current incubation with LeuDox lasted only 1 h.[138] Furthermore, the previous report treated living MES-SA cells with LeuDox raising the

possibility that LeuDox biotransformation occurred either extracellularly or in other subcellular locations; Dox produced could then traffic to endocytic organelles and become sequestered. In this study, direct treatment of the magnetically enriched endocytic organelle fraction ruled out this possibility and confirmed that LeuDox biotransformation occurs in the endocytic organelle fraction.

An aspect of the method that can be improved in the future is the functional status of endocytic organelles that have been magnetically isolated. Currently, incubation of LeuDox with endocytic organelles is adequate for 2-3 hours after isolation. Reduction of the duration of magnetic isolation time and stabilization of the functional status of the isolated organelles for longer times would extend the capabilities of the procedure described here. This could be done by providing ATP to enriched organelles to allow for proton gradients to be maintained for endocytic organelles.[205, 206] Reduction of the duration of the endocytic organelle technique could be done with more powerful magnets which would allow for increased flow rates of the biological sample.[207] Finally, a modified geometry of the magnetic apparatus could result in increased yields of endocytic organelles.[15, 170, 175]

4.5. Conclusions

This report demonstrated that intracellular biotransformation of LeuDox to Dox occurs in endocytic organelles, likely in lysosomes and late endosomes. Overall, the research describe here can determine the role of intracellular activation in the design of novel prodrugs. This technique may also be useful to determine other biotransformations that are attributed to lysosomes and other endocytic organelles. Intracellular biotransformation information may be critical in the future development of prodrugs with increased efficacy. Since we have shown LeuDox is biotransformed intracellularly in endocytic organelles, it may be advantageous to incorporate a liposome into LeuDox formulation, analogous to Dox and the liposome-form Doxil®. Doxil enter cells via nontargeted endocytosis allowing for Dox to be release in endocytic organelles.[208] A similar approach for LeuDox could also result in increased intracellular activation.

This methodology described here can also be applied to other prodrugs that may not only be activated by metalloproteases and other extracellular enzymes, but also intracellularly. Furthermore, this technique may be useful to determine other biotransformations that are attributed to lysosomes and other endocytic organelles. Although only MES-SA cells were used here, the potential of other cell lines (e.g. CCRF-CEM and CEM/C2 human leukemia cells[106]) to activate intracellularly LeuDox and other prodrugs could be investigated with the methodology described here. Ultimately, the methodology could be extended to animal tissues such as Balb/c nude mice[209] and rabbit,[195] as well as human tissues such as ovarian cancer,[210, 211] or samples acquired during clinical trials.[196]

In order to determine prodrug biotransformations from tissue, new techniques may need to be developed. Isolated tissues could be treated with nanoparticles similar to the treatment of cells with nanoparticles as described previously.[88] If this technique does not produce a sufficient yield of enriched endocytic organelles, magnetic immunoenrichment techniques may need to be developed for tissue. An antibody against a lysosome-enriched protein could be bound to a magnetic particle. Following binding between the antibody and protein, an external magnetic field can be used to enrich the magnetic particle with bound organelles.[212, 213]

Chapter 5

A Workflow for Preliminary Identification of Small Molecules Enriched in Autophagosomes and Activated Mast Cells Using UPLC-MS^{E}, Chemometrics, and Mass Spectral Evaluation

Joseph Koopmeiners developed the home-written programs for the linear mixed model. Audrey Meyer prepared mast cell secretion samples. Jose Antonio Rodriguez prepared enriched autophagosomes from rat liver tissue. Thane Taylor assisted in the removal of mitochondria in autophagosome enriched fractions from rat myoblast cell culture. Michelle Henderson assisted in Western blotting. Anna Maria Cuervo provided scientific insight in the preparation of autophagosomes. This work was supported by a Center for Analysis of Biomolecular Signaling training grant (University of Minnesota) and NIH grant AG020866. Individual support to C.P.S. (NIH GM8347), J.S.K. (NIH P30CA077598), J.A.R.N. (NIH AG031782, Spanish Ministerio de Educacion y Ciencia Fellowship, Revson Foundation Fellowship), T.H.T. and M.M.H. (NIH Chemistry Biology Interface Training Grant 5T32GM008700), and C.L.H. (NIH DP2 OD004258-01).

The high sensitivity, selectivity, and mass accuracy of LC/MS using high-resolution mass analyzers have made it a method of choice for the generation of metabolic signatures and databases. Failure to evaluate database identifications that are based solely on accurate mass measurements, however, may lead to erroneous identifications. This report describes a workflow based on ultra high performance liquid chromatography (UPLC) coupled to acquisition of low- and high-collision energy mass spectra (MS^e) for preliminary feature (a sample-specific chemical entity characterized by a unique constitution of chromatographic retention time, *m/z* and intensity) identification in the following biological systems: (a) rat liver autophagosomes; (b) rat myoblast autophagosomes; (c) chemically activated murine mast cells. The developed workflow consists of 5 steps: (1) UPLC/MS^e profiling of the systems of interest; (2) chemometric analysis to determine candidate features characteristic of these biological systems; (3) confirmation of candidate features via evaluation of extracted ion chromatograms (XICs); (4) database searching to provide potential identifications of confirmed features; (5) mass accuracy confirmation, evaluation of fragmentation patterns from MS^e spectra, and precursor-product XIC alignment to provide preliminary identifications of evaluated features. For rat liver-enriched autophagosome fractions, 114 confirmed features were determined from which 23 preliminary identifications were made. For rat myoblast-enriched autophagosome fractions, 130 confirmed features were determined from which 12 preliminary identifications were made. Chemometric approaches determined 2,656 confirmed features from activated mast cells from which 14 preliminary identifications were made. Precedent literature supports the biological relevance of many of the preliminary identifications made for the biological systems studied here.

5.1. Introduction

Liquid chromatography coupled to mass spectrometry (LC/MS) employing high resolution mass analyzers is often the method of choice for the analysis of compounds in biological systems due to its high sensitivity, selectivity, and mass accuracy.[214-216] A rapid and robust method for biological chemical profiling studies by LC/MS is UPLC/MS^e.[215, 217-219] UPLC/MS^e employing an orthogonal quadrupole-time-of-flight mass spectrometer can provide rapid, high peak-capacity separations with simultaneous

acquisition of low- and high-collision energy mass spectra with excellent mass accuracy for both parent and fragment ions. This combination allows more comprehensive validation of detected features (sample-specific chemical entities characterized by a unique constitution of chromatographic retention time, *m/z* and intensity) without the requirement to perform additional precursor-selected MS/MS experiments on those features.

The large amount of data generated by LC/MS(MS)-based profiling experiments, including UPLC/MS^e, requires the use of multivariate chemometric approaches for the detection of chemical entities specific to a given biological system. Orthogonal partial least squares with discriminate analysis (OPLS-DA) is a chemometric approach that classifies potential features into one of two comparative biological fractions.[220-223] Disadvantages of OPLS-DA include the failure to detect candidate features that are not well grouped into one of the two biological fractions due to a group-averaging effect from discriminate analysis.[224] Alternate approaches to using OPLS-DA for detecting candidate features include the t-test and linear mixed model (LMM) which compare the average intensity of XICs between samples[225] Both approaches provide similar information but the LMM is also able to partition the total variance into the biological and analytical variance when instrumental replicates are present.[225] The LMM is more powerful than the t-test, resulting in an increased number of detected candidate features, but is susceptible to model misspecification, which can result in inaccurate selection of candidate features and potential omission of some candidate features unique to a sample that have increased variation.[224] Incorrectly applied chemometric approaches in combination with misidentification of confirmed features by databases, the only criterion for which is the measured accurate mass of precursor ions, can result in the inadvertent determination of false-positive candidate features. Applying multiple chemometric approaches to a given data set can increase coverage for the detection of candidate features and can compensate for the limitations of detection for each individual chemometric approach.

Despite the advantages of LC/MS-based approaches combined with chemometrics for metabolite profiling studies, there are potential pitfalls.[226-228] Slight changes in

chromatographic retention times can result in misassignment of sample-specific features. Chemometric approaches used to detect candidate features with extracted ion chromatograms (XIC) near the peak intensity threshold may not be true positives. Ion suppression of chemical species due to co-eluting compounds can cause an inaccurate assessment of analyte relative abundance, cause increased variation in XIC quantification in replicate analyses, or cause complete loss of detection. Identification of confirmed features by database searches based solely on accurate mass measurement of precursor (parent) ions may lead to incorrect structural assignments.[228] In addition, for MS^e analyses, co-eluting species can result in complex low- and high-collision energy mass spectra that may limit the ability to confirm the precursor-product relationships for a given feature. These disadvantages are often multiplied by the inability to perform ideal numbers of replicate LC/MS examinations.

The numerous caveats regarding chemometric analysis and database searching summarized above make the evaluation of both chemometric-determined candidate features and database identifications imperative. As such, a workflow has been developed to evaluate and confirm the determination and preliminary identification of features resulting from chemometric analysis of UPLC/MS^e analyses of complex biological samples combined with structural database searching (Figure 5.1.). The workflow includes (1) untargeted UPLC/MS^e profiling of the systems of interest; (2) application of chemometrics to identify candidate features characteristic of these biological systems; (3) confirmation of identified features via evaluation of extracted ion chromatograms (XICs), referred to as Checkpoint 1 (Figure 5.1.); (4) database searching to provide potential identifications of confirmed features; (5) mass accuracy confirmation, evaluation of fragmentation patterns of each feature from simultaneously acquired high-collision energy mass spectra, and precursor-product XIC alignment to provide determinant identifications of confirmed features, referred to as Checkpoint 2 (Figure 5.1.). This workflow has been employed in a proof-of-principle study to identify compounds specific to autophagosomes. These are organelles that facilitate the degradation of intracellular components via a biological process called autophagy. Abnormal autophagy has been associated with multiple disease states including Parkinson's disease,[71, 229, 230]

Huntington's disease,[229] and Alzheimer's disease.[230, 231] To demonstrate broad applicability of the described approach for comparison of dissimilar biological systems at the molecular level, it has also been applied to the characterization of chemically stimulated mast cells that are known to play an important role in allergic/inflammatory response.[232]

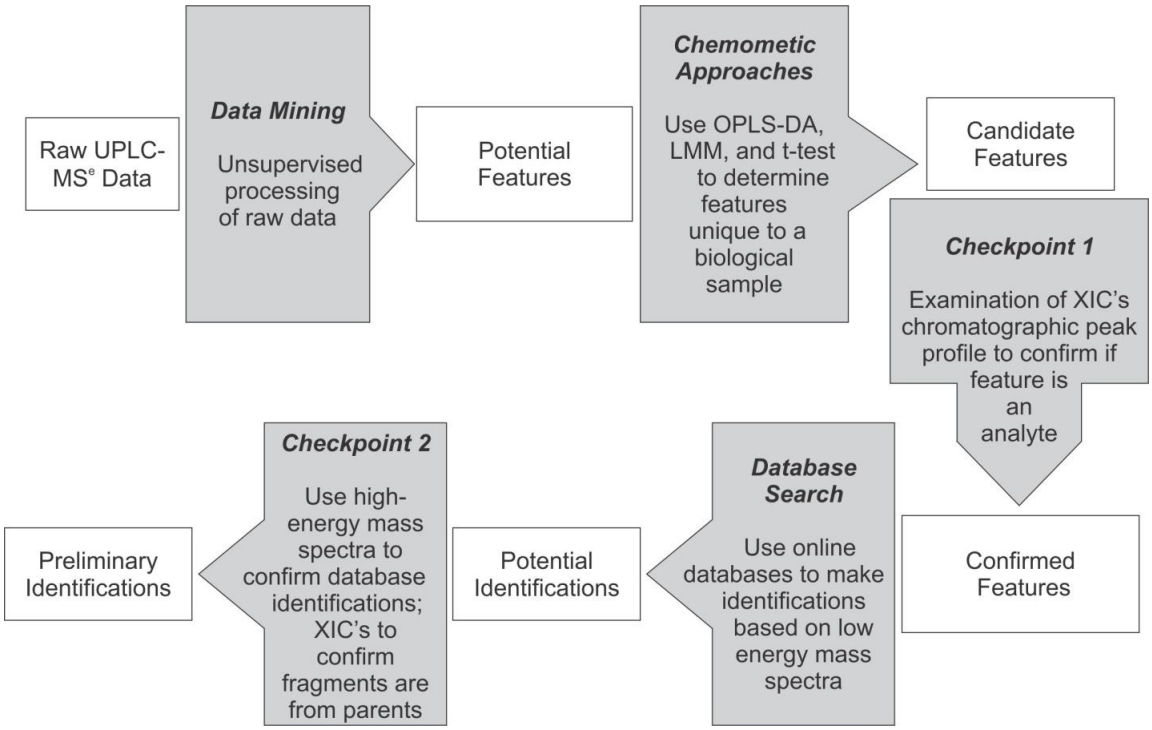

Figure 5.1. Workflow for determination, confirmation, and preliminary identification of features from UPLC/MS^e data.

5.2. Materials and Methods

5.2.1. Reagents

Metrizamide was purchased from Amresco (Solon, OH). Vinblastine sulfate, sucrose, gentamycin, Trizma-hydrochloric acid, potassium chloride, sodium chloride, d-glucose, calcium chloride, protease inhibitor cocktail (for mammalian cell and tissue extracts, in DMSO solution), sodium hydroxide, and magnesium chloride were from Sigma Aldrich (St. Louis, MO). Glycyl-L-phenylnaphthylamine was from Bachem (Torrance, CA). Methanol was from Fisher Scientific (Fairlawn, NJ). Dichloromethane

was from Mallinkrodt (Phillipsburg, NJ). Ultra LC/MS-grade methanol, acetonitrile, and water were from JT Baker (Center Valley, PA). Formic acid was from EMD (Darmstadt, Germany). Penicillin-streptomycin solution (PS) was from Life Technologies (Grand Island, NY). Anti-TNP IgE antibody was from BD Biosciences (San Jose, CA). CXCL10 was from Shenandoah Biotechnology (Warwick, PA). Dubelco's Modified Eagle Medium (DMEM) high glucose cell medium, bovine calf serum, and fetal bovine serum were from Thermo Scientific (Waltham, MA).

5.2.2. Enrichment of autophagosomes from rat liver

Male Wistar rats (200–250 g) were obtained from Jackson Laboratory. Autophagosomes were isolated from rat liver after 6 h starvation using a protocol modified from the literature.[233] Livers were harvested, minced and homogenized using a Teflon homogenizer prior to separation by differential centrifugation. A pellet containing the nuclear fraction and (up to 30%) unbroken cells was produced first. The supernatant was centrifuged at 100,000g and the pellet contained non-enriched organelles. Autophagosome fractions were enriched by differential centrifugation followed by discontinuous density metrizamide gradients as previously described.[20, 233]

5.2.3. Enrichment for autophagosomes from rat myoblast cell culture

L6 rat myoblast cells were cultured in 450 mL DMEM with 50 mL fetal bovine serum, and 100 μL gentamycin. For the enrichment of autophagosomes, cells were first treated with vinblastine sulfate dissolved in 0.9% sodium chloride at a final concentration of 50 μM in DMEM solution for 2 hours. Homogenization buffer consisted of 250 mM sucrose in deionized water (Millipore Synergy UV system, 18.2 mΩ/cm, Bedford, MA) adjusted to pH 7.2 with 100 mM sodium hydroxide. Cells were collected in homogenization buffer and centrifuged twice at 1,000g for 10 min. The cell pellet was resuspended in 1 mL homogenization buffer and 1% protease inhibitor cocktail. Cells were lysed with a Dounce homogenizer (clearance, 0.0025 in, Kontes Glass, Vineland, NJ). An organelle pellet was formed from the lysate with sequential 600g (to remove nuclei and cell debris) and 16,100g (to remove cytosol and cytosolic proteins) differential centrifugation steps. The resulting post-nuclear fraction was the control, non-enriched

fraction. To enrich for autophagosomes, mitochondria were immuno-removed with the Mitochondria Isolation Kit (MACS, Miltenyi Biotec, Auburn, CA) according to the manufacturer's procedure using the homogenization buffer described above. Lysosomes were osmotically lysed with 500 nM glycyl-L-phenylnapthylamine for 8 min at 37 °C at 200 rpm on a thermomixer. Following treatment, the fraction was centrifuged for 30 min -at 16,100g. The resulting organelle pellet was defined as the enriched autophagosome fraction. Protein quantitation was done with the Pierce BCA protein assay kit (Thermo Fisher, Rockford, IL) according to the manufacturer's procedure.

5.2.4. Extractions of autophagosome samples

A two step protocol for polar and nonpolar extractions was used for extractions of enriched autophagosome fractions.[234] Fractions were treated with 1.5 mL ice cold 1:1 v/v methanol:deionized water. Pellets were resuspended with a syringe, vortexed for 30 s, and incubated for 5 min. Samples were centrifuged at 16,100g for 10 min to pellet any non-extracted materials. The supernatant, defined as the polar extraction, was removed and kept on ice. The remaining pellet was treated with 1.5 mL ice cold 1:3 v/v dichloromethane:methanol. The pellet was resuspended with a syringe, vortexed for 30 s, and incubated for 5 min. The sample was centrifuged for 16,100g for 10 min to pellet any non-extracted materials. The supernatant, defined as the non-polar extraction, was removed and kept on ice. Extracted samples were vacuum concentrated overnight at room temperature to remove extraction solvent. Sample extracts were stored under nitrogen at 4° C until analysis.

5.2.5. Stimulation of mast cells

Murine peritoneal mast cells (MPMCs) were isolated via peritoneal lavage following euthanasia by CO_2 asphyxiation. Lavage was performed using approximately 8 mL per mouse of cell culture media composed of ice-cold high-glucose DMEM supplemented with 10% (v/v) BCS and 1% (v/v) PS, and 6-7 mL lavage fluid were recovered per mouse. After isolation, cells were pelleted at 450g, resuspended in fresh media, and cultured overnight on a confluent monolayer of NIH/3t3 fibroblasts

(purchased from American Type Culture Collection, Manassas, VA) with 0.5 µg/mL anti-TNP IgE.

MPMCs were washed three times with 37 °C Tris buffer (12.5 mM Trizma-HCl, 150 mM NaCl, 4.2 mM KCl, 5.6 mM glucose, 1.5 mM $CaCl_2$, and 1.4 mM $MgCl_2$, pH 7.4) to remove cell culture media, serum proteins, and cell debris. MPMCs were treated either with Tris buffer (2 cultures prepared) or with Tris buffer containing 200 ng/mL CXCL10 for 2 hr (2 cultures prepared). Each pair of cultures was then treated with either Tris buffer or Tris buffer containing 100 ng/mL TNP-ova for 2 hr. These treatments in series created four different activation conditions: (1) Tris buffer followed by Tris buffer, (2) Tris buffer followed by TNP-ova, (3) CXCL10 followed by Tris buffer, and (4) CXCL10 followed by TNP-ova.

Supernatants were collected and filtered using PTFE 0.2 µm centrifugal filter units at 14,000g for 5 min, then stored overnight at -80 °C. Prior to UPLC/MS^e analysis, samples were concentrated to 100 µL, and salts and proteins were precipitated via the addition of 1 mL ice cold ethanol. Samples were then centrifuged at 12,000g for 10 min, and supernatants were vacuum concentrated to approximately 30 µL. Tris buffer/TNP-ova and CXCL10/TNP-ova samples were reconstituted to 300 µL with LC/MS-grade water and analyzed by UPLC/MS^e. Tris buffer/Tris buffer and CXCL10/Tris buffer samples were stored at -80 °C, then reconstituted to 300 µL with LC/MS-grade water prior to UPLC/MS^e analysis.

Samples were resuspended prior to UPLC/MS^e analysis as previously described.[234] Briefly, both polar and nonpolar extracts were resuspended in 200 µL 1:1 v/v methanol:deionized water. Samples were vortexed for 30 s to resuspend the pellet followed by sonication for 30 min. The sample was centrifuged for 16,100g for 10 min to remove any non-resuspended materials.

5.2.6. UPLC/MS^e conditions

A Waters Acquity UPLC coupled to a Waters Synapt G2 HDMS quadrupole orthogonal acceleration time of flight mass spectrometer was used for UPLC/MS^e

analysis. The reversed-phase column used was a Waters HSS T3 C_{18} 2.1 mm x 100 mm column (1.7 μm diameter particles) operated at 35°C. The following 28 min linear gradient separations were employed at a flow rate of 0.40 mL/min using a mobile phase consisting of A: water containing 0.1% formic acid and B: acetonitrile containing 0.1% formic acid. The gradient profile for samples from polar extractions was: 3% B, 0 min to 5 min; 3% B to 97% B, 5 min to 18 min; 97% B, 18 min to 21 min; 97% B to 3% B, 21 min to 23 min; 3% B 23 min to 28 min. The gradient profile for nonpolar extractions was: 30% B, 0 min to 5 min; 30% B to 97% B, 5 min to 18 min; 97% B, 18 min to 21 min; 97% B to 3% B, 21 min to 23 min; 3% B, 23 min to 28 min. Dead time was 0.68 min for the polar separation and 0.54 min for the non-polar separation as determined by injection of acetone. Simultaneous low- and high-collision energy (CE) mass spectra were collected in centroid mode over the range *m/z* 50-1200 every 0.1 s during the chromatographic separation. MS^e parameters in positive electrospray ionization mode were as follows: capillary, 2.0 kV; sampling cone, 35.0 V; extraction cone, 5.0V; desolvation gas flow, 800 L/h; source temperature, 100 °C; desolvation temperature, 350 °C; cone gas flow, 20 L/h; trap CE, off (low CE collection), trap CE ramp 15V-65V (high CE collection); lockspray configuration consisted of infusion of a 5 μg/mL solution of leucine-enkephalin and acquisition of one mass spectrum (0.2 s scan, *m/z* 100-1200) every 10 s. Three lockspray *m/z* measurements of protonated leucine-enkephalin were averaged and used to apply corrections to measured *m/z* values during the course of the analysis. All MS^e parameters were identical in negative ionization mode except the following: capillary, 2.5 kV; sampling cone, 30.0 V; extraction cone, 4.0V.

5.2.7. UPLC/MS^e data analysis and workflow

Waters MarkerLynx™ was used for mining chromatographic and mass spectral data using three-dimensional peak integration and data set alignment to determine potential features. The parameters were set to achieve determination of 1000-2000 potential features specific to a given biological system. Data extraction parameters within Markerlynx™ were set as follows: extracted ion chromatogram tolerance was ±20 mDa, peak width assessment was done at half-height of the peak, peak-to-peak baseline noise

was 8.0 counts, marker intensity threshold was 100 counts, mass window was ±20 mDa, and the retention time window was ±0.10 min.

Chemometric analysis was used for determination of candidate, system-specific features from UPLC/MS^e data. The LMM and t-test approaches were implemented in the R programming language using a home-written script and OPLS-DA was used within Waters MarkerLynx™.[235] Candidate features (Figure 5.1.) were selected by comparing their relative abundance, as measured by XIC intensity, between control and either enriched or stimulated fractions. Experiments with no biological replicates but with three instrumental replicates (rat liver autophagosomes) were analyzed using the two-sample t-test for unequal variances. Experiments with both three biological replicates and three instrumental replicates each (rat skeletal autophagosomes and activated mast cells) were analyzed using LMM.[225] Analysis for the t-test and LMM was performed on the log-transformed scale and differences between biological samples were described by the ratio of geometric means. Multiple comparisons were accounted for by controlling the false discovery rate, which was calculated using the approach described in Benjamani and Yekutieli.[236] For autophagosome-enriched samples, potential features with a false discovery rate of 10% or less were selected as candidate features and for activated mast cells, features with a false discovery rate of 1% or less were selected as candidate features for Checkpoint 1 (Figure 5.1.). For determining candidate features with OPLS-DA, selected potential features were at the edges of the OPLS-DA-generated S plot (Figure 5.2.). An S plot is one option available for visualization of OPLS-DA data.[237] The enrichment of the preliminary feature in a biological system is plotted on the x-axis and correlation of enrichment is plotted on the y-axis. Features that were $> \left|0.001\right|$ for coefficient 2 (x-axis) and $> \left|0.90\right|$ for correlation (y-axis) were selected for checkpoint 1 (Figure 5.1.).

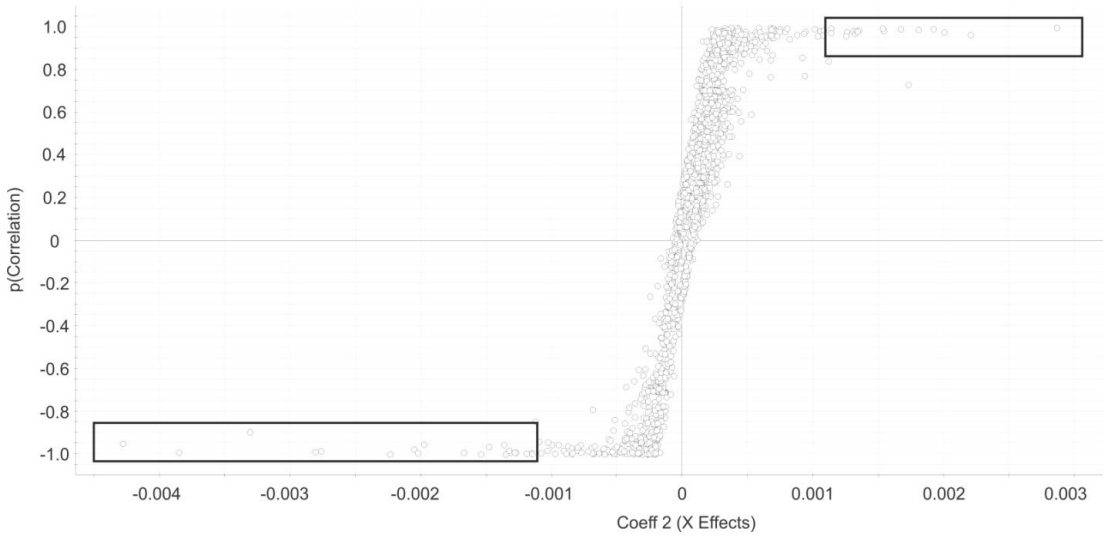

Figure 5.2. OPLS-DA-generated S-Plot from OPLS-DA chemometric approach for identification of rat liver autophagosome-specific candidate features. Candidate features are indicated by circles. Features approaching x = -0.004 are specific to autophagosome-enriched while features approaching x = 0.003 are specific to the control. Squares indicate the features selected in the autophagosome-enriched and control samples.

Confirmed features were determined at Checkpoint 1 (Figure 5.1.). All candidate features were examined with XICs from the low-collision energy mass spectra for a given *m/z* value with a 5 ppm mass tolerance. The candidate feature was rejected if the XIC appeared as a noise spike, had a very low signal-to-noise ratio (< 2), or if the XIC was not characterized as having a true chromatographic peak profile.

Database identifications were made using online database searches. All XIC-confirmed features for the autophagosome-enriched samples were selected for database searching. Due to the large number of confirmed features for activated mast cells, the top 250 confirmed features for the LMM and all confirmed features for the OPLS-DA were selected for database searching. Online databases included the Chemical Entities of Biological Interest, Human Metabolome Database, and Lipid MAPS databases with a mass tolerance of < 10 mDa. The ChemSpider database was used with the same mass tolerance when candidate features did not result in matches in the other databases.

Searches were made for the neutral mass values corresponding to $[M+H]^+$ and $[M-H]^-$ ions. All database identifications were selected for Checkpoint 2 (Figure 5.1.).

Features with database identifications were evaluated at Checkpoint 2. Checkpoint 2 consists of (1) XIC alignment of coeluting ions to verify the presence of putative precursor ions corresponding to the database-identified species; (2) corroboration of identity by comparison of fragmentation patterns observed in the high-collision energy mass spectra of each precursor with simulated fragmentation patterns calculated *in silico* using Waters MassFragment™ software; (3) manual precursor-product XIC alignment. MassFragment parameters were set as follows: the 20 most intense *m/z* species from the high-collision energy mass spectra were compared to theoretical fragments with a tolerance of 10 mDa. Double bond equivalence values were between -10 to 50, electron count was set to "both", maximum H deficit was 6, fragment number of bonds was 4, and scoring parameters were for aromatic (6), multiple (4), ring (2), phenyl (8), other (1), H-deficit (0), hetero modifier (0.5), alpha penalty (5), and max score (16). Preliminary identifications supported by the evaluation criteria described here are reported using their database identification number (CE:18337).[238]

5.2.8. Safety considerations

All Biosafety Level 2 guidelines were followed when working with cell culture and tissue. Biological waste was bleached for 30 min prior to disposal.

5.2.9. Animal considerations

All rat studies for autophagosome enrichment were conducted under an animal study protocol approved by the Albert Einstein College of Medicine Animal Institute Animal Care and Use Committee. Calorically restricted rats were allowed free access to water. All mice for mast cells were raised and euthanized according to an animal study protocol #0806A37663 approved by the University of Minnesota Institutional Animal Care and Use Committee.

5.3. Results and Discussion

Chemometric analysis of complex data sets such as those generated by UPLC/MS^{e} experiments expedites the determination of system-specific chemical features.[239] While chemometric approaches in concert with database searches have become essential to improving efficiency in systems biology research, there is the likelihood that some candidate features may be false positives and/or misidentified. Additionally, database identifications based only on mass accuracy measurements of detected precursor ions are often erroneous.[228] As such, evaluation of chemometrics-determined features and subsequent database-identified compounds becomes imperative to assigning reliable preliminary identifications. A detailed description of a workflow (Figure 5.1.) developed to appraise chemometric outputs and database identifications and ensure reliable determination of confirmed features and their preliminary identities follows. The application of this workflow toward preliminary identification of biologically relevant compounds specific to autophagy and mast cell stimulation is highlighted.

The developed workflow is comprised of the following: (1) untargeted UPLC/MS^{e} profiling of the systems of interest; (2) application of chemometrics to identify candidate features characteristic of these biological systems; (3) confirmation of candidate features via evaluation of extracted ion chromatograms (XICs); (4) database searching to provide potential identifications of confirmed features; (5) mass accuracy confirmation, evaluation of fragmentation patterns of each feature from acquired low- and high-collision energy mass spectra, and precursor-product XIC alignment to provide preliminary identifications of confirmed features.

This workflow was first applied to the analysis of two different enriched autophagosome samples, a "gold standard" of enrichment of autophagosomes prepared from rat liver tissue by density gradient centrifugation[20, 233] and a fraction of autophagosomes prepared from rat myoblast cell culture by differential centrifugation, immuno-depletion of mitochondria and osmotic lysis of lysosomes. For the rat liver sample, unwanted organelle types were removed by differential and density gradient centrifugation. Western blotting analysis revealed no detectable lysosome contamination (Figure C.1.). For the rat myoblast sample, cells were treated with vinblastine, which

increases the number of autophagosomes.[81] Mitochondria and lysosome levels were decreased from an enriched organelle pellet by immuno-depletion of mitochondria and glycyl-L-phenylnaphthylamine (GPN) lysis of lysosomes,[81] respectively. Western blotting analysis revealed no detectable mitochondria and a highly reduced level of lysosome in the enriched autophagosome fraction (Figure C.2.) consistent with previous published results for rat hepatocyte cells.[240]

Manual examination of total ion chromatograms resulting from UPLC/MS^e analysis of extracts of enriched autophagosomes as compared to a total organelle control proved inadequate to detect autophagosome-specific, XIC-confirmed features. As such, three chemometric approaches (OPLS-DA, t-test, and LMM) were used to maximize the number of detected candidate features specific to rat liver enriched autophagosomes and rat myoblast cell culture enriched autophagosomes. Applying multiple chemometric approaches to a given data set can increase coverage for the detection of candidate features, compensate for the limitations of detection for each individual chemometric approach, and provide additional confirmation of the validity of preliminary identifications. Of the 63 XIC-confirmed features determined with OPLS-DA for the enriched autophagosome samples, 34 were also detected with the LMM and t-test. Of the 401 confirmed features determined with OPLS-DA for the mast cell samples, 328 were also determined with the LMM.

5.3.1. Features and identifications from rat liver

For the enriched autophagosome fraction from rat liver tissue, multiple chemometric approaches detected 114 candidate features (Table C.1.). Confirmation of candidate features via evaluation of XICs (Checkpoint 1, Figure 5.1.) yielded 76 confirmed features (67% of detected candidate features). The percentage of common confirmed features determined with multiple chemometric approaches averaged 17% (Table C.1.). An online database search of the 76 confirmed features yielded 46 potential database identifications (Table C.1.). The percentage of common XIC-confirmed features identified with multiple chemometric approaches averaged 17% (Table C.1.). Checkpoint 2 scrutinized the online database identifications by manual examination of low- and high-

collision energy mass spectra and matching observed fragmentation patterns with simulated fragmentation patterns for the identified compound (determined using Waters MassFragment™), as well as precursor-product XIC alignment. Overall, 23 preliminary identifications were made following Checkpoint 2 (Table 5.1., Figure. C.3A.). Rejection of potential database identifications resulted primarily from one or both of the following criteria: (1) lack of supporting fragmentation pattern data from acquired high-collision energy mass spectra (MS^e) and/or (2) inconclusive precursor-product XIC alignment in complex spectra resulting from analyte coelution. While it is understood that these tentatively rejected identifications may in fact be valid, additional experiments including true precursor-selected MS/MS analysis, and/or UPLC/MS/MS analysis of standards, if available, will be required to make identifications. Figure 5.3. illustrates data supporting the identification of one such autophagosome-specific compound, 1-hexadecanoyl-sn-glycero-3-phosphoethanolamine (PE(16:0/0:0); LMGP02050002, Figure 5.3A.). Figure 5.3B. and 5.3C. show aligned low- and high-collision energy extracted ion chromatograms for *m/z* 454.294 in the analysis of an autophagosome-enriched fraction of rat liver, respectively. A trend plot (Figure 5.3D.) for the observed precursor ion indicates the relative abundance of this compound in the autophagosome-enriched fraction (Aps, Figure 5.3D) versus the non-enriched fraction (control, ctl, Figure 5.3D). Trend plot data was used to .calculate the fold-enrichments provided in Table 5.1. Figure 5.3E. and 5.3F. illustrate the low collision energy mass spectrum and high collision energy mass spectrum of PE(16:0/0:0), respectively. Elemental compositions, *m/z* values, and mass errors of observed fragment ions corresponding to theoretical fragment ions generated *in silico* using MassFragment™ are depicted in Figure 5.3G.

System[1]	Ext[2]	ESI[3]	*m/z*	T_R	p-value	FE[4]	Chem[5]	PI[6]	Mass Error (ppm)
Liver	NP	+	288.295	9.14	1.49×10^{-5}	P/A	t-test, OP	HMDB00269*	1.7
Liver	NP	+	288.295	8.85	8.62×10^{-6}	P/A	t-test, OP	HMDB00269*	1.7
Liver	NP	+	415.214	10.52	1.24×10^{-3}	1.85	t-test, OP	CHEBI31547	0.5
Liver	NP	+	601.438	17.80	1.08×10^{-4}	1.68	t-test, OP	LMGL02010051	7.4
Liver	NP	+	623.451	17.76	1.09×10^{-4}	1.74	t-test, OP	LMGP01011228	0.2
Liver	NP	+	755.525	17.42	6.34×10^{-4}	1.86	t-test	LMGP01010604	2.7
Liver	NP	+	265.109	7.68	3.39×10^{-4}	P/A	t-test	CS124129	0.6
Liver	NP	+	244.268	8.89	N.A.	2.18	OP	CS59037	1.9
Liver	Polar	+	361.276	15.10	9.73×10^{-5}	P/A	t-test	LMST03020020	0.6
Liver	Polar	+	454.294	14.55	4.91×10^{-6}	11.6	t-test, OP	LMGP02050002	2.0
Liver	Polar	+	522.355	14.98	1.81×10^{-4}	P/A	t-test	HMDB10385	0.1
Liver	Polar	+	524.371	15.99	2.58×10^{-5}	2.82	t-test, OP	LMGP01050123	0.2
Liver	Polar	+	570.352	14.34	2.52×10^{-6}	P/A	t-test	HMDB10403	0.6
Liver	Polar	+	300.294	13.11	4.23×10^{-5}	P/A	t-test	CHEBI16393	1.3

Liver	Polar	+	367.143	0.54	3.19×10^{-5}	P/A	t-test	CHEMBL421556	0.1
Liver	Polar	+	415.213	13.85	1.77×10^{-4}	3.23	t-test, OP	CS8129200	0.2
Liver	Polar	+	674.460	17.63	3.47×10^{-4}	P/A	t-test	LMGP01010523	2.3
Liver	Polar	+	415.213	13.41	N.A.	1.93	OP	CS9677319	0.4
Liver	Polar	+	482.324	15.90	N.A.	30.2	OP	HMDB11130	0.0
Liver	Polar	+	496.341	14.62	N.A.	2.60	OP	HMDB10382	0.2
Liver	Polar	+	520.339	13.99	N.A.	2.69	OP	HMDB10386	0.1
Liver	Polar	+	568.338	14.05	N.A.	9.22	OP	HMDB10404	0.3
Liver	NP	-	346.157	3.45	1.53×10^{-18}	79.3	LMM, OP	CHEBI51939	0.4
Liver	NP	-	655.426	16.76	1.39×10^{-31}	63.1	LMM, OP	HMDB11155	6.8
Myoblast	NP	+	286.273	9.88	3.78×10^{-88}	P/A	LMM	LMSP01040002	0.4
Myoblast	NP	+	288.291	9.26	6.80×10^{-39}	P/A	LMM, OP	LMSP01040003	0.4
Myoblast	NP	+	545.312	16.76	1.44×10^{-24}	29.7	LMM	CS8228689	0.3
Myoblast	Polar	+	273.168	9.11	6.65×10^{-5}	P/A	LMM	CS9087911	1.1
Myoblast	Polar	+	412.161	11.97	1.38×10^{-20}	59.4	LMM	CS21513528	1.1
Myoblast	Polar	+	454.211	11.14	6.36×10^{-6}	44.7	LMM	CS4644673	0.4
Myoblast	Polar	+	472.183	11.72	6.30×10^{-12}	40	LMM	CS10484174	0.1

Myoblast	Polar	+	520.162	14.25	2.17×10^{-7}	24.1	LMM	CHEBI63717	3.5
Myoblast	Polar	+	692.289	15.46	6.58×10^{-5}	53.6	LMM	CHEBI62469	4.1
Myoblast	Polar	+	777.322	15.89	0	P/A	LMM, OP	CHEBI16314	5.0
MCN (vs. MCTN)	NA	-	265.171	14.87	N.A.	P/A	OP	CHEBI47781	0.2
MCTN (vs. MCN)	NA	-	241.180	14.52	7.06×10^{-175}	381	LMM	HMDB10730	0.2
MCTN (vs. MCN)	NA	-	447.132	12.66	4.24×10^{-86}	514	LMM	CS4644613	0.7
MCTN (vs. MCN)	NA	+	437.249	8.02	1.48×10^{-3}	1480	LMM, OP	CHEBI57835	1.1
MCTN (vs. MCN)	NA	+	247.086	9.30	0	502	LMM	CHEBI38130	1.7
MCTN (vs. MCN)	NA	+	353.117	9.15	0	1190	LMM, OP	CHEBI61220	0.0
MCTN (vs. MCN)	NA	+	355.064	9.24	1.49×10^{-217}	834	LMM, OP	CHEBI18337	0.4
MCTN (vs. MCN)	NA	+	409.162	12.69	0	1220	LMM, OP	CS59230	0.9
MCTN (vs. MCN)	NA	+	481.261	8.31	0	2200	LMM, OP	CHEBI2535	1.7

MCTN (vs. MCN)	NA	+	525.289	8.47	0	1550	LMM, OP	CS20121381	0.3
MCTN (vs. MCN)	NA	+	569.313	8.61	0	1010	LMM, OP	CS382892	0.4
MCB (vs. MCCX)	NA	-	265.146	15.12	1.06×10^{-119}	875	LMM, OP	CHEBI45599	0.3
MCCX. (vs. MCB)	NA	+	525.291	8.36	1.53×10^{-3}	1530	LMM, OP	CS20121381	0.0
MCB (vs. MCCX)	NA	+	234.207	8.90	4.44×10^{-274}	2200	LMM, OP	CS16127	0.2
MCB (vs. MCCX)	NA	+	247.085	9.30	0	532	LMM	CS4522006	4.3
MCB (vs. MCCX)	NA	+	357.088	10.76	5.06×10^{-282}	1660	LMM, OP	CHEBI61723	0.0

Table 5.1. Preliminary identifications made from the biological systems studied here. [1]-Liver = enriched autophagosomes from liver; myoblast = enriched autophagosomes from rat myoblasts; MCN = mast cells, non-activated; MCTN = TNPova-activated mast cells; MCCX = CXCL10-activated mast cells; MCB = Both CXCL10- and TNPova-activated. [2]-Extractions performed were either nonpolar (NP) or polar (see materials & methods). NA = no extraction made. [3]-ESI analysis was performed in positive (+) and negative (-) ionization modes. [4]-Fold-enrichment = average intensity of analyte in experimental sample vs. control; P/A = present/absent. [5]-Chemometric analysis applied to acquired UPLC/MS^e data; OP = OPLS-DA. [6]-Preliminary identification provided in accordance with the metabolomic standards initiative. *-Denotes structural isomers detected.

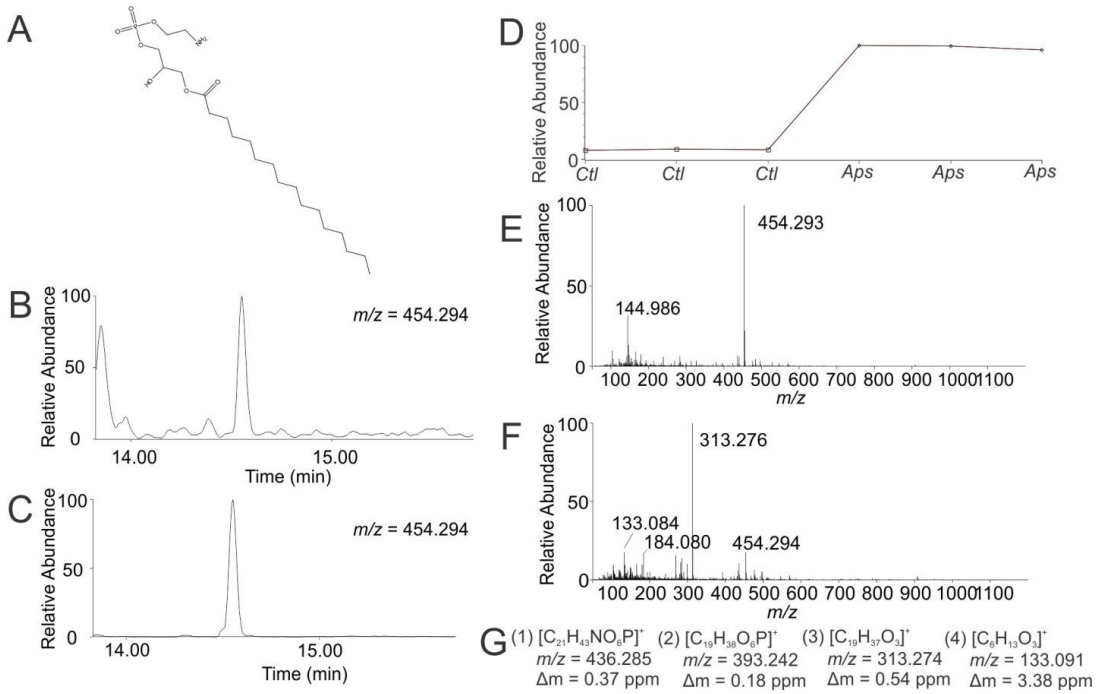

Figure 5.3. Preliminary identification of *m/z* 454.294 (PE 16:0/0:0) in autophagosome enriched fractions of rat liver (T_R = 14.55 min, p-value = 4.91 x 10^{-6}). (A) Structure of PE 16:0/0:0; (B) Low-collision energy XIC for *m/z* = 454.294; (C) High-collision energy XIC for *m/z* = 454.294; (D) Trend plot for *m/z* = 454.294 in control (Ctl) versus autophagosome-enriched (Aps) samples; (E) Low-collision energy mass spectrum at T_R = 14.55 min; (F) High-collision energy mass spectrum at T_R = 14.55 min; (G) Elemental compositions, *m/z* values, and mass error of observed fragment ions corresponding to theoretical fragment ions generated *in silico* using Mass Fragment™.

Many of the preliminary identifications for the rat liver autophagosome-enriched samples (Table 5.1., Figure C.3A.) appear to have biological relevance to autophagy. Since publications concerning autophagosome composition are limited, assessment of the relevance of preliminary identifications is difficult. Preliminary identification of PE(16:0/0:0) is of interest because it is a member of the phosphatidylethanolamine (PEA) family. PEA is a critical factor in autophagy due to its conjugation with Atg8 in the protein complex required for autophagosome formation.[73, 241] Sphinganine (HMDB00269), a sphingolipid base, represents another compelling preliminary

identification as sphingolipids have previously been shown to stimulate macroautophagy[242, 243] and accumulate in biological systems such as Niemman Pick C disease that also accumulate autophagosomes.[244, 245] While the biophysical function of sphingolipids in autophagy has not yet been fully determined, ceramide, a closely related compound to sphinganine, induces membrane curvature and formation of lipid rafts.[246] Based on our preliminary identification, it may be possible that sphinganine plays a similar structural role in autophagosomes.

Preliminary identifications also consisted of multiple lysophospholipids and glycerophospholipids including LysoPC(18:1(11Z)) (HMDB10385), PC(18:0/0:0) (LMGP01050123), LysoPC(22:5(7Z, 10Z, 13Z, 16Z, 19Z)) (HMDB10403), and LysoPC(18:2(9Z, 12Z)) (HMDB10386) (Table 5.1.). Lysophospholipids are involved in membrane fusion and elongation in macroautophagy[247] and alteration of these lysophospholipids causes disruption of autophagy-related organelle membranes by modifying lipid biosynthesis.[248] Lysophospholipids, such as PE 16:0/0:0 (LMGP02050002) are also important in membrane synthesis during autophagosome membrane elongation in macroautophagy.[247] Autophagy may also play a role in vitamin D regulation making the preliminary identification of 1α,23-dihydroxy-24,25,26,27-tetranorvitamin D3 (LMST03020020), a vitamin D3 metabolite, intriguing.[249] While the methodology and workflow presented here has proven invaluable as a tool to provide a first distillation of complex data sets and preliminary identifications of confirmed features, this does not preclude the need for comprehensive validation of these identifications via true precursor-selected MS/MS analysis, as well as UPLC/MS/MS of commercially available standards. In addition, examination of the quantitative effect of modified autophagy flux on levels of these preliminary identifications will further validate the association of these chemical entities with autophagosomes, providing insight into the function of diseases associated with autophagy[7-10, 250] as well as the composition and origin of autophagosome membranes.[59, 62, 251]

5.3.2. Features and identifications from rat myoblast cell culture

For the enriched autophagosome fractions from rat myoblast cell culture, chemometric approaches detected 130 candidate features. Overall, 112 XIC-confirmed features remained following Checkpoint 1 (Table C.1.). The percentage of common confirmed features identified with multiple chemometric approaches averaged 20% (Table C.1.). A database search of the confirmed features resulted in 69 potential database identifications. Of these potential database identifications, 12 were preliminary identifications following Checkpoint 2 (Table 5.1, Figure C.3B.). Figure 5.4. illustrates data supporting identification of the rat myoblast autophagosome-specific compound 3-{(4Z)-4-[(1,5-Dimethyl-3-oxo-2-phenyl-2,3-dihydro-1H-pyrazol-4-yl)hydrazono]-5-oxo-4,5-dihydro-1H-pyrazol-3-yl}-4-hydroxy-1-methyl-2(1H)-quinolinone (Figure 5.4A., identified as CS10484174 in the ChemSpider database). Figure 5.4B. and 5.4C. show aligned low- and high-collision energy extracted ion chromatograms for *m/z* 472.183 in the analysis of an autophagosome-enriched fraction of rat myoblasts. A trend plot showing relative fold-enrichment of CS10484174 in autophagosomes is illustrated in Figure 5.4D. Figure 5.4E. and 5.4F. illustrate the low- and high-collision energy mass spectra of CS10484174, respectively. Elemental compositions, *m/z* values, and mass errors of observed fragment ions corresponding to theoretical fragment ions of CS10484174, generated *in silico* using MassFragment™ are depicted in Figure 5.4G.

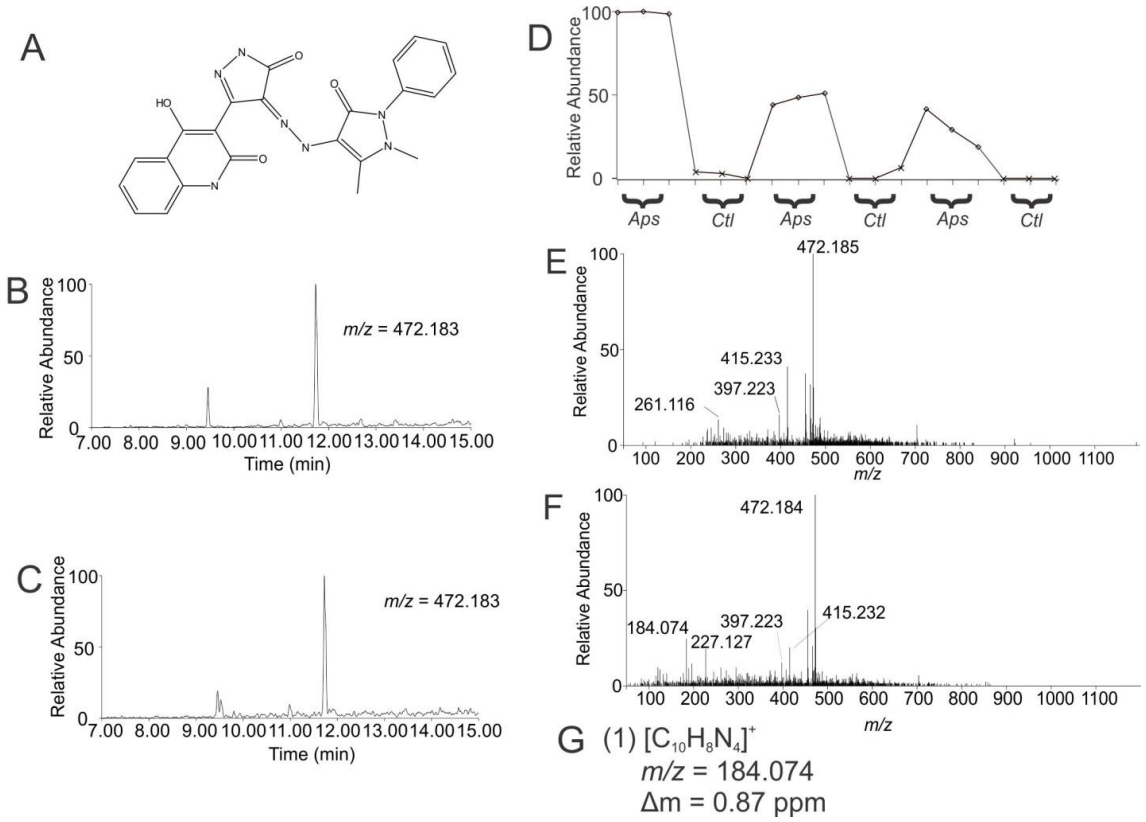

Figure 5.4. Preliminary identification of *m/z* 472.183 (3-{(4Z)-4-[(1,5-Dimethyl-3-oxo-2-phenyl-2,3-dihydro-1H-pyrazol-4-yl)hydrazono]-5-oxo-4,5-dihydro-1H-pyrazol-3-yl}-4-hydroxy-1-methyl-2(1H)-quinolinone , CS10484174) in autophagosome enriched fractions of rat myoblast (T_R = 11.72 min, p-value = 6.30 x 10^{-12}). (A) Structure of CS10484174; (B) Low-collision energy XIC for *m/z* = 472.183; (C) High-collision energy XIC for *m/z* = 472.183; (D) Trend plot for *m/z* = 472.183 in control (Ctl) versus autophagosome-enriched (Aps) samples; (E) Low-collision energy mass spectrum at T_R = 11.72 min; (F) High-collision energy mass spectrum at T_R = 11.72 min; (G) Elemental compositions, *m/z* values, and mass error of observed fragment ions corresponding to theoretical fragment ions generated *in silico* using Mass Fragment™.

Preliminary identifications of the rat myoblast-enriched autophagosomes again consisted of sphinganine (HMDB00269) as well as sphingosine, another type of sphingolipid. Other potentially interesting identifications include PA(P-16:0e/18:2(9Z,12Z) (HMDB11155) which is an intermediate product of ether lipid

metabolism according to the HMDB.[252] While this preliminary identification has not been explicitly detected in autophagosomes, autophagy is a well known pathway for lipid metabolism.[253] Other preliminary identifications such as the carbohydrate α-L-Fucp-(1->2)-β-D-Galp-(1->3)-β-D-GlcpNAc-(1->3)β-D-Galp (Chemical Entities of Biological Interest ID CHEBI:62469) and N-formylmethanofuran (CHEBI16314) were detected. These and other preliminary identifications made here are not known to be associated with any organelle. As such, validation via precursor-selected MS/MS, comparative analysis with synthetic standards, and quantitative correlation with autophagy will be required.

The percentage of database identifications made here is consistent with previous GC- and LC/MS-based metabolomic analyses of organelles. For rat liver-enriched autophagosomes, ~61% of confirmed features yielded potential database identifications. For rat myoblast cells, ~62% of confirmed features yielded potential database identifications. By comparison, Krueger et al. report that database identifications were made for ~46% of features from *Arabidopsis thaliana* leaf organelles using the KEGG (focus on nucleotide metabolites), KNApSAcK (focus on plant secondary metabolites), and an in-house database,[114] and a metabolite profiling study by Benkebilia et al. report database identifications for ~50% of features from subcellular soybean fractions using the NIST 02 Mass Spectral Library.[113] As databases continue to develop, percentages of database identifications and their reliability may increase but the importance of evaluation of such identifications using the criteria described here will remain high.

5.3.3. Features and identifications from activated mast cells

To further expand the application of the developed workflow to the identification of biological features, UPLC/MS^e analysis and the developed workflow was applied to the analysis of chemical secretions detected from activated mast cells. Of 2,656 detected candidate features, 1,661 were XIC-confirmed features following Checkpoint 1 (Table C.1.) meaning ~37% of the candidate features were removed. The percentage of common confirmed features identified with multiple chemometric approaches averaged 25% (Table C.1.). Since the number of confirmed features was large, preliminary

identification was attempted for only the 250 most statistically significant (based on p-value) confirmed features from the LMM chemometric approach and the 65 confirmed features detected by OPLS-DA. In total, 114 potential database identifications were made. The percentage of potential identifications made from online databases was ~36% for activated mast cells secretions. Overall, 14 of the potential database identifications were determined to be preliminary identifications following Checkpoint 2 (Table 5.1, Fig. C.3C.). Data supporting one such identification, the activated mast cell-specific compound 5-amino-6-(5'-phosphoribosylamino) uracil, is illustrated in Figure 5.5.

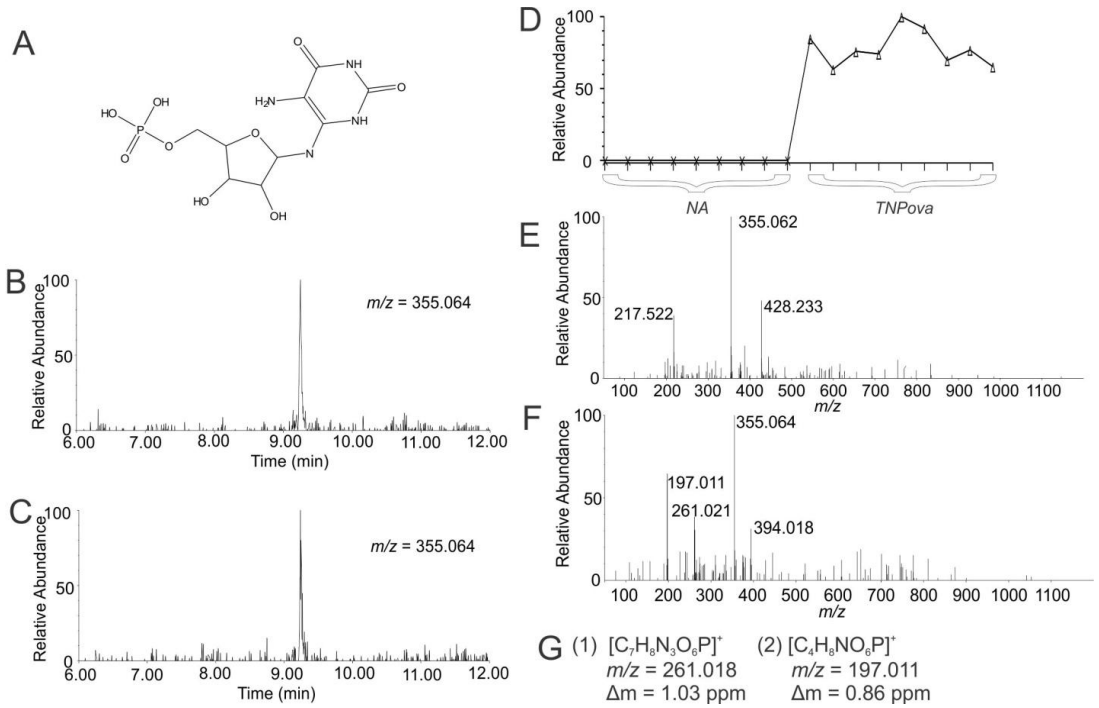

Figure 5.5. Preliminary identification of *m/z* 355.064 (-amino-6-(5'-phosphoribosylamino)uracil, CHEBI18337) in TNPova-activated mast cell secretions (T_R = 9.25 min, p-value = 1.49 x 10^{-217}). (A) Structure of CHEBI18337; (B) Low-collision energy XIC for *m/z* = 355.064; (C) High-collision energy XIC for *m/z* = 355.064; (D) Trend plot for *m/z* = 355.064 in non-activated (NA) versus TNPova-activated (Aps) samples; (E) Low-collision energy mass spectrum at T_R = 9.25 min; (F) High-collision energy mass spectrum at T_R = 9.25 min; (G) Elemental compositions, *m/z* values, and mass error of observed fragment ions corresponding to theoretical fragment ions generated *in silico* using Mass Fragment™.

Interesting preliminary identifications were also made for activated mast cells. 3-oxotetradecanoic acid (HMDB10730) is a known fatty acid involved in lipid synthesis. Glutathionylspermidinium (CHEBI57835) is particularly interesting in light of a recent study of mast cell granules in which it was found that, in addition to well-characterized amines such as serotonin and histamine, mast cell granules also contain polyamines such as spermidine, and these polyamines have roles in granule homeostasis.[254] Although

glutathionylspermidinium was not a compound detected in mast cell granules, it could be formed by an extracellular enzymatic reaction, and further studies should be performed on the potential importance of spermidine compounds in inflammation and mast cell function. D-pantetheine 4'-phosphate (CHEBI61723), a metabolite associated with coenzyme A biosynthesis, has a role in fatty acid biosynthesis, as well as enzymatic synthesis of peptides and additional biologically active metabolites according to the ChEBI database.[255] D-pantetheine 4'-phosphate was enriched in mast cell samples exposed to CXCL10 and TNP-ova versus TNP-ova alone, which highlights the need for further studies into the function of mast cells in inflammatory diseases such as asthma. Benzylpenicilloic acid (CHEBI61220) is a metabolite of the antibiotic penicillin, which was present in the cell culture conditions,[256] suggesting that this antibiotic metabolite was endocytosed by the mast cells during culturing, and subsequent secretion of this species took place upon mast cell activation and degranulation by TNP-ova.

5.4. Conclusions

LC/MS analysis of complex biological systems can detect thousands of potential features in a biological sample. Without chemometric analysis and examination of subsequent database identifications, however, chemical identities of the features may be incorrectly assigned, which compromises the biological relevance of the study. The workflow described here is applicable to a wide range of biological samples and results in more reliable, higher confidence preliminary identifications of system-specific features. This approach can be applied to any LC/MS profiling of dissimilar biological samples. In this study, a number of preliminary identifications specific to enriched autophagosome and activated mast cell fractions were made using UPLC/MS^e analysis combined with outputs from chemometric analyses, database search results, and evaluation of mass spectral data. Compounds identified in this way may prove to be essential to the composition and function of autophagosome organelles or as potential chemical messengers released during degranulation of mast cells.

Chapter 6

Describing the Temporal Nature of Autophagy at the Individual Organelle Level by Capillary Electrophoresis with Laser Induced Fluorescence Detection

Vratislav Kostal assisted in the transformation and selection of transfected cells. The LC3-GFP plasmid was a generous gift from the Professor Do-Hyung Kim laboratory from the University of Minnesota-Twin Cities. This work was funded by NIH grant AG020866.

Autophagy is a molecular pathway responsible for the degradation of intracellular cargo involving sequential formation of phagophores, autophagosomes and autolysosomes. These are known as autophagy organelles. The dynamic nature of autophagy and the multiple types of autophagy organelles present at a given time make current measurements, such as those done by Western blotting, insufficient to understand autophagy and its roles in aging and disease. Capillary electrophoresis coupled to laser induced fluorescence detection (CE-LIF) has been used previously to count and determine properties of individual organelles, but has never been used on autophagy organelles or for determination of temporal changes of such properties. Here we used CE-LIF to determine the number of autophagy organelles, their individual GFP-LC3 fluorescence intensities, and their individual electrophoretic mobilities from L6 cells expressing GFP-LC3 under basal and rapamycin-driven autophagy conditions. Under any of these two conditions, CE-LIF provided an individual organelle-based snapshot of autophagy. Furthermore to determine time-dependent changes of individual organelle properties, we treated cells with vinblastine which interrupts autophagy prior to formation of autolysosomes. Differences in organelle numbers and changes in both GFP-LC3 fluorescence levels and electrophoretic mobilities of individual organelles that occurred during the duration of the vinblastine treatment were determined. This provided the first report of the temporal nature of the autophagy process at the individual organelle level. These temporal observations point to differences in the properties of accumulating autophagosomes and disappearing autolysosomes. Surprisingly for rapamycin-enhanced autophagy, the temporal trends of individual organelle properties upon treatment with vinblastine were the opposite of the trends observed under basal autophagy conditions. These observations demonstrate that individual organelle analysis by CE-LIF is a powerful technology to investigate the complexity and temporal nature of autophagy, a process that plays critical roles in response to drug treatments, aging, and disease.

6.1. Introduction

Autophagy is a cellular pathway responsible for the degradation of intracellular components involving phagophores, autophagosomes, amphisomes, and autolysosomes (Figure 6.1). All these organelles have the protein LC3-II localized on their membrane,

which requires lipidation of the cytosolic LC3-I, a process occurring during the initial formation of phagophores.[57, 257, 258] Because of ubiquitous nature in autophagy organelles, LC3-II has been extensively used as an autophagy marker. However, this marker is present in phagophores that form around intracellular components to be degraded, in autophagosomes that form from phagophores, and in autolysosomes that form from fusion of autophagosomes with lysosomes.[63, 64] There is also an alternate route of which up to 5% of autophagosomes fuse with endosomes to form amphisomes that then mature into autolysosomes.[81, 82] Defects in autophagy have been associated with aging, cancer, and neurodegenerative diseases.[10]

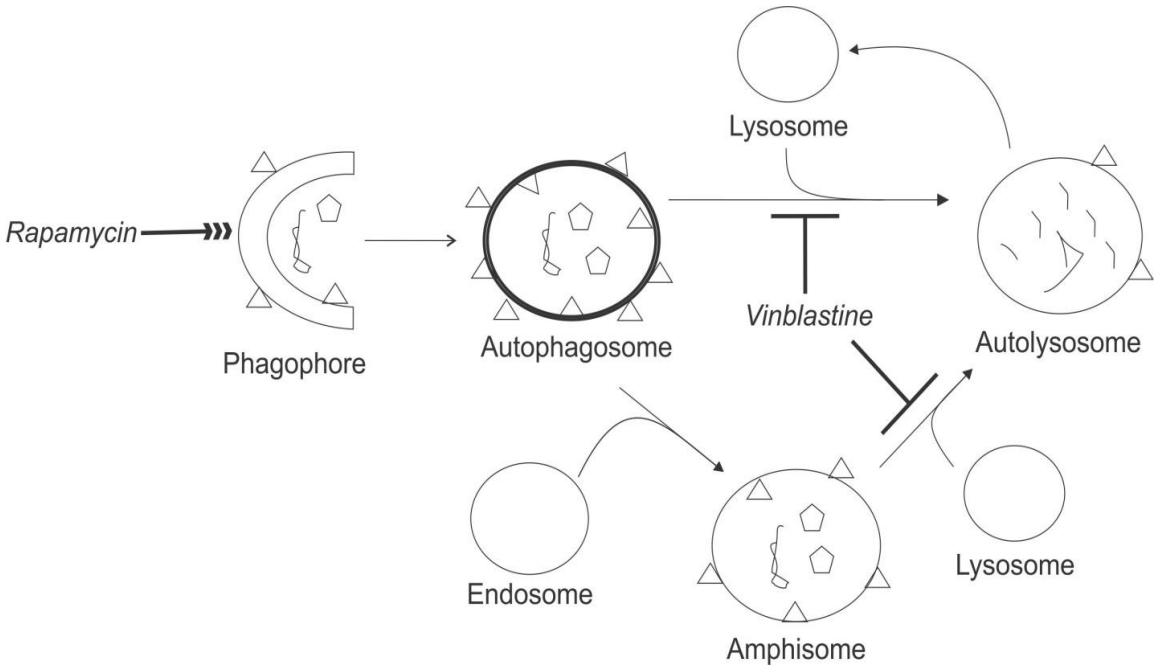

Figure 6.1. Autophagy Degradation of Intracellular Contents. Phagophores engulf intracellular components such organelles (pentagons) and have LC3-II localized on their membrane (triangles). Phagophores mature into autophagosomes. Autophagosomes either mature into autolysosomes by direct interaction with lysosomes or into amphisomes by fusing with endosomes. Because amphisomes are a small fraction (<5%), they will not be explicitly mentioned in this report. Autolysosomes degrade the components sequestered in autophagosomes and then are recycled to form lysosomes.[67] Treatment with vinblastine halts formation of autolysosomes, while rapamycin enhances the overall autophagy process.[81]

Several techniques such as Western blotting, fluorescence confocal microscopy, transmission electron microscopy and flow cytometry have been used to monitor autophagy. Western blots determine bulk amounts of LC3-II relative to LC3-1 or GFP-LC3-II relative to free GFP.[58, 259] Increased levels of LC3-II or free GFP indicate increased autophagy or degradation of intracellular components, respectively. Similarly, fluorescence confocal microscopy determines the number of fluorescently-labeled LC3-II organelles[30, 260-262] or fluorescently-labeled LC3-II organelles that are colocalized with fluorescently-labeled lysosomes. Transmission electron microscopy can also be used to evaluate autophagy based on the number of observed autophagosomes.[82] Lastly, flow cytometry determines levels of fluorescently labeled LC3-II in whole cells after the extraction of LC3-I with saponin treatment.[33] Overall, these techniques use LC3-II levels or organelle numbers to examine the extent of autophagy, or steady state, but additional observations are required to determine the rate at which autophagy occurs (i.e. autophagy flux), which is critical to understand cell function and disease.[29, 263] Ultimately, temporal measurements would tremendously benefit from analytical strategies that account for the temporal status of the autophagy process.

Inhibitors that halt autophagy at specific points of its pathway have been used to evaluate autophagy flux previously (Figure 6.1).[81, 82] This leads to accumulation of organelles upstream of the blockage point and degradation of organelles downstream from the blockage point during the duration of the inhibitor treatment. For instance, vinblastine treatment leads mainly to the accumulation of autophagosomes and the disappearance of autolysosomes.[81, 82] Measurements of samples with or without blockage by vinblastine are used to determine differences between accumulation and disappearance of the numbers and properties of autophagy organelles, providing an assessment of autophagy flux.[83] Both Western blotting and flow cytometry of whole cells have been used previously to estimate autophagy flux.[33, 83] Unfortunately, these approaches cannot provide a detailed account on whether changes are the result of different organelle numbers or changes in individual organelle properties (e.g. individual organelle content of LC3-II).

Capillary electrophoresis coupled to laser induced fluorescence detection (CE-LIF) is a technique previously used to determine the numbers and properties of individual, fluorescently-labeled organelles such as mitochondria, [93, 264] nuclei,[104] endosomes, and acidic organelles.[48, 107] Due to its excellent limits of detection,[48, 94, 104] CE-LIF can detect individual organelles tagged with low levels of a fluorescent marker. This technique has not been used to examine temporal changes such as those needed to assess autophagy flux.

This chapter describes the first use of individual organelle analysis by CE-LIF in combination with a treatment that halts autophagy (i.e. vinblastine) to determine time-dependent changes in number and properties of autophagosomes under basal and rapamycin-enhanced autophagy conditions. Relative to basal autophagy, rapamycin treatment resulted in the detection of a higher number of autophagy organelles at steady state, which is in agreement with rapamycin's effect previously observed through bulk measurements of autophagy markers. For temporal dependent measurements at basal autophagy, we observed a net accumulation of autophagy organelles (i.e. rate of appearance of autophagosomes exceeds that of disappearance of autolysosomes), with accumulated organelles having higher individual GFP-LC3 contents and more positive electrophoretic mobilities than those that disappeared. In contrast, under rapamycin-enhanced autophagy conditions, there was a net disappearance of autophagy organelles, with remaining organelles having lower GFP-LC3 contents and more negative electrophoretic mobilities than those that disappeared. These unexpected results suggest that rapamycin may regulate autophagy at various points of this process, an observation that could not have been done with conventional technologies. Future applications of CE-LIF combined with autophagy inhibitors could be used to examine autophagy flux under different conditions characterized by altered autophagy such as neurodegenerative diseases[6, 8] and aging.[6]

6.2. Theory

A sample collected at a given time contains a mixture of various autophagy organelle types (Figure 6.1). This mixture represents the steady state or snapshot of autophagy at a single time point. Comparison of two samples collected under different

conditions (e.g. basal versus rapamycin-enhanced) is commonly used to define differences between these two conditions such that

$$D = i_R - i_B \qquad \textbf{Equation 6.1}$$

where D is the difference in a measured property, i_R is the property observed under a given treatment (e.g. rapamycin treatment) and i_B is the corresponding basal condition. Bulk differences between two conditions can easily be determined by applying this equation to existing assays (e.g. Western blots). In this study we extend the use of this equation to the number of organelles, individual organelle GFP-LC3-II contents, and individual organelle electrophoretic mobilities.

To determine autophagy flux associated with a given condition, one approach is to measure the difference in organelle numbers before and after halting autophagy. Under steady state conditions discussed previously, the rate of appearance of a given type of autophagy organelle equals the rate of disappearance of a given type of autophagy organelle. That is,

$$\emptyset_{steady\ state} = R_A = R_D \qquad \textbf{Equation 6.2}$$

where Φ is autophagy flux, R_A is the rate of appearance and R_D is the rate of disappearance. When flux is blocked, for instance when vinblastine halts autolysosome formation, the rate of accumulation (R_A) and rate of disappearance (R_D) can be related to the number of detected organelles as follows:

$$N_T = N_o + R_A(\Delta t) - R_D(\Delta t) \qquad \textbf{Equation 6.3}$$

where N_o is the number of detected organelles before vinblastine treatment, N_T is the number of detected organelles after vinblastine treatment, and Δt is the duration of the treatment. The difference between the rate of accumulation and rate of disappearance of detected organelles can then be calculated as,

$$R_A - R_D = \frac{N_T - N_o}{\Delta t} \qquad \textbf{Equation 6.4}$$

When R_A - R_D is positive, the rate of formation of autophagosomes, and to a lesser extent phagophores and amphisomes, exceeds the rate of disappearance of

autolysosomes. When this difference is negative, the rate of disappearance of autolysosomes exceeds the rate of formation of the other autophagy organelles.

A similar calculation determines changes in properties of individual organelles,

$$D = \frac{i_t - i_o}{\Delta t} \qquad \textbf{Equation 6.5}$$

where D is the difference of the property of interest i_t, measured at time t, and the property i_o measured at the onset of autophagy blockage, divided by the duration of the autophagy blockage (Δt). In this study we used this equation to determine time-dependent changes in individual organelle contents of GFP-LC3-II and their electrophoretic mobilities. A similar interpretation to Equation 6.4, when D is positive in Equation 6.5, the property of interest is higher for forming organelles than for disappearing autolysosomes. When D is negative, the reverse is true.

Because individual organelle measurements are commonly represented as distributions, Equation 6.5 can be modified to compare the x^{th} percentile of two distributions as

$$D_x = \frac{i_{x,t} - i_{x,o}}{\Delta t} \qquad \textbf{Equation 6.6}$$

where D_x is the difference at the x^{th} percentile, $i_{x,t}$ and $i_{x,o}$ are values at x^{th} percentile for the property of interest measured at a given time, t, and at the onset of autophagy blockage, respectively. This equation was applied to individual organelle contents of GFP-LC3-II and their electrophoretic mobilities. The interpretation of Equation 6.6 is similar to that of Equation 6.5, but extends the concept to percentiles of individual organelle measurements.

6.3. Experimental

6.3.1 Materials, Reagents, and Buffers

Sucrose, 4-(2-hydroxyethyl)-1-piperazineethanesulfonic acid (HEPES), ethylenediaminetetraacetic acid (EDTA), vinblastine, rapamycin from *Streptomyces hygroscopicus*, gentamycin, protease inhibitor cocktail, Triton X-100, poly-L-lysine, and poly(vinyl alcohol) (99%+ hydrated, molecular weight 89,000 to 98,0000) were obtained

from Sigma Aldrich (Atlanta, GA). Rabbit polyclonal LC3 antibody was obtained from Novus Biologicals (Littleton, CO). Fluorescein, prolong gold antifade reagent with 4',6'-diamidino-2-phenylindole (DAPI), goat anti-rabbit AlexaFluor568 polyclonal antibody, AlignFlow flow cytometry beads (2.5 μm) and lipofectamine 2000 reagent were obtained from Invitrogen (Carlsbad, CA). Hydrochloric acid was obtained from Mallinckrodt (Phillipsburgh, NJ). Fetal bovine serum was obtained from Omega Scientific (Tarsana, CA). Dubelcco's Modified Eagle Medium (DMEM) high-glucose cell medium and geneticin were obtained from Gibco (Carlsbad, CA). D-Mannitol was obtained from Riedel-de Håen (Atlanta, GA). Sodium hydroxide was obtained from Fluka (Seelze, Switzerland). Phosphate buffered saline (10× concentration, 1.37 M NaCl, 27 mM KCl, 80 mM Na_2HPO_4, and 20 mM KH_2PO_4, pH 7.4) was obtained from BioRad (Hercules, CA). 0.5% trypsin-EDTA (10× concentration, no phenol red) was obtained from Life Technologies (Grand Island, NY). Formaldehyde and sodium chloride were obtained from Fisher Scientific (Pittsburgh, PA). Bovine serum albumin fraction V, heat shock, fatty acid free was obtained from Roche (Basel, Switzerland). Water was purified with a Millipore Synergy UV system (18.2 mΩ/cm, Bedford, MA).

Homogenization buffer was made by adding 11.99 g sucrose (70.0 mM), 19.52 g mannitol (214 mM), 611 mg HEPES (4.31 mM), and 724 mg EDTA (4.94 mM) to 500 mL deionized water and brought to pH 7.2 with 0.1 M HCl and 0.1 M NaOH. Capillary electrophoresis (CE) buffer was made by adding 42.88 g sucrose (250 mM), and 1.18 g HEPES (10.0 mM) to 500 mL deionized water and brought to pH 7.2 with 0.1 M HCl and 0.1 M NaOH. The CE buffer was photobleached with 120-mW LED lights with a λ_{max} at 472 nm for 72 h to reduce background fluorescence intensity.[103]

6.3.2 Cell Culture

To create the L6 cell line expressing GFP-LC3, transfections were done with a plasmid containing the EGFP-LC3 gene (plasmid 11546, Addgene)[265] and selected by fluorescence activated cell sorting. In brief, L6 cells (ATCC, Manassas, VA) were cultured to 70-90% confluence in a 24-well plate. DMEM medium volume was adjusted to 500 μL in each well. Both Lipofectamine 2,000 (Life Technologies, Grand Island, NY) transfection reagent (2.4 μL) and plasmid (800 ng) were diluted separately in 50 μL of

Opti-MEM medium each, and then mixed. After five minutes, this mixture was added to wells containing L6 cells and incubated for 48 h, collected by centrifugation at 1,000g for 10 min, and diluted to 2.5×10^6 cells/mL in 1× PBS containing 0.5% w/v bovine serum albumin. Non-transfected L6 cells were used as a control. Cells expressing GFP-LC3 were selected using fluorescence activated cell sorting (FACS) with a BD FACSAria 1 flow cytometer (BD Biosciences, San Jose, CA) using a 130-µm nozzle and a 20 mW, 488 nm-argon ion-laser. Only 32% of the cells were fluorescent. Thus, FACS was used a second time to sort one cell per in each well of 24-well plates. Fluorescent microscopy was used for up to one week following sorting to select fluorescent cell clones. Transfected cells were frozen for future use in liquid nitrogen at -80° C. The studies reported here used the same cell clone.

The original L6 cells and the clone expressing GFP-LC3 were maintained at 37°C, 5% CO_2 in DMEM supplemented with 10% fetal bovine serum containing either 100 µg/mL gentamycin or 150 µg/mL of each gentamycin and geneticin, respectively,. For maintenance, cells were released with trypsin in PBS (0.5% v/v) from T-flasks and then split 1:40 (v/v) into new flasks.

6.3.3 Autophagy Treatments

Once cells reached ~90% confluence, cells were treated with vinblastine, rapamycin, or both. For basal autophagy experiments, two different treatments were performed: One flask was treated with 50 µM vinblastine for two hours, while the second flask was untreated. For rapamycin-induced autophagy experiments, both flasks were treated with 267 µM rapamycin for 3 hours; one hour into this treatment, one flask was treated with 50 µM vinblastine for the remaining two hours, while the second one remained free from vinblastine. For both basal and rapamycin-induced autophagy experiments, cells were harvested by differential centrifugation at 1,000*g* for 10 minutes and then washed once by suspending in homogenization buffer and differential centrifugation at 1,000*g* for 10 minutes.

6.3.4 Organelle Isolation and Release

Post-nuclear fractions from GFP-LC3 expressing L6 cells (passages 14-24, 10^6-10^7 cells) were prepared. Cell disruption was done in an ice-cooled cell disruption bomb (Parr Instrument Co., Moline, IL) charged to 500-600 psi with nitrogen gas for a minimum of 15 min prior to pressure release. The lysate was collected in a 50-mL falcon tube. Unbroken cells and nuclei were removed by differential centrifugation at 600*g* for 10 minutes. Organelles were collected by differential centrifugation at 14,000*g* for 45 minutes. The organelle pellet was reconstituted with homogenization buffer, and centrifuged at 14,000*g* for 30 minutes. The organelle pellet was reconstituted with CE buffer (100 μL) and was resuspended with a 1.00-mL syringe (Hamilton, Reno NV) to break up the organelle pellet and minimize organelle aggregation. Protein concentrations were determined using the bichinchoninic acid protein assay according to the manufacturer (ThermoScientific, Wilmington, MA).

6.3.5 CE-LIF Instrumentation and Alignment

Poly-vinyl alcohol (PVA) coating of fused silica capillaries (150-μm outer diameter, 30-μm inner diameter, Polymicro, Phoenix, AZ) was done as previously described.[266] PVA was used to decrease non-specific binding of organelles to the fused silica capillary.[91] The current monitoring method was used to estimate the reduction of electroosmotic flow relative to an uncoated capillary.[267] Residual electroosmotic flows were 17 - 22% of that of uncoated capillaries. Capillaries were no longer used when GFP-labeled biological material began adhering to the outlet of the capillary. Prior to storage at room temperature, capillaries were flushed with methanol, deionized water, and air.

A previously described, a custom-built CE-LIF instrument[89] was used to determine numbers of autophagy organelles, individual autophagy organelle GFP-LC3-II levels, and individual autophagy organelle electrophoretic mobility. Briefly, a 488-nm argon-ion laser (10 mW) was used for fluorescence excitation. A 530 (± 17.5)-nm filter collected GFP and fluorescein fluorescence. The polyimide coating on the outlet of the capillary was burned to decrease fluorescence from this coating. Fluorescence was detected by a photomultiplier tube (R1477, Hamamatsu Corp., Bridgewater, NJ, 1 kV). Data were collected at 200 Hz and digitized by a NiDaq I/O data board (PCI-MIO-16XE-50, National Instruments, Austin, TX) controlled with Labview 5.1 software (National

Instruments). The limit of detection for a fluorescein standard was 11 ± 8 zmol (Ave ± St. Dev., n = 12). Capillary electrophoresis separations were performed at -297 V/cm for ~30 minutes. Hydrodynamic injection (104-cm height, 10 s injection) was used for sample introduction. In between separations, the capillary was washed with methanol and CE buffer for 5 minutes each. Methanol removed any remaining biological material and CE buffer re-equilibrated the capillary. For alignment of the instrument, please see Section D.3.

6.3.6 Data Analysis

CE-LIF data was analyzed using Igor Pro (WaveMetrics, Inc., Lake Oswego, OR) as previously described. [48] Organelle peaks were selected according to a threshold value defined as follows:

$$threshold = \bar{x} + 6\sigma \qquad \textbf{Equation 6.7}$$

where $\bar{x}$ is the average background intensity and σ is the standard deviation of the background intensity. This threshold eliminated at least 95% of background intensity peaks (seen with a threshold of $\bar{x}$ + 6σ).

In order to account for variations in contents of each sample, the number of organelle peaks was then normalized to the amount of protein in the sample injected, calculated as follows:

$$ng\ injected = V_i \times [protein] \qquad \textbf{Equation 6.8}$$

where V_i is the volume injected and [protein] is the protein concentration of the biological sample determined by the BCA assay.

Random non-specific events, which are detected prior to the time required by organelles to reach the detector appeared from 0 to ~ 450 – 500 s, which is termed pre-migration window. The number of peaks detected in the pre-migration window was 0.02 ± 0.02 peaks/s (Ave ± St. Dev., n = 12 runs). These events in the pre-migration window, were removed from further analysis. To determine the contribution of native fluorescence to GFP fluorescence detection organelles of non-transfected L6 cells were also examined

in the migration window that begins at 400 -500s (Figure 6.2A.). The number of detected peaks per ng protein in the sample was 6 ± 0 (Ave. ± St. Dev., n = 2 runs), while this number was 252 ± 78 events (Ave. ± St. Dev., n = 3 runs) in the sample from GFP-LC3 expressing cells. This suggests that 2% of the detected events in electropherograms of autophagy organelles from GFP-LC3 transfected cells were due to native fluorescence.

When samples have a large number of organelles, two or more organelles may produce one single detected event. Statistical overlap theory (SOT) was used to predict overlap of individual autophagy organelle events (See Appendix, Table D.3.).[268, 269] There is a saturation limit above which overlap precludes an accurate count of events. In regions of the electropherogram (bins) in which the number of the events exceeded the saturation limit, previously defined as 'm',[41, 42] m was used as a conservative number of events in the bin (See Appendix, Table D.3.). This saturation value was determined as described previously and is based on $log\frac{\sigma}{X}$ where σ is the peak width and X is the duration of the bin in seconds.[164]

Because the detector sensitivity varies from day-to-day, we corrected for variations in instrument sensitivity to allow for comparison of individual autophagy organelle fluorescence levels in separations performed on different days. This correction used the background intensity (c.f. Equation 6.7), assumed proportional to the LIF detector sensitivity. All the signal intensities of the detected peaks were normalized to that with the lowest background intensity level. This correction is particularly important because each condition (basal autophagy, untreated; basal autophagy, vinblastine-treated; rapamycin-induced autophagy, untreated; and rapamycin-induced autophagy, vinblastine-treated) was done on different days. Please see Supplementary Information Section D.3. for further information.

The electrophoretic mobilities of detected organelles (μ) are affected by run-to-run fluctuations. We used the observed ($\mu_{Flu,o}$) and known ($\mu_{Flu,r}$) electrophoretic mobilities of fluorescein to determine the electrophoretic mobilities of observed events ($\mu_{organelle}$) as follows:

$$\mu_{organelle} = \frac{L^2}{t \times V \times 1000} - (\mu_{correction}) \qquad \textbf{Equation 6.9}$$

$$\mu_{correction} = \mu_{\mathrm{Flu,o}} - \mu_{\mathrm{Flu},r}$$ **Equation 6.10**

where $\mu_{\mathrm{organelle}}$ is the mobility of a detected organelle, L is the length of the capillary, t is the organelle migration time, V is the separation voltage, $\mu_{\mathrm{Flu,o}}$ is the observed fluorescein electrophoretic mobility, and $\mu_{\mathrm{Flu,r}}$ is the reported electrophoretic mobility of fluorescein in a PVA-coated capillary.[270]

Quantile-quantile plots (QQ plots) were used to compare, in increments of 5%, the 5th through 95th percentiles of distributions of individual organelle fluorescence levels and electrophoretic mobilities. Comparisons of these distributions included (1) basal and rapamycin-enhanced autophagy steady states, and (2) vinblastine treated and untreated cells under basal and rapamycin-enhanced autophagy. If the two distributions are similar, their QQ plot approaches a diagonal line with slope equal to one. (i.e., line y = x). The distances between percentiles was also plotted to better understand the difference in percentiles.

6.3.7. Safety Considerations

Biosafety level 1 was observed for all procedures using L6 cells. Biological waste was treated with bleach for 30 min prior to disposal. Used cell culture supplies were autoclaved prior to disposal.

6.4. Results & Discussion

6.4.1. Detection of Individual Autophagy Organelles by CE-LIF

The first focus of this study was to determine the suitability of CE-LIF to measure the properties of autophagy organelles. Prior work demonstrated the use CE-LIF to determine the numbers and properties of other types of individual organelles.[48, 93, 104, 107, 264] To evaluate the utility of GFP-LC3 as a label for autophagy organelles, fluorescence confocal microscopy confirmed colocalization of GFP and anti-LC3 antibody at puncta (Section D.1.), which indicated GFP-LC3 is a suitable marker to monitor autophagy organelles by CE-LIF.

The CE-LIF analysis of organelles isolated from GFP-LC3 expressing L6 cells under conditions of basal autophagy, treated with vinblastine, treated with rapamycin, or treated with both rapamycin and vinblastine demonstrated detection of individual autophagy organelles (Figure 6.2). Representative electropherograms of individual organelles showed narrow peaks, (FWHM = 36 ± 16 ms (Ave ± St. Dev, n =12,567 peaks), a width defined by the organelle's travel time through the laser beam of the LIF detector (Figure 6.2F). These narrow events are expected when a fluorophore (i.e. GFP-LC3-II) is bound to an organelle. On the other hand, GFP-LC3-I, which is cytosolic, would be free in solution and would be detected as a band with broadening defined by diffusion and other band broadening effects.[103] A broad peak from GFP-LC3-I was not detected, because GFP-LC3-I was lost during removal of the cytosol by differential centrifugation during the fractionation procedure.[271] Because GFP-LC3-I does not interfere in the CE-LIF results, here we refer to GFP-LC3-II, the organelle bound form, as GFP-LC3. Lastly, to eliminate the possibility that the observed events were attributed to native fluorescence, we analyzed organelles isolated from L6 cells not expressing GFP-LC3 (Figure 6.2.A). The low number of detected organelle peaks in this control (Figure 6.2A) relative to analyses of GFP-LC3 expressing cells (Figure 6.2B-E) confirmed that the observed events are mainly due to GFP-LC3 fluorescence and not to autofluorescence or light scattering by organelles. Together, these results confirm that GFP-LC3 labeled organelles can be monitored by CE-LIF.

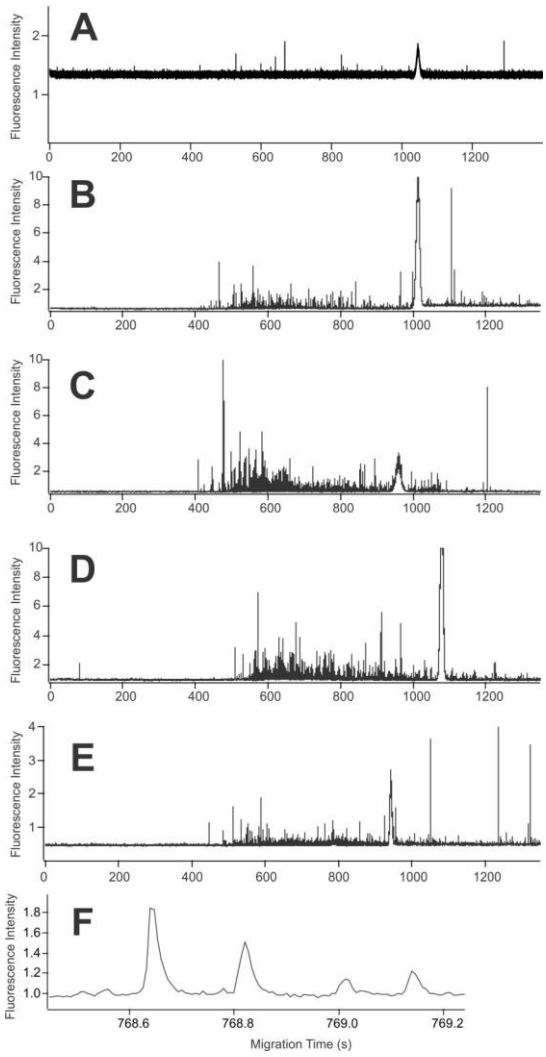

Figure 6.2. Electropherograms of L6 cells expressing GFP-LC3. (A) Non-transfected cells. (B)-(F) GFP-LC3 expressing cells. (B) Basal autophagy. (C) Basal autophagy after vinblastine treatment. (D) Rapamycin enhanced autophagy. (E) Rapamycin enhanced autophagy after vinblastine treatment. The broad peaks at ~1,000 s in (A)-(E) are fluorescein peaks. (F) Expansion of individual organelle detected events from (E). CE buffer: 250 mM sucrose, 10 mM HEPES, pH 7.2; -297 V/cm in a PVA coated capillary. Fluorescence detection at 530 ± 18 nm.

Next, we assessed the reproducibility of the individual organelle fluorescence intensity and electrophoretic mobility distributions obtained from replicate CE-LIF analysis of the same sample. QQ plots confirmed that both properties had adequate reproducibility (See Appendix, Figure D.3).[91, 93] Further improvements in reproducibility

of individual organelle properties may be attained as techniques for reproducible cell disruption and organelle isolation become available. Another option to enhance comparisons of distributions is to pool data from several replicates as previously done.[91, 93] This approach provided the means to compare distributions of individual organelle GFP-LC3 fluorescence intensities and electrophoretic mobility distributions resulting from the CE-LIF of basal and rapamycin enhanced autophagy.

6.4.2 Individual Organelle Comparisons of Autophagy Steady States

Individual organelle measurements were used to compare the steady states (snapshots) of basal and rapamycin-enhanced autophagy (c.f. Equation 6.1). These snapshots include: (1) the number of organelles present in the respective samples, (2) the distribution of individual organelle GFP-LC3 intensities, and (3) the distribution of individual organelle electrophoretic mobilities.

Samples from rapamycin-treated cells had higher numbers of autophagy organelles than untreated cells (174 ± 31 and 71 ± 15, events/ng protein, respectively; Avg. ± St. Dev., n = 3 runs). These results are in agreement with previous observations done by confocal fluorescence microscopy in which rapamycin-treatment increased the number of autophagy organelles detected in primary cortical neurons[272] and in normal rat kidney cells[260] relative to those numbers in untreated cells.

Surprisingly, when we analyzed the steady state contents of GFP-LC3 levels in individual autophagy organelles, the distributions of rapamycin-enhanced and basal autophagy were remarkably similar (Figure 6.3). This suggests that, although rapamycin enhances autophagy, the GFP-LC3 contents in autophagy organelles and the proportions of the various types of autophagy organelles at steady state remain about the same.

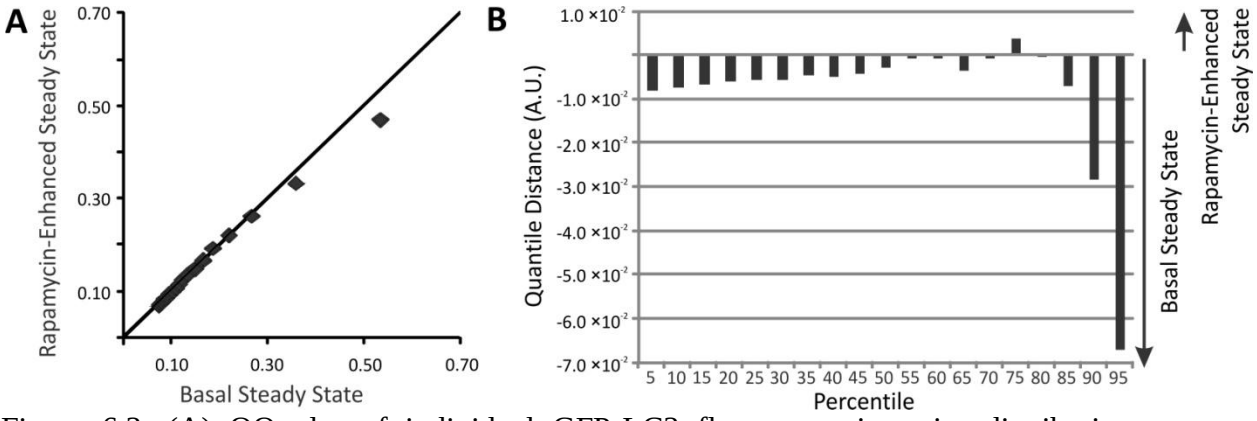

Figure 6.3. (A) QQ plot of individual GFP-LC3 fluorescent intensity distributions. Comparison of steady state distributions of individual GFP-LC3 levels under basal (x-axis) and rapamycin-enhanced (y-axis). Markers represent 5, 10, 15…95th percentiles. For percentiles with y = x, their intensity value is the same. (B) Changes in the distributions of individual GFP-LC3 levels. The change for a given percentile was calculated according to Equation 6.6.

Electrophoretic mobility has been associated with the surface charge of organelles.[93] Because individual organelle CE-LIF analysis reports individual electrophoretic mobilities (c.f. Equation 6.9), this technique is suitable to compare surface composition of individual organelles from cells with rapamycin-enhanced and basal autophagy. The electrophoretic mobilities of autophagy organelles were, in general, more positive when cells were treated with rapamycin relative to untreated cells (25th - 80th percentiles in Figure 6.4.). These observations suggest that rapamycin treatment not only enhances the number of autophagy organelles present at a given time but it is associated with a change in surface composition, which reflects on the sources of material that make up the surface of autophagy organelles and on interactions with other organelle types.

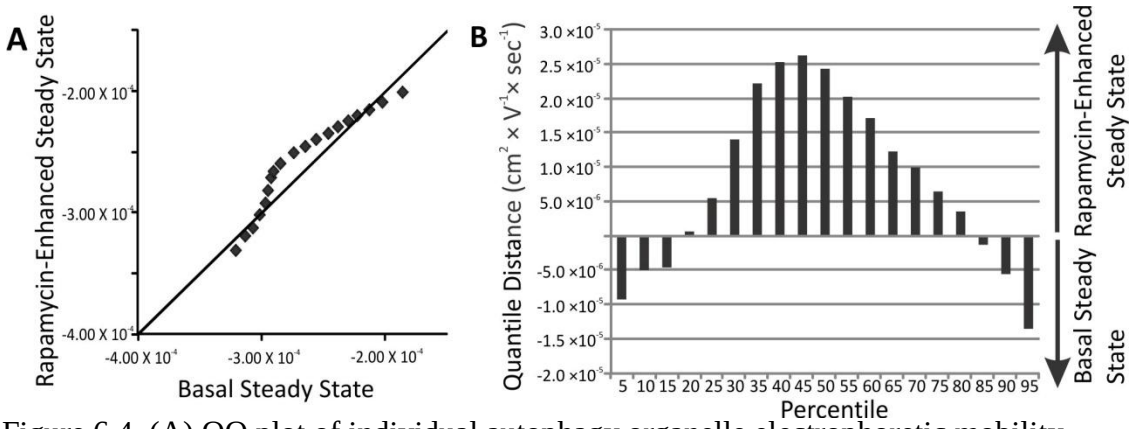

Figure 6.4. (A) QQ plot of individual autophagy organelle electrophoretic mobility distributions. Comparison of steady state distributions of individual electrophoretic mobility under basal (x-axis and rapamycin-enhanced (y-axis). Markers represent 5, 10, 15…95th percentiles. For percentiles with y = x, their electrophoretic mobility value is the same. (B) Changes in the distributions of individual autophagy organelle electrophoretic mobility. The change for a given percentiles was calculated according to Equation 6.6.

While bulk measurements (e.g. Western blot) are adequate to compare total marker levels (e.g. LC3-II levels) of various autophagy regimens, individual organelle CE-LIF analysis provides a more extensive description of the autophagy regiments. Using this technique, steady states (snapshots) of autophagy in cell cultures expressing GFP-LC3 we were able to count organelles as well as determine distributions of individual GFP-LC3 intensities and individual electrophoretic mobilities. Comparison of basal and rapamycin-enhance autophagy using individual organelle CE-LIF demonstrated that increases in autophagy markers are caused by a larger number of autophagy organelles and not by increase in the individual organelle GFP-LC3 contents. The analysis also suggests that surface composition and likely the origin of the biomolecules forming the surface of autophagy organelles are different for basal and rapamycin-enhanced autophagy.

6.4.3 Temporal Changes in Individual Autophagy Organelle Properties

We investigated autophagy dynamics in L6 cells undergoing either basal or rapamycin-enhanced autophagy. Treatment with vinblastine halts formation of autolysosomes by blocking fusion of autophagosomes and lysosomes,[81] leading to

accumulation of mostly autophagosomes and degradation of the autolysosomes which are formed prior to vinblastine treatment. Comparison of individual autophagy organelle properties in the presence and absence of vinblastine treatments allowed us to assess the dynamics associated with autolysosome formation (c.f. Equation 6.4). We characterized temporal changes in numbers of individual autophagy organelles that accumulate or disappear as well as the temporal changes in the distributions of individual organelle GFP-LC3 fluorescence and electrophoretic mobilities.

For basal autophagy, the numbers of detected organelle events were 107 ± 23 and 230 ± 59 events/ng protein (Avg. ± St. Dev., n = 3 run) for untreated and after a 2-hour vinblastine treatment, respectively. Using Equation 6.3, the calculated temporal change was 62 ± 32 events/(hour × ng protein). These results indicate that autophagosome formation is faster than disappearance of autolysosomes under basal autophagy conditions. Similarly for rapamycin-enhanced autophagy, the number of detected organelle events were 174 ± 31 and 49 ± 20 events/ng protein (Avg. ± St. Dev., n = 3 runs) for untreated and after a 2-hour vinblastine treatment, respectively; the temporal change in the number of detected organelle events was -63 ± 18 events/(hour × ng protein). The faster disappearance of autolysosomes relative to the rate of appearance of autophagosomes under conditions of rapamycin-enhanced autophagy suggests a rapid degradation of the autolysosome cargo. In agreement, previous studies reported increased levels of free GFP and free LC3 upon rapamycin treatment of HeLa cells expressing GFP-LC3[273] and increased levels of colocalization between DsRed-LC3 puncta and cathepsin D, a lysosomal protein, following rapamycin treatment in cortical neurons.[272] Thus, the study reported here provides evidence that the major effect of rapamycin is to increase the rate of degradation of autolysosome cargo.

Temporal changes in individual autophagy organelle GFP-LC3 distributions can be represented as QQ plots. In Figure 6.5.A the series of markers represent the 5, 10, 15… 95 percentiles of two distributions: organelles from cells treated with vinblastine (y-axis) and from untreated cells (x-axis). The diagonal indicates the location of the markers for identical distributions. Vertical deviations from the diagonal correspond to changes that occur during the vinblastine treatment. For basal autophagy, the organelles that

accumulate tend to have higher individual GFP-LC3 fluorescence signals than autolysosomes that are being degraded (Figure 6.5). In contrast, for rapamycin-enhanced autophagy, organelles that accumulate have lower individual GFP-LC3 fluorescence signals than autolysosomes that are being degraded.

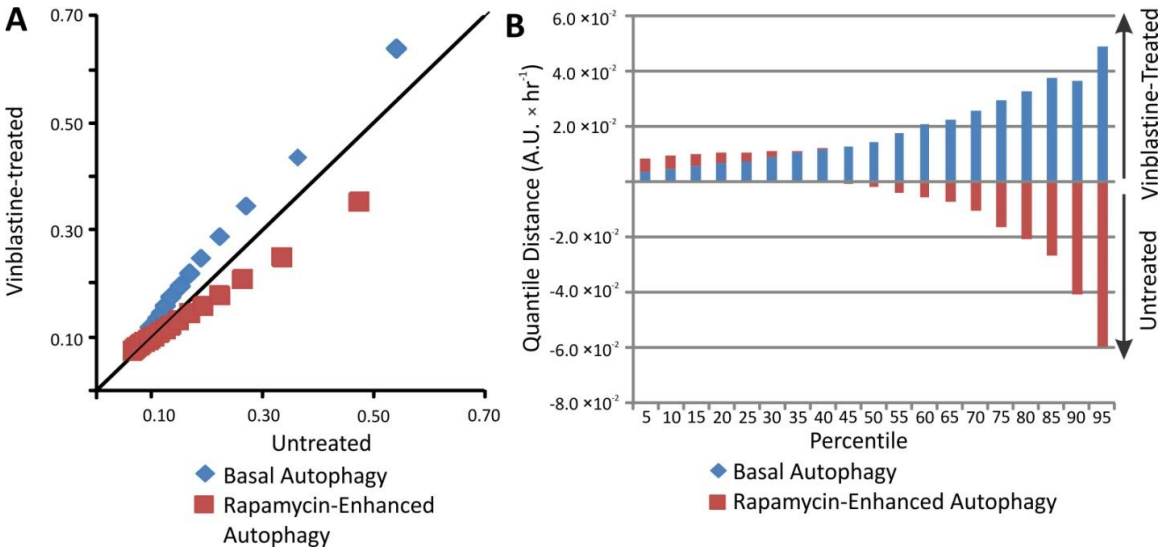

Figure 6.5. (A) Temporal changes in the distributions of individual GFP-LC3 levels. (B) Changes in the distributions of individual GFP-LC3 levels. The change for a given percentiles was calculated according to Equation 6.6.

Previous studies reported an increase in LC3-II signal when autophagosomes are accumulated upon autophagy blockage.[33, 84] In agreement with these studies, we observed an increase in the individual organelle GFP-LC3 distributions (c.f. Figure 6.5). Phagophores and autolysosomes may be represented by the lower percentiles in the QQ plots because: (1) phagophores are the first autophagy structures formed, which suggest lower GFP-LC3 levels and fluorescence than autophagosomes,[274] and (2) autolysosomes experience cleavage and degradation of GFP-LC3-II as the autolysosome matures and for GFP-LC3-II localized in the autolysosomal lumen, the low pH decreases the GFP fluorescence quantum efficiency.[67, 275, 276] Thus, it is not surprising that under basal conditions individual fluorescence GFP-LC3 levels increase upon vinblastine treatment, suggesting that the observed temporal changes are mainly due to the accumulation of autophagosomes.

In contrast, under rapamycin-enhanced autophagy conditions there was a partial decrease in the individual GFP-LC3 fluorescence intensity (50th to 95th percentile, Figure 6.5) during the duration of the vinblastine treatment. This change cannot be explained on the basis of low GFP-LC3 fluorescence intensities of phagophores or autolysosomes as autophagosomes still continue forming and accumulating during the vinblastine treatment. Consistent with our findings, others have observed decreased GFP-LC3-II levels by Western blotting,[83] but these studies did not reveal that only a subset of individual organelles (i.e. 50 to 95th percentile) showed this trend. Therefore, this CE-LIF individual organelle measurement confirms these bulk studies and defines that autophagosomes formed under rapamycin treatment have lower GFP-LC3-II contents.

Temporal changes in individual electrophoretic mobility distributions of autophagy organelles can be represented as QQ plots. Based on liposome models, we previously attributed electrophoretic mobility to variations in surface charge composition and not liposomal size.[93] Therefore we used QQ plots to gain an insight of temporal variations in surface compositions of autophagy organelles represented by their respective electrophoretic mobilities.

For basal conditions, vinblastine treatment revealed that the accumulated autophagy organelles (autophagosomes) had more positive electrophoretic mobility distribution than disappearing autolysosomes (Figure 6.6.). In contrast, for rapamycin-enhanced autophagy conditions, the accumulated organelles (autophagosomes) had a more negative electrophoretic mobility distribution than disappearing autolysosomes (Figure 6.6.). These changes, expressed as mobility units ($cm^2/(V \times s)$ per length of vinblastine exposure (h), are more clearly represented in Figure 6.6, where each percentile have different degrees of variation. Because phagophores continue forming and being transformed into autophagosomes during vinblastine treatment and amphisome numbers are low compared to autophagosomes,[81] the electrophoretic mobility changes observed are mainly attributed to autophagosome formation and disappearance of autolysosomes. Thus in regards to electrophoretic mobility, autophagosomes are more positive than autolysosomes under basal conditions while the opposite is observed under rapamycin-enhanced conditions.

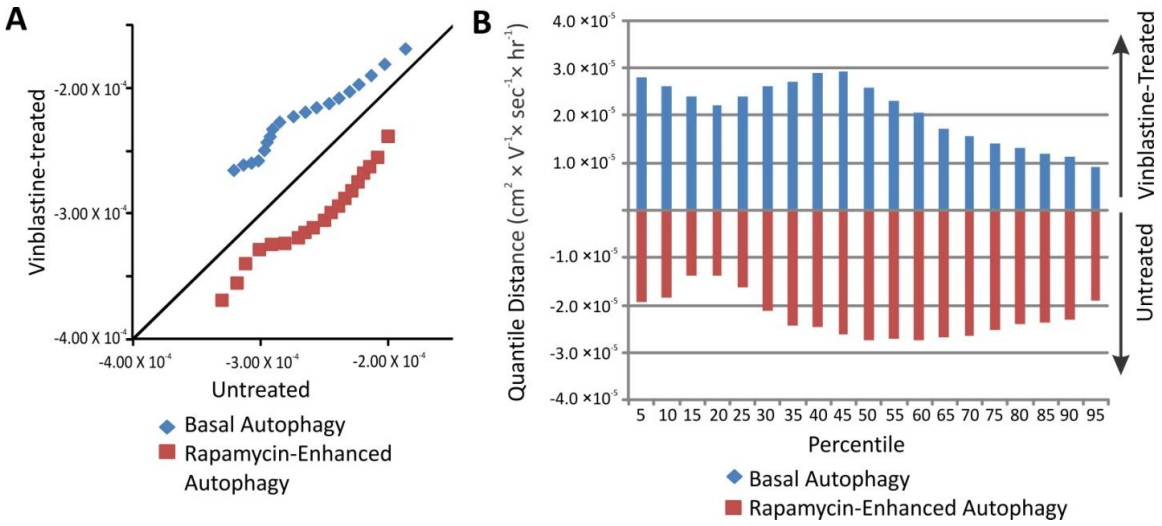

Figure 6.6. (A) Temporal changes in the distributions of individual electrophoretic mobilities. (B) Changes in the distributions of individual electrophoretic mobilities. The change for a given percentiles was calculated according to Equation 6.6.

Both lipid and protein compositions define the surface of autophagosomes and contribute to their surface charge and, in turn, to their electrophoretic mobilities. Considering the multiple sources of autophagosomes membrane components such as the plasma membrane, Golgi, ER, and mitochondria,[251, 277, 278] it is not surprising to observe highly heterogeneous individual electrophoretic mobilities. On the other hand, the dramatic temporal changes observed as a result of vinblastine treatment (Figure 6.6), correspond to differences in surface compositions of autophagosomes and autolysosomes. As autophagosomes accumulate and autolysosomes disappear these marked differences in become more pronounced with time. These differences suggest that forming autophagosomes have positive surface charges relative to autolysosomes under basal autophagy conditions, but this relationship reverses under rapamycin-induced autophagy conditions. These results suggest that the make up the membranes of autophagosomes and autolysosomes is dependent on the status of autophagy in the cell. In agreement, under starvation-enhanced autophagy, the omegasome forms in ER instead of the Golgi.[277] The omegasome is one source for autophagosome membrane components. Similarly, starvation induces use of outer mitochondrial membrane as a source

autophagosome membrane components.[62, 279] Together, these results imply that individual electrophoretic mobility changes are associated with differences between autophagy organelle types (autophagosomes and autolysosome) as well as with the sources of materials that make up the organelle membranes.

6.5. Conclusions

This study demonstrated that CE-LIF can be used to detect individual autophagy organelles based on the GFP-LC3-II label. Individual detection eliminates biases caused by cytosolic GFP-LC3-I, which is eliminated during sample preparation. Both individual GFP-LC3 fluorescence and electrophoretic mobilities are directly determined from CE-LIF data, which made possible comparisons of basal and rapamycin-enhanced autophagy as well as temporal changes reflected by accumulation autophagosomes and degradation of autolysosomes.

Comparison of snapshots of autophagy steady states revealed an increased number of autophagy organelles under rapamycin-enhanced conditions, fairly consistent levels of GFP-LC3 between the two states, and a more positive electrophoretic mobility for rapamycin-enhanced autophagy, which suggest a more positive surface charge. Temporal changes observed by inhibiting autophagy with vinblastine reveal that (1) autolysosome degradation is faster than autophagosome formation under rapamycin-enhanced autophagy; (2) autophagosomes have higher levels of GFP-LC3 than other organelles under basal autophagy but lower ones under rapamycin-induced autophagy; and (3) autophagosomes have more positive electrophoretic mobilities than the rest of the autophagy organelles under basal conditions, but a more negative electrophoretic mobilities than the rest of the autophagy organelles under rapamycin-enhanced autophagy.

Future developments will include use of fluorescent labels specific for autolysosomes and phagophores to obtain a more comprehensive description of the dynamics of autophagy. In addition, labeling of other organelle types may aid at monitoring autophagy sub-types such as mitophagy (degradation of mitochondria) and

pexophagy (degradation of peroxisomes). These advancements respond to a critical need for tools to investigate the role of autophagy flux in disease and aging.[6, 8, 9]

Chapter 7

Conclusions

The work described in this thesis provides new techniques for the high enrichment of endocytic organelles and determination of both endocytic organelle and autophagy-related organelle properties. Endocytic organelles were enriched using magnetic separation, allowing for the determination of the biotransformation of the prodrug *N*-L-leucyldoxorubicin (LeuDox) into the product doxorubin (Dox). The first untargeted determination of small molecules enriched in autophagosomes fractions was performed by UPLC-MS^{e}. This resulted in preliminarily identifications of compounds that will continue to be studied for their importance in maintaining proper autophagosome function and autophagy flux. Finally, the first technique was developed to determine temporal changes in the number and properties of accumulated autophagosomes and phagophores under basal and rapamycin enhanced autophagy by CE-LIF.

Current techniques for the enrichment of endocytic organelles do not result in fractions both free of unwanted organelles and with intact endocytic organelle membranes.[11, 13, 15, 213] The work described in Chapter 3 describes the enrichment of magnetically labeled endocytic organelles. Enriched fractions had no detectable mitochondria and peroxisomal activity when compared to endocytic organelle enriched fractions from differential centrifugation. Using capillary cytometry to detect individual endocytic organelles, a majority of enriched endocytic organelles maintained their acidic pH indicating the enriched organelles had intact membranes. This technique can be used to prepare endocytic organelle fractions to determine their properties such as small molecule composition and pH.

Magnetically enriched endocytic organelle fractions described in Chapter 3 were then used to determine the biotransformation of LeuDox to Dox specific to those fractions (work described in Chapter 4). About 10% of LeuDox was biotransformed to Dox in the enriched acidic organelle fraction accounting for ~45% of the total biotransformation detected in the post nuclear fraction. The remaining biotransformation of LeuDox to Dox occurred in the non-enriched fraction containing remaining endocytic organelles, other organelles, and cytosol. This suggests that endocytic organelles may play an important role in intracellular biotransformation of LeuDox to Dox in addition to the previously reported extracellular biotransformations.[49] This technique allows for the

determination of intracellular biotransformation of drugs and prodrugs and can be applied to other prodrugs that may not only be activated both extracellularly and intracellularly. Furthermore, this technique may be useful to determine other biotransformations that are attributed to lysosomes and other endocytic organelles.

New methods were also developed for determining the properties of autophagosomes. The small molecule composition of autophagosomes had previously not been determined including using non-targeted methods by liquid chromatography coupled to mass spectrometry. Preliminary identifications were assigned to features enriched or unique to autophagosomes by UPLC-MS^e (work described in Chapter 5). A rigorous data analysis procedure was developed to both select features that had extracted ion chromatograms with chromatographic peak profiles and to ensure daughter ions from high-collision energy mass spectra possessed matching extracted ion chromatograms with its parent ion. Enriched autophagosome fractions from rat myoblast cell culture and liver tissue had 187 features detected and 34 high confidence preliminary identifications. Many of the preliminary identifications made, such as PE(16:0/0:0) and sphinganine, have previously been associated with autophagy and autophagosomes indicating that the preliminary identifications made are of high-relevance to autophagy. In the future, identifications will be validated and investigated for their role in autophagy and proper autophagosome function.

The work described in Chapter 6 uses the labeling of autophagy organelles with GFP-LC3 to determine temporal changes in the number and properties of individual autophagy organelles by CE-LIF. The dynamic nature of autophagy and the multiple autophagy organelles involved make bulk measurements, such as those done by Western blotting, inadequate to understand autophagy and its roles in aging and disease. L6 cells expressing GFP-LC3 were treated with vinblastine, which halts autophagy just before formation of autolysosomes, to accumulate autophagosomes and phagophores from basal and rapamycin enhanced autophagy flux. Comparison of organelle numbers and changes in GFP-LC3 fluorescence intensities or electrophoretic mobilities of individual organelles, that either accumulated or disappeared during vinblastine treatment, provides individual-organelle level detail of the autophagy process. Under basal autophagy

conditions, there was a net accumulation of organelles, which mostly represent autophagosomes; because autolysosomes also degrade, the higher GFP-LC3 fluorescence and more positive electrophoretic mobility of individual organelles likely represent differences between these two organelle types. When autophagy was enhanced by rapamycin treatment, disappearance of autophagy organelles (autolysosomes) prevailed over formation of other autophagy organelles, the GFP-LC3 fluorescence of individual organelles decreased suggesting accumulation of organelles with lower levels of this marker, and the individual electrophoretic mobilities were more negative suggesting that organelles formed have a different surface composition. The dramatic contrast between time dependent changes in individual organelle properties between basal and rapamycin-driven conditions demonstrates an anticipated complexity of autophagy flux which likely plays critical role in response to drug treatments, aging, and disease.

The developments described in this thesis are new, improved methods for enriching endocytic organelles and new methods for investigating autophagosome composition and autophagy flux. Development of these techniques may lead to additional follow-up experiments to further increase our understanding of endocytic and autophagosome organelle properties in biological systems. Improved understanding of the properties of endocytic and autophagy organelles from biological systems of diseased states is needed. This may help determine and develop new therapeutic strategies that could compensate for dysfunctional autophagy flux or modified levels of autophagosome-enriched molecules. Improving the design of anti-cancer drugs to account for organelle-specific biotransformations can improve their efficacy. Developing new therapies for diseases with diminished or increased autophagy levels can be done by improved understanding of the composition of these organelles and their properties. Ultimately, the methodologies described in this thesis aim to improve the quality of life of patients receiving anti-cancer drugs and with autophagy-related diseases.

Chapter 8

Future Work

8.1. Introduction

The work described in the prvious chapters of this thesis points to future developments that could further optimize the new techniques described in the thesis, validate results, or apply this work to new biological systems. Experiments are discussed in this chapter that can lead to magnetically enriched autophagosome fractions (work described in Chapter 5), validation of preliminary identifications from enriched autophagosome samples (work described in Chapter 5), and detection of specific autophagy-related organelles to determine their properties for different autophagy conditions and to monitor organelle-specific autophagy (work described in Chapter 6).

8.2. Improving yield of endocytic organelle enrichment

In the work described in Chapter 3, enriched endocytic organelle fractions had a relatively low yield of lysosomes when compared to differential centrifugation (18 ± 6% vs. 42 ± 10%, based on lysosome enzymatic activity in the enriched fraction compared to whole cell lysate, avg. ± st. dev., n = 3). While the technique was sufficient to determine lysosomal enzymatic activity (work described in Chapter 3) and endocytic organelle-specific biotransformation (work described in Chapter 4), other methodologies could also be done following the development of methodologies that increases the endocytic organelle yield. For example, compositional studies of endocytic organelles would benefit as increased levels of endocytic-organelles would increase the detection of low-abundance endocytic organelle-enriched features (a sample-specific chemical entity characterized by a unique constitution of chromatographic retention time, *m/z* and intensity).

Increased endocytic organelle yield can be obtained by modification of the geometric arrangement of the PEEK tubing and its placement in the cavity of the home-built magnetic device. In the work described in Chapters 3 and 4, a single, linear section of PEEK tubing was held in the cavity of the home-built magnetic device. This geometrical arrangement guaranteed that PEEK tubing passed through the location of the device with maximum field strength (Figure 3.1, 8.1.A). The relatively small section of PEEK tubing held in the cavity, however, allowed for the collection of a relatively

decreased amount of the cell sample. This geometrical arrangement could be modified to increase the section of PEEK tubing to the magnetic cavity to capture additional magnetic-labeled organelles (Figure 8.1.B and 8.1.C). The geometries described in Figure 8.1.B and 8.1.C are not the only possibilities for magnetic enrichment that can potentially increase endocytic organelle yield but were selected for their simplicity to manipulate the PEEK tubing.[280]

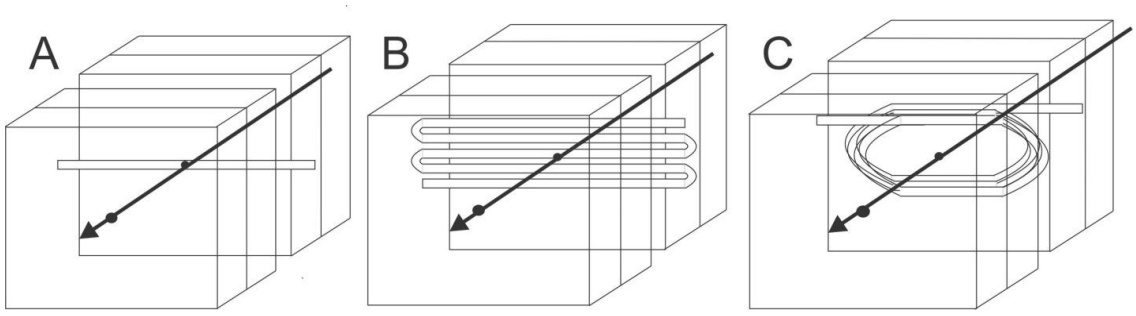

Figure 8.1. PEEK tubing geometries for magnetic enrichment. PEEK tubing is held in the magnetic cavity of a magnetic separator built with neodymium borate magnets (square blocks). The arrow depicts the magnetic field. (A) The geometric arrangement of PEEK tubing used in the work described in Chapter 3. (B-C) The geometric arrangements of PEEK tubing that could provide additional PEEK tubing and, therefore, capture increased volumes of magnetically labeled endocytic organelles and increase yield.

As indicated in Figure 3.1, the magnetic field is strongest in the middle of the magnetic setup (indicated by arrow in Figure 8.1.). PEEK tubing setups B and C increase the length of PEEK tubing and, therefore, the volume of biological sample that can be captured. However, the magnetic field strength is weaker in these positions. To capture magnetically labeled organelles in tubing located in areas of weaker magnetic field strength, either the applied fluid flow may need to be decreased, the magnetic strength of the magnetic field may need to be increased, or a combination of both. Equation 8.1 describes the forces (μ) of a magnetic particle in a tube:[281]

$$\mu_{total} = \mu_{flow} + \mu_{mag}$$ **Equation 8.1.**

When the total force becomes 0, Equation 8.1 indicates that the magnetic force and the fluid flow force are equal and the particle is held at a single location in a

magnetic field. Modeling can be performed to examine the optimized fluid flow for an applied magnetic field and a particle with a given magnetically susceptibility. The Arriaga lab is well equipped to perform these studies and optimization due to the availability of computer software to model magnetic fields and expertise in organelle enrichment. Following modeling to determine an initial set of parameters based on the PEEK tubing geometry, fluid rate, and magnetic field strength, initial parameters can be further optimized using the home-built magnetic device and liposomes containing magnetic nanoparticles.[89]

An additional modification of the procedure developed in Chapter 3 is to modify the duration of the treatment of cells with the dextran-coated iron oxide nanoparticles. This will allow for the targeting of lysosomes over late endosomes. In different types of cell culture, dextran traffics to cells and within cells at different rates. In the procedure described in Chapter 3, cells were treated for 30 min with dextran-coated nanoparticles followed by cell harvest. Previously in the literature, dextran targeting to lysosomes has been done with 30 min pulse with no chase,[282-284] 1 hr pulse and 1 hr chase,[285] and 4 hr pulse and 20 hr chase.[286] Lysosome enrichment may be maximized by ensuring dextran coated magnetic nanoparticles are localized in lysosomes (compared to late endosomes). Different pulse-chase combinations, such as those described above, can be used for the treatment of cells with dextran coated magnetic nanoparticles. To determine if increased numbers of lysosomes have been captured, tetramethylrhodamine- and fluorescein-labeled dextran will also be endocytosed and individual organelle pH will be determined by either capillary cytometry as described in Chapter 3[88] or CE-LIF.[48] If more lysosomes are captured following magnetic enrichment, histograms of organelle pH will show increased acidity (Figure 8.2.). In addition to treatment times for the pulse-chase, other factors such as additives to the cellular media and the coating of the nanoparticle may need to be considered as well.

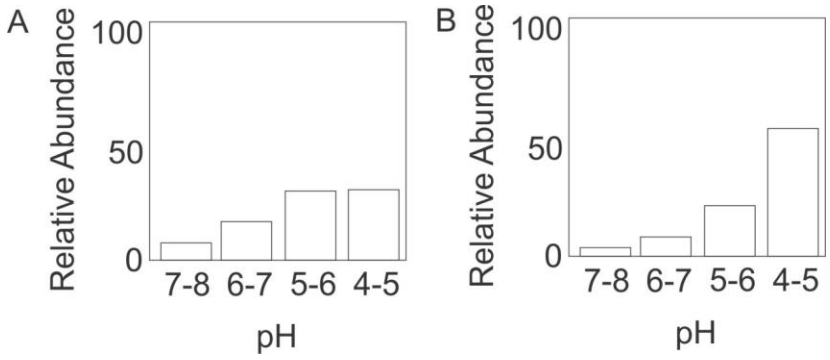

Figure 8.2. Hypothetical histograms indicating increased lysosomes have been captured due to a different pulse-chase treatment of dextran-coated nanoparticles. If a second pulse chase treatment (B) has a higher relative abundance of pH 4-5 organelles than an original pulse chase treatment (C), this suggests more lysosomes, with increased acidity, have been magnetically enriched.

8.3. Magnetic enrichment of autophagosomes

Organelle enrichment methods are still needed to enrich autophagosomes in high purity, high yield, with intact organelle membranes.[85] Chapter 5 describes the enrichment of autophagosomes from tissue and cell culture. Density gradient centrifugation provided an excellent purity of autophagosomes. Since cell culture was used instead of starting material as tissue, density gradient centrifugation could not be used for autophagosome enrichment.[8830, 281] It is difficult to increase the amount of starting material from cell culture when expensive pharmacological treatments such as vinblastine or when expensive SILAC-reagents are used to treat cell culture. To enrich autophagosomes from cell culture, vinblastine treatment was used to increase the yield of autophagosomes[81] and several steps were taken to remove unwanted organelles such as treatment with glycyl-L-phenyl-2-naphthylamine to osmotically lyse lysosomes and magnetic immunoenrichment to remove mitochondria.[81] While autophagosomes were enriched and lysosomes and mitochondria were not detected in the enriched fraction, other organelles that were not examined for their presence could remain in the autophagy-enriched fraction. While low levels of these organelles could be present due to macroautophagy of organelles, their enrichment levels should be diminished compared to autophagosomes.[75] Techniques are

needed to enrich autophagosomes from biological samples and cell culture by specifically selecting autophagosomes instead of the de-enrichment of other organelles.

Magnetic immunoenrichment of autophagosomes would provide a technique to enrich autophagosomes from tissue and cell culture. Magnetic immunoenrichment is described in Section 2.4. In brief, a magnetic nanoparticle is coated with an antibody for an organelle-specific protein. Following binding between the antibody and protein, an external magnetic field can be used to separate the magnetic and non-magnetic fractions. The organelle of interest, bound to the antibody, should be enriched in the magnetic fraction. Autophagosomes have a well-established protein marker, LC3-II, with many commercially available antibodies. Previous magnetic immunoenrichment techniques for organelles have been developed in the Arriaga lab resulting in organelle fractions that have intact membranes.[85, 213, 287]

Magnetic cell sorting has been thoroughly introduced and discussed in the literature. The technique separates magnetically labeled cells from non-labeled cells.[207, 281, 288-295] Cells are labeled with magnetic particles coated with antibodies against cellular surface proteins which cause magnetically-labeled cells to flow to different outlets due to an applied magnetic field. The techniques used in magnetic cell sorting can be used for organelle magnetic immunoenrichment to allow simultaneous enrichment of different types of magnetic, immunolabeled organelles. To perform magnetic immunoenrichment of organelles, proteins specific to an organelle must be identified (Table 8.1), antibodies for the organelle-specific proteins must be either commercially available or developed, and antibodies must be conjugated to the magnetic particles.[213, 287] Due to the availability of antibodies for autophagy-related organelle marker proteins, magnetic immuno-enrichment could be applied for the magnetic immunoenrichment of autophagy-related organelles. Organelles may be labeled with antibody-coated magnetic particles with varying magnetic susceptibility.[281, 288, 293, 295] This will allow organelles to be directed to different outlets in a magnetic separator when an external magnetic field is applied (Figure 8.3). [21, 26, 27, 29] In the event that an organelle can bind multiple antibody-bound magnetic particle, controls will be needed to determine the resolution of magnetic separation of organelle types. Continuous separation would allow for increased yield of

magnetically separated organelles. Two different magnetic separator designs have been previously designed for cells that are capable of separating cells and particles with greater than 90% purity of the eluted fraction (Figure 8.3.) making these magnetic separators excellent candidates for organelle magnetic immunoenrichment.[281, 288]

Organelle	**Marker Protein**
Phagophore	LC3,[296] Beclin 1[297]
Autophagosome	LC3, GATE-16[296, 298]
Amphisome	LC3, Mannose-6-phosphate receptor[299]
Autolysosome	LC3, LAMP1[300]
Lysosome	LAMP1[300]
Late Endosome	Mannose-6-phosphate receptor[299]

Table 8.1. Autophagy-related organelle proteins for fluorescent labeling.

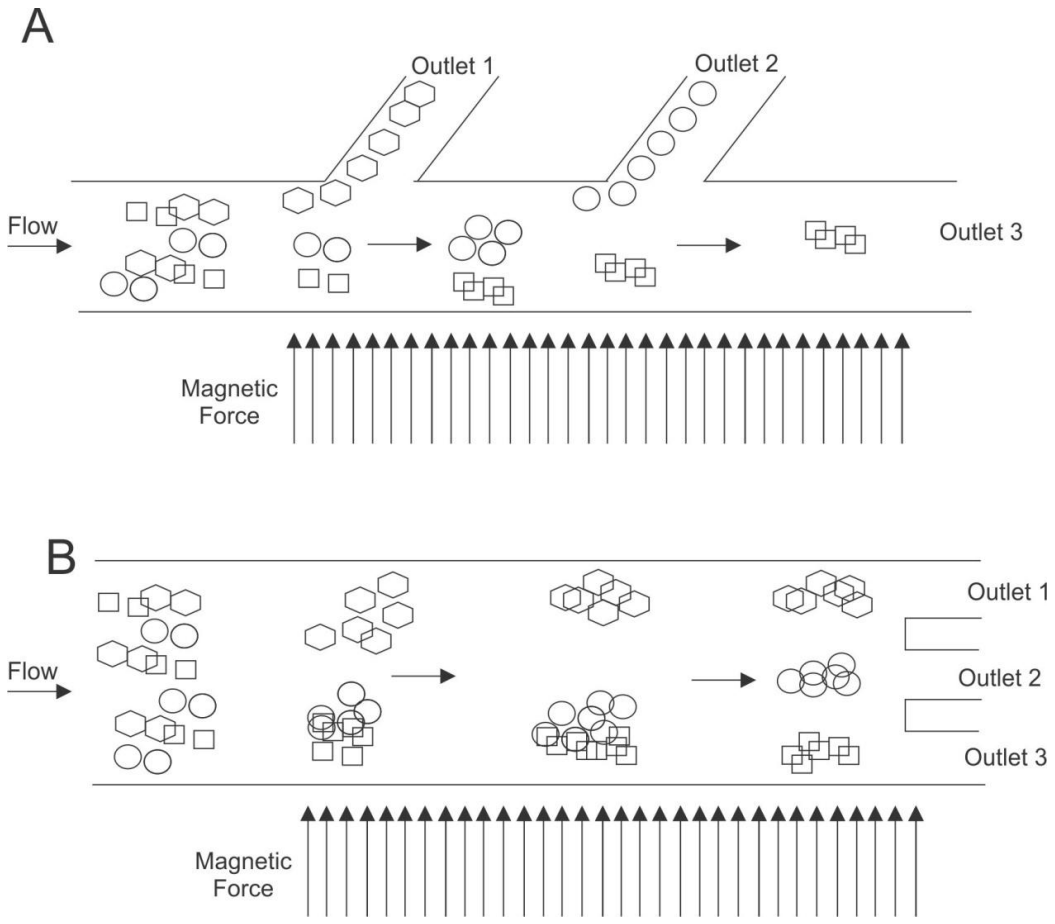

Figure 8.3. Organelle magnetic immunoenrichment design. (A) Buffer flow is perpendicular to the magnetic field. Magnetically labeled autophagy-related organelles (hexagons, squares, and spheres) are separated based on their magnetic susceptibility in the flow device. Outlets are built along the length of the flow channel.[288] (B) Similar to A except all outlets are at the end of the separation device.[281]

8.4. Building online databases to improve number of preliminary identifications

As described in Chapter 5, UPLC-MS^e was used to make preliminary identifications of features from an enriched autophagosome fraction. These features and preliminary identifications may be important to maintain proper autophagosome function and autophagy flux. Of the 185 features detected with the workflow from enriched autophagosome fractions, 153 were not identified with online database searches. Increasing the number of entries of small molecules in mass spectrometry databases will

increase the number of additional preliminary identifications and will decrease the experimental time needed to validate preliminary identifications.

LipidMAPS, Chemical Entities of Biological Interest, and the Human Metabolome Database are databases used for making preliminary identifications of features from biological samples, including features of organelles, and together contain over 75,000 biologically-relevant small molecules. Additional database entries produced by the LC-MS community will increase the numbers of database entries and can lead to increased number of preliminary identifications in future studies and retroactive searches of completed studies. Making additional preliminary identifications will lead to increased numbers of validated identifications and lead to increased understanding of autophagosomes and endocytic organelles.

Additional evidence supporting preliminary identifications would provide increased confidence in database identification. In the workflow described in Chapter 5, theoretical fragments are predicted with MassFragment software and compared to detected fragments. Currently, only predicted high-collision energy mass spectra can be used for structure elucidation for high-accuracy mass spectra. The METLIN database contains about 11,000 high-resolution MS^2 metabolites.[301] There are no online databases, however, that combine high-mass accuracy mass spec and MS^2 for database identifications of features. Comparing detected daughter ions from high-collision energy mass spectra to online databases that have parent and daughter mass spectra standards would provide increased confidence in a preliminary identification when compared to theoretical fragmentation.

Building databases will likely require the scientific community as a whole and would make additional preliminary identifications difficult to perform quickly. Furthermore, it is difficult to learn of updates for online databases. Mass spectra of chemical standards can be used to determine if potential identifications made from databases are correct, however, this could prove to be expensive and time-consuming. Alternative methods of mass spectrometry, such as targeted methods like MS^2, could be used to collect mass spectra of features. Fragments of small molecules can be identified to determine the identity of an unknown compound. For example, the identifies of

triglycerides could be determined by first identifying the compounds of the side chain fatty acids.

8.5. Validation of preliminary identifications

The work described in chapter 5 concludes by making several preliminary identifications of features enriched in autophagosomes. Validation of preliminary identifications is always needed to confirm the identification.[302] Validation with commercial standards is relatively straightforward if high quality commercial standards are available. The standard is examined using the same methodology used for examining the feature located in the biological sample. This includes comparison of extracted ion chromatograms, low energy mass spectra, and high energy mass spectra. If the preliminary identification is correct, the mass spectra of the biological feature and the commercial standard should be very similar. The Arriaga lab is equipped to perform these experiments in the chemistry department's mass spectrometry facility provided standards can be acquired (such as the commercial standard for sphinganine (Avanti Polar lipids, Alabaster, AL).

Validation can also be done while comparing autophagosomes samples from different autophagy flux conditions. For enriched autophagosome samples, a pharmacochemical treatment can be used to increase the number of autophagosomes[81] and therefore increase the concentration of autophagosome-specific compounds. Likewise, siRNA techniques could be used to decrease the number of autophagosomes[303] and therefore decrease the concentration of autophagosome-specific compounds. Tandem mass spectrometry can be performed with a triple quadrupole mass spectrometer to monitor a specific parent ion and specific daughter fragments.[304] The autophagosome sample can be spiked with an isotope-labeled standard and run simultaneously. The detected daughter *m/z* fragments should be similar between the isotope standard and the biological feature, however, the *m/z* values will be different due to the isotope labeling. Features associated with autophagosomes will have increased levels for biological systems with accumulated autophagosomes when compared to a control sample. Features not associated with autophagosomes will have decreased levels for biological systems without autophagosomes. Using isotopically labeled standards to validate preliminary

identifications made in the work described in Chapter 5 will both validate and provide associations between the validated compounds and different autophagy flux conditions.

8.6. Determination of selective autophagy with CE-LIF

Chapter 6 presents the first study of temporal changes of individual organelle numbers, GFP-LC3-II levels, and electrophoretic mobility of accumulated autophagosomes and phagophores following pharmacological treatment of basal autophagy and rapamycin enhanced autophagy levels by CE-LIF. One drawback of this study, however, is that the properties of different types of autophagy-related organelles could not be directly determined because LC3 is localized in phagophores, amphisomes, autolysosomes, and autophagosomes.[305]

Autophagy-related organelles (phagophores, autophagosomes, amphisomes, and autolysosomes) have unique combinations of proteins that could be used for their specific detection (Table 8.1.).[57] Laser induced fluorescence detectors can be set up to detect four fluorescently labeled proteins specific for an organelle type (one laser induced fluorescence detector per protein). This instrument is depicted in Figure 8.4. Up to four different organelle-specific proteins can be detected allowing specific autophagy-related organelles to be detected. This may determine specific autophagy organelle properties such as marker protein levels and electrophoretic mobilities from biological systems with different autophagy levels. Furthermore, this could determine if specific autophagy organelles have increased numbers under different autophagy levels.

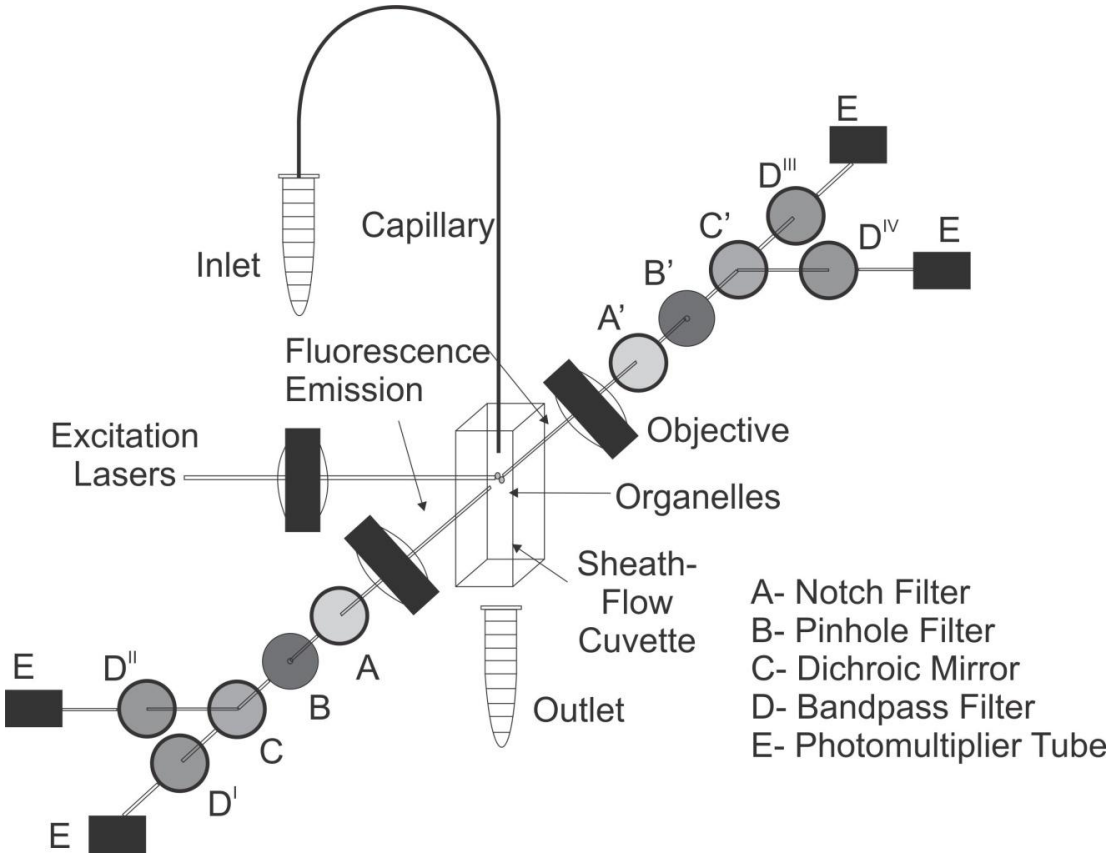

Figure 8.4. CE-LIF instrument with four LIF detectors. Thus allows detection of four fluorescently labeled organelle-specific proteins. Two excitation lasers can be focused on the sheath flow cuvette to excite four fluorescently-labeled proteins specific for four different organelles. Four different bandpass filters will be used to detect four different fluorophores.

Determination of autophagy levels of organelle-specific autophagy levels such as lipophagy (lipid droplets),[306] mitophagy (mitochondria),[307] pexophagy (peroxisomes),[308] reticulophagy (endoplasmic reticulum),[309] and ribophagy (ribosomes),[309] is determined with multiple measurements of the levels of autophagosome and the autophagocytosed organelle by Western blotting, fluorescence confocal microscopy, and transmission electron microscopy.[29, 310] Similar to macroautophagy, however, temporal changes of individual organelle numbers, GFP-LC3-II levels, and electrophoretic mobility of these organelles are still unknown. Therefore, a need exists to determine organelle-specific autophagy organelles properties similar to the work described in Chapter 6.

To determine temporal changes associated with the organelle-specific accumulation of individual autophagy organelles from different autophagy levels, individual autophagy organelle numbers and properties will be determined. Fluorescently-labeled proteins can be used to label autophagocytosed and non autophagocytosed organelles in organelle-specific autophagy pathways. Proteins unique to autophagy-targeted organelles and to the non autophagy-targeted organelle can be labeled (Table 8.2.). Increased and decreased organelle-specific autophagy can be triggered using multiple techniques such as increased Parkin levels by cellular transfection to increase mitophagy[311] and 3-methyl adenine to decrease mitophagy.[76]

Organelle	**Marker Proteins**	**Reference**
Lipid Droplet	Perilipin-2	312
Autophagy-targeted Mitochondria	PINK1, Parkin, VDAC1, TOM22	76, 313-315
Non Autophagy-targeted Mitochondria	VDAC1, TOM22	42, 44-46
Peroxisome	Pex14	316
Endoplasmic Reticulum	p28	317
Ribosome	S6	318

Table 8.2. Organelle-specific proteins for monitoring selective autophagy.

Properties will be determined such as the numbers of autophagosome events with internalized, autophagocytosed organelles such as mitochondria, fluorescent protein levels of autophagy organelles such as LC3-II, fluorescent protein levels of autophagocytosed organelles such as Parkin, and electrophoretic mobility of autophagy organelles and non-autophagocytosed organelles. The number and properties of non autophagy-targeted organelles, such as mitochondria not undergoing mitophagy, will also

be determined. The instrumental setup proposed for detecting different autophagy-related organelles can also be used to monitor selective autophagy pathways.

8.7. Conclusion

This chapter describes additional work needed to advance the enrichment and analysis of endocytic organelle and autophagosome fractions. Increasing the yield of endocytic organelles will allow for additional applications of the technique, such as determining features unique or increased in lysosomes by UPLC-MS. Magnetic immuno-enrichment of autophagosomes and autophagy-related organelles may provide a highly enriched sample that is prepared relatively quickly and can be used to determine autophagosome properties. Making additional database identifications and validating identifications from autophagosome enriched fractions will provide new insights into how autophagosomes function. Finally, labeling of specific autophagy-related organelles will allow for the determination of the temporal changes of specific autophagy organelles and insight into organelle-specific autophagy such as mitophagy. These advancements will provide new insights to the work described in the thesis by expanding the applications of the highly enriched organelle fractions, confirm the preliminary identifications of autophagosomes providing new chemical markers for future studies of autophagy, and understanding of the properties of each autophagy organelle e.g. phagophores, autophagosomes, amphisomes, and autolysosomes, for different autophagy levels and organelle-specific autophagy levels. These will be new markers and properties to study lysosome- and autophagosome-associated disorders.

Bibliography

(1) Heard, J. M.; Bruyere, J.; Roy, E.; Bigou, S.; Ausseil, J.; Vitry, S., Storage problems in lysosomal diseases, *Biochemical Society Transactions,* **2010**, *38* 1442-1447.
(2) Lübke, T.; Lobel, P.; Sleat, D. E., Proteomics of the lysosome, *Biochimica et Biophysica Acta (BBA) - Molecular Cell Research,* **2009**, *1793* (4), 625-635.
(3) Vellodi, A., Lysosomal storage disorders, *British Journal of Haematology,* **2005**, *128* (4), 413-431.
(4) Walkley, S. U., Pathogenic mechanisms in lysosomal disease: a reappraisal of the role of the lysosome, *Acta Paediatrica,* **2007**, *96* 26-32.
(5) Fehrenbacher, N.; Jäättelä, M., Lysosomes as Targets for Cancer Therapy, *Cancer Research,* **2005**, *65* (8), 2993-2995.
(6) Cuervo, A. M., Autophagy and aging: keeping that old broom working, *Trends in Genetics,* **2008**, *24* (12), 604-612.
(7) Cuervo, A. M., Autophagic failure in aging: are lipids the ones to blame?, *Autophagy,* **2009**, *5* (6), 904-905.
(8) Cuervo, A. M., Autophagy: in sickness and in health, *Trends in Cell Biology,* **2004**, *14* (2), 70-77.
(9) Cuervo, A. M.; Bergamini, E.; Brunk, U. T.; Dröge, W.; Ffrench, M.; Terman, A., Autophagy and aging: the importance of maintaining "clean" cells, *Autophagy,* **2005**, *1* (3), 131-140.
(10) Mizushima, N.; Levine, B.; Cuervo, A. M.; Klionsky, D. J., Autophagy fights disease through cellular self-digestion, *Nature,* **2008**, *451* (7182), 1069-1075.
(11) Rodriguez-Paris, J. M.; Nolta, K. V.; Steck, T. L., Characterization of lysosomes isolated from Dictyostelium-discoideum by magnetic fractionation, *Journal of Biological Chemistry,* **1993**, *268* (12), 9110-9116.
(12) Wang, Y. a. A., E, Monitoring incorporation, transformation and subcellular distribution of N-L-leucyl-doxorubicin in uterine sarcoma cells using capillary electrophoretic techniques, *Cancer Letters,* **2007**.
(13) Cuervo, A. M.; Dice, J. F.; Knecht, E., A population of rat liver lysosomes responsible for the selective uptake and degradation of cytosolic proteins, *Journal of Biological Chemistry,* **1997**, *272* (9), 5606-5615.
(14) Sipos, G.; Fuller, R. S. In *Guide to Yeast Genetics and Molecular and Cell Biology, Pt C*, 2002; Vol. 351, pp 351-365.
(15) Diettrich, O.; Mills, K.; Johnson, A. W.; Hasilik, A.; Winchester, B. G., Application of magnetic chromatography to the isolation of lysosomes from fibroblasts of patients with lysosomal storage disorders, *FEBS Letters,* **1998**, *441* (3), 369-372.
(16) Dejong, J.; Vermorken, J. B.; Vandervijgh, W. J. F., Analysis and pharmacokinetics of a new prodrug N-L-leucyldoxorubicin and its metabolites in plasma using HPLC with fluorescence detection, *Journal of Pharmaceutical and Biomedical Analysis,* **1992**, *10* (4), 309-314.
(17) Bennis, S.; Garcia, C.; Robert, J., Aspects of the cellular pharmacology of Nl-leucyldoxorubicin in human tumor cell lines, *Biochemical pharmacology,* **1993**, *45* (9), 1929-1931.
(18) Dejong, J.; Geijssen, G. J.; Munniksma, C. N.; Vermorken, J. B.; Vandervijgh, W. J. F., Plasma pharmacokinetics and pharmacodynamics of a new prodrug N-L-

leucyldoxorubicin and its metabolites in a phase-I clinical trial *Journal of Clinical Oncology*, **1992**, *10* (12), 1897-1906.
(19) Wang, Y.; Arriaga, E. A., Monitoring incorporation, transformation and subcellular distribution of N-l-leucyl-doxorubicin in uterine sarcoma cells using capillary electrophoretic techniques, *Cancer Letters*, **2008**, *262* (1), 123-132.
(20) Koga, H.; Kaushik, S.; Cuervo, A. M., Altered lipid content inhibits autophagic vesicular fusion, *Faseb Journal*, **2010**, *24* (8), 3052-3065.
(21) Asanuma, K., MAP-LC3, a promising autophagosomal marker, is processed during the differentiation and recovery of podocytes from PAN nephrosis, *The FASEB Journal*, **2003**.
(22) Mizushima, N., In Vivo Analysis of Autophagy in Response to Nutrient Starvation Using Transgenic Mice Expressing a Fluorescent Autophagosome Marker, *Molecular Biology of the Cell*, **2003**, *15* (3), 1101-1111.
(23) Mizushima, N.; Levine, B.; Cuervo, A.; Klionsky, D., Autophagy fights disease through cellular self-digestion, *Nature*, **2008**, *451* 1069.
(24) Mizushima, N.; Yamamoto, A.; Hatano, M.; Kobayashi, Y.; Kabeya, Y.; Suzuki, K.; Tokuhisa, T.; Ohsumi, Y.; Yoshimori, T., Dissection of autophagosome formation using Apg5-deficient mouse embryonic stem cells, *Journal of Cell Biology*, **2001**, *152* (4), 657-667.
(25) Mizushima, N.; Yamamoto, A.; Matsui, M.; Yoshimori, T.; Ohsumi, Y., In vivo analysis of autophagy in response to nutrient starvation using transgenic mice expressing a fluorescent autophagosome marker, *Molecular Biology of the Cell*, **2004**, *15* (3), 1101-1111.
(26) Mizushima, N.; Yoshimori, T.; Ohsumi, Y., The Role of Atg Proteins in Autophagosome Formation, *Annual Review of Cell and Developmental Biology, Vol 27*, **2011**, *27* 107-132.
(27) Sou, Y.-s.; Tanida, I.; Komatsu, M.; Ueno, T.; Kominami, E., Phosphatidylserine in Addition to Phosphatidylethanolamine Is an in Vitro Target of the Mammalian Atg8 Modifiers, LC3, GABARAP, and GATE-16, *Journal of Biological Chemistry*, **2006**, *281* (6), 3017-3024.
(28) Cuvillier, O.; Pirianov, G.; Kleuser, B.; Vanek, P. G.; Coso, O. A.; Gutkind, J. S.; Spiegel, S., Suppression of ceramide-mediated programmed cell death by sphingosine-1-phosphate, *Nature*, **1996**, *381* (6585), 800-803.
(29) Klionsky, D. J.; Abeliovich, H.; Agostinis, P.; Agrawal, D. K.; Aliev, G.; Askew, D. S.; Baba, M.; Baehrecke, E. H.; Bahr, B. A.; Ballabio, A.; Bamber, B. A.; Bassham, D. C.; Bergamini, E.; Bi, X. N.; Biard-Piechaczyk, M.; Blum, J. S.; Breclesen, D. E.; Brodsky, J. L.; Brumell, J. H.; Brunk, U. T.; Bursch, W.; Camougrand, N.; Cebollero, E.; Cecconi, F.; Chen, Y. Y.; Chin, L. S.; Choi, A.; Chu, C. T.; Chung, J. K.; Clarke, P. G. H.; Clark, R. S. B.; Clarke, S. G.; Clave, C.; Cleveland, J. L.; Codogno, P.; Colombo, M. I.; Coto-Montes, A.; Cregg, J. M.; Cuervo, A. M.; Debnath, J.; Demarchi, F.; Dennis, P. B.; Dennis, P. A.; Deretic, V.; Devenish, R. J.; Di Sano, F.; Dice, J. F.; DiFiglia, M.; Dinesh-Kumar, S.; Distelhorst, C. W.; Djavaheri-Mergny, M.; Dorsey, F. C.; Droge, W.; Dron, M.; Dunn, W. A.; Duszenko, M.; Eissa, N. T.; Elazar, Z.; Esclatine, A.; Eskelinen, E. L.; Fesues, L.; Finley, K. D.; Fuentes, J. M.; Fueyo, J.; Fujisaki, K.; Galliot, B.; Gao, F. B.; Gewirtz, D. A.; Gibson, S. B.; Gohla, A.; Goldberg, A. L.;

Gonzalez, R.; Gonzalez-Estevez, C.; Gorski, S.; Gottlieb, R. A.; Haussinger, D.; He, Y. W.; Heidenreich, K.; Hill, J. A.; Hoyer-Hansen, M.; Hu, X.; Huang, W. P.; Iwasaki, A.; Jaattela, M.; Jackson, W. T.; Jiang, X.; Jin, S. K.; Johansen, T.; Jung, J. U.; Kadowaki, M.; Kang, C.; Kelekar, A.; Kessel, D. H.; Kiel, J.; Kim, H. P.; Kimchi, A.; Kinsella, T. J.; Kiselyov, K.; Kitamoto, K.; Knecht, E.; Komatsu, M.; Kominami, E.; Konclo, S.; Kovacs, A. L.; Kroemer, G.; Kuan, C. Y.; Kumar, R.; Kundu, M.; Landry, J.; Laporte, M.; Le, W. D.; Lei, H. Y.; Lenardo, M. J.; Levine, B.; Lieberman, A.; Lim, K. L.; Lin, F. C.; Liou, W.; Liu, L. F.; Lopez-Berestein, G.; Lopez-Otin, C.; Lu, B.; Macleod, K. F.; Malorni, W.; Martinet, W.; Matsuoka, K.; Mautner, J.; Meijer, A. J.; Melendez, A.; Michels, P.; Miotto, G.; Mistiaen, W. P.; Mizushima, N.; Mograbi, B.; Monastyrska, I.; Moore, M. N.; Moreira, P. I.; Moriyasu, Y.; Motyl, T.; Munz, C.; Murphy, L. O.; Naqvi, N. I.; Neufeld, T. P.; Nishino, I.; Nixon, R. A.; Noda, T.; Nurnberg, B.; Ogawa, M.; Oleinick, N. L.; Olsen, L. J.; Ozpolat, B.; Paglin, S.; Palmer, G. E.; Papassideri, I.; Parkes, M.; Perlmutter, D. H.; Perry, G.; Piacentini, M.; Pinkas-Kramarski, R.; Prescott, M.; Proikas-Cezanne, T.; Raben, N.; Rami, A.; Reggiori, F.; Rohrer, B.; Rubinsztein, D. C.; Ryan, K. M.; Sadoshima, J.; Sakagami, H.; Sakai, Y.; Sandri, M.; Sasakawa, C.; Sass, M.; Schneider, C.; Seglen, P. O.; Seleverstov, O.; Settleman, J.; Shacka, J. J.; Shapiro, I. M.; Sibirny, A.; Silva-Zacarin, E. C. M.; Simon, H. U.; Simone, C.; Simonsen, A.; Smith, M. A.; Spanel-Borowski, K.; Srinivas, V.; Steeves, M.; Stenmark, H.; Stromhaug, P. E.; Subauste, C. S.; Sugimoto, S.; Sulzer, D.; Suzuki, T.; Swanson, M. S.; Takeshita, F.; Talbot, N. J.; Talloczy, Z.; Tanaka, K.; Tanida, I.; Taylor, G. S.; Taylor, J. P.; Terman, A.; Tettamanti, G.; Thompson, C. B.; Thumm, M.; Tolkovsky, A. M.; Tooze, S. A.; Truant, R.; Tumanovska, L. V.; Uchiyama, Y.; Ueno, T.; Uzcategui, N. L.; van der Klei, I.; Vaquero, E. C.; Vellai, T.; Vogel, M. W.; Wang, H. G.; Webster, P.; Wiley, J. W.; Xi, Z. J.; Xiao, G.; Yahalom, J.; Yang, J. M.; Yap, G.; Yin, X. M.; Yoshimori, T.; Yu, L.; Yue, Z. Y.; Yuzaki, M.; Zabirnyk, O.; Zheng, X. X.; Zhu, X.; Deter, R. L.; Tabas, I., Guidelines for the use and interpretation of assays for monitoring autophagy in higher eukaryotes, *Autophagy*, **2008**, *4* (2), 151-175.

(30) Fader, C. M.; Sanchez, D.; Furlan, M.; Colombo, M. I., Induction of autophagy promotes fusion of multivesicular bodies with autophagic vacuoles in K562 cells, *Traffic*, **2008**, *9* (2), 230-250.

(31) Chan, L. L. Y.; Shen, D.; Wilkinson, A. R.; Patton, W.; Lai, N.; Chan, E.; Kuksin, D.; Lin, B.; Qiu, J., A novel image-based cytometry method for autophagy detection in living cells, *Autophagy*, **2012**, *8* (9), 1371-1382.

(32) Phadwal, K.; Alegre-Abarrategui, J.; Watson, A. S.; Pike, L.; Anbalagan, S.; Hammond, E. M.; Wade-Martins, R.; McMichael, A.; Klenerman, P.; Simon, A. K., A novel method for autophagy detection in primary cells Impaired levels of macroautophagy in immunosenescent T cells, *Autophagy*, **2012**, *8* (4), 677-689.

(33) Eng, K. E.; Panas, M. D.; Hedestam, G. B. K.; McInerney, G. M., A novel quantitative flow cytometry-based assay for autophagy, *Autophagy*, **2010**, *6* (5), 634-641.

(34) Ciechanover, A., Proteolysis: from the lysosome to ubiquitin and the proteasome, *Nature Reviews Molecular Cell Biology*, **2005**, *6* (1), 79-86.

(35) Schulze, H.; Sandhoff, K., Lysosomal Lipid Storage Diseases, *Cold Spring Harbor Perspectives in Biology*, **2011**, *3* (6).
(36) Cox, T. M.; Cachon-Gonzalez, M. B., The cellular pathology of lysosomal diseases, *Journal of Pathology*, **2012**, *226* (2), 241-254.
(37) Liu, B., Therapeutic potential of cyclodextrins in the treatment of Niemann-Pick type C disease, *Clinical Lipidology*, **2012**, *7* (3), 289-301.
(38) Platt, F. M.; Boland, B.; van der Spoel, A. C., Lysosomal storage disorders: The cellular impact of lysosomal dysfunction, *Journal of Cell Biology*, **2012**, *199* (5), 723-734.
(39) Schopfer, K.; Miebach, E.; Beck, M.; Pitz, S., Lysosomal Storage Diseases - Update and New Therapeutic Options, *Klinische Monatsblatter fur Augenheilkunde*, **2011**, *228* (2), 144-160.
(40) Soldati, T.; Schliwa, M., Powering membrane traffic in endocytosis and recycling, *Nat. Rev. Mol. Cell Biol.*, **2006**, *7* (12), 897-908.
(41) Conner, S. D.; Schmid, S. L., Regulated portals of entry into the cell, *Nature*, **2003**, *422* (6927), 37-44.
(42) Falcone, S.; Cocucci, E.; Podini, P.; Kirchhausen, T.; Clementi, E.; Meldolesi, J., Macropinocytosis: regulated coordination of endocytic and exocytic membrane traffic events, *Journal of Cell Science*, **2006**, *119* (22), 4758-4769.
(43) Bright, N. A.; Gratian, M. J.; Luzio, J. P., Endocytic Delivery to Lysosomes Mediated by Concurrent Fusion and Kissing Events in Living Cells, *Current Biology*, **2005**, *15* (4), 360-365.
(44) Shurety, W.; Stewart, N. L.; Stow, J. L., Fluid-Phase Markers in the Basolateral Endocytic Pathway Accumulate in Response to the Actin Assembly-promoting Drug Jasplakinolide, *Molecular Biology of the Cell*, **1998**, *9* (4), 957-975.
(45) Arbab, A. S.; Wilson, L. B.; Ashari, P.; Jordan, E. K.; Lewis, B. K.; Frank, J. A., A model of lysosomal metabolism of dextran coated superparamagnetic iron oxide (SPIO) nanoparticles: implications for cellular magnetic resonance imaging, *NMR in Biomedicine*, **2005**, *18* (6), 383-389.
(46) Shi, H.; He, X. X.; Yuan, Y.; Wang, K. M.; Liu, D., Nanoparticle-Based Biocompatible and Long-Life Marker for Lysosome Labeling and Tracking, *Analytical Chemistry*, **2010**, *82* (6), 2213-2220.
(47) Beyenbach, K. W.; Wieczorek, H., The V-type H+ ATPase: molecular structure and function, physiological roles and regulation, *Journal of Experimental Biology*, **2006**, *209* (4), 577-589.
(48) Chen, Y.; Arriaga, E. A., Individual acidic organelle pH measurements by capillary electrophoresis, *Analytical Chemistry*, **2006**, *78* (3), 820-826.
(49) Ndolo, R. A.; Forrest, M. L.; Krise, J. P., The role of lysosomes in limiting drug toxicity in mice, *Journal of Pharmacology and Experimental Therapeutics*, **2010**, *333* (1), 120-128.
(50) Jiang, L. W.; Maher, V. M.; McCormick, J. J.; Schindler, M., Alkalinization of the lysosomes is correlated with ras transformation of murine and human fibroblasts, *Journal of Biological Chemistry*, **1990**, *265* (9), 4775-4777.
(51) Gong, Y., Separate Roles for the Golgi Apparatus and Lysosomes in the Sequestration of Drugs in the Multidrug-resistant Human Leukemic Cell Line HL-60, *Journal of Biological Chemistry*, **2003**, *278* (50), 50234-50239.

(52) Kokkonen, N.; Rivinoja, A.; Kauppila, A.; Suokas, M.; Kellokumpu, I.; Kellokumpu, S., Defective Acidification of Intracellular Organelles Results in Aberrant Secretion of Cathepsin D in Cancer Cells, *Journal of Biological Chemistry*, **2004**, *279* (38), 39982-39988.
(53) Dejong, J.; Munniksma, C. N.; Guerand, W. S.; Bast, A.; Vandervijgh, W. J. F., Fully Automated-determination of a new Anthracylcine N-L-leucyldoxoruybicin and 6 Metabolites in Plasma by High-Performance Liquid-Chromatography with Online Sample Handling, *Journal of Chromatography-Biomedical Applications,* **1992**, *574* (2), 273-281.
(54) Wang, C. W.; Klionsky, D. J., The molecular mechanism of autophagy, *Molecular Medicine,* **2003**, *9* (3-4), 65-76.
(55) Shintani, T.; Klionsky, D. J., Autophagy in Health and Disease: A Double-Edged Sword, *Science,* **2004**, *306* (5698), 990-995.
(56) Reggiori, F.; Klionsky, D. J., Autophagosomes: biogenesis from scratch?, *Current Opinion in Cell Biology*, **2005**, *17* (4), 415-422.
(57) Kabeya, Y.; Mizushima, N.; Ueno, T.; Yamamoto, A.; Kirisako, T.; Noda, T.; Kominami, E.; Ohsumi, Y.; Yoshimori, T., LC3, a mammalian homolog of yeast Apg8p, is localized in autophagosome membranes after processing *EMBO Journal,* **2003**, *22* (17), 4577-4577.
(58) Tanida, I.; Minematsu-Ikeguchi, N.; Ueno, T.; Kominami, E., Lysosomal turnover, but not a cellular level, of endogenous LC3 is a marker for autophagy, *Autophagy,* **2005**, *1* (2), 84-91.
(59) Longatti, A.; Tooze, S. A., Vesicular trafficking and autophagosome formation, *Cell Death and Differentiation,* **2009**, *16* (7), 956-965.
(60) Morvan, J.; Kochl, R.; Watson, R.; Collinson, L. M.; Jefferies, H. B. J.; Tooze, S. A., In vitro reconstitution of fusion between immature autophagosomes and endosomes, *Autophagy,* **2009**, *5* (5), 676-689.
(61) Tooze, S. A.; Jefferies, H. B. J.; Kalie, E.; Longatti, A.; McAlpine, F. E.; McKnight, N. C.; Orsi, A.; Polson, H. E. J.; Razi, M.; Robinson, D. J.; Webber, L. L., Trafficking and Signaling in Mammalian Autophagy, *Iubmb Life,* **2010**, *62* (7), 503-508.
(62) Tooze, S. A.; Yoshimori, T., The origin of the autophagosomal membrane, *Nature Cell Biology,* **2010**, *12* (9), 831-835.
(63) Klionsky, D. J., The molecular machinery of autophagy: unanswered questions, *Journal of Cell Science*, **2005**, *118* (1), 7-18.
(64) Massey, A. C.; Zhang, C.; Cuervo, A. M., Chaperone-mediated autophagy in aging and disease, *Current Topics in Developmental Biology*, **2006**, *73* 205-235.
(65) Fader, C. M.; Colombo, M. I., Autophagy and multivesicular bodies: two closely related partners, *Cell Death and Differentiation*, **2009**, *16* (1), 70-78.
(66) Fader, C. M.; Sanchez, D. G.; Mestre, M. B.; Colombo, M. I., TI-VAMP/VAMP7 and VAMP3/cellubrevin: two v-SNARE proteins involved in specific steps of the autophagy/multivesicular body pathways, *Biochimica Et Biophysica Acta-Molecular Cell Research,* **2009**, *1793* (12), 1901-1916.
(67) Chen, Y.; Yu, L., Autophagic lysosome reformation, *Experimental Cell Research,* **2013**, *319* (2), 142-146.

(68) Cuervo, A., Autophagy: Many paths to the same end, *Molecular and Cellular Biochemistry*, **2004**, *263* (1), 55-72.
(69) Tsukada, M.; Ohsumi, Y., Isolation and characterization of autophagy-defective mutants of Saccharomyces cerevisiae, *FEBS Letters*, **1993**, *333* (1–2), 169-174.
(70) Suzuki, K.; Kirisako, T.; Kamada, Y.; Mizushima, N.; Noda, T.; Ohsumi, Y., The pre-autophagosomal structure organized by concerted functions of APG genes is essential for autophagosome formation, *EMBO Journal*, **2001**, *20* (21), 5971-5981.
(71) Xie, Z. P.; Klionsky, D. J., Autophagosome formation: core machinery and adaptations, *Nature Cell Biology*, **2007**, *9* 1102-1109.
(72) Kabeya, Y.; Mizushima, N.; Ueno, T.; Yamamoto, A.; Kirisako, T.; Noda, T.; Kominami, E.; Ohsumi, Y.; Yoshimori, T., LC3, a mammalian homologue of yeast Apg8p, is localized in autophagosome membranes after processing, *EMBO Journal*, **2000**, *19* (21), 5720-5728.
(73) Nebauer, R.; Rosenberger, S.; Daum, G., Phosphatidylethanolamine, a limiting factor of autophagy in yeast strains bearing a defect in the carboxypeptidase Y pathway of vacuolar targeting, *Journal of Biological Chemistry*, **2007**, *282* (23), 16736-16743.
(74) Nair, U.; Jotwani, A.; Geng, J.; Gammoh, N.; Richerson, D.; Yen, W.-L.; Griffith, J.; Nag, S.; Wang, K.; Moss, T.; Baba, M.; McNew, James A.; Jiang, X.; Reggiori, F.; Melia, Thomas J.; Klionsky, Daniel J., SNARE Proteins Are Required for Macroautophagy, *Cell*, **2011**, *146* (2), 290-302.
(75) Jin, M.; Liu, X.; Klionsky, D. J., SnapShot: Selective Autophagy, *Cell*, **2013**, *152* (1–2), 368-368.e362.
(76) Narendra, D.; Tanaka, A.; Suen, D.; Youle, R., Parkin is recruited selectively to impaired mitochondria and promotes their autophagy, *The Journal of Cell Biology*, **2008**, *183* 795.
(77) Rajawat, Y. S.; Hilioti, Z.; Bossis, I., Aging: central role for autophagy and the lysosomal degradative system, *Ageing research reviews*, **2009**, *8* (3), 199-213.
(78) Harris, H.; Rubinsztein, D. C., Control of autophagy as a therapy for neurodegenerative disease, *Nature Reviews Neurology*, **2012**, *8* (2), 108-117.
(79) Huang, W.-P.; Scott, S. V.; Kim, J.; Klionsky, D. J., The Itinerary of a Vesicle Component, Aut7p/Cvt5p, Terminates in the Yeast Vacuole via the Autophagy/Cvt Pathways, *Journal of Biological Chemistry*, **2000**, *275* (8), 5845-5851.
(80) Kuma, A.; Matsui, M.; Mizushima, N., LC3, an Autophagosome Marker, Can be Incorporated into Protein Aggregates Independent of Autophagy: Caution in the Interpretation of LC3 Localization, *Autophagy*, **2007**, *3* (4), 323-328.
(81) Seglen, P. O.; Brinchmann, M. F., Purification of autophagosomes from rat hepatocytes, *Autophagy*, **2010**, *6* (4), 542-547.
(82) Berg, T. O.; Fengsrud, M.; Stromhaug, P. E.; Berg, T.; Seglen, P. O., Isolation and characterization of rat liver amphisomes - evidence for fusion of autophagosomes with both early and late endosomes, *Journal of Biological Chemistry*, **1998**, *273* (34), 21883-21892.
(83) Mizushima, N.; Yoshimori, T.; Levine, B., Methods in mammalian autophagy research, *Cell*, **2010**, *140* (3), 313-326.

(84) Mizushima, N.; Yoshimori, T., How to interpret LC3 immunoblotting, *Autophagy*, **2007**, *3* (6), 542-545.
(85) Satori, C. P.; Kostal, V.; Arriaga, E. A., Review on recent advances in the analysis of isolated organelles, *Analytica Chimica Acta*, **2012** (0).
(86) Adler, J.; Parmryd, I., Quantifying colocalization by correlation: the pearson correlation coefficient is superior to the mander's overlap coefficient, *Cytometry Part A*, **2010**, *77A* (8), 733-742.
(87) Chen, Y.; Xiong, G.; Arriaga, E. A., CE analysis of the acidic organelles of a single cell, *Electrophoresis*, **2007**, *28* (14), 2406-2415.
(88) Satori, C. P.; Kostal, V.; Arriaga, E. A., Individual organelle pH determinations of magnetically enriched endocytic organelles via laser-induced fluorescence detection, *Analytical Chemistry*, **2011**, *83* (19), 7331-7339.
(89) Duffy, C. F.; Gafoor, S.; Richards, D. P.; Admadzadeh, H.; O'Kennedy, R.; Arriaga, E. A., Determination of properties of individual liposomes by capillary electrophoresis with postcolumn laser-induced fluorescence detection, *Analytical Chemistry*, **2001**, *73* (8), 1855-1861.
(90) Kostal, V.; Arriaga, E. A., Recent advances in the analysis of biological particles by capillary electrophoresis, *Electrophoresis*, **2008**, *29* (12), 2578-2586.
(91) Whiting, C. E.; Arriaga, E. A., CE-LIF analysis of mitochondria using uncoated and dynamically coated capillaries, *Electrophoresis*, **2006**, *27* (22), 4523-4531.
(92) Chiu, D. T.; Lillard, S. J.; Scheller, R. H.; Zare, R. N.; Rodriguez-Cruz, S. E.; Williams, E. R.; Orwar, O.; Sandberg, M.; Lundqvist, J. A., Probing Single Secretory Vesicles with Capillary Electrophoresis, *Science*, **1998**, *279* (5354), 1190-1193.
(93) Duffy, C. F.; Fuller, K. M.; Malvey, M. W.; O'Kennedy, R.; Arriaga, E. A., Determination of electrophoretic mobility distributions through the analysis of individual mitochondrial events by capillary electrophoresis with laser-induced fluorescence detection, *Analytical Chemistry*, **2001**, *74* (1), 171-176.
(94) Wu, S.; Dovichi, N. J., High-sensitivity fluorescence detector for fluorescein isothiocyanate derivatives of amino acids separated by capillary zone electrophoresis, *Journal of Chromatography A*, **1989**, *480* (0), 141-155.
(95) Helenius, A.; Mellman, I.; Wall, D.; Hubbard, A., Endosomes, *Trends in Biochemical Sciences*, **1983**, *8* (7), 245-250.
(96) Duffy, C. F.; MacCraith, B.; Diamond, D.; O'Kennedy, R.; Arriaga, E. A., Fast electrophoretic analysis of individual mitochondria using microchip capillary electrophoresis with laser induced fluorescence detection, *Lab on a Chip*, **2006**, *6* (8), 1007-1011.
(97) Fuller, K. M.; Arriaga, E. A., Advances in the analysis of single mitochondria, *Current Opinion in Biotechnology*, **2003**, *14* (1), 35-41.
(98) Johnson, R. D.; Navratil, M.; Poe, B. G.; Xiong, G. H.; Olson, K. J.; Ahmadzadeh, H.; Andreyev, D.; Duffy, C. F.; Arriaga, E. A., Analysis of mitochondria isolated from single cells, *Analytical and Bioanalytical Chemistry*, **2007**, *387* (1), 107-118.
(99) Kostal, V.; Arriaga, E. A., Capillary Electrophoretic Analysis Reveals Subcellular Binding between Individual Mitochondria and Cytoskeleton, *Analytical Chemistry*, **2011**, *83* (5), 1822-1829.

(100) Li, D.; Navratil, M.; Poe, B. G.; Moraes, C. T.; Arriaga, E. A., Capillary electrophoretic analysis of the superoxide production by individual mitochondria isolated from cybrid cells, *Febs Journal*, **2006**, *273* 65-65.
(101) Navratil, M.; Poe, B. G.; Arriaga, E. A., Quantitation of DNA Copy Number in Individual Mitochondrial Particles by Capillary Electrophoresis, *Analytical Chemistry*, **2007**, *79* (20), 7691-7699.
(102) Poe, B.; Duffy, C.; Greminger, M.; Nelson, B.; Arriaga, E., Detection of heteroplasmy in individual mitochondrial particles, *Analytical and Bioanalytical Chemistry*, **2010**, *397* (8), 3397-3407.
(103) Wolken, G. G.; Kostal, V.; Arriaga, E. A., Capillary Isoelectric Focusing of Individual Mitochondria, *Analytical Chemistry*, **2011**, *83* (2), 612-618.
(104) Gunasekera, N.; Musier-Forsyth, K.; Arriaga, E., Electrophoretic behavior of individual nuclear species as determined by capillary electrophoresis with laser-induced fluorescence detection, *Electrophoresis*, **2002**, *23* (13), 2110-2116.
(105) Chen, Y.; Walsh, R. J.; Arriaga, E. A., Selective Determination of the Doxorubicin Content of Individual Acidic Organelles in Impure Subcellular Fractions, *Analytical Chemistry*, **2005**, *77* (8), 2281-2287.
(106) Eder, A. R.; Arriaga, E. A., Capillary electrophoresis monitors enhancement in subcellular reactive oxygen species production upon treatment with doxorubicin, *Chemical Research in Toxicology*, **2006**, *19* (9), 1151-1159.
(107) Fuller, K. M.; Arriaga, E. A., Analysis of individual acidic organelles by capillary electrophoresis with laser-induced fluorescence detection facilitated by the endocytosis of fluorescently labeled microspheres, *Analytical Chemistry*, **2003**, *75* (9), 2123-2130.
(108) Swartz, M. E., UPLC™: An Introduction and Review, *Journal of Liquid Chromatography & Related Technologies*, **2005**, *28* (7-8), 1253-1263.
(109) Han, X.; Gross, R. W., Shotgun lipidomics: Electrospray ionization mass spectrometric analysis and quantitation of cellular lipidomes directly from crude extracts of biological samples, *Mass Spectrometry Reviews*, **2005**, *24* (3), 367-412.
(110) Dettmer, K.; Aronov, P. A.; Hammock, B. D., Mass spectrometry-based metabolomics, *Mass Spectrometry Reviews*, **2007**, *26* (1), 51-78.
(111) Plumb, R. S.; Johnson, K. A.; Rainville, P.; Smith, B. W.; Wilson, I. D.; Castro-Perez, J. M.; Nicholson, J. K., UPLC/MSE; a new approach for generating molecular fragment information for biomarker structure elucidation, *Rapid Communications in Mass Spectrometry*, **2006**, *20* (13), 1989-1994.
(112) Keerberg, O.; Ivanova, H.; Keerberg, H.; Parnik, T.; Talts, P.; Gardestrom, P., Quantitative analysis of photosynthetic carbon metabolism in protoplasts and intact leaves of barley. Determination of carbon fluxes and pool sizes of metabolites in different cellular compartments, *Biosystems*, **2011**, *103* (2), 291-301.
(113) Benkeblia, N.; Shinano, T.; Osaki, M., Metabolite profiling and assessment of metabolome compartmentation of soybean leaves using non-aqueous fractionation and GGMS analysis, *Metabolomics*, **2007**, *3* (3), 297-305.
(114) Krueger, S.; Giavalisco, P.; Krall, L.; Steinhauser, M. C.; Bussis, D.; Usadel, B.; Flugge, U. I.; Fernie, A. R.; Willmitzer, L.; Steinhauser, D., A topological map of

the compartmentalized Arabidopsis thaliana leaf metabolome, *Plos One*, **2011**, *6* (3), 1-16.
(115) Melo, T.; Videira, R. A.; Andre, S.; Maciel, E.; Francisco, C. S.; Oliveira-Campos, A. M.; Rodrigues, L. M.; Domingues, M. R. M.; Peixoto, F.; Oliveira, M. M., Tacrine and its analogues impair mitochondrial function and bioenergetics: a lipidomic analysis in rat brain, *Journal of Neurochemistry*, **2012**, *120* (6), 998-1013.
(116) Kiebish, M. A.; Han, X.; Cheng, H.; Chuang, J. H.; Seyfried, T. N., Brain Mitochondrial Lipid Abnormalities in Mice Susceptible to Spontaneous Gliomas, *Lipids*, **2008**, *43* (10), 951-959.
(117) Bird, S. S.; Marur, V. R.; Sniatynski, M. J.; Greenberg, H. K.; Kristal, B. S., Lipidomics Profiling by High-Resolution LC-MS and High-Energy Collisional Dissociation Fragmentation: Focus on Characterization of Mitochondrial Cardiolipins and Monolysocardiolipins, *Analytical Chemistry*, **2011**, *83* (3), 940-949.
(118) Angelini, R.; Vitale, R.; Patil, V. A.; Cocco, T.; Ludwig, B.; Greenberg, M. L.; Corcelli, A., Lipidomics of intact mitochondria by MALDI-TOF/MS, *The Journal of Lipid Research*, **2012**, *53* (7), 1417-1425.
(119) Horn, P. J.; Ledbetter, N. R.; James, C. N.; Hoffman, W. D.; Case, C. R.; Verbeck, G. F.; Chapman, K. D., Visualization of Lipid Droplet Composition by Direct Organelle Mass Spectrometry, *Journal of Biological Chemistry*, **2010**, *286* (5), 3298-3306.
(120) Andreyev, A. Y.; Fahy, E.; Guan, Z. Q.; Kelly, S.; Li, X. A.; McDonald, J. G.; Milne, S.; Myers, D.; Park, H.; Ryan, A.; Thompson, B. M.; Wang, E.; Zhao, Y. H.; Brown, H. A.; Merrill, A. H.; Raetz, C. R. H.; Russell, D. W.; Subramaniam, S.; Dennis, E. A., Subcellular organelle lipidomics in TLR-4-activated macrophages, *Journal of Lipid Research*, **2010**, *51* (9), 2785-2797.
(121) Mukherjee, S.; Ghosh, R. N.; Maxfield, F. R., Endocytosis, *Physiological Reviews*, **1997**, *77* (3), 759-803.
(122) Winchester, B., Lysosomal metabolism of glycoproteins, *Glycobiology*, **2005**, *15* (6), 1R-15R.
(123) Kolter, T.; Sandhoff, K., Lysosomal degradation of membrane lipids, *FEBS Letters*, **2010**, *584* (9), 1700-1712.
(124) Tanaka, M.; Ilo, T.; Tabata, T., Purification and Characterization of a Carboxylesterase from Rabbit Liver Lysosomes, *Journal of Biochemistry*, **1987**, *101* 619-624.
(125) Zhao, M.; Antunes, F.; Eaton, J. W.; Brunk, U. T., Lysosomal enzymes promote mitochondrial oxidant production, cytochrome c release and apoptosis, *European Journal of Biochemistry*, **2003**, *270* (18), 3778-3786.
(126) Hsu, K. F.; Wu, C. L.; Huang, S. C.; Wu, C. M.; Hsiao, J. R.; Yo, Y. T.; Chen, Y. H.; Shiau, A. L.; Chou, C. Y., Cathepsin L mediates resveratrol-induced autophagy and apoptotic cell death in cervical cancer cells, *Autophagy*, **2009**, *5* (4), 451-460.
(127) Dietz, H. C., New Therapeutic Approaches to Mendelian Disorders, *New England Journal of Medicine*, **2010**, *363* (9), 852-863.

(128) Kohler, A.; Pluta, H. J., Lysosomal Injury and MFO activity in the liver of flounder (Platichtys-Flesus L) in relation to histopathology of hepatic degeneration and carcinogensis *Marine Environmental Research,* **1995**, *39* (1-4), 255-260.
(129) Schiffmann, R.; Murray, G. J.; Treco, D.; Daniel, P.; Sellos-Moura, M.; Myers, M.; Quirk, J. M.; Zirzow, G. C.; Borowski, M.; Loveday, K.; Anderson, T.; Gillespie, F.; Oliver, K. L.; Jeffries, N. O.; Doo, E.; Liang, T. J.; Kreps, C.; Gunter, K.; Frei, K.; Crutchfield, K.; Selden, R. F.; Brady, R. O., Infusion of alpha-galactosidase A reduces tissue globotriaosylceramide storage in patients with Fabry disease, *Proceedings of the National Academy of Sciences of the United States of America,* **2000**, *97* (1), 365-370.
(130) Grabowski, G. A.; Leslie, N.; Wenstrup, R., Enzyme therapy for Gaucher disease: the first 5 years, *Blood Reviews,* **1998**, *12* (2), 115-133.
(131) Pimplikar, S. W.; Nixon, R. A.; Robakis, N. K.; Shen, J.; Tsai, L. H., Amyloid-Independent Mechanisms in Alzheimer's Disease Pathogenesis, *Journal of Neuroscience,* **2010**, *30* (45), 14946-14954.
(132) Della Valle, M. C.; Sleat, D. E.; Zheng, H. Y.; Moore, D. F.; Jadot, M.; Lobel, P., Classification of Subcellular Location by Comparative Proteomic Analysis of Native and Density-shifted Lysosomes, *Molecular & Cellular Proteomics,* **2011**, *10* (4).
(133) Trotter, M. W. B.; Sadowski, P. G.; Dunkley, T. P. J.; Groen, A. J.; Lilley, K. S., Improved sub-cellular resolution via simultaneous analysis of organelle proteomics data across varied experimental conditions, *Proteomics,* **2010**, *10* (23), 4213-4219.
(134) de Araujo, M. E. G.; Huber, L. A.; Stasyk, T., Latex beads internalization and quantitative proteomics join forces to decipher the endosomal proteome, *Expert Review of Proteomics,* **2011**, *8* (3), 303-307.
(135) Pourahmad, J.; Ross, S.; O'Brien, P. J., Lysosomal involvement in hepatocyte cytotoxicity induced by Cu2+ but not Cd2+, *Free Radical Biology and Medicine,* **2001**, *30* (1), 89-97.
(136) Renard, C.; Vanderhaeghe, H. J.; Claes, P. J.; Zenebergh, A.; Tulkens, P. M., Influence of conversion of penicillin-G into a basic derivative on its accumulation and subcellular-localization in cultured macrophages, *Antimicrobial Agents and Chemotherapy,* **1987**, *31* (3), 410-416.
(137) Agoston, M.; Orsi, F.; Feher, E.; Hagymasi, K.; Orosz, Z.; Blazovics, A.; Feher, J.; Vereckei, A., Silymarin and vitamin E reduce amiodarone-induced lysosomal phospholipidosis in rats, *Toxicology,* **2003**, *190* (3), 231-241.
(138) Wang, Y. H.; Arriaga, E. A., Monitoring incorporation, transformation and subcellular distribution of N-L-leucyl-doxorubicin in uterine sarcoma cells using capillary electrophoretic techniques, *Cancer Letters,* **2008**, *262* (1), 123-132.
(139) Claude, A., Fractionation of Mammalian Liver Cells by Differential Centrifugation, *Journal of Experimental Medicine,* **1946**, *84* (1), 51-59.
(140) Arai, K.; Kanaseki, T.; Ohkuma, S., Isolation of highly purified lysosomes from rat-liver- identification of electron carrier components on lysosomal membranes, *Journal of Biochemistry,* **1991**, *110* (4), 541-547.

(141) Arborgh, B.; Ericsson, J.; Claumann, H., Method for the Isolation of Iron-loaded Lysosomes from Rat Liver, *FEBS Letters*, **1973**, *32* (1), 190-194.
(142) Henning, R.; Plattner, H., Isolation of Rat Liver Lysosomes by Loading with Colloidal Gold, *Biochimica et Biophysica Acta*, **1974**, *354* 114-120.
(143) Alberts, B.; Johnson, A.; Lewis, J.; Raff, M.; Roberts, K.; Walter, P. *Molecular Biology of the Cell, 4th ed.*; Garland Science: New York, 2002.
(144) Marsh, M., Endosome and lysosome purification by free-flow electrophoresis, *Methods in Cell Biology*, **1989**, *31* 319-334.
(145) Franzreb, M.; Siemann-Herzberg, M.; Hobley, T. J.; Thomas, O. R. T., Protein purification using magnetic adsorbent particles, *Applied Microbiology and Biotechnology*, **2006**, *70* (5), 505-516.
(146) Yavuz, C. T.; Prakash, A.; Mayo, J. T.; Colvin, V. L., Magnetic separations: From steel plants to biotechnology, *Chemical Engineering Science*, **2009**, *64* (10), 2510-2521.
(147) Thiel, A.; Scheffold, A.; Radbruch, A., Immunomagnetic cell sorting - pushing the limits, *Immunotechnology*, **1998**, *4* (2), 89-96.
(148) Tomasello, E.; Desmoulins, P. O.; Chemin, K.; Guia, S.; Cremer, H.; Ortaldo, J.; Love, P.; Kaiserlian, D.; Vivier, E., Combined natural killer cell and dendritic cell functional deficiency in KARAP/DAP12 loss-of-function mutant mice, *Immunity*, **2000**, *13* (3), 355-364.
(149) Hornig-Do, H. T.; Gunther, G.; Bust, M.; Lehnartz, P.; Bosio, A.; Wiesner, R. J., Isolation of functional pure mitochondria by superparamagnetic microbeads, *Analytical Biochemistry*, **2009**, *389* (1), 1-5.
(150) Gao, W. T.; Kang, J. H.; Liao, Y.; Ding, W. X.; Gambotto, A. A.; Watkins, S. C.; Liu, Y. J.; Stolz, D. B.; Yin, X. M., Biochemical Isolation and Characterization of the Tubulovesicular LC3-positive Autophagosomal Compartment, *Journal of Biological Chemistry*, **2010**, *285* (2), 1371-1383.
(151) Luers, G. H.; Hartig, R.; Mohr, H.; Hausmann, M.; Fahimi, H. D.; Cremer, C.; Volkl, A., Immuno-isolation of highly purified peroxisomes using magnetic beads and continuous immunomagnetic sorting, *Electrophoresis*, **1998**, *19* (7), 1205-1210.
(152) Duvvuri, M.; Krise, J. P., A novel assay reveals that weakly basic model compounds concentrate in lysosomes to an extent greater than pH-partitioning theory would predict, *Molecular Pharmaceutics*, **2005**, *2* (6), 440-448.
(153) Slovakova, M.; Minc, N.; Bilkova, Z.; Smadja, C.; Faigle, W.; Futterer, C.; Taverna, M.; Viovy, J. L., Use of self assembled magnetic beads for on-chip protein digestion, *Lab on a Chip*, **2005**, *5* (9), 935-942.
(154) Gassner, A. L.; Morandini, J.; Josserand, J.; Girault, H. H., Ring magnets for magnetic beads trapping in a capillary, *Analytical Methods*, **2011**, *3* (3), 614-621.
(155) Chen, S. P.; Yu, X. D.; Xu, J. J.; Chen, H. Y., Lab-on-a-chip for analysis of triglycerides based on a replaceable enzyme carrier using magnetic beads, *Analyst*, **2010**, *135* (11), 2979-2986.
(156) Chen, H. X.; Busnel, J. M.; Gassner, A. L.; Peltre, G.; Zhang, X. X.; Girault, H. H., Capillary electrophoresis immunoassay using magnetic beads, *Electrophoresis*, **2008**, *29* (16), 3414-3421.

(157) Takeuchi, T.; Pang, M.; Amano, K.; Koide, J.; Abe, T., Reduced protein tyrosine phosphatase (PTPase) activity of CD45 on peripheral blood lymphocytes in patients with systemic lupus erythematosus (SLE), *Clinical and Experimental Immunology*, **1997**, *109* (1), 20-26.
(158) Zhang, Z. Y.; Clemens, J. C.; Schubert, H. L.; Stuckey, J. A.; Fischer, M. W. F.; Hume, D. M.; Saper, M. A.; Dixon, J. E., Expression, purification, and physicochemical characterization of a recombinant yersinia protein tyrosine phosphatase *Journal of Biological Chemistry*, **1992**, *267* (33), 23759-23766.
(159) Masters, B.; Bilimoria, M.; Kamin, H., The Mechanism of 1- and 2-Electron Trnasfers Catalyzed by Reduced Triphosphopyridine Nucleotide-Cytochdome c Reductase, *Journal of Biological Chemistry*, **1965**, *240* (10), 4081-4088.
(160) Bissbort, S. H.; Vermaak, W. J. H.; Elias, J.; Bester, M. J.; Dhatt, G. S.; Pum, J. K. W., Novel test and its automation for the determination of erythrocyte acetylcholinesterase and its application to organophosphate exposure, *Clinica Chimica Acta*, **2001**, *303* (1-2), 139-145.
(161) Csanyi, L., Simultaneous spectrophotometric determination of hydrogen peroxide and peroxyacids of sulfur, *Analytical Chemistry*, **1970**, *42* (6), 680-682.
(162) Aviram, I.; Shaklai, N., The association of human-erythrocyte catalase with the cell-membrane, *Archives of Biochemistry and Biophysics*, **1981**, *212* (2), 329-337.
(163) Andreyev, D.; Arriaga, E. A., Simultaneous laser-induced fluorescence and scattering detection of individual particles separated by capillary electrophoresis, *Analytical Chemistry*, **2007**, *79* (14), 5474-5478.
(164) Davis, J. M.; Arriaga, E. A., Evaluation of peak overlap in migration-time distributions determined by organelle capillary electrophoresis: Type-II error analogy based on statistical-overlap theory, *Journal of Chromatography A*, **2009**, *1216* (35), 6335-6342.
(165) Terrell, G. R.; Scott, D. W., Oversmoothed Nonparametric Density Estimates, *Journal of the American Statistical Association*, **1985**, *80* (389), 209-214.
(166) Whiting, C. E.; Arriaga, E. A., Evaluation of individual particle capillary electrophoresis experiments via quantile analysis, *Journal of Chromatography A*, **2007**, *1157* (1-2), 446-453.
(167) Lemieux, B.; Percival, M. D.; Falgueyret, J. P., Quantitation of the lysosomotropic character of cationic amphiphilic drugs using the fluorescent basic amine Red DND-99, *Analytical Biochemistry*, **2004**, *327* (2), 247-251.
(168) Duzgunes, N.; Majumdar, S.; Goren, M. B., Fluorescence methods for monitoring phagosome lysosome fusion in human macrophages, *Methods in Enzymology*, **1993**, *221* 234-238.
(169) Sallusto, F.; Cella, M.; Danieli, C.; Lanzavecchia, A., Dendritic cells use macropinocytosis and the mannose receptor to concentrate macromolecules in the major histocompatability complex class-II compartment- down regulation by cytokines and bacterial products, *Journal of Experimental Medicine*, **1995**, *182* (2), 389-400.
(170) Beveridge, J. S.; Stephens, J. R.; Latham, A. H.; Williams, M. E., Differential Magnetic Catch and Release: Analysis and Separation of Magnetic Nanoparticles, *Analytical Chemistry*, **2009**, *81* (23), 9618-9624.

(171) Geisow, M. J.; Hart, P. D.; Young, M. R., Temporal changes of lysosome and phagosome pH during phagolysosome formation in macrophages- studies by spectroscopy, *Journal of Cell Biology*, **1981**, *89* (3), 645-652.
(172) Schindler, M.; Grabski, S.; Hoff, E.; Simon, S. M., Defective pH regulation of acidic compartments in human breast cancer cells (MCF-7) is normalized in adriamycin-resistant cells (MCF-7adr), *Biochemistry*, **1996**, *35* (9), 2811-2817.
(173) Sathe, T. R.; Agrawal, A.; Nie, S. M., Mesoporous silica beads embedded with semiconductor quantum dots and iron oxide nanocrystals: Dual-function microcarriers for optical encoding and magnetic separation, *Analytical Chemistry*, **2006**, *78* (16), 5627-5632.
(174) Ellinger, I.; Klapper, H.; Fuchs, R., Fluid-phase marker transport in rat liver: Free-flow electrophoresis separates distinct endosome subpopulations, *Electrophoresis*, **1998**, *19* (7), 1154-1161.
(175) Ostergaard, S.; Blankenstein, G.; Dirac, H.; Leistiko, O., A novel approach to the automation of clinical chemistry by controlled manipulation of magnetic particles, *Journal of Magnetism and Magnetic Materials*, **1999**, *194* (1-3), 156-162.
(176) Gleich, B.; Hellwig, N.; Bridell, H.; Jurgons, R.; Seliger, C.; Alexiou, C.; Wolf, B.; Weyh, T., Design and evaluation of magnetic fields for nanoparticle drug targeting in cancer, *Ieee Transactions on Nanotechnology*, **2007**, *6* (2), 164-170.
(177) Meany, D. L.; Poe, B. G.; Navratil, M.; Moraes, C. T.; Arriaga, E. A., Superoxide released into the mitochondrial matrix, *Free Radical Biology and Medicine*, **2006**, *41* (6), 950-959.
(178) Johnson, S. A.; Richardson, D. S., Anthracyclines in haematology: pharmacokinetics and clinical studies, *Blood Reviews*, **1998**, *12* (1), 52-71.
(179) Hortobagyi, G. N., Anthracyclines in the treatment of cancer - an overview, *Drugs*, **1997**, *54* 1-7.
(180) Maluf, F. C.; Spriggs, D., Anthracyclines in the treatment of gynecologic malignancies, *Gynecologic Oncology*, **2002**, *85* (1), 18-31.
(181) Tewey, K.; Rowe, T.; Yang, L.; Halligan, B.; Liu, L., Adriamycin-induced DNA damage mediated by mammalian DNA topoisomerase II, *Science*, **1984**, *226* (4673), 466-468.
(182) Zhang, S.; Liu, X.; Bawa-Khalfe, T.; Lu, L.-S.; Lyu, Y. L.; Liu, L. F.; Yeh, E. T., Identification of the molecular basis of doxorubicin-induced cardiotoxicity, *Nature Medicine*, **2012**, *18* 1639-1642.
(183) de Bruijn, P.; Verweij, J.; Loos, W. J.; Kolker, H. J.; Planting, A. S. T.; Nooter, K.; Stoter, G.; Sparreboom, A., Determination of doxorubicin and doxorubicinol in plasma of cancer patients by high-performance liquid chromatography, *Analytical Biochemistry*, **1999**, *266* (2), 216-221.
(184) Jeyaseelan, R.; Poizat, C.; Wu, H. Y.; Kedes, L., Molecular mechanisms of doxorubicin-induced cardiomyopathy - selective suppression of Reiske iron-sulfur protein, ADP/ATP translocase, and phosphofructokinase genes is associated with ATP depletion in rat cardiomyocytes, *Journal of Biological Chemistry*, **1997**, *272* (9), 5828-5832.
(185) Singal, P. K.; Deally, C. M. R.; Weinberg, L. E., Subcellular effects of adriamycin in the heart- a concise review *Journal of Molecular and Cellular Cardiology*, **1987**, *19* (8), 817-828.

(186) Wadler, S.; Fuks, J. Z.; Wiernik, P. H., Phate-I and phase-II agents in cancer therapy. 1. Anthracyclines and related-compounds *Journal of Clinical Pharmacology*, **1986**, *26* (7), 491-509.
(187) Zhou, S. Y.; Starkov, A.; Froberg, M. K.; Leino, R. L.; Wallace, K. B., Cumulative and irreversible cardiac mitochondrial dysfunction induced by doxorubicin, *Cancer Research*, **2001**, *61* (2), 771-777.
(188) Baldini, N.; Scotlandi, K.; Serra, M.; Shikita, T.; Zini, N.; Ognibene, A.; Santi, S.; Ferracini, R.; Maraldi, N. M., Nuclear immunolocalization of P-glycoprotein in multidrug-resistant cell-lines showing similar mechanisms of doxorubicin distribution *European Journal of Cell Biology*, **1995**, *68* (3), 226-239.
(189) Abbaszadegan, M. R.; Cress, A. E.; Futscher, B. W.; Bellamy, W. T.; Dalton, W. S., Evidence for cytoplasmic P-glycoprotein location associated with increased multidrug resistance and resistance to chemosensitizers, *Cancer Research*, **1996**, *56* (23), 5435-5442.
(190) Lüpertz, R.; Wätjen, W.; Kahl, R.; Chovolou, Y., Dose- and time-dependent effects of doxorubicin on cytotoxicity, cell cycle and apoptotic cell death in human colon cancer cells, *Toxicology*, **2010**, *271* (3), 115-121.
(191) Mordente, A.; Meucci, E.; Silvestrini, A.; Martorana, G. E.; Giardina, B., New developments in anthracycline-induced cardiotoxicity, *Current Medicinal Chemistry*, **2009**, *16* (13), 1656-1672.
(192) Bennis, S.; Garcia, C.; Robert, J., Aspects of the cellular pharmacology of N-L-leucyldoxorubicin in human tumor-cell lines, *Biochemical Pharmacology*, **1993**, *45* (9), 1929-1931.
(193) Breistol, K.; Hendriks, H. R.; Berger, D. P.; Langdon, S. P.; Fiebig, H. H.; Fodstad, O., The antitumour activity of the prodrug N-L-leucyl-doxorubicin and its parent compound doxorubicin in human tumour xenografts, *European Journal of Cancer*, **1998**, *34* (10), 1602-1606.
(194) Deprez-de Campeneere, D.; Baurain, R.; Trouet, A., Accumulation and metabolism of new anthracycline derivatives in the heart after IV injection into mice, *Cancer Chemotherapy Pharmacology*, **1982**, *8* (2), 193-197.
(195) Jaenke, R. S.; Deprez-DeCampeneere, D.; Trouet, A., Cardiotoxicity and Comparative Pharmacokinetics of Six Anthracyclines in the Rabbit, *Cancer Research*, **1980**, *40* (10), 3530-3536.
(196) Canal, P., Robert, J., Ramon, M., Baurain, R., Tresca, P., de Forni, M., Marty, M., Pujade-Lauraine, E., Bugat, R., Magis, A, and Belpomme, D. , Human pharmacokinetics of *N*-L-leucyldoxorubicin, a new antrhacycline deriviate, and its correlation with clinical toxicities., *Clin Pharmacol Ther*, **1992**, *51* 249-259.
(197) Masquelier, M.; Baurain, R.; Trouet, A., Amino acid and dipeptide derivatives of daunorubicin. 1. Synthesis, physicochemical properties, and lysosomal digestion, *Journal of Medicinal Chemistry*, **1980**, *23* (11), 1166-1170.
(198) Mueller, B. M. In *Attempts to Understand Metastasis Formation I*; Günthert, U., Birchmeier, W., Eds.; Springer Berlin Heidelberg, 1996; Vol. 213/1, pp 65-80.
(199) Bröker, L. E.; Kruyt, F. A. E.; Giaccone, G., Cell death independent of caspases: a review, *Clinical Cancer Research*, **2005**, *11* (9), 3155-3162.
(200) Trouet, A.; Masquelier, M.; Baurain, R.; Deprezdecampeneere, D., A covalent linkage between daunorubicin and proteins that is stable in serum and reversible

by lysosomal hydrolases, as required for a lysosomotropuc drug-carrier conjugate-in vitro and in vivo studies *Proceedings of the National Academy of Sciences of the United States of America-Biological Sciences,* **1982**, *79* (2), 626-629.
(201) Trouet, A., Isolation of modified liver lysosomes, *Methods in Enzymology,* **1974**, *31* 323-329.
(202) Tatosian, D. A.; Shuler, M. L., A novel system for evaluation of drug mixtures for potential efficacy in treating multidrug resistant cancers, *Biotechnology and Bioengineering,* **2009**, *103* (1), 187-198.
(203) Anderson, A. B.; Gergen, J.; Arriaga, E. A., Detection of doxorubicin and metabolites in cell extracts and in single cells by capillary electrophoresis with laser-induced fluorescence detection, *Journal of Chromatography B: Analytical Technologies in the Biomedical and Life Sciences*, **2002**, *769* (1), 97-106.
(204) Eder, A. R.; Chen, J. S.; Arriaga, E. A., Separation of doxorubicin and doxorubicinol by cyclodextrin-modified micellar electrokinetic capillary chromatography, *Electrophoresis,* **2006**, *27* (16), 3263-3270.
(205) Jonas, A. J.; Smith, M. L.; Allison, W. S.; Laikind, P. K.; Greene, A. A.; Schneider, J. A., Proton-translocating ATPase and lysosomal cystine transport, *Journal of Biological Chemistry*, **1983**, *258* (19), 11727-11730.
(206) Temesvari, L. A.; Rodriguez-Paris, J. M.; Bush, J. M.; Zhang, L.; Cardelli, J. A., Involvement of the vacuolar proton-translocating ATPase in multiple steps of the endo-lysosomal system and in the contractile vacuole system of Dictyostelium discoideum, *Journal of Cell Science,* **1996**, *109* (6), 1479-1495.
(207) Zborowski, M.; Sun, L. P.; Moore, L. R.; Williams, P. S.; Chalmers, J. J., Continuous cell separation using novel magnetic quadrupole flow sorter, *Journal of Magnetism and Magnetic Materials*, **1999**, *194* (1-3), 224-230.
(208) Nielsen, U. B.; Kirpotin, D. B.; Pickering, E. M.; Hong, K.; Park, J. W.; Refaat Shalaby, M.; Shao, Y.; Benz, C. C.; Marks, J. D., Therapeutic efficacy of anti-ErbB2 immunoliposomes targeted by a phage antibody selected for cellular endocytosis, *Biochimica et Biophysica Acta (BBA) - Molecular Cell Research*, **2002**, *1591* (1–3), 109-118.
(209) Breistol, K.; Hendriks, H. R.; Fodstad, O., Superior therapeutic efficacy of N-L-leucyl-doxorubicin versus doxorubicin in human melanoma xenografts correlates with higher tumour concentrations of free drug, *European Journal of Cancer*, **1999**, *35* (7), 1143-1149.
(210) Houba, P. H. J.; Boven, E.; Meulen-Muileman, I. H. v. d.; Leenders, R. G. G.; Scheeren, J. W.; Pinedo, H. M.; Haisma, H. J., A novel doxorubicin-glucuronide prodrug DOX-GA3 for tumour-selective chemotherapy: distribution and efficacy in experimental human ovarian cancer, *British Journal of Cancer,* **2001**, *84* (4), 550-557.
(211) Boven, E.; Hendriks, H. R.; Erkelens, C. A. M.; Pinedo, H. M., The anti-tumour effects of the prodrugs N-l-leucyl-doxorubicin and vinblastine-isoleucinate in human ovarian cancer xenografts, *British Journal of Cancer,* **1992**, *66* (6), 1044-1047.
(212) Wang, Y. H.; Taylor, T. H.; Arriaga, E. A., Analysis of the bioactivity of magnetically immunoisolated peroxisomes, *Analytical and Bioanalytical Chemistry*, **2012**, *402* (1), 41-49.

(213) Nylandsted, J.; Becker, A. C.; Bunkenborg, J.; Andersen, J. S.; Dengjel, J.; Jaattela, M., ErbB2-associated changes in the lysosomal proteome, *Proteomics*, **2011**, *11* (14), 2830-2838.
(214) Wilson, I. D.; Plumb, R.; Granger, J.; Major, H.; Williams, R.; Lenz, E. A., HPLC-MS-based methods for the study of metabonomics, *Journal of Chromatography B-Analytical Technologies in the Biomedical and Life Sciences*, **2005**, *817* (1), 67-76.
(215) Castro-Perez, J. M.; Kamphorst, J.; DeGroot, J.; Lafeber, F.; Goshawk, J.; Yu, K.; Shockcor, J. P.; Vreeken, R. J.; Hankemeier, T., Comprehensive LC-MSE lipidomic analysis using a shotgun approach and its application to biomarker detection and identification in osteoarthritis patients, *Journal of Proteome Research*, **2010**, *9* (5), 2377-2389.
(216) Wang, X. J.; Sun, H.; Zhang, A. H.; Wang, P.; Han, Y., Ultra-performance liquid chromatography coupled to mass spectrometry as a sensitive and powerful technology for metabolomic studies, *Journal of Separation Science*, **2011**, *34* (24), 3451-3459.
(217) Ivleva, V. B.; Yu, Y. Q.; Gilar, M., Ultra-performance liquid chromatography/tandem mass spectrometry (UPLC/MS/MS) and UPLC/MSE analysis of RNA oligonucleotides, *Rapid Communications in Mass Spectrometry*, **2010**, *24* (17), 2631-2640.
(218) Ma, J. J.; Kang, L. P.; Zhou, W. B.; Yu, H. S.; Liu, P.; Ma, B. P., Identification and characterization of saponins in extract of Ziziphi spinosae Semen (ZSS) by ultra-performance liquid chromatography-electrospray ionization-quadrupole time-of-flight tandem mass spectrometry (UPLC-ESI-QTOF-MSE), *Journal of Medicinal Plants Research*, **2011**, *5* (26), 6152-6159.
(219) Kang, L. P.; Yu, K. T.; Zhao, Y.; Liu, Y. X.; Yu, H. S.; Pang, X.; Xiong, C. Q.; Tan, D. W.; Gao, Y.; Liu, C.; Ma, B. P., Characterization of steroidal glycosides from the extract of Paris Polyphylla var. Yunnanensis by UPLC/Q-TOF MSE, *Journal of Pharmaceutical and Biomedical Analysis*, **2012**, *62* 235-249.
(220) Trygg, J.; Wold, S., Orthogonal projections to latent structures (O-PLS), *Journal of Chemometrics*, **2002**, *16* (3), 119-128.
(221) Barker, M.; Rayens, W., Partial least squares for discrimination, *Journal of Chemometrics*, **2003**, *17* (3), 166-173.
(222) Bylesjö, M.; Rantalainen, M.; Cloarec, O.; Nicholson, J. K.; Holmes, E.; Trygg, J., OPLS discriminant analysis: combining the strengths of PLS-DA and SIMCA classification, *Journal of Chemometrics*, **2006**, *20* (8-10), 341-351.
(223) Westerhuis, J. A.; Hoefsloot, H. C. J.; Smit, S.; Vis, D. J.; Smilde, A. K.; van Velzen, E. J. J.; van Duijnhoven, J. P. M.; van Dorsten, F. A., Assessment of PLSDA cross validation, *Metabolomics*, **2008**, *4* (1), 81-89.
(224) Westerhuis, J.; Velzen, E. J.; Hoefsloot, H. J.; Smilde, A., Multivariate paired data analysis: multilevel PLSDA versus OPLSDA, *Metabolomics*, **2010**, *6* (1), 119-128.
(225) Verbeke, G.; Molenberghs, G. *Linear mixed models for longitudinal data*; Springer, 2000.

(226) Daszykowski, M.; Walczak, B., Use and abuse of chemometrics in chromatography, *TRAC Trends in Analytical Chemistry,* **2006**, *25* (11), 1081-1096.
(227) Boccard, J.; Veuthey, J. L.; Rudaz, S., Knowledge discovery in metabolomics: an overview of MS data handling, *Journal of Separation Science,* **2010**, *33* (3), 290-304.
(228) Theodoridis, G.; Gika, H. G.; Wilson, I. D., Mass spectrometry-based holistic analytical approaches for metabolite profiling in systems biology studies, *Mass Spectrometry Reviews,* **2011**, *30* (5), 884-906.
(229) Rubinsztein, D. C.; DiFiglia, M.; Heintz, N.; Nixon, R. A.; Qin, Z.-H.; Ravikumar, B.; Stefanis, L.; Tolkovsky, A., Autophagy and Its possible roles in nervous system diseases, damage and repair, *Autophagy,* **2005**, *1* (1), 11-22.
(230) Rubinsztein, D. C., The roles of intracellular protein-degradation pathways in neurodegeneration, *Nature,* **2006**, *443* (7113), 780-786.
(231) Yu, W. H.; Cuervo, A. M.; Kumar, A.; Peterhoff, C. M.; Schmidt, S. D.; Lee, J.-H.; Mohan, P. S.; Mercken, M.; Farmery, M. R.; Tjernberg, L. O.; Jiang, Y.; Duff, K.; Uchiyama, Y.; Näslund, J.; Mathews, P. M.; Cataldo, A. M.; Nixon, R. A., Macroautophagy—a novel β-amyloid peptide-generating pathway activated in Alzheimer's disease, *The Journal of Cell Biology,* **2005**, *171* (1), 87-98.
(232) Theoharides, T. C.; Kalogeromitros, D., The critical role of mast cells in allergy and inflammation, *Annals of the New York Academy of Sciences,* **2006**, *1088* (1), 78-99.
(233) Marzella, L.; Ahlberg, J.; Glaumann, H., Isolation of autophagic vacuoles from rat liver: morphological and biochemical characterization, *J Cell Biol,* **1982**, *93* (1), 144-154.
(234) Masson, P.; Alves, A. C.; Ebbels, T. M. D.; Nicholson, J. K.; Want, E. J., Optimization and evaluation of metabolite extraction protocols for untargeted metabolic profiling of liver samples by UPLC-MS, *Analytical Chemistry,* **2010**, *82* (18), 7779-7786.
(235) Team, R. D. C.; R Foundation for Statistical Computing: Vienna, Austria, 2011.
(236) Benjamini, Y.; Yekutieli, D., The control of the false discovery rate in multiple testing under dependency, *The Annals of Statistics,* **2001**, *29* (4), 1165-1188.
(237) Azizan, K. A.; Baharum, S. N.; Ressom, H. W.; Noor, N. M., GC-MS analysis and PLS-DA validation of the trimethyl silyl-derivatization techniques, **2012**.
(238) Fiehn, O.; Robertson, D.; Griffin, J.; Werf, M.; Nikolau, B.; Morrison, N.; Sumner, L.; Goodacre, R.; Hardy, N.; Taylor, C.; Fostel, J.; Kristal, B.; Kaddurah-Daouk, R.; Mendes, P.; Ommen, B.; Lindon, J.; Sansone, S.-A., The metabolomics standards initiative (MSI), *Metabolomics,* **2007**, *3* (3), 175-178.
(239) Trygg, J.; Holmes, E.; Lundstedt, T., Chemometrics in metabonomics, *Journal of Proteome Research,* **2006**, *6* (2), 469-479.
(240) Stromhaug, P. E.; Berg, T. O.; Fengsrud, M.; Seglen, P. O., Purification and characterization of autophagosomes from rat hepatocytes, *Biochemical Journal,* **1998**, *335* 217-224.
(241) Ichimura, Y.; Kirisako, T.; Takao, T.; Satomi, Y.; Shimonishi, Y.; Ishihara, N.; Mizushima, N.; Tanida, I.; Kominami, E.; Ohsumi, M.; Noda, T.; Ohsumi, Y., A

ubiquitin-like system mediates protein lipidation, *Nature*, **2000**, *408* (6811), 488-492.
(242) Scarlatti, F.; Bauvy, C.; Ventruti, A.; Sala, G.; Cluzeaud, F.; Vandewalle, A.; Ghidoni, R.; Codogno, P., Ceramide-mediated macroautophagy involves inhibition of protein kinase B and up-regulation of Beclin 1, *Journal of Biological Chemistry*, **2004**, *279* (18), 18384-18391.
(243) Zheng, W.; Kollmeyer, J.; Symolon, H.; Momin, A.; Munter, E.; Wang, E.; Kelly, S.; Allegood, J. C.; Liu, Y.; Peng, Q.; Ramaraju, H.; Sullards, M. C.; Cabot, M.; Merrill Jr, A. H., Ceramides and other bioactive sphingolipid backbones in health and disease: lipidomic analysis, metabolism and roles in membrane structure, dynamics, signaling and autophagy, *Biochimica et Biophysica Acta (BBA) - Biomembranes*, **2006**, *1758* (12), 1864-1884.
(244) Pacheco, C. D.; Lieberman, A. P., The pathogenesis of Niemann–Pick type C disease: a role for autophagy?, *Expert Reviews in Molecular Medicine*, **2008**, *10* null-null.
(245) Young, M. M.; Kester, M.; Wang, H.-G., Sphingolipids: regulators of crosstalk between apoptosis and autophagy, *Journal of Lipid Research*, **2013**, *54* (1), 5-19.
(246) Goñi, F. M.; Alonso, A., Biophysics of sphingolipids I. Membrane properties of sphingosine, ceramides and other simple sphingolipids, *Biochimica et Biophysica Acta (BBA) - Biomembranes*, **2006**, *1758* (12), 1902-1921.
(247) Dall'Armi, C.; Hurtado-Lorenzo, A.; Tian, H.; Morel, E.; Nezu, A.; Chan, R. B.; Yu, W. H.; Robinson, K. S.; Yeku, O.; Small, S. A.; Duff, K.; Frohman, M. A.; Wenk, M. R.; Yamamoto, A.; Di Paolo, G., The phospholipase D1 pathway modulates macroautophagy, *Nat Commun*, **2010**, *1* 142.
(248) Menna-Barreto, R. F. S.; Salomao, K.; Dantas, A. P.; Santa-Rita, R. M.; Soares, M. J.; Barbosa, H. S.; de Castro, S. L., Different cell death pathways induced by drugs in Trypanosoma cruzi: an ultrastructural study, *Micron*, **2009**, *40* (2), 157-168.
(249) Høyer-Hansen, M.; Nordbrandt, S. P. S.; Jäättelä, M., Autophagy as a basis for the health-promoting effects of vitamin D, *Trends in Molecular Medicine*, **2010**, *16* (7), 295-302.
(250) Martinez-Vicente, M.; Cuervo, A., Autophagy and neurodegeneration: when the cleaning crew goes on strike, *Lancet neurology*, **2007**, *6* 352.
(251) Cuervo, A. M., The plasma membrane brings autophagosomes to life, *Nature Cell Biology*, **2010**, *12* (8), 735-737.
(252) Wishart, D. S.; Knox, C.; Guo, A. C.; Eisner, R.; Young, N.; Gautam, B.; Hau, D. D.; Psychogios, N.; Dong, E.; Bouatra, S.; Mandal, R.; Sinelnikov, I.; Xia, J.; Jia, L.; Cruz, J. A.; Lim, E.; Sobsey, C. A.; Shrivastava, S.; Huang, P.; Liu, P.; Fang, L.; Peng, J.; Fradette, R.; Cheng, D.; Tzur, D.; Clements, M.; Lewis, A.; De Souza, A.; Zuniga, A.; Dawe, M.; Xiong, Y.; Clive, D.; Greiner, R.; Nazyrova, A.; Shaykhutdinov, R.; Li, L.; Vogel, H. J.; Forsythe, I., HMDB: a knowledgebase for the human metabolome, *Nucleic Acids Research*, **2009**, *37* (Database), D603-D610.
(253) Singh, R.; Kaushik, S.; Wang, Y.; Xiang, Y.; Novak, I.; Komatsu, M.; Tanaka, K.; Cuervo, A. M.; Czaja, M. J., Autophagy regulates lipid metabolism, *Nature*, **2009**, *458* (7242), 1131-1135.

(254) García-Faroldi, G.; Rodríguez, C. E.; Urdiales, J. L.; Pérez-Pomares, J. M.; Dávila, J. C.; Pejler, G.; Sánchez-Jiménez, F.; Fajardo, I., Polyamines are present in mast cell secretory granules and are important for granule homeostasis, *PLoS ONE*, **2010**, *5* (11), e15071.
(255) de Matos, P.; Alcántara, R.; Dekker, A.; Ennis, M.; Hastings, J.; Haug, K.; Spiteri, I.; Turner, S.; Steinbeck, C., Chemical entities of biological interest: an update, *Nucleic Acids Research*, **2010**, *38* (suppl 1), D249-D254.
(256) Siles, R. I.; Hsieh, F. H., Allergy blood testing: a practical guide for clinicians, *Cleveland Clinic Journal of Medicine*, **2011**, *78* (9), 585-592.
(257) Polson, H. E. J.; de Lartigue, J.; Rigden, D. J.; Reedijk, M.; Urbé, S.; Clague, M. J.; Tooze, S. A., Mammalian Atg18 (WIPI2) localizes to omegasome-anchored phagophores and positively regulates LC3 lipidation, *Autophagy*, **2010**, *6* (4), 506-522.
(258) Liang, X. H.; Jackson, S.; Seaman, M.; Brown, K.; Kempkes, B.; Hibshoosh, H.; Levine, B., Induction of autophagy and inhibition of tumorigenesis by beclin 1, *Nature*, **1999**, *402* (6762), 672-676.
(259) Welter, E.; Thumm, M.; Krick, R., Quantification of nonselective bulk autophagy in S. cerevisiae using Pgk1-GFP, *Autophagy*, **2010**, *6* (6), 794-797.
(260) Jahreiss, L.; Menzies, F. M.; Rubinsztein, D. C., The itinerary of autophagosomes: from peripheral formation to kiss-and-run fusion with lysosomes, *Traffic*, **2008**, *9* (4), 574-587.
(261) Furuta, N.; Fujita, N.; Noda, T.; Yoshimori, T.; Amano, A., Combinational soluble N-ethylmaleimide-sensitive factor attachment protein receptor proteins VAMP8 and Vti1b mediate fusion of antimicrobial and canonical autophagosomes with lysosomes, *Molecular Biology of the Cell*, **2010**, *21* (6), 1001-1010.
(262) Narendra, D.; Tanaka, A.; Suen, D. F.; Youle, R. J., Parkin is recruited selectively to impaired mitochondria and promotes their autophagy, *Journal of Cell Biology*, **2008**, *183* (5), 795-803.
(263) Tanida, I.; Waguri, S. In *Protein Misfolding and Cellular Stress in Disease and Aging: Concepts and Protocols*; Bross, P., Gregersen, N., Eds.; Humana Press: New York, NY, 2010; Vol. 648, pp 193-214.
(264) Strack, A.; Duffy, C. F.; Malvey, M.; Arriaga, E. A., Individual mitochondrion characterization: a comparison of classical assays to capillary electrophoresis with laser-induced fluorescence detection, *Analytical Biochemistry*, **2001**, *294* (2), 141-147.
(265) Jackson, W. T.; Giddings, T. H., Jr.; Taylor, M. P.; Mulinyawe, S.; Rabinovitch, M.; Kopito, R. R.; Kirkegaard, K., Subversion of cellular autophagosomal machinery by RNA viruses, *PLoS Biology*, **2005**, *3* (5), e156.
(266) Gilges, M.; Kleemiss, M. H.; Schomburg, G., Capillary zone electrophoresis separations of basic and acidic proteins using poly(vinyl alcohol) coatings in fused silica capillaries, *Analytical Chemistry*, **1994**, *66* (13), 2038-2046.
(267) Huang, X.; Gordon, M. J.; Zare, R. N., Current-monitoring method for measuring the electroosmotic flow rate in capillary zone electrophoresis, *Analytical Chemistry*, **1988**, *60* (17), 1837-1838.

(268) Davis, J. M.; Arriaga, E. A., Evaluation of peak overlap in migration-time distributions determined by organelle capillary electrophoresis: type-II error analogy based on statistical-overlap theory, *J. Chromatogr., A*, **2009**, *1216* (35), 6335-6342.
(269) Davis, J. M.; Arriaga, E. A., Estimation of migration-time and mobility distributions in organelle capillary electrophoresis with statistical-overlap theory, *Analytical Chemistry*, **2010**, *82* (1), 307-315.
(270) Kostal, V.; Fonslow, B. R.; Arriaga, E. A.; Bowser, M. T., Fast determination of mitochondria electrophoretic mobility using micro free-flow electrophoresis, *Analytical Chemistry*, **2009**, *81* (22), 9267-9273.
(271) Graham, J. M.; Rickwood, D. *Subcellular fractionation : a practical approach*; Oxford University Press, USA: New York, NY, 1997.
(272) Boland, B.; Kumar, A.; Lee, S.; Platt, F. M.; Wegiel, J.; Yu, W. H.; Nixon, R. A., Autophagy induction and autophagosome clearance in neurons: relationship to autophagic pathology in Alzheimer's disease, *The Journal of Neuroscience*, **2008**, *28* (27), 6926-6937.
(273) Ni, H. M.; Bockus, A.; Wozniak, A. L.; Jones, K.; Weinman, S.; Yin, X. M.; Ding, W. X., Dissecting the dynamic turnover of GFP-LC3 in the autolysosome, *Autophagy*, **2011**, *7* (2), 188-204.
(274) Polson, H. E. J.; de Lartigue, J.; Rigden, D. J.; Reedijk, M.; Urbe, S.; Clague, M. J.; Tooze, S. A., Mammalian Atg18 (WIPI2) localizes to omegasome-anchored phagophores and positively regulates LC3 lipidation, *Autophagy*, **2010**, *6* (4), 506-522.
(275) Kimura, S.; Noda, T.; Yoshimori, T., Dissection of the autophagosome maturation process by a novel reporter protein, tandem fluorescent-tagged LC3, *Autophagy*, **2007**, *3* (5), 452-460.
(276) Han, K.; Kwon, H. W.; Kang, H.; Kim, J.; Lee, M. S.; Choi, M. Y., Dynamics of macroautophagy: modeling and oscillatory behavior, *Physica a-Statistical Mechanics and Its Applications*, **2012**, *391* (3), 686-692.
(277) Axe, E. L.; Walker, S. A.; Manifava, M.; Chandra, P.; Roderick, H. L.; Habermann, A.; Griffiths, G.; Ktistakis, N. T., Autophagosome formation from membrane compartments enriched in phosphatidylinositol 3-phosphate and dynamically connected to the endoplasmic reticulum, *Journal of Cell Biology*, **2008**, *182* (4), 685-701.
(278) Suzuki, K.; Ohsumi, Y., Current knowledge of the pre-autophagosomal structure (PAS), *FEBS Letters*, **2010**, *584* (7), 1280-1286.
(279) Hailey, D. W.; Rambold, A. S.; Satpute-Krishnan, P.; Mitra, K.; Sougrat, R.; Kim, P. K.; Lippincott-Schwartz, J., Mitochondria supply membranes for autophagosome biogenesis during starvation, *Cell*, **2010**, *141* (4), 656-667.
(280) Pamme, N., On-chip bioanalysis with magnetic particles, *Current Opinion in Chemical Biology*, **2012**, *16* (3-4), 436-443.
(281) Pamme, N.; Wilhelm, C., Continuous sorting of magnetic cells via on-chip free-flow magnetophoresis, *Lab on a Chip*, **2006**, *6* (8), 974-980.
(282) Duclos, S.; Corsini, R.; Desjardins, M., Remodeling of endosomes during lysosome biogenesis involves `kiss and run' fusion events regulated by rab5, *Journal of Cell Science*, **2003**, *116* (5), 907-918.

(283) Haggie, P. M.; Verkman, A. S., Unimpaired Lysosomal Acidification in Respiratory Epithelial Cells in Cystic Fibrosis, *Journal of Biological Chemistry,* **2009**, *284* (12), 7681-7686.
(284) Humphries, W. H. I. V.; Szymanski, C. J.; Payne, C. K., Endo-Lysosomal Vesicles Positive for Rab7 and LAMP1 Are Terminal Vesicles for the Transport of Dextran, *PLoS ONE,* **2011**, *6* (10), e26626.
(285) Naroeni, A.; Jouy, N.; Ouahrani-Bettache, S.; Liautard, J.-P.; Porte, F., Brucella suis-Impaired Specific Recognition of Phagosomes by Lysosomes due to Phagosomal Membrane Modifications, *Infection and Immunity,* **2001**, *69* (1), 486-493.
(286) Conn, P. M. *Imaging and Spectroscopic Analysis of Living Cells: Live Cell Imaging of Cellular Elements and Functions*; Elsevier Science, 2012.
(287) Wang, Y.; Taylor, T. H.; Arriaga, E. A., Analysis of the bioactivity of magnetically immunoisolated peroxisomes, *Analytical and Bioanalytical Chemistry*, **2011**, *402* (1), 41-49.
(288) Adams, J. D.; Kim, U.; Soh, H. T., Multitarget magnetic activated cell sorter, *Proceedings of the National Academy of Sciences of the United States of America,* **2008**, *105* (47), 18165-18170.
(289) Hartig, R.; Hausmann, M.; Cremer, C., Continuous Focusing of Biological Particles by Continuous Immuno Magnetic Sorter- Technique and Applications, *Electrophoresis,* **1995**, *16* (5), 789-792.
(290) Kim, J.; Lee, H. H.; Steinfeld, U.; Seidel, H., Fast Capturing on Micromagnetic Cell Sorter, *IEEE Sensors Journal*, **2009**, *9* (8), 908-913.
(291) McCloskey, K. E.; Chalmers, J. J.; Zborowski, M., Magnetic Cell Separation: Characterization of Magnetophoretic Mobility, *Analytical Chemistry,* **2003**, *75* (24), 6868-6874.
(292) McCloskey, K. E.; Moore, L. R.; Hoyos, M.; Rodriguez, A.; Chalmers, J. J.; Zborowski, M., Magnetophoretic cell sorting is a function of antibody binding capacity, *Biotechnology Progress,* **2003**, *19* (3), 899-907.
(293) Pamme, N.; Eijkel, J. C. T.; Manz, A., On-chip free-flow magnetophoresis: Separation and detection of mixtures of magnetic particles in continuous flow, *Journal of Magnetism and Magnetic Materials,* **2006**, *307* (2), 237-244.
(294) Sajja, V. S. K.; Hanley, T. R.; Gapsis, H.; Guernsey, B.; Kennedy, D. J.; Taylor, M. J.; Papas, K. K.; Todd, P. W., Application of Magnetic Particle Tracking Velocimetry to Quadrupole Magnetic Sorting of Porcine Pancreatic Islets, *Biotechnology and Bioengineering,* **2011**, *108* (9), 2107-2117.
(295) Schneider, T.; Karl, S.; Moore, L. R.; Chalmers, J. J.; Williams, P. S.; Zborowski, M., Sequential CD34 cell fractionation by magnetophoresis in a magnetic dipole flow sorter, *Analyst,* **2010**, *135* (1), 62-70.
(296) Kabeya, Y.; Mizushima, N.; Yamamoto, A.; Oshitani-Okamoto, S.; Ohsumi, Y.; Yoshimori, T., LC3, GABARAP and GATE16 localize to autophagosomal membrane depending on form-II formation, *Journal of Cell Science,* **2004**, *117* (13), 2805-2812.
(297) Weidberg, H.; Shvets, E.; Elazar, Z. In *Annual Review of Biochemistry, Vol 80*; Kornberg, R. D., Raetz, C. R. H., Rothman, J. E., Thorner, J. W., Eds.; Annual Reviews: Palo Alto, 2011; Vol. 80, pp 125-156.

(298) Shpilka, T.; Weidberg, H.; Pietrokovski, S.; Elazar, Z., Atg8: an autophagy-related ubiquitin-like protein family, *Genome Biology,* **2011**, *12* (7).
(299) Lombardi, D.; Soldati, T.; Riederer, M. A.; Goda, Y.; Zerial, M.; Pfeffer, S. R., RAB9 Functions in Transport between Late Endosomes and the trans-Golgi Network, *EMBO Journal,* **1993**, *12* (2), 677-682.
(300) Matteoni, R.; Kreis, T. E., Translocation and clustering of endosomes and lysosomes depends on microtubules, *The Journal of Cell Biology,* **1987**, *105* (3), 1253-1265.
(301) Smith, C. A.; Maille, G. O.; Want, E. J.; Qin, C.; Trauger, S. A.; Brandon, T. R.; Custodio, D. E.; Abagyan, R.; Siuzdak, G., METLIN: A Metabolite Mass Spectral Database, *Therapeutic Drug Monitoring,* **2005**, *27* (6), 747-751.
(302) Sumner, L. W.; Amberg, A.; Barrett, D.; Beale, M. H.; Beger, R.; Daykin, C. A.; Fan, T. W.-M.; Fiehn, O.; Goodacre, R.; Griffin, J. L., Proposed minimum reporting standards for chemical analysis, *Metabolomics,* **2007**, *3* (3), 211-221.
(303) Sou, Y.-s.; Waguri, S.; Iwata, J.-i.; Ueno, T.; Fujimura, T.; Hara, T.; Sawada, N.; Yamada, A.; Mizushima, N.; Uchiyama, Y.; Kominami, E.; Tanaka, K.; Komatsu, M., The Atg8 Conjugation System Is Indispensable for Proper Development of Autophagic Isolation Membranes in Mice, *Molecular Biology of the Cell,* **2008**, *19* (11), 4762-4775.
(304) Kitteringham, N. R.; Jenkins, R. E.; Lane, C. S.; Elliott, V. L.; Park, B. K., Multiple reaction monitoring for quantitative biomarker analysis in proteomics and metabolomics, *Journal of Chromatography B,* **2009**, *877* (13), 1229-1239.
(305) Rubinsztein, David C.; Shpilka, T.; Elazar, Z., Mechanisms of Autophagosome Biogenesis, *Current Biology,* **2012**, *22* (1), R29-R34.
(306) Weidberg, H.; Shvets, E.; Elazar, Z., Lipophagy: Selective Catabolism Designed for Lipids, *Developmental Cell,* **2009**, *16* (5), 628-630.
(307) Kim, I.; Rodriguez-Enriquez, S.; Lemasters, J. J., Selective degradation of mitochondria by mitophagy, *Archives of Biochemistry and Biophysics,* **2007**, *462* (2), 245-253.
(308) Dunn, W. A.; Cregg, J. M.; Kiel, J.; van der Klei, I. J.; Oku, M.; Sakai, Y.; Sibirny, A. A.; Stasyk, O. V.; Veenhuis, M., Pexophagy - The selective autophagy of peroxisomes, *Autophagy,* **2005**, *1* (2), 75-83.
(309) Cebollero, E.; Reggiori, F.; Kraft, C., Reticulophagy and Ribophagy: Regulated Degradation of Protein Production Factories, *International Journal of Cell Biology,* **2012**, *2012*.
(310) Zhu, J.; Dagda, R.; Chu, C. In *Neurodegeneration*; Manfredi, G., Kawamata, H., Eds.; Humana Press, 2011; Vol. 793, pp 325-339.
(311) Chan, N. C.; Salazar, A. M.; Pham, A. H.; Sweredoski, M. J.; Kolawa, N. J.; Graham, R. L. J.; Hess, S.; Chan, D. C., Broad activation of the ubiquitin–proteasome system by Parkin is critical for mitophagy, *Human Molecular Genetics,* **2011**, *20* (9), 1726-1737.
(312) Blanchette-Mackie, E. J.; Dwyer, N. K.; Barber, T.; Coxey, R. A.; Takeda, T.; Rondinone, C. M.; Theodorakis, J. L.; Greenberg, A. S.; Londos, C., Perilipin is located on the surface layer of intracellular lipid droplets in adipocytes, *Journal of Lipid Research,* **1995**, *36* (6), 1211-1226.

(313) Narendra, D. P.; Jin, S. M.; Tanaka, A.; Suen, D. F.; Gautier, C. A.; Shen, J.; Cookson, M. R.; Youle, R. J., PINK1 Is Selectively Stabilized on Impaired Mitochondria to Activate Parkin, *PLoS Biology*, **2010**, *8* (1).
(314) Geisler, S.; Holmstrom, K. M.; Skujat, D.; Fiesel, F. C.; Rothfuss, O. C.; Kahle, P. J.; Springer, W., PINK1/Parkin-mediated mitophagy is dependent on VDAC1 and p62/SQSTM1, *Nature Cell Biology*, **2010**, *12* (2), 119-U170.
(315) Saeki, K.; Suzuki, H.; Tsuneoka, M.; Maeda, M.; Iwamoto, R.; Hasuwa, H.; Shida, S.; Takahashi, T.; Sakaguchi, M.; Endo, T.; Miura, Y.; Mekada, E.; Mihara, K., Identification of mammalian TOM22 as a subunit of the preprotein translocase of the mitochondrial outer membrane, *Journal of Biological Chemistry*, **2000**, *275* (41), 31996-32002.
(316) van Zutphen, T.; Veenhuis, M.; van der Klei, I. J., Pex14 is the sole component of the peroxisomal translocon that is required for pexophagy, *Autophagy,* **2008**, *4* (1), 63-66.
(317) Koegler, E.; Bonnon, C.; Waldmeier, L.; Mitrovic, S.; Halbeisen, R.; Hauri, H. P., p28, A Novel ERGIC/cis Golgi Protein, Required for Golgi Ribbon Formation, *Traffic*, **2010**, *11* (1), 70-89.
(318) Mutoh, T.; Rudkin, B. B.; Guroff, G., Differential Responses of the Phosphorylation of Ribosomal Protein-S6 to Nerve Growth-Factor and Epidermal Growth-Factor in PC12-cells, *Journal of Neurochemistry*, **1992**, *58* (1), 175-185.

Appendix A

Supplementary Material to Chapter 3

Individual organelle pH determinations via laser-induced fluorescence detection of magnetically-enriched endocytic organelles

A.1. Imaging

Fluorescent regions were defined by those pixels with fluorescence intensities above the threshold, defined as the background plus five times the standard deviation of the background. Cross-talk caused by detection of Lysotracker Red and AlexaFluor488-FeDex in the wrong imaging setting was calculated by treating cells with only one fluorescent label and observing the preparation with the two fluorescence microscope filter sets. When cells were treated with only LysoTracker Red, pixels in the green image had on average 9.1% of cross-talk from the red image. This factor was subtracted from the green image to obtain a corrected fluorescence representative of AlexaFluor488-FeDex. There was no detectable cross-talk from the AlexaFluor488-FeDex into the red image.

Manders coefficients M1 and M2 were used to evaluate colocalization of fluorophores in image overlays (Figure 3.3, Figure A-1). These coefficients were calculated as:

$$M_1 = \frac{\sum R_{i,coloc}}{\sum R_i} \qquad \textbf{Equation A.1.}$$

$$M_2 = \frac{\sum G_{i,coloc}}{\sum G_i} \qquad \textbf{Equation A.2.}$$

where $R_{i,coloc}$ = 1 for any pixel with LysoTracker Red fluorescence that also has colocalized AlexaFluor 488 fluorescence, $G_{i,coloc}$ = 1 for any pixel with AlexaFluor488-FeDex fluorescence that also has colocalized LysoTracker Red fluorescence, R_i is total number of pixels showing Lysotracker Red fluorescence, and G_i is the total number of pixels showing AlexaFluor 488 fluorescence.

The intensity correlation quotient (ICQ) was used to compare the trends of fluorescence intensities of AlexaFluor 488 and LysoTracker Red in image overlays. The ICQ was calculated as:

$$ICQ = \frac{\sum sign(R_i > R_{av}) = sign(G_i > G_{av})}{N} - 0.5 \qquad \textbf{Equation A.3.}$$

where R_i and G_i are the LysoTracker Red and AlexaFluor488-FeDex fluorescence at pixel (i), respectively, R_{av} and G_{av} are the respective average intensities for N pixels with colocalized fluorescence, while sign($R_i > R_{av}$) and sign($G_i > G_{av}$) represent the sign (i.e. positive or negative) resulting from comparing the pixel (i) fluorescence intensity relative to the average fluorescence intensity. When both signs are the same, a value of "1" is added. ICQ values range from 0.5 (direct correlation) to -0.5 (inverse correlation).

A.2. Determination of the pH of individual organelles

A.2.1. Synthesis of liposomes used as pH standards

Aliquots of 187 μL of 1.29 × 10-2 M phosphatidylcholine, 169 μL of 1.3 × 10-2 M phosphatidylethanolamine, 30 μL of 2.5 × 10-2 M cholesterol, and 9 μL of 2.3 × 10-2 M phosphatidylserine (all in chloroform) were added and mixed in a 5 mL round bottom flask.[48] The mixture was swirled and concentrated under a stream of nitrogen gas. The sample was dried overnight in a dessicator. Aliquots of 500 μL of various buffers representing various pHs were added to separate round bottom flasks: 10 mM HEPES (pH 7.92), 4 mM phosphate (pHs 7.45 & 6.87), 4 mM succinate (pH 5.89), and 4 mM citrate (pHs 5.05, 4.02, and 3.07). To each flask, Fluorescein-TMRM-conjugated dextran was added to the buffer in the flask (0.4 mg/mL HEPES, 0.4 mg/mL phosphate, 0.5 mg/mL succinate, 1.0 mg/mL 5.05 citrate, 1.9 mg/mL 4.02 citrate, and 3.5 mg/mL 3.07 citrate) and vortexed 5 minutes to form liposomes. After two hours swelling at 4°C, liposomes were centrifuged at 13,200g and washed with their respective buffer. Liposome sample was diluted 1,000x v/v with buffer M and analyzed as described in Chapter 3. Liposomes were analyzed within 48 hours to avoid degradation.

A.2.2 LIF detection of liposomes

Liposomes were delivered to the LIF detector using the same conditions described in the Experimental for the delivery of organelles. Coincidence peaks were identified as described previously. An x-y plot was used to determine the slope (R) of the fluorescein fluorescence intensity versus the TMRM fluorescence intensity for each pH tested. This slope is unique for each pH and is represented as "R". The R values for each pH yield the calibration curve:

$$logR = (0.14 \pm 0.01) \times pH + (0.71 \pm 0.05)$$ **Equation A.4.**

where the errors of the slope and the intercept are determined from the linear fit. The data for this calibration curve are shown in Figure S.3. Since there is also an error associated with "R", we used the maximum error of "R" (i.e., (σ_R = 0.05 at pH 7.9) in combination with the errors of the slope (σ_m) and the intercept (σ_b) to estimate the error of each pH (σ_{pH}) determined from the calibration curve. The expression used to determine σ_{pH} is:

$$\sigma_{pH} = pH\sqrt{\frac{\left(\frac{0.434\sigma_R}{R}\right)^2+\left(\frac{\sigma_b}{b}\right)^2}{\log(r-b)}+\left(\frac{\sigma_m}{m}\right)^2}$$ **Equation A.5.**

A.3. Figures

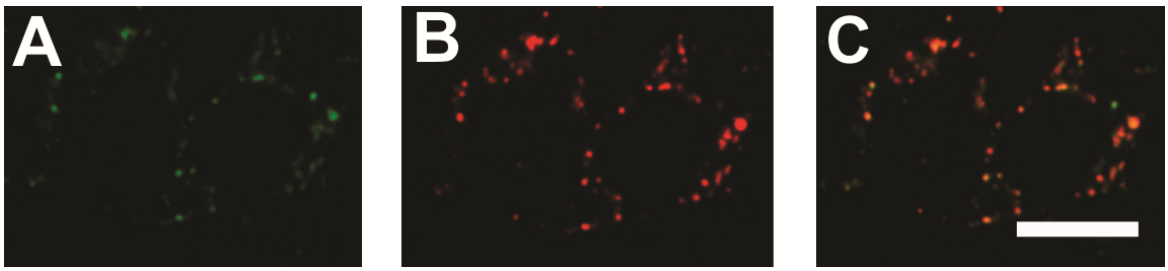

Figure A.1. Confocal microscopy imaging colocalization (A) AlexaFluor488-FeDex detection. (B) LysoTracker Red detection. (C) Overlay. This method was done to create Figure 3.3. in Chapter 3 and perform M1, M2, and ICQ analysis. Scale bar = 10 μm

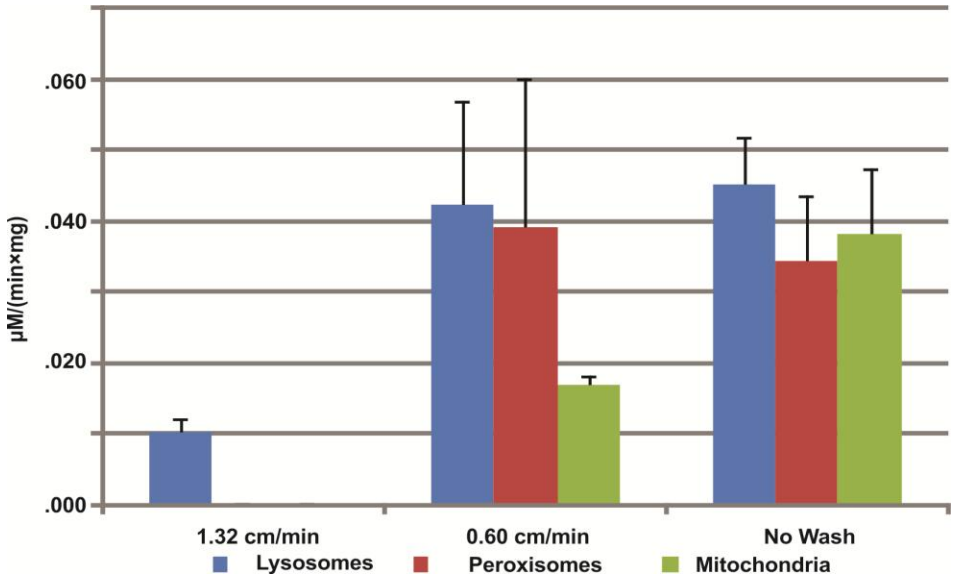

Figure A.2. Selection of washing flow rates. The pNPP (lysosomal), catalase (peroxisomal), and DCIP (mitochondrial) assays were used to determine the composition of the magnetically retained material. All assays were done in triplicate. Thin bars are one standard deviation.

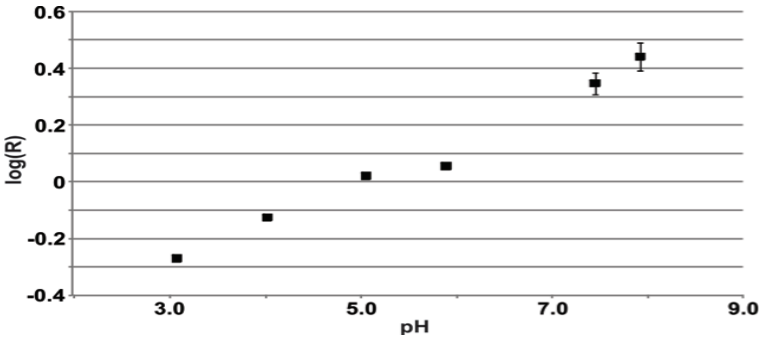

Figure A.3. Calibration curve for pH of individual organelles. Liposomes used as standards contained fluorescein/TMRM-bound dextran. The error bars correspond to the standard deviation of the slope determined from the x-y plot for each pH.

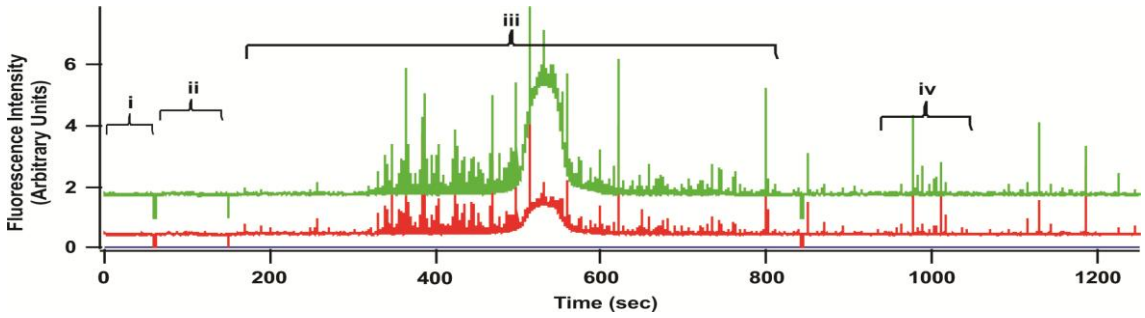

Figure A.4. Raw data from LIF detection shown in Figure 3.4.

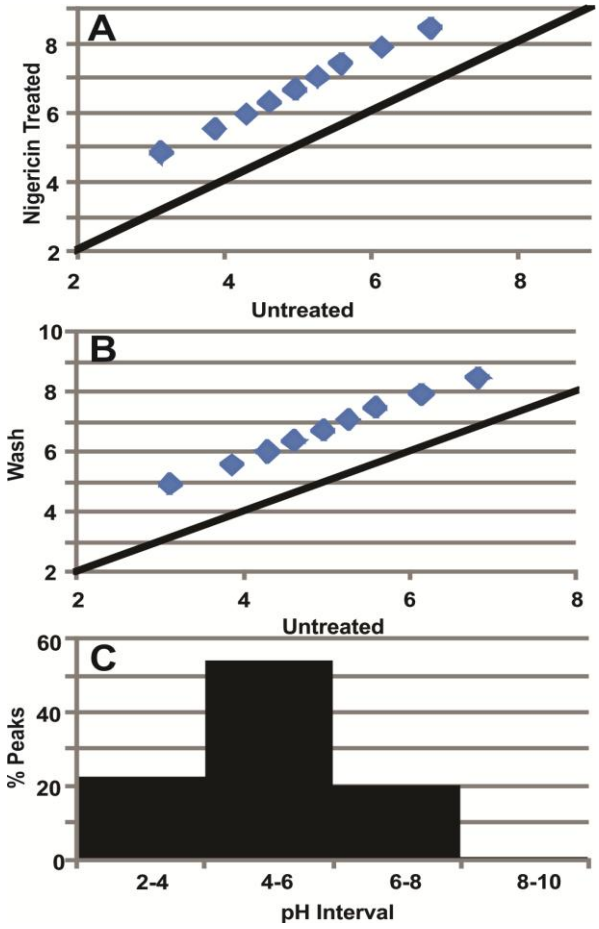

Figure A.5. Comparisons of individual organelle pH values. (A) Q-Q plot comparing pH of unretained organelles from cells not exposed (x-axis) and treated with nigericin (y-axis). (B) Q-Q plot comparing unretained organelles from cells not exposed to FeDex (x-axis) and exposed to FeDex (y-axis). This data was used to determine the correction factor (Table A.1). (C) Corrected data showing the number of unretained organelles within a given pH interval from cells treated with FeDex.

A.4. Tables

Quantile (%)	FeDex Treated	Untreated	Difference
10	4.85	3.14	1.71
20	5.52	3.88	1.64
30	5.95	4.31	1.64
40	6.30	4.63	1.67
50	6.65	4.97	1.68
60	7.01	5.28	1.73
70	7.40	5.60	1.80
80	7.86	6.15	1.71
90	8.41	6.83	1.58
100	10.60	8.69	1.91
		Average	1.7
		S.D.	0.1

Table A.1. Corrections and controls of pH for organelles containing FeDex. The raw data for organelles containing both FeDex and fluorescein/TMRM-bound dextran (Figure S.4 were corrected with a median filter to eliminate the broad band and to determine coincident events as described in the section A.5 (Figure 3.4). Shifting in pH could be caused by treatment with nigericin (Figure S.5A). This is expected because nigericin is a protonophore that dissipates the pH gradient. It was noticed that when FeDex was present all the pH values were shifted (Figure S.5B). Therefore the pH distributions of FeDex treated and untreated were compared quantile by quantile in increments of 10% (Table S.1). The average difference, 1.7 ± 0.1 pH units, was used to adjust the pH of organelles treated with FeDex. An example of the corrected data is shown in Figure S.5C.

Appendix B

Supplementary Material to Chapter 4

Magnetically Enriched Endocytic Organelles from Uterine Sarcoma Cells Biotransform the Prodrug *N*-L-Leucyldoxorubicin into Doxorubicin

B.1. Figures

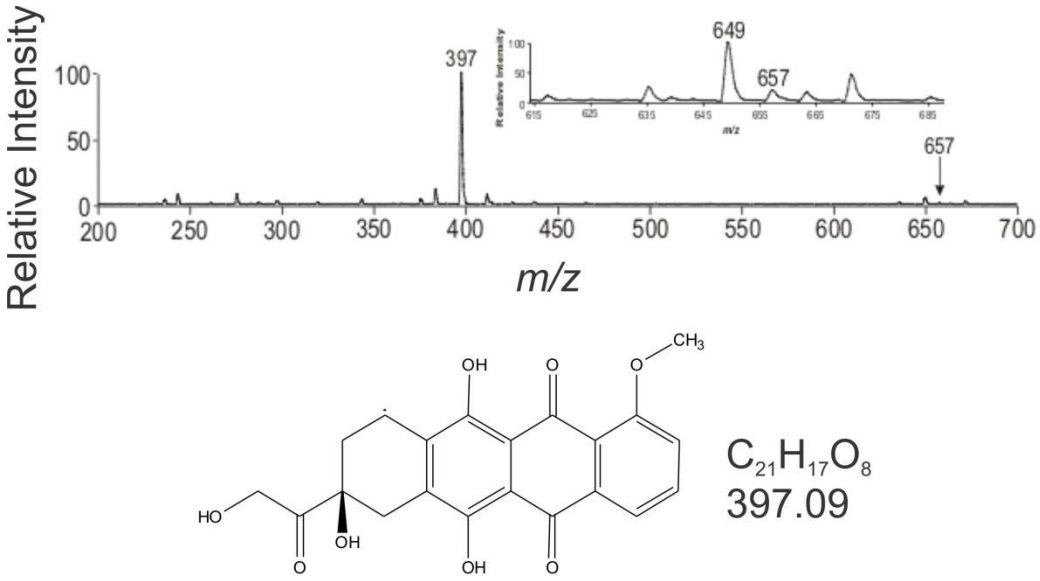

Figure B.1. Mass spectrometry of LeuDox. LeuDox sample analysis resulted in a clean mass spectrum with the major and minor peaks decreasing in magnitude during formation of Dox. When characterizing the LeuDox synthesis product, one other *m/z* value was detected by mass spectrometry that has the anthracycline ring and could be detected by fluorescent detection (*m/z* = 397). A Waters Acquity Triple Quadrupole instrument was used with electrospray ionization in positive ion mode. Direct infusion of purified Leu-Dox (10^{-4} M in methanol) resulted in the expected *m/z* value of the parent ion (*m/z* = 657).

Appendix C

Supplementary Material to Chapter 5

UPLC-MSe, Chemometrics, and Mass Spectral Evaluation Criteria for Preliminary Identification of Chemical Entities Specific to Enriched Autophagosomes and Activated Mast Cells

C.1. Tables

System[1]	Ext[2]	ESI[3]	Potential Features	Candidate Features	Confirmed Features	% CF[4]	Potential IDs	Preliminary IDs
Liver	Polar	+	2086	62	45	11	28	14
Liver	NP	+	1045	49	28	23	18	9
Liver	NP	-	437	3	3	0	0	0
Myoblast	Polar	+	1440	56	51	19	37	7
Myoblast	NP	+	2008	55	45	22	28	3
Myoblast	NP	-	1624	19	16	19	4	2
MCN (vs. MCX)	NA	-	4765	10	10	39	1	0
MCCX (vs. MCN)	NA	-	4765	11	8	0	6	0
MCN (vs. MCTN)	NA	+	1914	398	286	23	3	1
MCTN (vs. MCN)	NA	+	1914	181	136	50	24	6
MCN (vs. MCTN)	NA	-	2843	487	186	3	12	1
MCTN (vs. MCN)	NA	-	2843	266	102	41	23	2
MCB (vs. MCCX)	NA	+	1804	187	168	13	19	3
MCCX (vs. MCB)	NA	+	1804	449	431	33	2	0

MCB (vs. MCCX)	NA	-	2985	248	148	4	20	1
MCCX (vs. MCB)	NA	-	2985	418	186	15	4	0

Table C.1. Summary of workflow. [1]- Liver = enriched autophagosomes from liver; myoblast = enriched autophagosomes from rat myoblasts; MCN = mast cells, non-activated; MCTN = TNPova-activated mast cells; MCCX = CXCL10-activated mast cells; MCB = Both CXCL10- and TNPova-activated. [2]- Extractions performed were either nonpolar (NP) or polar (see materials & methods). NA = no extraction made. [3]- ESI analysis was performed in positive (+) and negative (-) ionization modes. [4]- % C.F. = the percentage of common confirmed features detected in a system by OPLS-DA and either LMM or t-test.

C.2. Figures

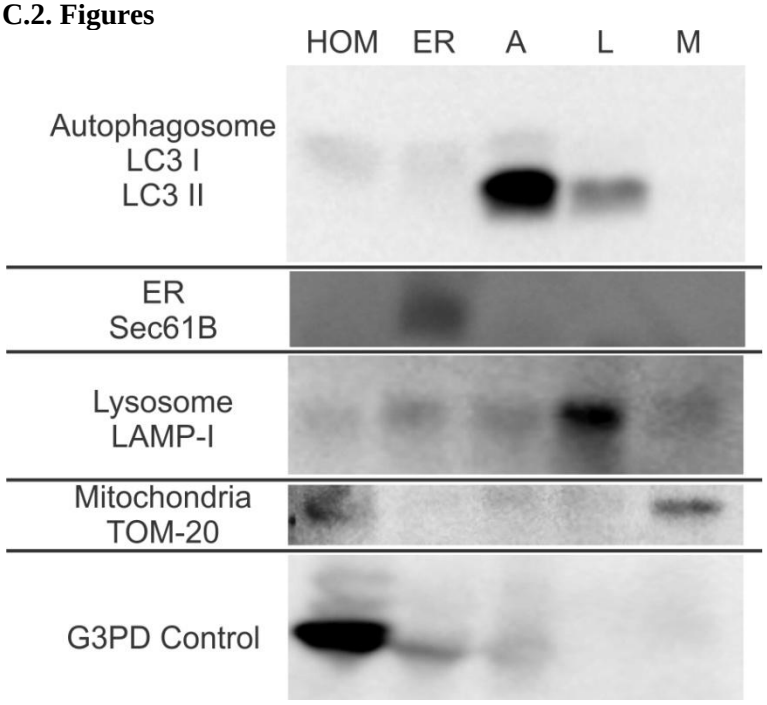

Figure C.1. Western blots of rat liver autophagosome-enriched fractions revealed the autophagosome fraction was free of contamination from other organelles. From rat liver homogenate (HOM), a pellet containing the nuclear fraction and (up to 30%) unbroken cells was produced. The supernatant was centrifuged at 17000g and the pellet is enriched in autophagosomes, lysosomes and mitochondria. The supernatant was centrifuged at 100000g and the pellet contains the vesicles in the non autophagosome, endoplasmic reticulum enriched fraction (ER). From the 17000g pellet fraction, autophagosome (A), lysosome (L), and mitochondria (M) were separated by differential centrifugation in discontinuous density metrizamide gradients as described in the manuscript. Experimental antibodies were anti-LC3 (1:500 v/v dilution, rabbit, NB-2220, Novus Biologicals, Littleton, CO), anti-SEC61B antibody (1:2000 v/v dilutionb, rabbit, NB100-74530) Novus Biologicals (Littleton, CO), anti-LAMP1 antibody (1:1000 v/v, rabbit, ab24170, Abcam, Cambridge, MA), anti-Tom20 antibody FL-145 (1:500 v/v dilution, rabbit, sc-11415, Santa Cruz Biotechnology, Santa Cruz, CA), and anti-G3PD antibody (1:500 v/v dilution, rabbit, 600-401-A33, 600-401-A33, Rockland, Gilbertsville, PA). Anti-rabbit (R21459) or anti-mouse (G21234) IgG (H+L) horseradish peroxidase secondary antibodies (1:5,000 v/v dilution, goat, Invitrogen, Carlsbad, CA) were used for

chemiluminescence detection (Renaissance, NEN-Life Science Products). Membranes were exposed to BioMax Light Kodak films (Kodak Scientific Films) for increasing periods of time ranging from 5 s to 10 min.

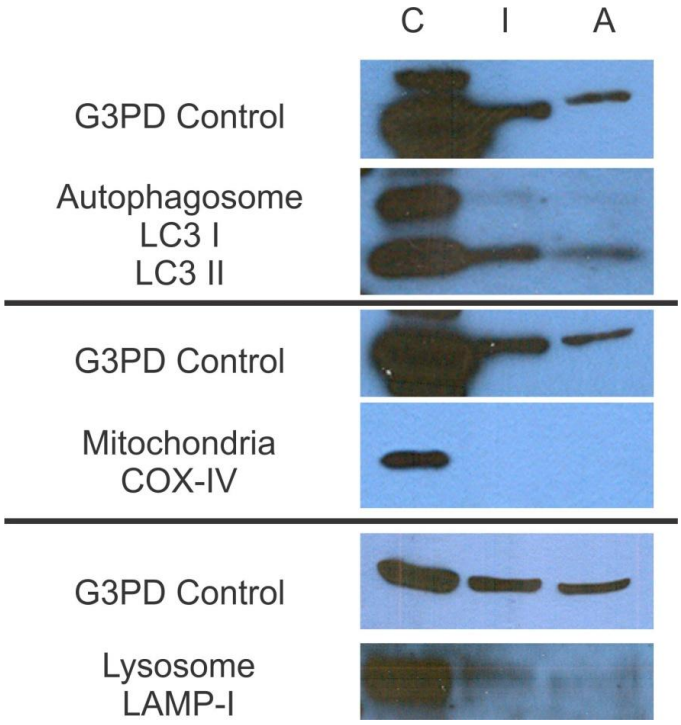

Figure C.2. Western blots of autophagosome-enriched fractions from rat myoblasts show minimal mitochondria and lysosome contamination. Non-enriched, control organelle fraction (C), a semi-enrichment fraction (I), and the autophagosome-enriched fraction (A) were loaded onto a 15.0% "12+2" well SDS-PAGE gel (Criterion, Hercules, CA). Precision Plus Protein Dual Color standards (BioRad, USA) were used as a ladder for determination of molecular weights. The gel was run for 125 V for 60 min. Proteins were transferred onto a nitrocellulose membrane, 0.45 μm (BioRad, Germany). Transfer was done at constant voltage (100 V) for 2 h. Experimental antibodies were anti-LC3 (1:500 v/v dilution, rabbit, NB-2220, Novus Biologicals, Littleton, CO), anti-LAMP1 antibody (1:1000 v/v, rabbit, ab24170, Abcam, Cambridge, MA), and anti-COX-IV (1:500 v/v dilution, mouse, ab14744, Abcam,Cambridge, MA). Antibodies were diluted in 4% skim milk (Nestle, Eden Prarie, MN) in TBS/T solution (BioRad, USA). Anti-rabbit (R21459) or anti-mouse (G21234) IgG (H+L) horseradish peroxidase secondary antibodies (1:5,000 v/v dilution, goat, Invitrogen, Carlsbad, CA) were used for chemiluminescent detection. Membranes were imaged on a SRX-101A from Konica Minolta using Super Signal West Femto Maximum Sensitivity Substrate (Thermo Fisher, Rockford, IL). Glyceraldehyde 3-

phosphate dehydrogenase (G3PD) was used as a positive control for the Western blotting system to ensure lanes contained protein. anti-G3PD antibodies were used for determination of G3PD as a loading control (1:500 v/v dilution, rabbit, 600-401-A33, Rockland, Gilbertsville, PA).

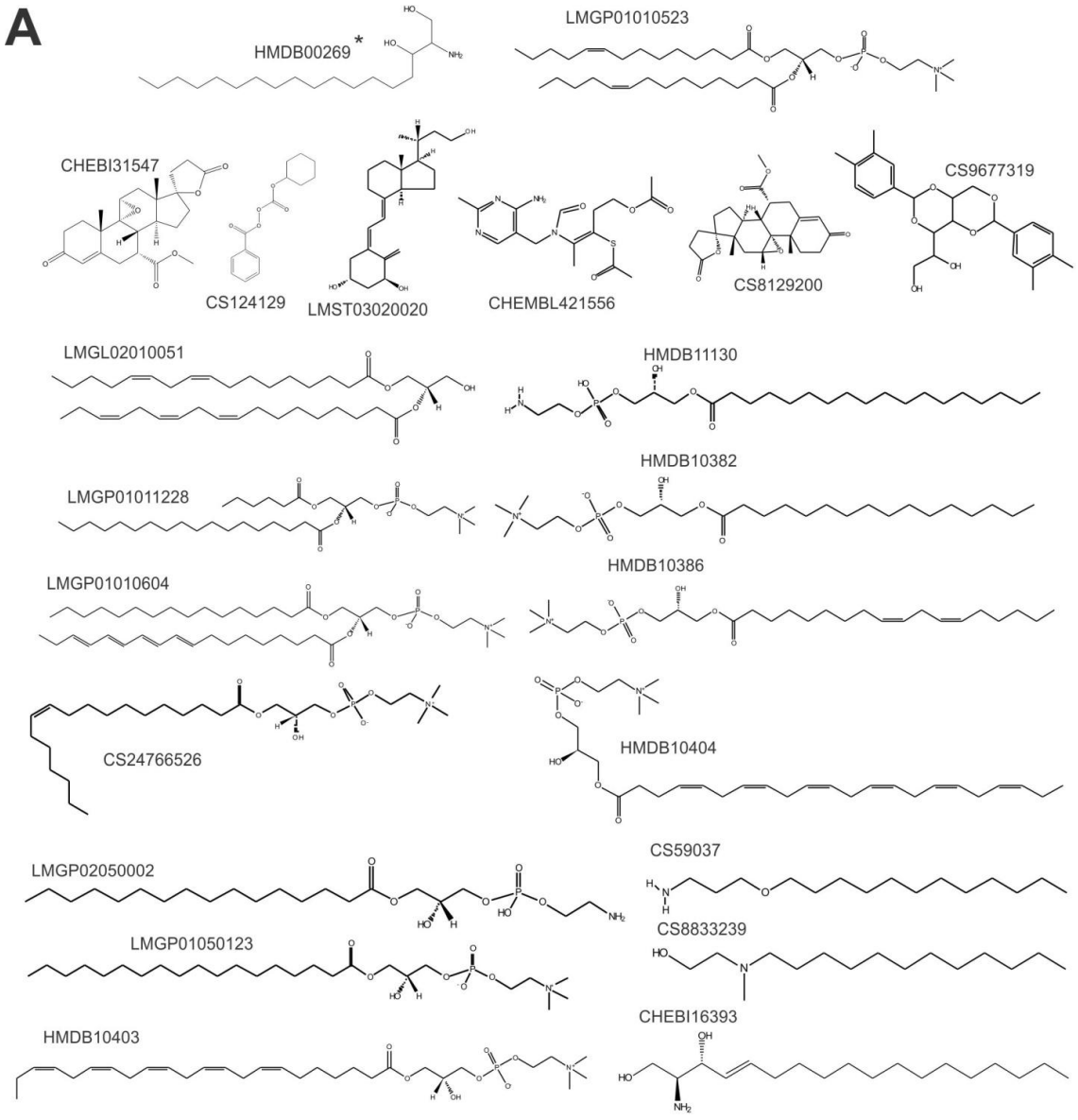
A
HMDB00269*
LMGP01010523
CHEBI31547
CS124129
LMST03020020
CHEMBL421556
CS8129200
CS9677319
LMGL02010051
HMDB11130
HMDB10382
LMGP01011228
HMDB10386
LMGP01010604
CS24766526
HMDB10404
CS59037
LMGP02050002
CS8833239
LMGP01050123
CHEBI16393
HMDB10403

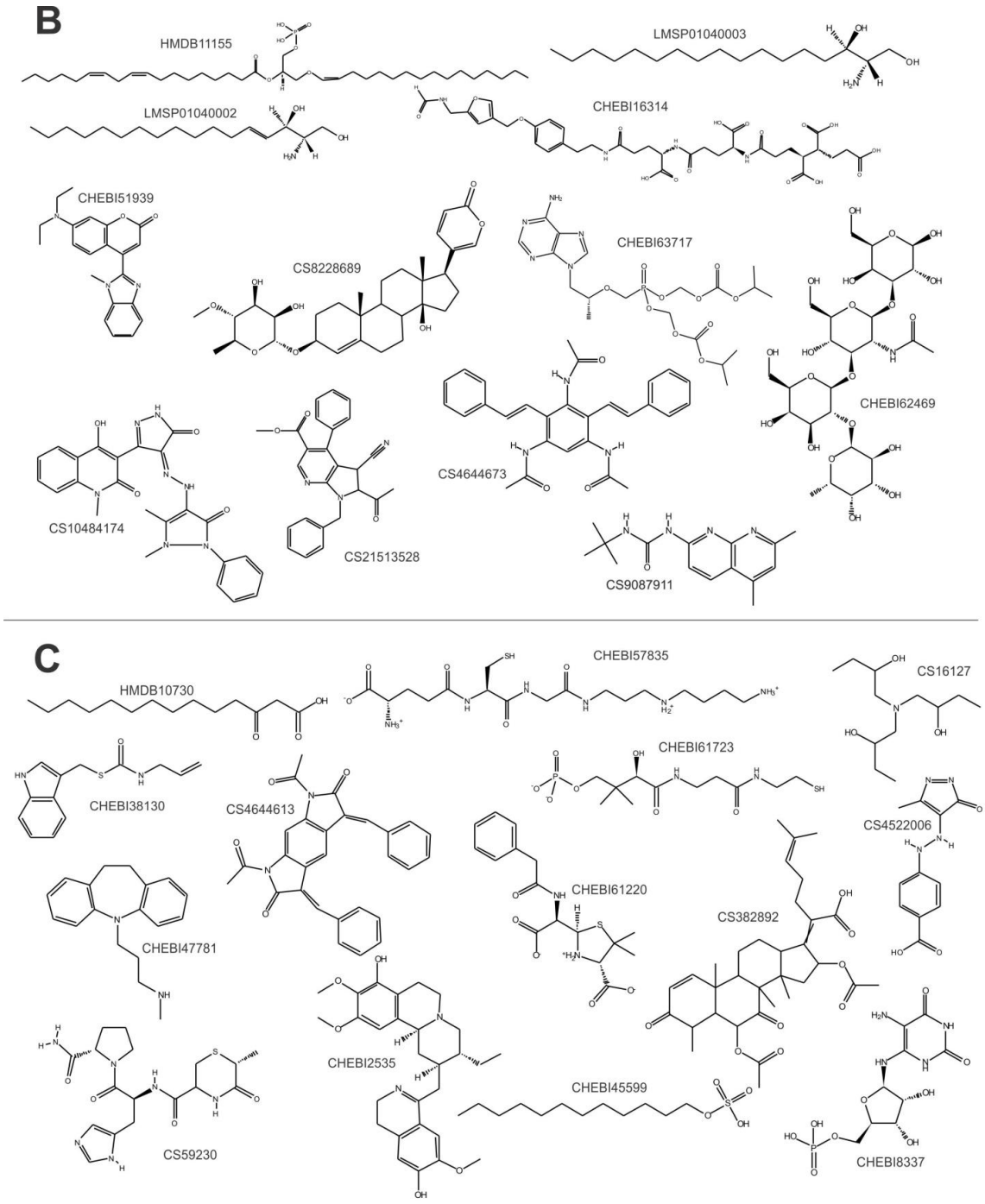

Figure C.3. Structures of preliminary identifications made for (A) rat liver autophagosomes, (B) rat myoblast autophagosomes, and (C) chemically activated mast cells. Two structural isomers of compound HMDB00269(*) were detected in enriched rat liver autophagosomes (Table 5.1.).

Appendix D

Supplementary Material to Chapter 6

Describing the temporal nature of autophagy at the individual organelle level by Capillary Electrophoresis with Laser Induced Fluorescence Detection

D.1. Fluorescence Confocal Microscopy

Preparation of cells for fluorescent confocal microscopy was done as previously described.[88] Briefly, LabTek 4 chambered coverslips were incubated with poly-L-lysine (100 μL) for 30 min. prior to cell culture to improve cellular attachment to the coverslip. Cells were treated with vinblastine, rapamycin, or both vinblastine and rapamycin. Cells were fixed with 4% v/v formaldehyde in water, then permeabilized with 10% v/v Triton X-100 in water, and finally incubated with 5% w/v BSA to reduce non-specific binding of antibodies.[88] Cells were then incubated with rabbit anti-LC3 antibody (1 μL in 250 μL; 2% w/v BSA in 1× PBS) overnight. Cells were then washed with 1× PBS three times for 5 minutes with PBS. Cells were then incubated with goat anti-rabbit AlexaFluor568 secondary antibody specific to anti-LC3 antibody (1 μL in 250 μL; 2% w/v BSA in 1× PBS) for 1 hour. Cells were again washed with 1× PBS three times for 5 minutes to remove unbound antibody.

Images were acquired with an Olympus IX81 inverted microscope (Melville, NY) as previously described.[88] Data analysis of microscopy images was done with Simple PCI 5.3 (Compix Inc., Cranberry Township, PA) as previously described.[88] Colocalization was calculated between GFP-LC3 and anti-LC3 fluorescent signals using Equations D.1., D.2., D.3., and D.4.[86] The M2 coefficient confirmed the GFP-transfected protein was LC3 (Table D.1). The R and ICQ coefficients indicated a 70-95% correlation between GFP and AlexaFluor568 (See Appendix, Table D.1). GFP-labeled organelles were observed in all samples with more intense organelles appearing in the vinblastine-treated samples (Figure D.1).

D.2.Microscopy Correlation and Colocalization Equations

Five regions of interest (ROIs) of the extracellular background were assessed to remove native fluorescence. The average ROI fluorescence (Ave_{ROI}) and standard deviation (σ_{ROI}) were determined. To remove native fluorescence, the sum of Ave_{ROI} and $5\sigma_{ROI}$ were subtracted from each image. WCIF Image J-W, version 1.43s (National Institutes of Health) was used to calculate the Manders overlap coefficients (R, M1 and

M2), Pearsons Correlation Coefficient (r), and intensity correlation coefficient (ICQ). The Pearsons Correlation Coefficient was calculated as follows:

$$r = \frac{\sum(R_i - R_a) \times (G_i - G_a)}{\sqrt{\sum(R_i - R_a)^2 \times \sum(G_i - G_a)^2}}$$ **Equation D.1.**

where R_i is red fluorescence intensity in pixel (i), R_a is the average red fluorescence intensity, G_i is green fluorescence intensity in pixel (i), G_a is the average green fluorescence intensity. This coefficient measures the linear relationship between the intensities of two fluorophores on a pixel-by-pixel basis. Its range is from -1 to +1.

The Manders Overlap Coefficient (R) was calculated as follows:

$$R = \frac{\sum(R_i) \times (G_i)}{\sqrt{\sum(R_i)^2 \times \sum(G_i)^2}}$$ **Equation D.2.**

where the parameters are the same as those defined for the Pearson Correlation Coefficient. Its range is from 0 to +1.

The M2 Coefficient gives the number of green fluorescence pixels (GFP) that also register red fluorescence (AlexaFluor568) was calculated as follows:

$$M2 = \frac{\sum G_{i,coloc}}{\sum G_i}$$ **Equation D.3.**

where $G_{i,coloc}$ is the number of green fluorescence pixels with colocalized red fluorescence, and G_i is the total number of pixels registering green fluorescence. Its range is from 0 to +1.

The ICQ was calculated as follows:

$$ICQ = \frac{\sum(R_i > R_a) = (G_i > G_a)}{N} - 0.5$$ **Equation D.4.**

where the expression in the numerator refers to counting the number of pixels where both red (R_i) and green (G_i) fluorescence in pixel (i) are above or below their respective average, (R_a and G_a), and N is the total number of pixels. The range of ICQ is from -0.5 to +0.5.

	R	R	M2	ICQ
Control (n=7)	0.79 ± 0.08	0.57 ± 0.15	0.94 ± 0.08	0.24 ± 0.15
Vinblastine-treated (n=6)	0.84 ± 0.08	0.61 ± 0.08	1.00 ± 0.00	0.21 ± 0.05
Rapamycin-treated (n=7)	0.95 ± 0.02	0.78 ± 0.08	0.98 ± 0.03	0.32 ± 0.06

Table D.1. Summary of colocalization analysis of GFP and Immunolabeling with a secondary antibody labeled with AlexaFluor 569.

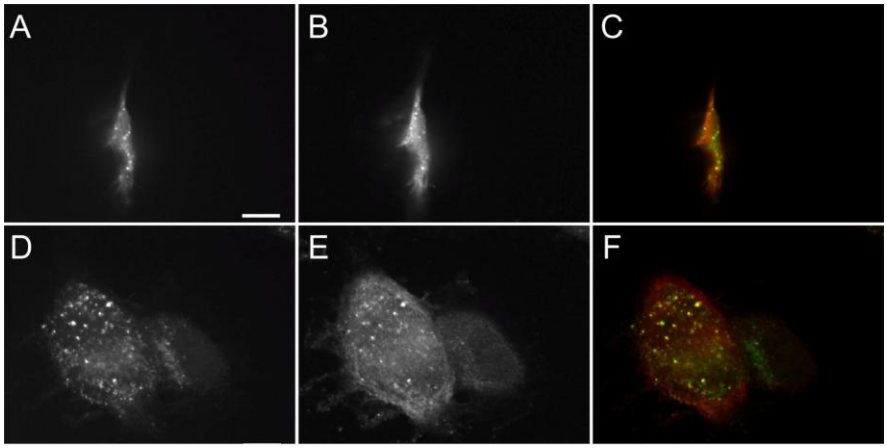

Figure D.1. Exemplary fluorescence confocal microscopy of two different vinblastine-treated L6 cells expressing GFP-LC3. Green fluorescence is from GFP-LC3 and red fluorescence is from the secondary antibody labeled with AlexaFluor 586. (A) AlexaFluor 568 fluorescence of vinblastine-treated cell. (B) GFP fluorescence of vinblastine-treated cell. (C) Overlay of (A) and (B). (D) AlexaFluor 568 fluorescence of vinblastine-treated cell. (E) GFP fluorescence of vinblastine-treated cell. (F) Overlay of (D) and (E). Scale bar = 10 μm.

D.3. Detector calibration and correction for variations in sensitivity and electrophoretic mobility.

To align the custom built instrument, AlignFlow flow cytometry alignment beads (Life Technologies, Grand Island, NY, 1:100 v:v in CE buffer) were used to align the PMT detector. (Figure D.2.). All relative standard deviations determined for the AlignFlow beads were below or equal to 27%, which is the manufacturer's reported value (Table D.2.). This indicates the custom built instrument was aligned and that reproducible measurements of the fluorescence intensity of individual organelles can be made. Any detected changes in the GFP-LC3 levels of organelles on a given day can be attributed to differences in the autophagy organelles rather than the alignment.

Changes in detector sensitivity were determined to correct for changes in organelle GFP-LC3 levels as described in Section 6.4.6. Since sensitivity can change from day to day, a correction factor needed to be applied for changing sensitivity so that organelle values are not biased because of a changed sensitivity on different days. In order to make this correction, we needed to confirmed that the alignment was the main source of any changes in detector sensitivity rather than changes in optics such as cleanliness and distances between optics. The expected decrease in standard deviation of the electropherogram background was calculated, which is proportional to the loss of background fluorescence signal. Overall, the percent difference between the calculated and observed standard deviation was between 2-14% for the four different days which separations were run. This difference suggests that the alignment of the custom-built instrument was the main cause for changing sensitivity and potential changes in GFP-LC3 levels and confirms that the background can be used to make corrections. These low deviations suggest there may be a slight change in the cleanliness of the optics of the custom-built CE instrument and the proximity between the capillary tip and laser may have changed for separations done on different days.

While individual autophagy organelle fluorescence levels were corrected for differences in sensitivity of the fluorescence detector, detection of low-intensity autophagy organelle events such as phagophores and autolysosomes may not be detected in some electropherograms due to changes in limits of detection. This can cause some comparisons of organelle quantiles to be slightly skewed due to the inability to detect all individual organelles. The two treatments that were the most affected by this are the

untreated and rapamycin-treated conditions. If we assume lower intensity events were not detected, detection of these low intensity events could lower the GFP-LC3-II values of all the percentile values (Figure 6.3). This would make the distance values between quantiles for the lowest percentiles larger in magnitude. The magnitude of this change in distance is undeterminable, if a change occurs. Overall, it is important to reiterate that when comparing percentiles of organelle events, these are comparisons of only the *detected* organelle events. Additional optimization of the custom-built CE-LIF instrument and development of new probes with increased fluorescence emission levels could optimize the detection of all autophagy organelle events.

Experiment	%RSD	Points Per Peak	n
Basal	15	10	212
Vinblastine	13	15	154
Rapamycin	26	15	199
Both Vinblastine and Rapamycin	13	12	145

Table D.2. Alignment of CE-LIF detector prior to individual organelle detection. AlignFlow beads were delivered to the detector using 10psi to align the detector and minimize the relative standard deviation (%RSD) of peak intensities. The observed %RSD was comparable to the %RSD of the AlignFow beads provided by Life Technologies (28%) suggesting that the custom-built instrument was aligned to provide reproducible fluorescence intensity levels of particles or organelles. The points per peak values suggest particles were not undersampled and that reported %RSD values are accurate. To confirm that 10 psi provided a linear flow of beads similar to the separation voltage used for autophagy organelle separation, (-300 V/cm), alignment with AlignFlow beads was also done at -297 V/cm. This separation voltage resulted in a %RSD for bead intensity of 19.3% with 13 points per peak. These values are comparable to values obtained with 10 psi. AlignFlow Beads first appeared after ~275 sec when using 10 psi. Using the pre-migration window for autophagosomes (450-500 sec), we can estimate the linear flow from voltage-based alignment and separations to be 2-fold reduced compared to the linear flow from pressure-based alignment, however, this reduction does not appear to change the alignment values.

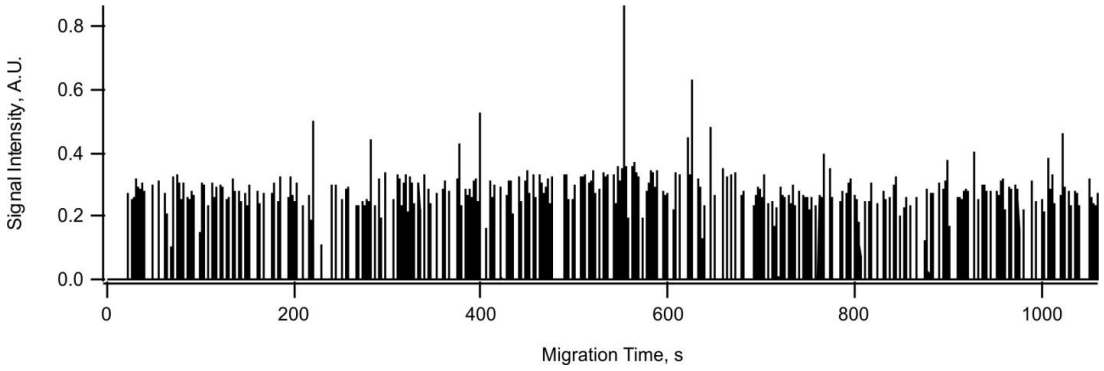

Figure D.2. Alignment of CE-LIF detector for individual organelle detection. AlignFlow beads were diluted in CE buffer (1% v/v) and were flowed through the capillary at 10 psi. The %RSD of the beads was 15% and the average points per peak was 10.

Basal autophagy, no vinblastine	Trial 1	Trial 2	Trial 3
$m_{critical}$	152	100	98
α	0.13	0.17	0.17
P	134	84	83
X	97	67	77
Bins	12	14	14
BWO	0	3	5
$m_{detected}$		128, 135, 230,	117, 167, 123, 140, 157
Basal autopahgy, vinblastine	Trial 1	Trial 2	Trial 3
$m_{critical}$	197	182	196
α	0.11	0.11	0.11
P	177	163	175
X	87.4	77.3	86.6
Bins	15	20	17
BWO	3	7	5
$m_{detected}$	322, 321, 235	299, 831, 683, 414, 430, 278, 464	274, 364, 298, 258, 294
Rapamycin-enhanced autophagy, no vinblastine	Trial 1	Trial 2	Trial 3
$m_{critical}$	251	284	281
α	0.09	0.09	0.09
P	229	261	257

X	107.6	104.6	128.1
Bins	15	17	16
BWO	2	3	1
$m_{detected}$	399, 389	553, 684, 324	473
Rapamycin-enhanced autophagy, Vinblastine	Trial 1	Trial 2	Trial 3
$m_{critical}$	254	277	284
α	0.09	0.09	0.09
P	232	254	260
X	109.4	125.6	130.1
Bins	13	14	10
BWO	0	1	0
$m_{detected}$		286	

Table D.3. Estimation of organelle events from observed peaks. A conservative number of organelles ($m_{critical}$) was used for bins showing saturation ($m_{detected} > m_{critical}$). Saturation is defined based on Statistical Overlap Theory, where $m_{detected}$ is the number of observed peaks in a bin, $m_{critical}$ is the maximum number of organelle events per bin that can be detected without predicted overlap, α is the type-1 error (Equation 6.9), X is the bin width in seconds, and BWO is the number of Bins With predicted Overlap.

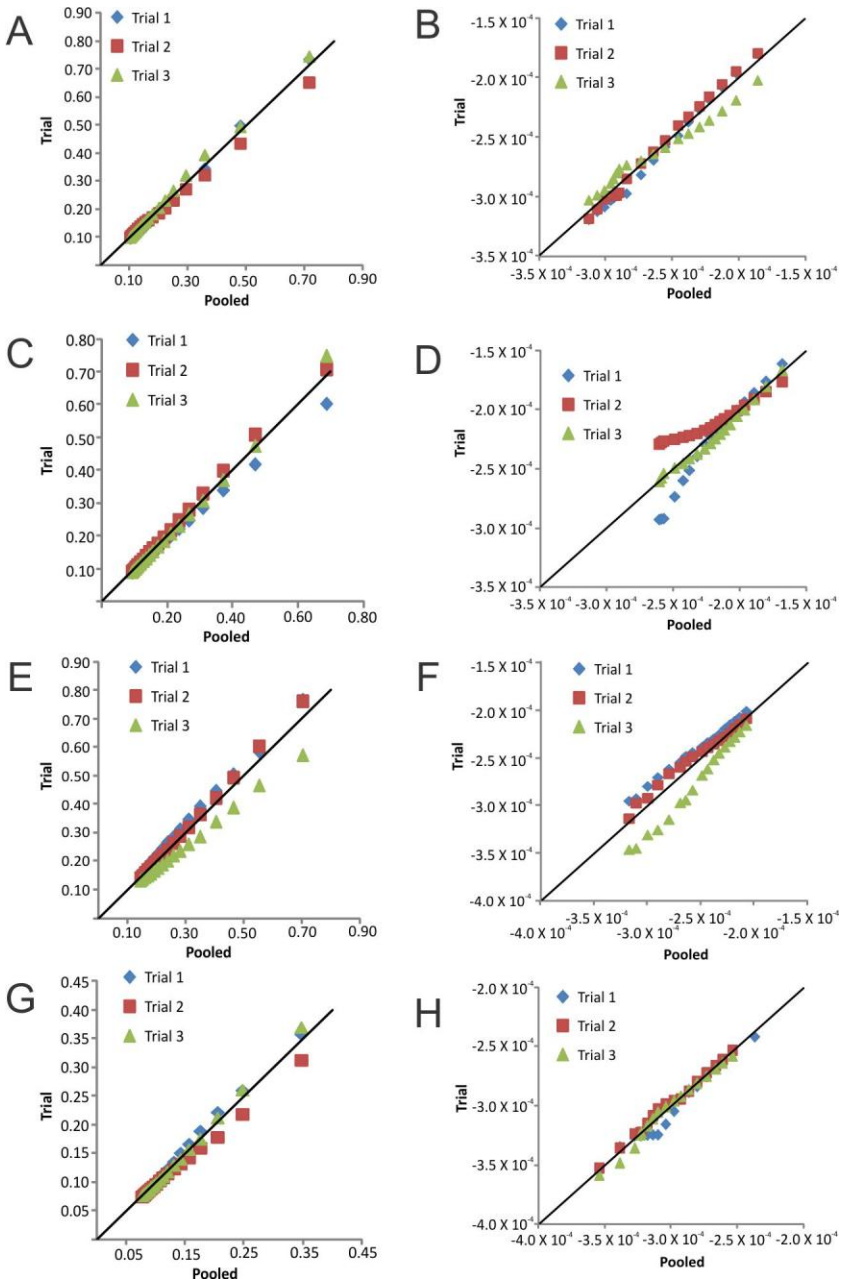

Figure D.3. Reproducibility CE-LIF runs. QQ plots of each replicate (y-axis) versus the pooled data (x-axis). (A) GFP-LC3 fluorescence intensity, basal autophagy. (B) Electrophoretic mobility, basal autophagy. (C) GFP-LC3 fluorescence intensity, basal autophagy and vinblastine treatment. (D): Electrophoretic mobility, basal autophagy and vinblastine treatment. (E): GFP-LC3 fluorescence intensity, rapamycin-enhanced autophagy. (F) Electrophoretic mobility, rapamycin-enhanced autophagy. (G): GFP-LC3 fluorescence intensity, rapamycin-enhanced